

# **Carrier Dynamics and Light Amplification in Triple-Cation Perovskites**

Zur Erlangung des akademischen Grades einer  
Doktorin der Ingenieurwissenschaften (Dr.-Ing.)

von der KIT-Fakultät für

Elektrotechnik und Informationstechnik  
des Karlsruher Instituts für Technologie (KIT)

angenommene

Dissertation

von

**M.Sc. Allegro, Isabel**

geb. in Porto, Portugal

Tag der mündlichen Prüfung: 11. Dezember 2023

Hauptreferent: Prof. Dr. rer. nat. Uli Lemmer

Korreferentin: Prof. Dr. María A. Díaz-García



# Abstract

Hybrid perovskite semiconductors have recently emerged as promising optical gain media for lasers, as high-absorbing direct-bandgap semiconductors, motivated by their rapid progress in the field of photovoltaics. These hybrid materials combine the advantages of organic and inorganic semiconductors: a broad spectral gain and compatibility with solution processing methods, like organic semiconductors, and a high charge carrier mobility, typical of inorganic semiconductors. This makes perovskites a promising candidate for low-cost electrically-pumped laser diodes with relevance to commercial applications. To reach this goal, it is still necessary to optimise this material based on the underlying photophysical mechanisms limiting its performance, and develop cost-efficient resonators compatible with thin-film diode structures. The primary objectives of this work are to gain insights into perovskite photophysics with a focus on the processes relevant to light amplification. Based on these results, strategies to improve the amplified spontaneous emission (ASE) performance and radiative efficiency are investigated. Another goal is the development of versatile, cost-efficient fabrication techniques for resonators enabling low-threshold perovskite lasers.

This thesis reports the results of a temperature-dependent study of the carrier dynamics in 3D perovskites, elucidating the factors determining the ASE threshold, which limit their performance at room temperature. In particular, the bimolecular and Auger recombination rates are determined by analysing carrier dynamics at high excitation densities, which are measured on high refractive index substrates to suppress ASE and its associated fast carrier depletion. The two main results of this study are that i) above 250 K, the ASE threshold exceeds the carrier density at which radiative bimolecular emission dominates, and Auger losses contribute to an increase in the threshold. And ii) at lower temperatures, the temperature-dependent ASE arises from a combined effect of an exponentially decreasing bimolecular recombination rate and a reduced photoluminescence emission within the ASE band due to spectral broadening.

Strategies pursued to increase the radiative emission in perovskites and overcome their temperature limitations encompassed the incorporation of surface and bulk additives in 3D perovskites, and the fabrication of quasi-2D perovskites with long-chain cations. Firstly, surface passivation layers, commonly employed to reduce the defect density in perovskites, are investigated concerning their waveguide passivation effects. A cladding layer with a refractive index of  $n > 1$  reduces scattering losses in the perovskite, increasing the photon density in the film and decreasing the ASE threshold. The results of this study demonstrate that this waveguide passivation effect is more significant than defect passivation. A poly(methyl methacrylate) layer on a perovskite film showed a reduction in the ASE threshold by approximately 39 %, primarily attributed to optical waveguide passivation.

Further reducing the defect density did not affect the ASE behaviour, highlighting the significance of waveguide passivation compared to defect passivation. The second approach involved a bulk passivation of triple-cation perovskites with potassium, resulting in an optimal ASE threshold that was 30 % lower than that of undoped films. The enhanced ASE performance is attributed to the grain boundary passivation effect by potassium, which reduce non-radiative losses and improve radiative efficiency. Finally, a comparison between quasi-2D and 3D CsPbBr<sub>3</sub> perovskites demonstrates superior ASE performance in 3D films, with a threshold approximately 90 % lower than their quasi-2D counterparts. The difference lies in the nature of the excited carrier species. Radiative recombination of free carriers in 3D films dominates at the threshold density of  $n_{\text{th}} \approx 10^{18} \text{ cm}^{-3}$ . In contrast, excitons in quasi-2D films suffer from significant non-radiative Auger losses at  $n_{\text{th}}$ . This investigation led to a novel approach to fabricating high-quality 3D films with low ASE thresholds through a high-temperature annealing process of quasi-2D perovskites.

Regarding laser devices, triple-cation perovskite films were integrated into different resonator cavities using innovative and cost-efficient techniques. These methods encompass the fabrication of a perovskite second-order distributed feedback (DFB) laser through the nano-structuring of perovskite films using low-cost gelatin stamps. This approach yields high-quality resonators and lasers with excellent performance characteristics, including a narrow linewidth of 0.32 nm, a low threshold of 81  $\mu\text{J}/\text{cm}^2$  and a prominent linear polarisation. The flexibility and versatility of the nanoimprint method make it applicable to various photonic structures and application fields. Additionally, this research explores two directly printed cavities with triple-cation perovskite films as initial proof-of-concept studies. One involves a DFB structure with directly printed SU-8 lines, enabling multimode lasing. This fabrication method offers the advantage of easy adaptability to design different resonator geometries and can be further refined to achieve single-mode DFB lasing. The second concept involves the processing of a microcavity using two inkjet-printed distributed Bragg reflectors (DBRs), with a perovskite thin film sandwiched between them through a planar hot-pressing process. The results reveal successful lamination, resulting in high reflectivity of nearly 100 %, a single cavity resonance, and a Q-factor comparable to reported vertical-cavity surface-emitting lasers.

# Zusammenfassung

Hybride Perowskit-Halbleiter haben sich zuletzt als vielversprechende optische Verstärkermedien für Laser erwiesen, da sich bei der Nutzung als hochabsorbierende Halbleiter mit direkter Bandlücke im Bereich der Photovoltaik rasante Fortschritte ergeben haben. Dabei vereinen diese Hybridmaterialien die Vorteile von organischen und anorganischen Halbleitern: Eine breite spektrale Verstärkung und die Möglichkeit zur flüssigprozessierten Herstellung, ähnlich wie bei organischen Halbleitern, sowie eine hohe Ladungsträgerbeweglichkeit, welche typisch für anorganische Halbleiter ist. Dies macht Perowskite zu einem vielversprechenden Kandidaten für kostengünstige, elektrisch gepumpte Laserdioden, die für kommerzielle Anwendungen relevant sind. Um dieses Ziel zu erreichen, muss das Material hinsichtlich der zugrundeliegenden photophysikalischen Mechanismen, die seine Leistung begrenzen, optimiert werden. Des Weiteren müssen kosteneffiziente Resonatoren entwickelt werden, die mit Dünnschichtdiodenstrukturen kompatibel sind.

Das Hauptziel dieser Arbeit ist es, Erkenntnisse über die Photophysik von Perowskiten zu gewinnen, wobei der Schwerpunkt auf den für die Lichtverstärkung relevanten Prozessen liegt. Auf der Grundlage dieser Ergebnisse werden Strategien zur Verbesserung des ASE-Verhaltens und der Strahlungseffizienz erarbeitet und untersucht. Ein weiteres Ziel ist die Entwicklung vielseitiger und kosteneffizienter Herstellungsverfahren für Resonatoren, die Perowskitlaser mit niedrigen Pumpschwellen ermöglichen. In dieser Arbeit werden die Ergebnisse einer temperaturabhängigen Untersuchung über die Ladungsträgerdynamik in 3D-Perowskiten vorgestellt, die dazu dient die Einflussfaktoren auf die ASE-Schwelle zu identifizieren und welche sich limitierend auf das Verhalten bei Raumtemperatur auswirken. Insbesondere werden die bimolekulare- und Auger-Rekombinationsraten bestimmt, indem die Ladungsträgerdynamik mithilfe von Substraten mit hohem Brechungsindex gemessen wird. Dies bewirkt die Unterdrückung der durch ASE verursachten Ladungsträgerverarmung und ermöglicht die Messung genauer Rekombinationsraten bei hohen Anregungsdichten. Oberhalb von 250 K übersteigt die ASE-Schwelle die Ladungsträgerdichte, bei der die bimolekulare Strahlungsemission dominiert und womit schließlich Auger-Verluste zu einer Erhöhung der Schwelle beitragen. Bei niedrigeren Temperaturen ergibt sich der temperaturbedingte Anstieg der ASE-Schwelle durch die Zusammenwirkung einer exponentiell abnehmenden bimolekularen Rekombination und einem geringeren Photolumineszenzanteil innerhalb des ASE-Bandes aufgrund einer spektralen Verbreiterung.

Bei den Versuchen die Strahlungsemission in Perowskiten zu erhöhen, um Temperaturbeschränkungen zu überwinden, wurden Oberflächen- und Bulkzusatzstoffe für 3D-Perowskite untersucht und das ASE-Verhalten von Quasi-2D- und 3D-Perowskiten miteinander verglichen. Eine Oberflächenabdeckschicht auf einem Perowskit-Wellenleiter

hat zwei Auswirkungen: Wellenleiterpassivierung durch Verringerung der Streuverluste und Erhöhung der Photonendichte in der Schicht. Hinzu kommt die Defektpassivierung durch Abschwächung von Fallenzuständen und die Verringerung der damit verbundenen nicht-strahlenden Rekombinationsverluste. Eine Poly(methylmethacrylat)-Schicht verringert den ASE-Schwellenwert um 39 %, was primär auf die Passivierung der optischen Wellenleiter zurückzuführen ist. Eine weitere Verringerung der Störstellendichte hatte keinen Einfluss auf das ASE-Verhalten. Die Passivierung von Dreifachkation-Perowskiten durch Kaliumdotierung führt zu einer optimalen ASE-Schwelle, die 30 % niedriger ist als bei undotierten Filmen. Das verbesserte ASE-Verhalten wird auf den Passivierungseffekt der Korngrenzen durch Kaliumkomplexe zurückgeführt, der nicht-strahlenden Verluste reduziert und die Strahlungseffizienz verbessert. Schließlich zeigt ein direkter Vergleich zwischen Quasi-2D- und 3D CsPbBr<sub>3</sub>-Perowskiten, dass 3D-Filme ein besseres ASE-Verhalten aufweisen und der dazugehörige Schwellenwert etwa 90 % niedriger ist als bei den Quasi-2D-Äquivalente. Die Ursache für diesen signifikanten Unterschied liegt an der Art der angeregten Ladungsträger: Die strahlende Rekombination freier Ladungsträger in 3D-Filmen dominiert bei einer Schwellendichte von  $n_{th} \approx 10^{18} \text{ cm}^{-3}$ , während Exzitonen in Quasi-2D-Filmen unter erheblichen nicht-strahlenden Auger-Verlusten bei  $n_{th}$  leiden. Diese Untersuchung führte zu einem neuartigen Ansatz für die Herstellung hochwertiger 3D-Schichten durch ein Hochtemperatur-Temperverfahren für Quasi-2D-Perowskite.

In Bezug auf Laserbauteile wurden Dreifachkation-Perowskitfilme mit Hilfe neuartiger, kostengünstiger Techniken in verschiedene Resonatoren integriert. Dies beinhaltet einen Perowskit-Laser mit verteilter Rückkopplung (DFB) zweiter Ordnung, der durch die erfolgreiche Nanostrukturierung dünner Schichten mit kostengünstigen Gelatinestempeln erreicht wurde. Das Ergebnis sind hochqualitative Resonatoren und Laser mit exzellenter Performance, einer geringen Linienbreite (0,32 nm), einem niedrigen Schwellenwert (81  $\mu\text{J}/\text{cm}^2$ ) und einer ausgeprägten linearen Polarisation. Der Nanoimprint-Ansatz mit Gelatinestempeln ist flexibel und vielseitig, so dass sie auch für andere photonische Strukturen und Anwendungen verwendet werden können. Zusätzlich zu den DFBs wurden zwei direkt gedruckte Kavitäten mit Dreifachkation-Perowskit-Filmen in einer vorläufigen Machbarkeitsstudie getestet: Es wurde eine DFB-Struktur mit direkt gedruckten SU-8-Linien entwickelt, die Multimode-Lasern ermöglicht. Diese Herstellungsmethode bietet den Vorteil, dass sie sich leicht an verschiedene Resonatorgeometrien anpassen lässt und weiter verfeinert werden kann, um Singlemode-DFB-Laser zu realisieren. Schließlich wurde eine Mikrokavität hergestellt, die aus zwei mit Tintenstrahl gedruckten Bragg-Spiegeln (DBR) besteht. Dazu wurde eine Perowskit-Dünnschicht zwischen zwei DBRs mithilfe eines planaren Heißpressverfahren eingebettet. Die Ergebnisse zeigen die erfolgreiche Laminierung mit einer Reflektivität von fast 100 % mit einer einzigen Kavitätsresonanz und resultiert in einem Q-Faktor, der mit dem von berichteten oberflächenemittierenden Lasern mit vertikalem Resonator vergleichbar ist.

# Contents

<b>Abstract</b> . . . . .	<b>i</b>
<b>Zusammenfassung</b> . . . . .	<b>iii</b>
<b>List of Publications</b> . . . . .	<b>ix</b>
<b>Supervised Student Projects</b> . . . . .	<b>xi</b>
<b>I Introduction</b>	<b>1</b>
1 Motivation and Objectives . . . . .	3
2 Organisation of the Thesis . . . . .	7
<b>II Theoretical Background and Methods</b>	<b>9</b>
<b>3 Light Amplification and Laser Fundamentals</b> . . . . .	<b>11</b>
3.1 Spontaneous and stimulated emission . . . . .	11
3.2 Amplified spontaneous emission . . . . .	12
3.3 Optical waveguides . . . . .	14
3.4 Laser fundamentals . . . . .	15
3.4.1 Distributed feedback lasers . . . . .	17
3.4.2 Random feedback lasing . . . . .	19
<b>4 Hybrid Perovskite Semiconductors</b> . . . . .	<b>21</b>
4.1 Crystal structure . . . . .	21
4.2 Optoelectronic properties . . . . .	23
4.3 Carrier recombination dynamics . . . . .	25
4.3.1 Recombination mechanisms . . . . .	25
4.3.2 Dynamics by ABC and Shockley-Read-Hall models . . . . .	27
<b>5 Fabrication and Characterisation Methods</b> . . . . .	<b>31</b>
5.1 Perovskite thin film processing . . . . .	31
5.2 Surface treatment methods . . . . .	33
5.3 Thermal nanoimprint lithography . . . . .	34

5.4	Optical characterization techniques . . . . .	37
5.4.1	Steady-state photoluminescence spectroscopy . . . . .	37
5.4.2	Photoluminescence quantum yield . . . . .	38
5.4.3	Ultraviolet–visible spectroscopy . . . . .	39
5.4.4	Time-resolved photoluminescence spectroscopy . . . . .	39
5.4.5	Transient reflection spectroscopy . . . . .	40
5.5	Morphological characterization techniques . . . . .	42
5.5.1	Atomic force microscopy . . . . .	42
5.5.2	Scanning electron microscopy . . . . .	43
5.5.3	Profilometry . . . . .	43
 <b>III Results and Discussion</b>		 <b>45</b>
 <b>6 Temperature-dependent Carrier Dynamics and Amplified Spontaneous Emission</b>		 <b>47</b>
6.1	Temperature-dependent bimolecular and Auger recombination rates . . .	48
6.1.1	Introduction . . . . .	48
6.1.2	Amplified spontaneous emission suppression . . . . .	49
6.1.3	Transient reflection and carrier dynamics modelling . . . . .	51
6.2	Factors determining the amplified spontaneous emission threshold . . .	59
6.2.1	Introduction . . . . .	59
6.2.2	Temperature-dependent amplified spontaneous emission threshold	60
6.2.3	Impact of non-radiative Auger losses . . . . .	61
6.2.4	Contribution of bimolecular rate and spectral broadening . . . . .	63
6.3	Summary . . . . .	66
 <b>7 Strategies for Enhanced ASE by Tuning of Optical and Compositional Properties</b>		 <b>67</b>
7.1	Light confinement and defect mitigation via surface passivation . . . . .	68
7.1.1	Introduction . . . . .	68
7.1.2	ASE performance for different surface layers . . . . .	69
7.1.3	Defect mitigation by surface passivation . . . . .	71
7.1.4	Scattering losses and photon density in cladded films . . . . .	73
7.2	Amplified spontaneous emission in quasi-2D and 3D CsPbBr <sub>3</sub> perovskites	76
7.2.1	Introduction . . . . .	76
7.2.2	Optimisation of quasi-2D films . . . . .	76
7.2.3	Formation of 3D films by high-temperature annealing . . . . .	78
7.2.4	Excitonic versus free-carrier recombination . . . . .	79
7.3	Triple-cation perovskites with potassium additive . . . . .	82
7.3.1	Introduction . . . . .	82
7.3.2	Optical and morphological properties of K-doped films . . . . .	83
7.4	Summary . . . . .	86

<b>8 Triple-cation Perovskite Lasers</b> . . . . .	<b>89</b>
8.1 Distributed feedback lasers by nanoimprint lithography with polymeric gratings . . . . .	90
8.1.1 Introduction . . . . .	90
8.1.2 Design of perovskite distributed feedback lasers . . . . .	91
8.1.3 Dichromated gelatin gratings . . . . .	96
8.1.4 Nanoimprint lithography with gelatin gratings . . . . .	98
8.1.5 Optical characteristics of distributed feedback lasers . . . . .	100
8.2 Proof-of-concept studies on printed laser resonators . . . . .	105
8.2.1 Lasers with nano-printed SU-8 gratings . . . . .	106
8.2.2 Perovskite micro-cavities with inkjet printed mirrors . . . . .	108
8.3 Summary . . . . .	111
<b>IV Conclusion</b> . . . . .	<b>113</b>
<b>9 Conclusion and Outlook</b> . . . . .	<b>115</b>
<b>Bibliography</b> . . . . .	<b>119</b>
<b>List of Figures</b> . . . . .	<b>139</b>
<b>List of Tables</b> . . . . .	<b>143</b>
<b>Acronyms and Abbreviations</b> . . . . .	<b>145</b>
<b>Acknowledgements</b> . . . . .	<b>147</b>
<b>V Appendix</b> . . . . .	<b>149</b>
<b>A Literature Summary of Recombination Rate Coefficients</b> . . . . .	<b>151</b>
<b>B Literature Summary of Solution-processed Second-order DFB Lasers</b> . . . . .	<b>152</b>
<b>C Topography of Triple-cation Perovskite Thin Film</b> . . . . .	<b>154</b>
<b>D Characterisation of Nanoimprinted Lasers With Used Stamps</b> . . . . .	<b>155</b>



# List of Publications

## Publications in peer-reviewed journals and submitted manuscripts

- Allegro, I.; I. A. Howard; Lemmer, U. Improving Light Amplification in Perovskites by Light Confinement and Defect Passivation. *in preparation*
- Martens, M.; Allegro, I.; Lemmer, U.; Colsmann, A.; Röhm, H.; "Laser-induced Periodic Surface Structures in Triple Cation Mixed Halide Perovskites for Printable DFB Lasers" *Advanced Optical Materials*, *in preparation*
- Pascual, M.; Bigan, N.; M'Barki, A.; Mental, R.; Allegro, I.; Lemmer, U. "All-printed SU8-perovskite DFB laser" 2023. Proc. SPIE 12433, *Advanced Fabrication Technologies for Micro/Nano Optics and Photonics XVI*, 124330E (15 March 2023)
- Li, Y.; Hu, H.; Farag, A.; Feeney, T.; Allegro, I.; Lemmer, U.; Paetzold, U. W.; Howard, I. A. "Enhancement of Amplified Spontaneous Emission by Electric Field in CsPbBr<sub>3</sub> Perovskites" 2023. *Nano Lett.* 23 (5), 1637–1644
- Allegro, I.; Bonal, V.; Mamleyev, E. R.; Villalvilla, J. M.; Quintana, J. A.; Jin, Q.; Díaz-García, M. A.; Lemmer, U. "Distributed Feedback Lasers by Thermal Nanoimprint of Perovskites Using Gelatin Gratings" 2023. *ACS Applied Materials & Interfaces*, 15 (6), 8436–8445
- Li, Y.; Roger, J.; Allegro, I.; Fischer, J. C.; Jin, Q.; Lemmer, U.; Howard, I. A.; Paetzold, U. W. "Lasing from Laminated Quasi-2D/3D Perovskite Planar Heterostructures" 2022. *Advanced Functional Materials*, 32 (27)
- Ruiz-Preciado, M. A.; Gota, F.; Fassel, P.; Hossain, I. M.; Singh, R.; Laufer, F.; Schackmar, F.; Feeney, T.; Farag, A.; Allegro, I.; ... Paetzold, U. W. "Monolithic Two-Terminal Perovskite/CIS Tandem Solar Cells with Efficiency Approaching 25%" 2022. *ACS Energy Letters*, 7 (7), 2273–2281
- Donie, Y. J.; Yuan, Y.; Allegro, I.; Schackmar, F.; Hossain, I. M.; Huber, R.; Roger, J.; Paetzold, U. W.; Gomard, G.; Lemmer, U. "A Self-Assembly Method for Tunable and Scalable Nano-Stamps: A Versatile Approach for Imprinting Nanostructures" 2022. *Advanced Materials Technologies*, 7 (6)
- Kaiser, M.; Li, Y.; Allegro, I.; Richards, B. S.; Paetzold, U. W.; Howard, I. A. "Interpreting the Time-Resolved Photoluminescence of Quasi-2D Perovskites" 2021. *Advanced Materials Interfaces*, 8 (24)

- Li, Y.; Allegro, I.; Kaiser, M.; Malla, A. J.; Richards, B. S.; Lemmer, U.; Paetzold, U. W.; Howard, I. A. "Exciton Versus Free Carrier Emission: Implications for Photoluminescence Efficiency and Amplified Spontaneous Emission Thresholds in Quasi-2D and 3D Perovskites" 2021. *Materials Today*, 49, 35–47
- Kaiser, M.; Li, Y.; Schwenzer, J.; Jakoby, M.; Allegro, I.; Gerhard, M.; Koch, M.; Ducinkas, A.; Richards, B. S.; Graetzel, M.; Milić, J. V.; Paetzold, U. W.; Howard, I. A. "How Free Exciton-Exciton Annihilation Lets Bound Exciton Emission Dominate the Photoluminescence of 2D-Perovskites Under High-Fluence Pulsed Excitation at Cryogenic Temperatures" 2021. *Journal of Applied Physics*, 129 (12)
- Allegro, I.; Li, Y.; Richards, B. S.; Paetzold, U. W.; Lemmer, U.; Howard, I. A. "Bimolecular and Auger Recombination in Phase-Stable Perovskite Thin Films from Cryogenic to Room Temperature and Their Effect on the Amplified Spontaneous Emission Threshold" 2021. *The Journal of Physical Chemistry Letters*, 12 (9), 2293–2298
- Kohler, D.; Allegro, I.; Wondimu, S. F.; Hahn, L.; Freude, W.; Koos, C. "Lasing in Si<sub>3</sub>N<sub>4</sub>-organic Hybrid (SiNOH) Waveguides" 2020. *Optics Express*, 28 (4), 5085–5104
- Brenner, P.; Bar-On, O.; Jakoby, M.; Allegro, I.; Richards, B.S.; Paetzold, U.W.; Howard, I.A.; Scheuer, J.; Lemmer, U. "Continuous Wave Amplified Spontaneous Emission in Phase-Stable Lead Halide Perovskites" 2019. *Nature Communications*, 10 (1)

## Conference contributions

### Oral presentations:

- Allegro, I.; Li, Y.; Richards, B. S.; Lemmer, U.; Paetzold, U. W.; Howard, I. A. "Temperature-Dependent Amplified Spontaneous Emission (ASE) Threshold in Phase-Stable 3D Perovskite Films" *Organic and Hybrid Light Emitting Materials and Devices XXV* 11808, 118081B
- Allegro, I.; Li, Y.; Richards, B. S.; Lemmer, U.; Paetzold, U. W.; Howard, I. A. "Factors Influencing the Temperature-Dependent Amplified Spontaneous Emission (ASE) Threshold in Phase-Stable 3D Perovskite Films" 2021 Virtual MRS Spring Meeting

### Poster presentations:

- Allegro, I.; Bonal, V.; Mamleyev, E. R.; Villalvilla, J. M.; Quintana, J. A.; Jin, Q.; Díaz-García, M. A.; Lemmer, U. "Perovskite Distributed Feedback Lasers by Using Gelatin Grating for Thermal Nanoimprint" 2023 SPIE Organic Photonics + Electronics, San Diego, CA, USA
- Allegro, I.; Brenner, P.; Bar-On, O.; Jakoby, M.; Richards, B. S.; Paetzold, U. W.; Howard, I. A.; Scheuer, J.; Lemmer, U. "Continuous Wave Amplified Spontaneous Emission in Phase-Stable Triple Cation Lead Halide Perovskite Thin Films" 2019 CLEO/Europe-EQEC, Munich, Germany, IEEE

# Supervised Student Projects

- **Gamal Mohamed:** "Influence of Thermal Nanoimprint Parameters on Triple Cation Perovskites", *research project within the master in optics and photonics* (2019)
- **Yvonne Martínez:** "Lasing in Silicon Nitride - Perovskite (SiNP) Resonators", *master thesis in optics and photonics* (2019)
- **Christian Rainer:** "Triple Cation Perovskite Distributed Feedback Lasers by Thermal Nanoimprint Lithography", *master thesis in electrical engineering* (2019)
- **Avishek Sarbajna:** "Assembling of a Cryostat System for a TCSPC Setup for Measuring Temperature-dependent Steady-state and Time-resolved Photoluminescence (TRPL) of Perovskite Films", *internship* (2020)
- **Seyed Saeed Nazemosadatarsanjani:** "Variable Stripe Length Method (VSLM) Setup for Measuring Optical Gain in Perovskite Thin Films", *internship* (2020)
- **Lesly Kelly Fährnich :** "Passivation Strategies of Lead Halide Perovskite Films for Low Threshold Lasing Applications", *master thesis in optics and photonics* (2021)
- **Jona Wohletz:** "Entwicklung von Perowskitfilmen als Verstärkungsmedium für Laseranwendungen im grünen Spektralbereich", *bachelor thesis in electrical engineering* (2021)
- **Patrick Ehrmann:** "Triple Cation Perovskite Vertical-Cavity Surface-Emitting Lasers (VCSELs) with Solution Processed Distributed Bragg Reflectors (DBRs)", *master thesis in electrical engineering* (2022)
- **Maximilian Büttner:** "Temperature-dependent, Time-resolved Photoluminescence of Perovskite Thin Films to Analyze Trap-mediated and Bimolecular Recombination", *research project within the master in optics and photonics* (2023)



# **Part I**

## **Introduction**



# 1 Motivation and Objectives

Since Theodore Maiman's pioneering demonstration of the first laser in 1960, employing a ruby crystal, lasers have found extensive use in various application areas, including science, communication, medicine, and the automotive industry.<sup>[1]</sup> Presently, lasers serve as key components in everyday life, from facilitating transactions at supermarket cash registers to enabling high-precision ophthalmic procedures. The properties that render lasers unique and compelling for such a broad spectrum of applications include their narrow linewidth, temporal and spatial coherence, and ability to generate ultrashort pulses. Most commercial lasers are based on laser diodes comprising inorganic single-crystal semiconductors, such as III-V compounds, as laser active media, owing to their excellent optoelectronic properties. However, these materials exhibit several drawbacks that incentivised research into alternative laser materials: i) Inorganic semiconductors are epitaxially grown on highly crystalline substrates, which is a high-cost fabrication method and presents challenges for implementation in integrated photonics applications; ii) They possess a narrow emission spectrum, resulting in a limited selection of laser wavelengths; And iii) an efficiency gap exists in the green wavelength range (520–530 nm) due to the lack of reliable inorganic materials emitting within this range.<sup>[2]</sup> Therefore, optical materials with broad wavelength selectivity to address the 'green gap' are of significant interest as alternative gain media for laser applications. Moreover, some novel materials are compatible with flexible and cost-effective deposition techniques, which can positively impact high throughput and large-scale manufacturing.

Organic semiconductors and colloidal quantum dots (CQDs) have emerged as promising alternatives due to their broad wavelength selectivity and compatibility with solution-processing fabrication methods and various substrate materials, including flexible substrates. However, they face challenges like low charge-carrier mobility, low thermal conductivity, and high non-radiative losses at high carrier densities. In laser diode applications, achieving efficient current flow through the device relies on high electrical mobility. Laser operation demands high current densities, resulting in significant Joule heating. Thus, high thermal conductivity also plays an essential role in dissipating the generated heat. The substantial resistive heating, attributed to the low mobility and low thermal conductivity, typically observed in organic semiconductors and CQDs, presents a considerable challenge when incorporating them into a laser diode configuration. More recently, hybrid perovskite semiconductors have emerged as an alternative direct bandgap semiconductor, combining the best of both worlds: compatibility with solution processing methods, high gain, broad emission spectrum, and long carrier lifetimes. Furthermore, perovskites exhibit a high ambipolar charge carrier mobility, which is advantageous for diode configurations. Figure 1.1 compares the material classes discussed for laser diode

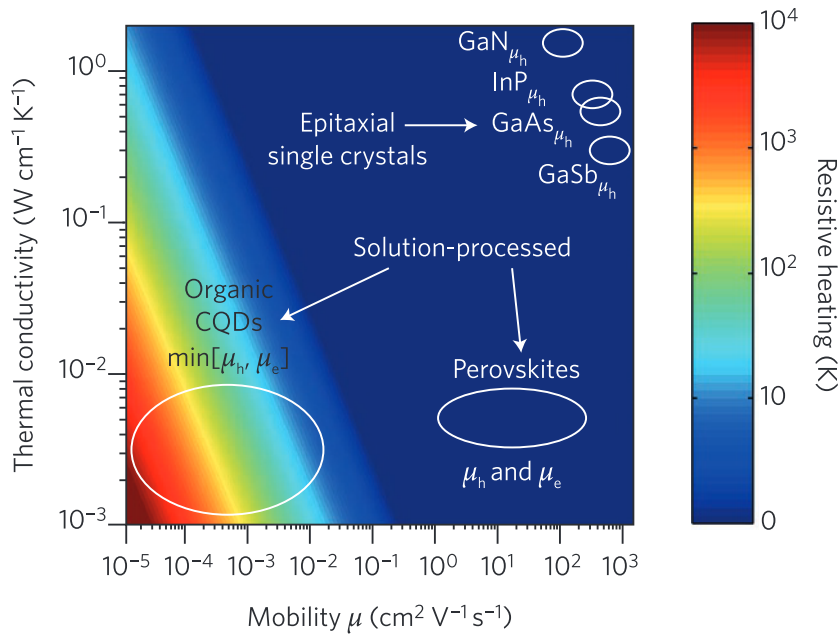


**Figure 1.1:** Comparison of epitaxially-grown single crystals, and solution-processed organic semiconductors, CQDs, and perovskites, as gain media for laser diode applications. The materials' suitability for usage in a laser diode configuration is compared regarding their resistive heating, which depends on the material thermal conductivity and charge carrier mobility. The resistive heating is calculated based on the materials parameters and typical laser diode operation parameters: a current density of  $1 \text{ kAcm}^{-2}$ , a film thickness of  $200 \text{ nm}$ , and a threshold carrier density of  $5 \cdot 10^{18} \text{ cm}^{-3}$ . The predicted heating does not account for heat generated by non-radiative recombination mechanisms. Reproduced with permission from Springer Nature, from [3] Copyright 2016.

applications regarding the expected temperature rise caused by resistive heating under typical injection conditions. Epitaxially-grown single crystals and solution-processed organic semiconductors, CQDs, and perovskites are arranged in the 2D plot according to their material properties, i.e., thermal conductivity (y-axis) and carrier mobility (x-axis), and the colour scheme represents the projected heating during laser operation. Commercially available epitaxial crystals exhibit high mobility and conductivity, and do not encounter significant heating issues, as indicated in the top right corner of Figure 1.1. In contrast, at the bottom left corner, organic semiconductors' and CQDs' low mobility and thermal conductivity result in substantial heating during electrical injection, leading to a temperature increase considerably higher than inorganic semiconductors. Despite perovskites' low thermal conductivity, their high and balanced charge carrier mobility results in a significantly lower temperature increase under electrical pumping compared to the other solution-processed materials.<sup>[3]</sup> Remarkable progress was made in recent years towards the goal of continuous-wave (CW) and eventually electrically-pumped perovskite lasing, with the achievement of optically-pumped room-temperature CW lasing in a thin film and (optically-excited) CW lasing in a contacted laser diode configuration at  $110$

---

K.<sup>[4, 5]</sup> Thus, hybrid perovskites are a new and promising candidate for solution-processed, electrically-driven integrated laser sources.

In this context, several challenges exist in the field of perovskite lasing. This thesis explores these limitations, with a primary focus on two key objectives:

1. **Investigate material photophysics and the limitations of light amplification in perovskites**

To optimise their performance, it is essential to understand the underlying photophysical mechanisms relevant for lasing or ASE operation in perovskites. In particular, unravelling the carrier dynamics as a function of temperature is key, as the temperature is the main limiting factor for achieving CW and electrically-pumped operation.

2. **Fabricate low-cost resonator structures for efficient perovskite lasers**

Another significant achievement in the field of perovskite lasers is to combine flexible and low-cost semiconductor fabrication processes with laser resonators built using cost-efficient methods. The developed resonator geometries should be compatible with the perovskite material and a thin film diode configuration, enabling implementation in an integrated laser diode.

The next section provides an overview of the thesis organisation, including where to locate the detailed studies and discussions on the previous objectives.



## 2 Organisation of the Thesis

This thesis is divided into four main parts – *Introduction*, *Theoretical Background and Methods*, *Results and Discussion*, and *Conclusion*. After the current *Introduction*, the second part – *Theoretical Background and Methods* – introduces the theory and methodologies needed to understand part III *Results and Discussion*. It starts with **Chapter 3** discussing the fundamentals of lasing operation and light amplification in active media, followed by **Chapter 4**, which dives into the specifics of hybrid perovskites, such as their crystal structure, optoelectronic properties, and fundamentals of carrier dynamics. The last chapter of this part deals with the fabrication and characterisation methodologies employed within the framework of this work (**Chapter 5**). The central part of this thesis – *Results and Discussion* – reports on the three primary studies performed as a novel contribution to the field, in **Chapters 6 to 8**. Here, each chapter starts with a short description of the main objectives and the organisation of the chapter sections. This is followed by a note about publications resulting from the work presented therein, and contributions from colleagues, peers, and collaboration partners. **Chapter 6** investigates the temperature-dependent carrier dynamics in phase-stable, triple-cation 3D perovskite thin films, and their effect on the ASE threshold in these films. Motivated by these results and to further increase the radiative recombination in perovskite films to achieve lower ASE thresholds, **Chapter 7** encompasses studies on optical and material composition approaches to enhance light amplification in perovskite films. Finally, **Chapter 8** focuses on developing low-cost fabrication methods for laser resonators compatible with a perovskite laser diode geometry. In the *Conclusion*, **Chapter 9** concludes the significance of the advances provided by this work in a broader research context and suggests future work on the topic.



## **Part II**

# **Theoretical Background and Methods**



# 3 Light Amplification and Laser Fundamentals

This chapter presents the basic principles of light generation, propagation and amplification in semiconductors. These concepts are presented with a focus on hybrid perovskites and serve as a foundation for the analyses in Part III – Results and Discussion. Section 3.1 elucidates the fundamental mechanisms involved in light-matter interactions, followed by Sections 3.2 and 3.3, which deal with the ASE process and the main properties of optical waveguides, respectively. Finally, Section 3.4 introduces the fundamentals of lasing.

## 3.1 Spontaneous and stimulated emission

The term *laser* is an acronym for light amplification by stimulated emission of radiation, used to describe a device that generates and amplifies light with particular properties. Three fundamental processes describe the interaction between an electron transition between different energy levels in a material and a photon. They can be described in a simplified two-level system with energies  $E_1$  and  $E_2$  for the ground and excited state, respectively (Figure 3.1). In inorganic semiconductors or perovskites, these levels represent the valence band maximum (VBM) and conduction band minimum (CBM). Absorption (or stimulated absorption) refers to the process of an electron in  $E_1$  absorbing the energy of an incoming photon and transitioning to a higher-energy state  $E_2$  (given that the photon energy  $h\nu$  is higher than the energy difference between the two levels  $\Delta E$ ). Spontaneous emission describes a photon emission from an excited system that occurs spontaneously (triggered by a vacuum fluctuation), and the photon's phase, polarisation, and propagation direction properties are random. In this transition, an electron in  $E_2$  transits to  $E_1$  and releases a photon with energy  $h\nu = \Delta E$ . This type of transition results in incoherent radiation and is responsible for the luminescence of an excited optical medium. Stimulated emission differs from spontaneous emission in the origin of the light emission: An electron in  $E_2$  can be *stimulated* to transition to  $E_1$  by an incoming photon if said photon possesses the necessary resonant energy  $\Delta E$ . The stimulated emitted photon is identical to the incoming photon (same wavelength, polarisation, phase, and direction), and this effect allows for coherent light amplification, the fundamental principle of a laser.

The transition rate of each process is described by the Einstein coefficients  $A_i$ ,  $B_i$ , and the occupancy of each state  $N_i$ :  $A_{21}N_2$  (spontaneous emission),  $B_{21}N_2$  (stimulated emission), and  $B_{12}N_1$  (stimulated absorption), where  $B_{21} = B_{12}$ . In thermal equilibrium ( $dN/dt = 0$ ), the ground state is mostly populated, i.e.,  $N_1 > N_2$ , so the dominant process upon a photon

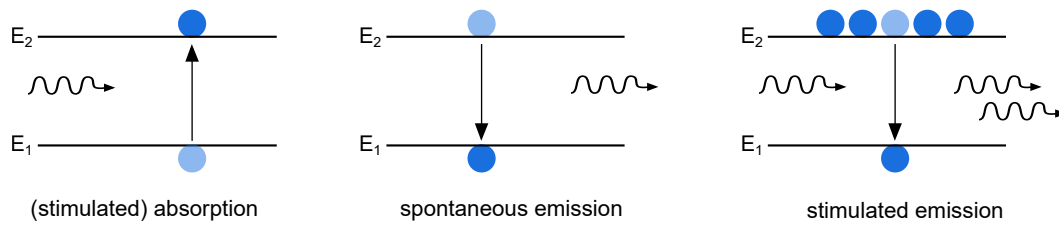


**Figure 3.1:** Fundamental interaction processes of a photon and a two-level material system – absorption, spontaneous emission, and stimulated emission.

arrival is absorption ( $E_1 \rightarrow E_2$ ). For stimulated emission to dominate over absorption, the excited-state population must be higher than the ground state ( $N_2 > N_1$ ) given that  $B_{21} = B_{12}$ . This is called *population inversion*, and for reaching this state, a minimum of a three-level system is required.<sup>[6]</sup> Figure 3.2a illustrates a three (solid lines) and four-level (dashed lines) system with a simplified schematic of the energy levels: a pump level  $E_p$ ; upper and lower levels of the stimulated emission process,  $E_u$  and  $E_l$ , respectively; and, for the four-level system, a ground state  $E_0$ . For the three-level system,  $E_0$  corresponds to the lower level of stimulated emission ( $E_l$ ). To reach population inversion, carriers are pumped into  $E_p$  (short-lived state) and quickly relax to  $E_u$  (long-lived state), where they build up a population for inversion. A four-level system requires a comparatively lower excited carrier density in  $E_u$  to achieve a population inversion since  $E_l$  is mainly unoccupied, in contrast to a three-level system where  $E_l = E_0$ . After a population inversion is achieved, stimulated emission occurs between  $E_u$  and  $E_l$  (or  $E_0$  for a three-level system), and in the case of a four-level system, carriers quickly relax to  $E_0$ . Perovskite semiconductors are equivalent to three-level systems, where the pump level corresponds to the absorbed energy level above the bandgap, and the VBM and CBM correspond to the lower and upper laser level (Figure 3.2b).<sup>[7]</sup> Here, the band occupation is described by quasi-Fermi levels with energies  $F_C$  and  $F_V$  for electrons in the conduction band and holes in the valence band, respectively. The necessary condition for population inversion in such a semiconductor (Figure 3.2b) – the Bernard-Duraffourg inversion condition – states that the difference between the quasi-Fermi levels must surpass the bandgap energy  $E_g$  (or the photon energy  $h\nu$ , i.e.,  $F_C - F_V \geq E_g$ ).

## 3.2 Amplified spontaneous emission

ASE, also known as ‘mirror-less lasing’, describes light amplification in a material by stimulated emission without the influence of a cavity. As discussed in the previous section, a high excitation can create a population inversion in a material so that stimulated emission dominates over spontaneous emission. Supposing the excitation is enough to obtain net gain in the material, i.e., the gain  $g$  surpasses the losses  $\alpha$  and  $g_{\text{net}} = g - \alpha > 0$ , light propagating along the excited region will be amplified exponentially (the exponent in Equation 3.1 exceeds unity). This can be visualised in the following equation – the Lambert-

Beer law of absorption<sup>[6]</sup> – describing the light intensity  $I$  as a function of propagation length  $z$  in a material:

$$I(z) = I_0 e^{g_{\text{net}}(\lambda)z} \quad (3.1)$$

where  $I_0$  is the initial intensity and  $g_{\text{net}}(\lambda)$  is the net spectral gain per length. The spectral region of highest gain experiences the highest amplification and once ASE sets in, there is an emission narrowing with typical linewidths of 5 – 20 nm. Along with the emission narrowing, ASE is also characterised by a threshold behaviour where the output emission increases much strongly with excitation, indicating the transition from spontaneous to stimulated emission. This is similar to the lasing threshold behaviour presented in Section 3.4. Further, the ASE peak is usually situated on the low energy side of the PL spectrum due to its typical lower absorption losses. The main loss mechanisms involved in the ASE process are re-absorption and propagation losses, such as scattering. For light amplification in a laser (discussed in Section 3.4), additional out-coupling losses come into play. Given that ASE arises from a competition between gain and losses, it can be used to assess a material's suitability as laser active medium – lower ASE thresholds translate to higher  $g_{\text{net}}$  and lower laser thresholds. For the onset of ASE, both a high gain and a long propagation length are required (Equation 3.1), and the latter can be easily achieved, for instance, in optical waveguides, discussed in the following section.

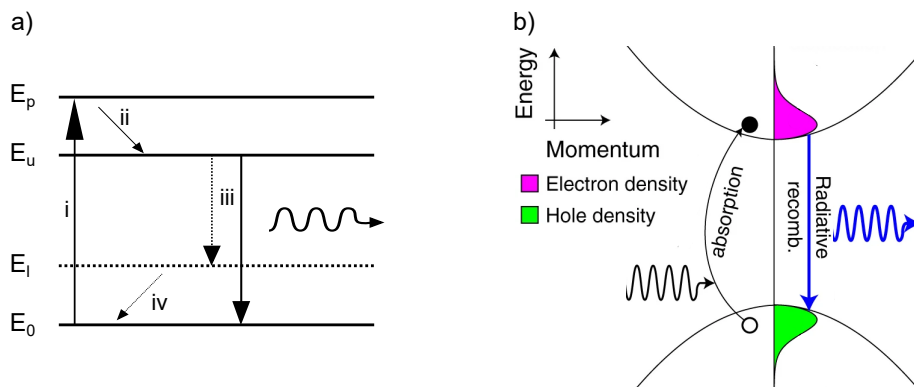


**Figure 3.2:** Schematic of the energy levels and respective transition processes to generate a population inversion and stimulated emission. a) Simplified diagram of localised energy levels for a three- (solid lines) and four-level (dashed lines) system, and the transitions associated with i) pumping, ii) relaxation onto the upper laser level, iii) stimulated emission, and iv) for a four-level system – relaxation onto the ground state. b) Corresponding band picture for the case of perovskite semiconductors with absorption (black arrow) generating an electron-hole pair in their respective bands (respective carrier densities in pink and green), relaxation onto the band edges (not explicitly illustrated), and radiative emission (blue arrows), adapted from [8] used under Creative Commons license <http://creativecommons.org/licenses/by/4.0/>.

### 3.3 Optical waveguides

Waveguiding is a fundamental process in various laser devices and is particularly relevant for ASE. The optical waveguides relevant to this work consist of slab waveguides: They confine light to a specific layer (the so-called waveguide), which has a higher refractive index than its surroundings  $n_2 > n_1, n_3$ , where  $n_1$ ,  $n_2$  and  $n_3$  are the refractive indices of cladding, waveguide (core) and substrate, respectively, depicted in Figure 3.3. This refractive index configuration allows total internal reflection at the bottom and top surfaces of the core, provided the incident angle surpasses the critical angle. In the configuration in Figure 3.3, the refractive index variation is along the  $x$ -direction and stays constant in  $y$ , and the propagation occurs along the  $z$ -axis. The optical modes allowed to propagate in a waveguide possess different field distributions and depend on the layers' refractive indices and thickness  $d$  (assuming the top and bottom layers surrounding the waveguide core are thick enough that the field decreases to zero at the top and bottom edges). The waveguide modes can be calculated by solving the wave equation, and they are classified, according to their polarisation, in transverse electric (TE) and transverse magnetic (TM) modes, depending on what field component is oriented along the  $y$ -axis – *transverse* to the propagation direction ( $z$ -axis). TE modes possess an electric field vector pointing in the  $y$ -direction, which has the components  $E_y$ ,  $H_x$ , and  $H_z$ ; whereas TM modes possess the components  $H_y$ ,  $E_x$  and  $E_z$ . The mode profile ( $|E_y|^2$ ) of the fundamental TE mode is illustrated in Figure 3.3. TE modes can be described with the general plane wave solution:

$$E_y(x, y, z) = E_y(x)e^{i(\omega t - \beta z)} \quad (3.2)$$

with propagation constant  $\beta$ , which determines the effective refractive index  $n_{\text{eff}}$  of a mode, along with the wave number  $k_0$  as follows:

$$n_{\text{eff}} = \frac{\beta}{k_0}. \quad (3.3)$$

The  $n_{\text{eff}}$  is the refractive index the propagating mode experiences given its overlap with the three materials ( $n_1, n_2, n_3$ ) and is hence bound by the lowest value  $n_{\text{min}}$  and the highest  $n_2$ , i.e.,  $n_{\text{min}} < n_{\text{eff}} < n_2$ . To determine the  $n_{\text{eff}}$  of a mode, the wave equation needs to be solved with the Ansatz in Equation 3.2 and the appropriate boundary conditions.<sup>[9]</sup>

One additional important factor related to the field distribution in optical waveguides is the overlap (or confinement) factor  $\Gamma$ , which describes how much spatial overlap exists between the optical field and the waveguide core.<sup>1</sup> For the waveguide presented in Figure 3.3, it can be calculated by:

$$\Gamma = \frac{\int_0^d S_z dx}{\int_{-\infty}^{\infty} S_z dx} \quad (3.4)$$

where  $S_z$  is the longitudinal component of the Poynting vector. Definitions other than the one in Equation 3.4 and discussions on defining the overlap factor are presented

<sup>1</sup> The overlap factor is not necessarily restricted to the mode overlap with the waveguide layer but can be defined as the overlap of the mode with any specific layer or region, specified by the interval of the integral in the numerator in Equation 3.4.

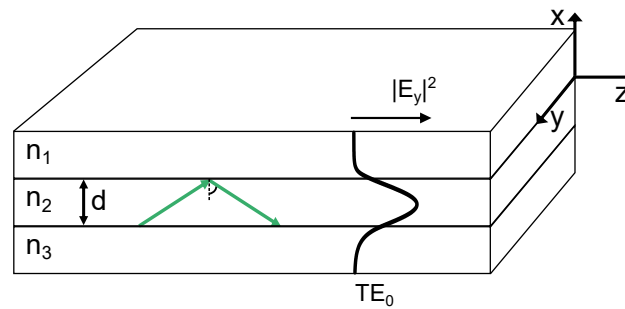


**Figure 3.3:** Schematic of a slab waveguide with refractive indices  $n_1$ ,  $n_2$ , and  $n_3$ , for cladding, waveguide core (of thickness  $d$ ), and substrate, respectively. Two green arrows illustrate the total internal reflection at the top surface of the waveguide, and a black curve on the waveguide represents the fundamental  $TE_0$  mode field distribution as  $|E_y|^2$ .

elsewhere.<sup>[10]</sup> Gain and losses in a slab waveguide – relevant for both ASE and lasing – are influenced by the waveguide parameters discussed in this section, such as  $n_i$  and  $\Gamma$ . The gain  $g$  is determined by the material gain  $g_{\text{mat}}$  and  $\Gamma$  as:

$$g = g_{\text{mat}} \cdot \Gamma. \quad (3.5)$$

TE modes usually possess a stronger confinement (higher  $\Gamma$ ) than TM modes, therefore, TE modes provide a higher gain (Equation 3.5) than TM modes given  $\Gamma_{\text{TE}} > \Gamma_{\text{TM}}$ . Losses in a slab waveguide for the case of ASE – re-absorption and propagation losses – are influenced by the layer stack geometry. In effect, propagation losses depend strongly on surface scattering losses, which are related to the refractive indices of the interface,  $\beta$  and  $k_0$  (Equation 3.3).<sup>[11]</sup> Similarly, re-absorption losses depend on  $\Gamma$  as it gives the overlap of the emitted light with the absorbing gain material. As discussed in the following section, resonator losses are only relevant in laser devices.

### 3.4 Laser fundamentals

This section introduces the basic principles of lasers, including a more detailed description of DFB lasers in Section 3.4.1 and random lasing in Section 3.4.2. Any laser consists of three fundamental parts:

1. an active medium;
2. an excitation (pump) source; and
3. a resonating cavity.

The pump source renders energy to achieve a population inversion. The resonator provides optical feedback so light oscillates inside the active medium and builds up stimulated emission. One key property to describe a resonant cavity is its quality factor ( $Q$ -factor), which effectively quantifies the losses of the resonator. It is defined as the ratio of stored energy to dissipated energy and, for an optical resonator, can be calculated by the ratio

of the resonance wavelength by the resonance linewidth, i.e.  $Q\text{-factor} = \lambda / \Delta \lambda$ . In addition to providing feedback, a laser resonator defines the resonance condition for the oscillating modes, for which there is constructive interference after a cavity round-trip. In the classical case of a Fabry-Pérot resonator, two mirrors at each end of the gain medium provide the feedback, where one mirror has a reflectivity of 100 % and the second – the out-coupling mirror – possesses a reflectivity  $R < 100$  %. In this case, the resonant laser wavelength is an integer multiple of twice the resonator length. The spectral selectivity provided by the resonator leads to very narrow emission linewidths, typically in the order of 0.1-5 nm.<sup>[12]</sup> Laser linewidths are generally narrower than those of ASE (Section 3.2); however, the linewidth alone cannot distinguish these two processes. Overall, there are four main properties characteristic of the lasing emission:

1. a spectral narrowing;
2. a clear threshold behaviour of both linewidth and emission intensity;
3. an emission characteristic (and influenced by) the gain medium and resonator; and
4. an output consisting of a beam.

These demonstrate unequivocally the lasing process and differentiate it from other effects, such as ASE.<sup>[13]</sup> The first two points are also observed for ASE (even if with slightly different parameters or shapes), and 3. and 4. are unique in lasing. All four should be demonstrated for clear proof of lasing.

The lasing process can be described mathematically by the laser rate equations, which give the temporal evolution of the excited state density  $N_{\text{exc}}$  and emitted photon density in the laser mode  $N_{\text{ph}}$  as follows:

$$\begin{aligned}
 \frac{dN_{\text{ph}}}{dt} &= \underbrace{B_{21}N_{\text{ph}}N_{\text{exc}}}_{\text{stimulated emission}} + \underbrace{\gamma A_{21}N_{\text{exc}}}_{\text{spontaneous emission into lasing mode}} - \underbrace{\frac{N_{\text{ph}}}{\tau_{\text{ph}}}}_{\text{photon loss}} \\
 \frac{dN_{\text{exc}}}{dt} &= \underbrace{R}_{\text{pump rate}} - B_{21}N_{\text{ph}}N_{\text{exc}} - \underbrace{A_{21}N_{\text{exc}}}_{\text{spontaneous emission}} - \underbrace{\frac{N_{\text{exc}}}{\tau_{\text{exc}}}}_{\text{non-radiative losses}}
 \end{aligned} \tag{3.6}$$

where  $B_{21}$  and  $A_{21}$  are the Einstein coefficients for spontaneous and stimulated emission, respectively;  $\gamma$  is the fraction of spontaneous emission coupled into the lasing mode;  $\tau_{\text{ph}}$  is the photon lifetime in the resonator;  $\tau_{\text{exc}}$  is the excited state lifetime associated with non-radiative recombination (higher-order non-radiative losses are not considered in this simplified equations); and  $R$  is the pump rate. Solving these equations for the steady-state condition ( $d/dt = 0$ ) yields the evolution of  $N_{\text{exc}}$  and  $N_{\text{ph}}$  as a function of  $R$ . The contribution of spontaneous emission is ignored to simplify the solution, i.e.  $A_{21} = 0$ , resulting in two solutions: below the lasing threshold ( $N_{\text{ph}} = 0$ ) and above the lasing threshold ( $N_{\text{ph}} \neq 0$ ). Figure 3.4 illustrates the schematic solution by plotting the values of  $N_{\text{exc}}$  and  $N_{\text{ph}}$  as a function of  $R$ . The first solution (below threshold) yields  $N_{\text{ph}} = 0$  and  $N_{\text{exc}} = R \cdot \tau_{\text{exc}}$ . No photons are generated, and the excited state density increases linearly with  $R$  and

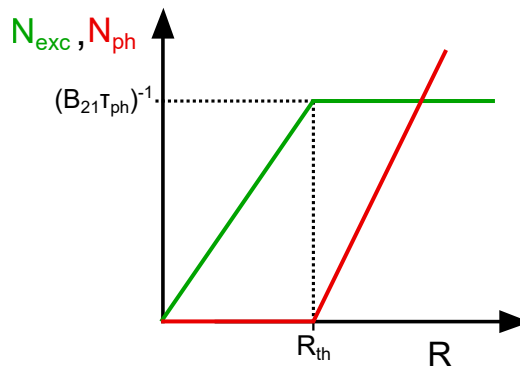


**Figure 3.4:** Schematic solution of the laser rate equations with  $N_{\text{exc}}(R)$  (green line) and  $N_{\text{ph}}(R)$  (red line) curves. The increase in  $N_{\text{exc}}$  with excitation density is proportional to  $R \cdot \tau_{\text{exc}}$ . After the lasing threshold  $R_{\text{th}} = (B_{21} \cdot \tau_{\text{exc}} \cdot \tau_{\text{ph}})^{-1}$ ,  $N_{\text{exc}}(R)$  stays constant at  $(B_{21} \tau_{\text{ph}})^{-1}$  and  $N_{\text{ph}}$  increases with a slope of  $\tau_{\text{ph}}$ . The red curve corresponds to the input-output characteristics or, for optical pumping, the light-in-light-out curve of a laser (or ASE), and the slope of the curve after  $R_{\text{th}}$  is called *slope efficiency*.

$\tau_{\text{exc}}$  (green line for  $R < R_{\text{th}}$ , Figure 3.4). The second solution describes the behaviour above threshold and yields  $N_{\text{exc}} = (B_{21} \tau_{\text{ph}})^{-1} = \text{constant}$  and  $N_{\text{ph}} = R \cdot \tau_{\text{ph}} - (B_{21} \tau_{\text{exc}})^{-1}$ , resulting in a pump threshold of  $R_{\text{th}} = (B_{21} \cdot \tau_{\text{exc}} \cdot \tau_{\text{ph}})^{-1}$ . The slope of  $N_{\text{ph}}$  above threshold is called *slope efficiency* as it indicates how efficiently the input power is converted into stimulated emission. The previous solutions show that both the laser threshold and the slope efficiency depend primarily on the material parameters  $B_{21}$  and  $\tau_{\text{exc}}$ , and on the photon lifetime  $\tau_{\text{ph}}$ , which is related to the optical losses. Hence, the losses in a resonator (or waveguide, for the case of ASE) are directly related to the laser threshold and slope: The lower  $\alpha$ , the lower  $R_{\text{th}}$  and the higher the slope efficiency. The plot of  $N_{\text{ph}}(R)$  is also known as the input-output characteristics of a laser or, for optically-pumped lasers (or ASE), the light-in light-out curve (red line, Figure 3.4). In practical experiments (Chapters 7 and 8), there is a contribution from spontaneous emission into the ASE or lasing mode, so the curve  $N_{\text{ph}}$  below threshold is not zero like in Figure 3.4. The laser (or ASE) threshold can be graphically determined with the light-in-light-out curve by fitting the linear parts of the emission (below and above threshold) with two linear fits and taking their intersection as the threshold value. Other methods to determine thresholds are discussed elsewhere,<sup>[14]</sup> however, in the framework of this thesis, all thresholds are determined with the previously mentioned method (denominated as the ‘slope general’ method).

### 3.4.1 Distributed feedback lasers

The feedback in a DFB laser originates from a periodic modulation of the refractive index along the gain medium, typically realised with a grating. Figure 3.5 schematically depicts the working principle of a thin film DFB laser: In this example, the gain medium (orange) consists of a slab waveguide with a structured surface shaped like a square grating, with a top cladding layer (blue). In such a waveguide structure, the modulation corresponds to an  $n_{\text{eff}}$  variation. Light generated and propagating inside the waveguide is partially

reflected at the grating teeth, so two coupled counter-propagating modes oscillate within the structure.<sup>[15]</sup> The refractive index modulation can be achieved by varying its real or imaginary part (i.e., gain). Depending on which part of the refractive index is modulated, the DFB is denoted as index-coupled (real part), gain-coupled (imaginary part), or mixed-coupled (both real and imaginary parts). The total coupling coefficient  $\kappa_t = \kappa + i\kappa_i$  describes the coupling strength of such a structure, with a feedback coupling coefficient  $\kappa$  (index coupling) and  $i\text{Im}(\kappa)$  for gain coupling. The material properties and grating geometry, such as grating height or duty cycle, influence the refractive index modulation and thus the coupling coefficient and feedback in this distributed cavity (Chapter 8).

The Bragg condition gives the wavelength for constructive interference between the two modes as a function of the modulation period  $\Lambda$ :

$$m\lambda_{\text{Bragg}} = 2n_{\text{eff}}\Lambda \quad (3.7)$$

where  $m$  is an integer denoting the grating order. The DFB grating order determines the scattering direction: For  $m = 1$ , scattering occurs solely in the grating direction along which the waveguide modes propagate. The lower scattering orders are scattered out of the waveguide for higher order DFBs (e.g.  $m = 2$ ). The scattering along the grating direction is responsible for the coupling of the two propagating modes and thus the feedback, whereas the scattering in other directions results in radiating waves, whose emission angle depends on the constructive interference condition (Figure 3.5).<sup>[15, 16]</sup> First-order DFBs lasers provide feedback and emission by first-order diffraction, in-plane with the grating structure (Figure 3.5). In second-order gratings ( $m = 2$ ), the feedback (in-plane) is provided by second-order diffraction and emission is enabled by first-order diffraction, at  $90^\circ$  for  $m = 2$ . Thus, a second-order DFB is a surface-emitting laser (Figure 3.5). In second-order (and higher order) gratings, where the emission is not in-plane but coupled out of the resonator,  $\kappa_t$  has an additional negative imaginary term to describe the radiation losses.<sup>[17]</sup> Therefore, the index coupling coefficient  $\kappa$  of different order DFBs is not necessarily comparable due to the additional losses of the radiation mode. Detailed mathematical expressions for feedback and radiation coupling coefficients are outside this thesis's scope and presented elsewhere.<sup>[16, 18]</sup>

The constructive interference of the coupled modes in the waveguide results in a stopband centred around  $\lambda_{\text{Bragg}}$ , where propagation inside the cavity is suppressed.<sup>[15]</sup> This stopband is different for index, gain, and mixed-coupling: For a purely index-coupled DFB, the resonant laser mode arises at the stopband edge ( $\lambda_{\text{lasing}} \approx \lambda_{\text{Bragg}}$ ) and for a gain or mixed-coupled resonator,  $\lambda_{\text{lasing}} = \lambda_{\text{Bragg}}$ . Thus, the Bragg condition can calculate or approximate the lasing wavelength (Equation 3.7). Perovskite DFB lasers have demonstrated emission characteristics encompassing both index-coupling and mixed-coupling behaviours. This results in lasing emission positioned either at the centre of the stopband (indicative of gain or mixed-coupling) or at the stopband edge (typical of index-coupling).<sup>[19]</sup>

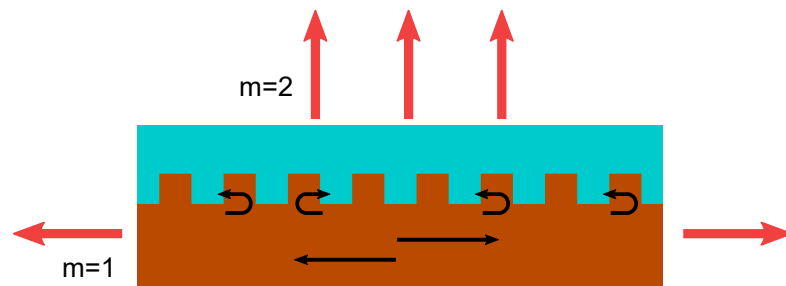


**Figure 3.5:** Schematic of a DFB laser with a structured gain medium acting as a waveguide (orange) and a planar cladding layer (blue). The grating feedback and counter-propagating waves are illustrated with black arrows, and the laser emission is indicated by red arrows for first ( $m = 1$ ) and second-order ( $m = 2$ ) DFB lasers.

### 3.4.2 Random feedback lasing

Section 3.4 mentions the typical Fabry-Pérot resonator with two mirrors providing feedback, and the previous section discusses lasers with periodic, distributed feedback in detail. One central and common aspect of a resonator is the constructive interference of waves, which enables light amplification. In a laser with random feedback, light is reflected by irregularly distributed scattering centres, which make forming closed loops possible, where light can oscillate and interfere constructively (Figure 3.6). The resonance condition dictates that after a cavity round-trip (in this case, an entire cycle in the closed loop), the phase shift must be an integer multiple of  $2\pi$ . Random lasing can be sustained if the resonance condition is met. In order to achieve random lasing, it is necessary to have a structure or material configuration which provides these multiple scattering events, as well as a high gain. For instance, a heterogeneous perovskite film with many grain boundaries, defects or a high roughness could provide such scattering centres and enable random lasing.<sup>[20]</sup> Given its random nature, it is challenging to demonstrate random lasing and determine the exact origin of the feedback loop. For instance, it would not be easy to test the influence of the ‘resonator’ on the emission (a requirement mentioned in Section 3.4).

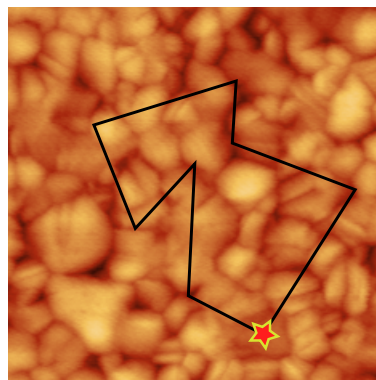


**Figure 3.6:** Schematic illustration of random lasing in a polycrystalline perovskite film where light emitted in the film (red star) undergoes multiple scattering events at grain boundaries forming a closed path (black line), which satisfies the resonance condition.



## 4 Hybrid Perovskite Semiconductors

This chapter introduces the fundamentals of hybrid perovskite semiconductors, starting with their crystal structure in Section 4.1 followed by their characteristic optoelectronic properties (Section 4.2). Section 4.3 explores perovskites carrier dynamics, particularly the basic recombination mechanisms of charge carriers and the most common models used to describe their transient behaviour.

### 4.1 Crystal structure

The name perovskite refers to the crystal structure of the mineral calcium titanate with a chemical formula  $ABX_3$  ( $CaTiO_3$ ), whose lattice structure is displayed in Figure 4.1a. Crystals exhibiting this structure with cations  $A^{2+}$  ( $A^+$ ) and  $B^{4+}$  ( $B^{2+}$ ), and anion  $X^{2-}$  ( $X^-$ ) are termed perovskites. Perovskites combining organic and inorganic ions are termed *hybrid* perovskites. In lead halide perovskites, the B ion is lead ( $Pb^{2+}$ ), and the X ion is a halide, typically bromine ( $Br^-$ ), iodine ( $I^-$ ), or a combination of both. The lead ion is surrounded by halide ions in the crystal to form an octahedron lattice, supported by the A cation in the interstices (Figure 4.1a). The A cation is generally a small positively charged ion ( $Cs^+$ ,  $K^+$ ,  $Rb^+$ ), an organic molecule such as methylammonium (MA) and formamidinium (FA), or a combination of these (Figure 4.1b). Perovskites with more than one A-site cation are called multi-cation, e.g., double or triple-cation perovskites.

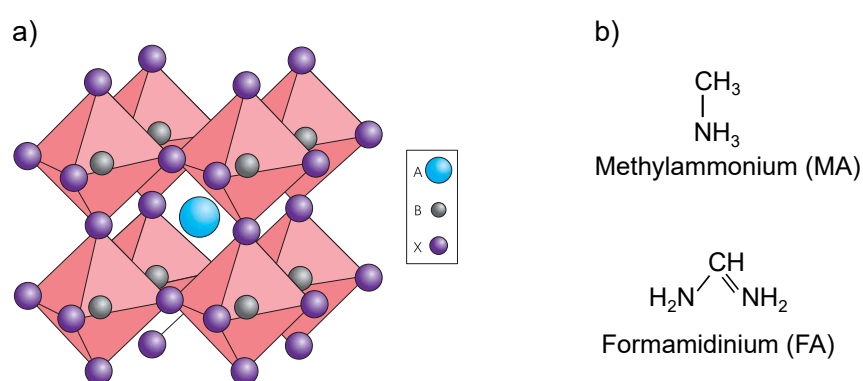


**Figure 4.1:** Cubic perovskite crystal structure and chemical composition of organic cation molecules. a) Crystal lattice with large cation A (blue), small cation B (grey spheres in octahedra centres), and anion X (purple). For the standard triple-cation perovskite, A is a mixture of Cs, MA, and FA, B is Pb, and X is a mixture of the halides I and Br. Reproduced with permission from Springer Nature, [21] Copyright 2014. b) Molecular structure of organic cations MA and FA.

The size of the ions and molecules making up the perovskite lattice determines its crystal phase. The typical cubic lattice can be shifted into a pseudo-cubic, tetragonal, or orthorhombic phase, depending on the perovskite composition. The Goldschmidt tolerance factor is a parameter used to quantify this crystal distortion based on the ionic radii of the constituent ions.<sup>[22]</sup> In addition, temperature can also change the lattice structure and perovskite crystal phase. Common perovskite materials reported in the literature, such as methylammonium lead iodide (MAPI) or double-cation perovskites, typically possess two phase transitions with temperature: one around 150 K from orthorhombic to tetragonal and a second one around 300 K (from tetragonal to cubic).<sup>[23, 24]</sup> The crystal structure strongly correlates with the material optoelectronic properties, as discussed in Section 4.2.

In this work, mainly triple-cation perovskites are investigated, with a hybrid mix of organic and inorganic A-cations: Cs, MA, and FA, lead (Pb) as the B cation, and a mix of bromine and iodine as halide anions. The specific chemical composition can be represented as  $\text{Cs}_{0.1}(\text{MA}_{0.17}\text{FA}_{0.83})_{0.9}\text{Pb}_{0.84}(\text{I}_{0.83}\text{Br}_{0.17})_{2.68}$ . Triple-cation perovskites with Cs, MA, and FA were reported as superior materials due to their higher thermal and ambient stability, reproducibility and device stability in solar cell applications.<sup>[25]</sup> The non-stoichiometric composition mentioned previously was optimised to yield thin films with low ASE thresholds,<sup>[26]</sup> and its cation excess emerging from the lead deficiency (molar ratio  $\text{Pb}/\text{A} = 0.84$ ) is hypothesised to passivate under-coordinated lead ions and improve the optical properties of perovskites.<sup>[27]</sup> One additional and exceptional characteristic of this composition is that it exhibits no phase transition from cryogenic to room temperature, making it ideal for studying temperature-dependent optoelectronic properties without the influence of a changing crystal phase.<sup>[28]</sup> Throughout this thesis, perovskites with this specific composition are denoted as *standard triple-cation perovskites*. Due to their three-dimensional crystal structure, the perovskites discussed so far are known as bulk or 3D perovskites. This denomination distinguishes them from other perovskite structures with different dimensionalities, such as perovskite nanoparticles or 2D perovskites (discussed in the following). In the context of this dissertation, unless explicitly stated otherwise, the term ‘perovskite’ refers to 3D perovskites.

### Quasi-2D perovskites

2D perovskites consist of single octahedral sheets (formed by the B cation and the X anions) sandwiched between long-chained organic spacer cations ( $n = 1$ , Figure 4.2). For this case, the spacer molecule replaces the A-site cation (green ‘small cation’, in Figure 4.2). Suppose the perovskite layers are comprised of multiple sheets. In that case, they are termed quasi-2D perovskites, and the parameter  $n$  denotes the number of individual sheets making up the perovskite layer (Figure 4.2). In this context, the large spacer only replaces the small cation in the outer sheets of the perovskite layer. Figure 4.2 illustrates the energy confinement effect in quasi-2D perovskites by showing the energy levels of the spacer and perovskite layers: The lower bandgap of the perovskite material gives rise to a quantum well structure between spacer and perovskite. As depicted in Figure 4.2, an increasing  $n$  value (from left to right) leads to wider quantum wells and a lower bandgap of the perovskite. The limit of  $n = \infty$  corresponds to a 3D perovskite.

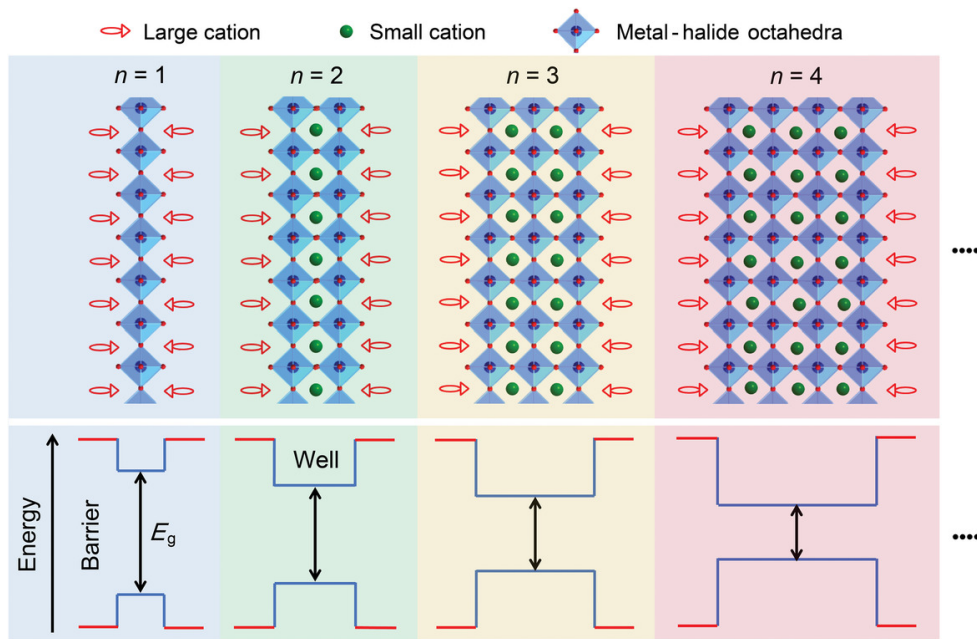


**Figure 4.2:** Schematic of (quasi-)2D perovskite crystal structure. Top: 2D and quasi-2D perovskites with different octahedra sheet thicknesses confined by large spacer cations, from  $n = 1$  to  $n = 4$ . Bottom: Corresponding energy levels of the spacer and perovskite regions demonstrate an energetic quantum well formation with different well thicknesses and bandgap for different  $n$  values. Reprinted from [31] with permission. Copyright 2019 WILEY-VCH Verlag GmbH & Co. KGaA, Weinheim.

The exciton binding energy  $E_b$  is higher in (quasi-)2D perovskites than in 3D structures due to quantum confinement effects, and excitons are generally the dominating species in these materials (in contrast to 3D materials, where free charge carriers are the dominant population).<sup>[29]</sup> Solution-processed (quasi-)2D perovskite films typically display a mixed-phase structure consisting of a distribution of  $n$ -values phases.<sup>[30]</sup> Consequently, such films give rise to a multiple quantum well (MQW) structure with a heterogeneous energy landscape, where charge carriers funnel into the lower bandgap phases to reach equilibrium.

## 4.2 Optoelectronic properties

The optoelectronic properties of hybrid perovskites are strongly influenced by their crystal structure and chemical composition: Their crystalline nature gives rise to an electronic band structure with a direct bandgap, where the VBM and CBM are formed by the orbitals of B (Pb) and X (halides) ions. Changing the halide (or halide ratio) makes tuning the bandgap across the visible and near-infrared wavelength range possible. The A-cation mainly determines the structural and phase stability and does not directly affect the band-edge states. However, it can influence the material bandgap by tilting the octahedra or changing the lattice size. Temperature can have a similar effect, in which lattice expansion

(or contraction) can lead to a bandgap shift and a phase transition at specific temperatures (Section 4.1). The possibility of directly changing perovskites' bandgap by composition engineering makes them very attractive for laser and light emission applications.<sup>[3, 27, 32]</sup>

Perovskites exhibit high absorption coefficients ( $\approx 10^5 \text{ cm}^{-1}$ ), and their absorption is also directly related to their electronic band structure.<sup>[33]</sup> The absorption spectrum possesses contributions from excitonic resonances and continuum states, and  $E_b$  was reported in the 5 - 60 meV range for different material systems.<sup>[34, 35]</sup> These  $E_b$  values are higher than those of typical inorganic semiconductors but still significantly lower than organic semiconductors and allow for exciton dissociation into free charge carriers at room temperature.<sup>1</sup> Whether the excited state population in hybrid perovskites comprises an exciton gas (similar to organic semiconductors) or a conductive plasma of free charge carriers (occurring in inorganic semiconductors) is still debated. However, strategies to distinguish between these two are presented in several reports, and the conclusions demonstrate that optical excitation well above the bandgap leads to a population of primarily free carriers.<sup>[34, 36, 37]</sup> Carrier mobilities for MAPI were reported in the range of 0.2 - 100  $\text{cm}^2\text{V}^{-1}\text{s}^{-1}$  for different compositions and measurement techniques, and measurements of individual electron  $\mu_e$  and hole  $\mu_h$  mobilities demonstrated generally a higher  $\mu_h$ . For triple-cation perovskites, mobilities of  $\mu_h \approx 30 \cdot \mu_e$  were measured.<sup>[38]</sup> Diffusion lengths of at least 1  $\mu\text{m}$  and an increasing diffusion for samples with high compositional and crystalline disorder were reported.<sup>[39, 40]</sup>

In the context of perovskite optoelectronic properties, it is essential to consider the photoluminescence (PL) characteristics under optical pumping. The PL emission of perovskites originates from photo-excited carriers, which thermalised to the band edges after excitation and is related to the previous absorption and bandgap considerations. In general, the PL shape of a semiconductor is influenced on the high energy side by the carrier distribution in the bands and on the low energy side by the absorption edge.<sup>[41]</sup> Figure 4.3 displays exemplary absorption and PL spectra where the perovskites' Stokes shift is observable (typically less than  $\sim 20$  meV). This small Stokes shift leads to a strong re-absorption of the PL upon propagation within a perovskite film, resulting in spectral distortions and a red-shift of the PL maximum (Figure 4.3).<sup>[3, 42]</sup> Hence, different sample and detection geometries generate altered PL spectral shapes, including central wavelength and linewidth. Triple-cation perovskites present typical linewidths between 20 - 60 nm, depending on the halide composition.<sup>[26]</sup> Overall, many optoelectronic properties of perovskites are still being explored, and some conclusions are debated, which can account for literature reports with contradicting results.

---

<sup>1</sup> Compared to commonly employed compositions such as MAPI and MAPbBr<sub>3</sub>, triple-cation perovskites were reported to have lower  $E_b$ .<sup>[32]</sup>

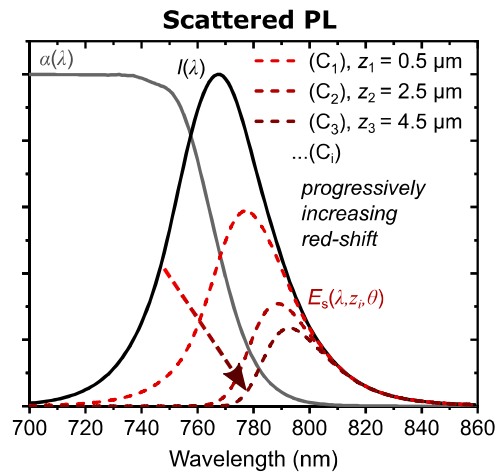


**Figure 4.3:** Perovskite absorption  $\alpha(\lambda)$  (grey solid line) and internal PL spectrum  $I(\lambda)$  (black solid line) evidencing the typical small Stokes shift observed in perovskites. The dashed red lines correspond to scattered PL emission  $E_s$  after a certain propagation length  $z_i$  inside a film (where the emitted light is reflected at different angles  $\theta$ ). The longer the light propagates inside the film (higher  $z_i$ ), the stronger the re-absorption and the PL red-shift, and the lower the PL signal. Reprinted from [42], Copyright 2021, with permission from Elsevier.

### 4.3 Carrier recombination dynamics

As a new hybrid semiconductor, perovskite recombination mechanisms and carrier dynamics have been extensively studied to understand the underlying material photophysics and improve its performance in optoelectronic devices. This chapter presents the fundamental carrier recombination mechanisms (Section 4.3.1) and the most common models utilised to describe these processes and fit measured decay dynamics (Section 4.3.2).

#### 4.3.1 Recombination mechanisms

Photo-generated carriers in perovskites reach an equilibrium state through various energy relaxation processes: Upon optical excitation above the bandgap, carriers thermalise to the band edges.<sup>[43]</sup> At the band edges, carriers undergo different recombination mechanisms, radiative and non-radiative, to achieve equilibrium. These are elucidated in the following for free charge carriers (electrons and holes) in a 3D perovskite and illustrated in Figure 4.4. **Defect-assisted recombination** consists of a monomolecular process involving a charge carrier and a trap state. Three possible defect-assisted processes exist: trapping, de-trapping, and trap recombination. In this context, only electron traps are considered since perovskite trap states were reported to consist of crystal vacancies acting as shallow electron traps mainly.<sup>[44–46]</sup> However, the inverse process involving a hole trap is equally possible and can be described analogously. Trapping consists of an electron falling into a localised defect state, releasing the energy difference as a phonon. This interaction is proportional to the electron density  $n$ , density of trap states  $N_t$  and trapping rate coefficient  $k_t$  (Figure 4.4, left). Trapped electrons can transition back into the conduction band provided enough thermal energy (de-trapping) or recombine non-radiatively with a hole

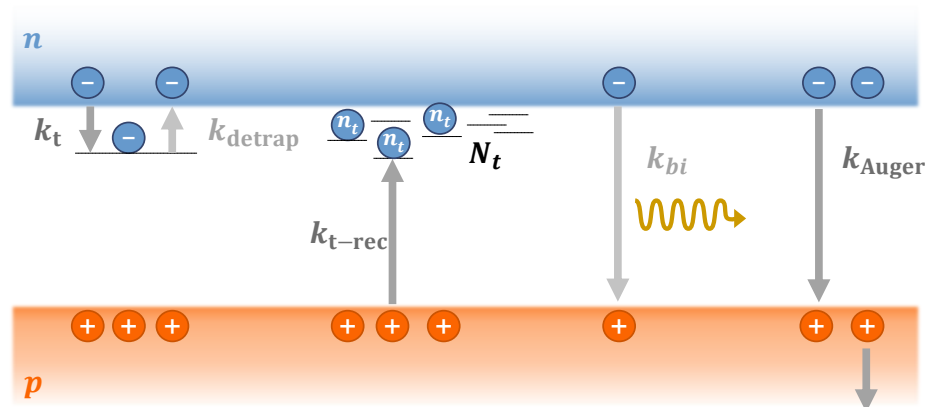


**Figure 4.4:** Schematic representation of perovskite recombination mechanisms. The conduction band and electrons are represented in blue, the valence band and holes in orange, and electron trap states within the bandgap are depicted with horizontal black lines. Carrier transitions are indicated with grey arrows with the associated rate coefficient next to it. Trap-assisted processes are represented by the rate coefficients  $k_t$  (trapping),  $k_{\text{detrap}}$  (de-trapping), and  $k_{t\text{-rec}}$  (trap recombination), and the total trap density is given by  $N_t$ . Bimolecular recombination ( $k_{\text{bi}}$ ) leads to photon emission (yellow arrow), and the Auger process ( $k_{\text{Auger}}$ ) is exemplified with a hole as the third particle taking up the resulting energy from the electron-hole recombination.

in the valence band (trap recombination). The de-trapping rate scales with the density of trapped electrons  $n_t$  and the coefficient  $k_{\text{detrap}}$ . Trap recombination is proportional to  $n_t$ , hole density  $p$  and the associated rate coefficient  $k_{t\text{-rec}}$  (Figure 4.4, centre). **Bimolecular recombination** is a second-order process consisting of a band-to-band recombination of an electron-hole pair resulting in a photon emission with the respective energy difference. This transition is the sole radiative recombination process when considering free carriers. It is proportional to  $n \cdot p$  and the rate  $k_{\text{bi}}$ .<sup>2</sup> **Auger (band-to-band) recombination** is a third-order, non-radiative process involving bimolecular recombination of an electron-hole pair where a third carrier takes up the released energy. This process depends on the respective carrier densities ( $n^2 \cdot p$  or  $n \cdot p^2$ ) and the rate coefficient  $k_{\text{Auger}}$ . For (quasi-)2D perovskites, excitons govern the dynamics, and the main recombination mechanisms are the monomolecular radiative recombination of an exciton and the non-radiative Auger process, i.e., exciton-exciton annihilation (EEA), a second-order process.<sup>[50]</sup> All recombination processes depend strongly on the carrier density and occur at different time scales.<sup>[51]</sup>

For light-emitting applications, it is essential to consider the interplay between radiative and non-radiative recombination mechanisms, which depends strongly on the excitation density. This interplay can be assessed by the photoluminescence quantum efficiency (PLQE), defined as the number of emitted photons per absorbed photons. Figure 4.5 displays the PLQE of a 3D MAPI film as a function of carrier density where the following trend of radiative efficiency is observable: At low carrier density ( $n \sim 10^{15} \text{ cm}^{-3}$ ), non-radiative monomolecular processes govern the dynamics and the radiative efficiency is low. As  $n$  increases, higher-order recombination processes begin to dominate the dynamics. For

<sup>2</sup> The existence of a non-radiative bimolecular process was proposed as a trap-assisted Auger process, but it remains a debated topic without a consensus and is therefore not included in this study.<sup>[8, 23, 47-49]</sup>

3D perovskites, this means that the PLQE increases with carrier density until the radiative bimolecular process dominates the dynamics ( $n \approx 10^{18} \text{ cm}^{-3}$ ). It decreases again when non-radiative Auger losses kick in at high carrier densities (Figure 4.5). In contrast, (quasi-)2D perovskites possess their highest radiative efficiency at low  $n$  ( $n \sim 10^{15} \text{ cm}^{-3}$ ) due to the efficient monomolecular radiative exciton recombination process at this density.<sup>[36]</sup> Given the recombination mechanisms in the material and their rate coefficients, it is possible to calculate the PLQE at a specific carrier density. Details on the equations and models needed for this are detailed in the next section.

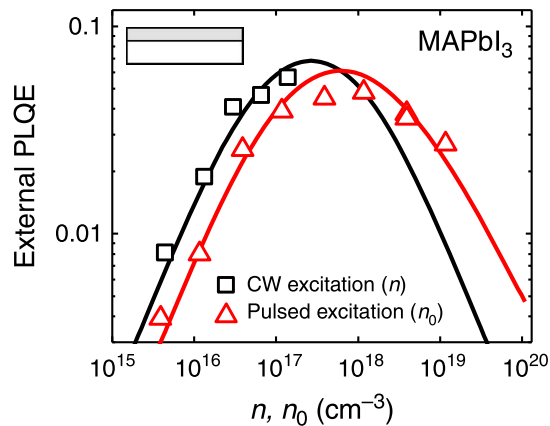


**Figure 4.5:** PLQE of a MAPI film for pulsed (red data) and CW (black data) excitation, as a function of initial carrier density  $n_0$  (pulsed excitation) and steady-state density  $n$  (CW pump). In 3D perovskites, the radiative efficiency increases with carrier density until  $n \approx 10^{17}$ - $10^{18} \text{ cm}^{-3}$ , where radiative bimolecular recombination dominates, and decreases for higher  $n$  due to non-radiative Auger losses. Adapted from [52] licensed under CC BY 4.0 (creativecommons.org/licenses/by/4.0).

### 4.3.2 Dynamics by ABC and Shockley-Read-Hall models

The transient signal of photo-excited perovskite samples can be analysed to study carrier dynamics and the individual recombination processes mentioned in the previous section. The most common experimental methods utilised for this are time-resolved photoluminescence (TRPL), transient absorption (TA) and terahertz spectroscopy.<sup>[24, 29, 50]</sup> Accurately fitting decay dynamics and extracting correct rate coefficients is a complex process that requires careful consideration of the model employed to achieve accurate results and interpretations. Measurement conditions, including substrate material, temperature, carrier density range, and laser repetition rate, must be considered as they influence the data acquired.<sup>[51, 53]</sup> Various models were proposed to describe and fit decay curves, resulting in different parameters and interpretations of the recombination processes. The two most prevalent and accepted models are the ABC and Shockley-Read-Hall (SRH) models.<sup>[53]</sup> Both models consider only free charge carriers as the carrier species in the material. Exciton formation from these free carriers and subsequent radiative recombination involves a bimolecular process. Consequently, distinguishing this process from radiative bimolecular recombination is impractical, and thus, an eventual exciton contribution to the dynamics is encompassed within the rate constant  $k_{\text{bi}}$ .<sup>[23]</sup>

The primary distinction between the ABC and SRH models lies in how they describe trap-assisted recombination processes: The SRH model considers them in more detail, i.e., it individually describes all three processes (trapping, de-trapping, and trap recombination). Consequently, it considers three carrier populations – electrons  $n$ , trapped electrons  $n_t$ , and holes  $p$  – where  $n + n_t = p$ , and the carrier dynamics is described by three differential equations:

$$\begin{aligned}\frac{dn(t)}{dt} &= G(t) - k_t[N_t - n_t(t)]n(t) + k_{\text{detrap}}n_t(t) - k_{\text{bi}}n(t)p(t) - k_{\text{Auger}}n(t)^2p(t) \\ \frac{dn_t(t)}{dt} &= k_t[N_t - n_t(t)]n(t) - k_{\text{detrap}}n_t(t) - k_{\text{t-rec}}n_t(t)p(t) \\ \frac{dp(t)}{dt} &= G(t) - k_{\text{t-rec}}n_t(t)p(t) - k_{\text{bi}}n(t)p(t) - k_{\text{Auger}}n(t)^2p(t)\end{aligned}\quad (4.1)$$

where  $G(t)$  is the generation rate, and  $k_i$  are the rate coefficients corresponding to the different recombination processes (detailed in Section 4.3.1). The standard SRH model includes only trap-assisted and bimolecular processes; however, the SRH model employed in this thesis is analogous to the ‘SRH+’ model proposed by Kiligaridis *et al.*, which includes an Auger term to describe dynamics at high carrier densities. This term is the last in the expressions for  $dn/dt$  and  $dp/dt$  with the coefficient  $k_{\text{Auger}}$  (Equation 4.1). In contrast to the thorough description of trap-assisted processes by the SRH model, the simpler ABC model specifies only one trap-assisted process, i.e., trapping, described by the rate coefficient  $A$ . In this case, de-trapping is typically not considered, and the trap recombination process is assumed to occur much faster than trapping ( $k_{\text{t-rec}} \gg k_t \approx A$ ), leading to significant consequences for the dynamics modelling and interpretation with the ABC model: A filled trap is immediately emptied due to the fast trap recombination and is available for the next trapping event. This means there is no trapped electron population (in terms of SRH parameters,  $n_t = 0$ ), and trap saturation effects are neglected, such as the slow-down of the trapping process once most traps are filled. Thus, both hole and electron populations are equal ( $n = p$ ), and the dynamics is described by a single population, e.g.,  $n(t)$ , as follows:

$$\frac{dn(t)}{dt} = G(t) - An(t) - Bn(t)^2 - Cn(t)^3. \quad (4.2)$$

In the ABC model, the coefficients ‘ $B$ ’ and ‘ $C$ ’ are identical to the coefficients  $k_{\text{bi}}$  and  $k_{\text{Auger}}$  (Equation 4.2). Finally, the ABC model does not explicitly consider trap density; however, it is encompassed within the  $A$  coefficient, which can be described as  $A = k_t \cdot N_t$  in terms of SRH parameters.<sup>[53]</sup>

By considering the  $n_t$  population, the SRH model accounts for charge carrier accumulation effects, e.g., trap saturation. This is particularly relevant when exciting films at high repetition rates or with a long pulse (or CW) pump and can cause the shape of the TRPL curves to depend strongly on carrier density and pulse rate, rendering conclusions based on the ABC model unreliable.<sup>[23]</sup> Neither of the models explicitly accounts for carrier transport, such as diffusion, and both assume a spatially homogeneous charge-carrier

distribution throughout the thin film.<sup>3</sup> Further, the initial charge carrier density  $n_0$  used to solve the rate equations is typically calculated by assuming an ideal case where each absorbed photon generates an electron-hole pair. A significant contribution from carrier diffusion, e.g., for much thicker films, would lead to an apparent reduction in bimolecular recombination.<sup>[55]</sup> Similarly, strong re-absorption effects result in an apparent slower bimolecular recombination.<sup>[56]</sup>

Figure 4.6 presents fluence-dependent TRPL curves simulated with the SRH and ABC models using the parameters in Table 4.1. The decay curves range from low excitation density,  $n_0 < N_t$ , up to carrier densities above typical threshold values where Auger dominates  $n_0 > n_{th} \sim 10^{18} \text{ cm}^{-3}$ . These curves exemplify qualitatively TRPL curve shapes when different recombination processes and assumptions (i.e., ABC versus SRH model) are considered. As a rule, a fluence-dependent data set is needed to fit all coefficients in the rate equations (Equations 4.1 or 4.2) since monomolecular, bimolecular, and Auger dominate the dynamics at different carrier density regimes.<sup>[51]</sup> The main differences between the two models are related to the trap-assisted processes (discussed previously) and can be recognised from the decay curve shapes: The curves simulated with the SRH model (Figure 4.6a) exhibit an initial fast decay at low excitation densities ( $n_0 < N_t \sim 10^{16} \text{ cm}^{-3}$ ) corresponding to the initial trapping of electrons, while most trap states are empty, and de-trapping has not yet set in. This quick drop saturates due to the onset of a de-trapping process, which raises trapped electrons back to the conduction band and slows down the effective carrier loss by trapping. At high fluences ( $n_0 > 10^{16} \text{ cm}^{-3}$ ), this fast decay is not

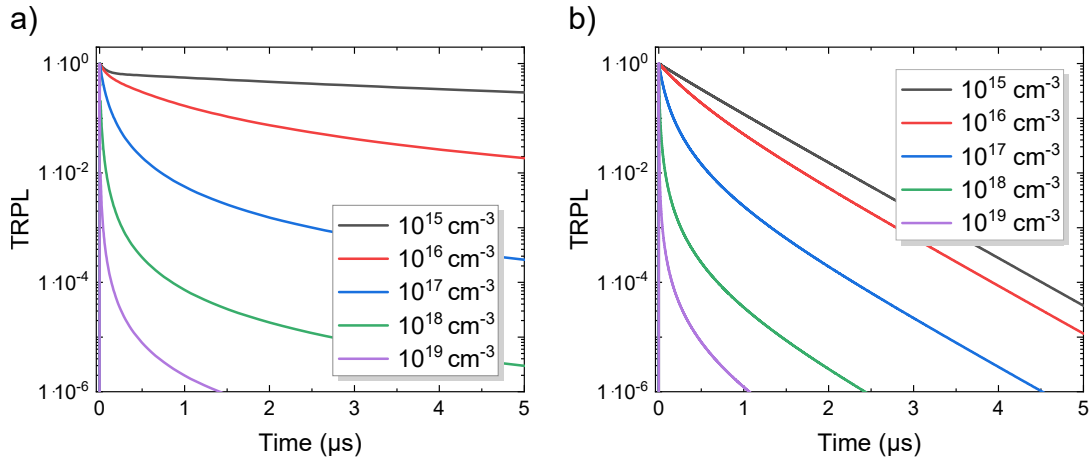


**Figure 4.6:** TRPL decay curves simulated with ABC and SRH models. The simulation consists of solving Equations 4.2 and 4.1 with MATLAB's ordinary differential equation (ODE) solver and plotting the radiative term as a function of time delay to get the TRPL curves for the a) SRH ( $PL = k_{bi}np$ ) and b) ABC ( $PL = Bn^2$ ) models. The excitation rate  $G(t)$  was a Gaussian with 0.8 ns time width, centred at time  $t = 0$  ns, and the initial conditions (before pulse arrival) were set to zero, i.e.  $n(0) = p(0) = n_t(0) = 0$ .

<sup>3</sup> The carrier density is regarded as a uniform distribution when the film is thin enough ( $\sim 200$  nm) by considering the fast carrier diffusion process.<sup>[51, 54]</sup>

distinguishable since higher-order processes dominate over trapping. For the ABC model, the low-density decay curves ( $n_0 < 10^{16} \text{ cm}^{-3}$ ) do not exhibit this feature because this model does not include a time-dependent de-trapping term (Figure 4.6b).<sup>[23]</sup> The TRPL decay appears approximately linear on the semi-logarithmic scale due to the ABC trapping term  $dn(t)/dt = A \cdot n$ : At low fluences (or long time delays), the  $n(t)$  decay follows a single exponential ( $n(t) \propto e^{A \cdot t}$ ) and the TRPL is given by  $B \cdot n(t)^2$  (Figure 4.6b). Moreover, the decay of the ABC curves appears much faster than that of the SRH model since the ABC model neglects the presence of a trap recombination process, slowing down the overall decay at low  $n_0$ . So for the ABC model, the long tail slope of all curves ( $n_0$ ) appears identical, in contrast to the SRH curves, where the long delay slope is determined by either the trapping process (when most trap states are empty:  $n \ll N_t$ ) or the trap-recombination process (if most trap states are filled). At high fluences, i.e.,  $n > 10^{16} \text{ cm}^{-3}$ , the initial decay of both models appears near-identical since high-order processes govern the dynamics, and these are described identically for both models (Equations 4.1 and 4.2). Similarly, suppose the assumptions of the ABC model are valid for a specific material or measurement condition, e.g., trap recombination occurs very fast  $k_{t\text{-rec}} \gg k_t$ , or de-trapping is negligible. In that case, this simplified ABC model can fit and model data accurately. However, the  $A$  parameter related to trap-assisted processes cannot be separated into the two parameters  $k_t$  and  $N_t$  and be related to a specific recombination process.

In this work, both models are used to analyse carrier dynamics measured at different excitation fluences and time delays: The analysis in Chapter 6 is based on an adapted ABC model valid for the specific measurement conditions, i.e., high fluences and short delays. In Chapter 7, the SRH model is used to investigate the trap density in perovskite films, given that only this model includes this parameter separately.

**Table 4.1:** Parameters used for model simulation, based on reported values of similar perovskite materials in the literature.<sup>[8, 23, 24, 57-61]</sup>

$k_t$	$N_t$	$k_{\text{detrapp}}$	$k_{t\text{-rec}}$	$A$	$k_{\text{bi}}(B)$	$k_{\text{Auger}}(C)$
$10^{-10} \text{ cm}^3\text{s}^{-1}$	$5 \cdot 10^{16} \text{ cm}^{-3}$	$10^7 \text{ s}^{-1}$	$10^{-10} \text{ cm}^3\text{s}^{-1}$	$10^6 \text{ s}^{-1}$	$10^{-10} \text{ cm}^3\text{s}^{-1}$	$10^{-28} \text{ cm}^6\text{s}^{-1}$

# 5 Fabrication and Characterisation Methods

This chapter presents the details of the fabrication approaches utilised throughout this thesis. In particular, the processing of perovskite thin films (Section 5.1), different surface treatment methods (Section 5.2), and the nanoimprint lithography (NIL) process employed for structuring and flattening of perovskite thin films detailed in Section 5.3. Additionally, the characterisation methods used to study the different samples and laser devices are introduced in the last two sections, i.e., morphological characterisation in Section 5.4 and optical characterisation in Section 5.5.

## 5.1 Perovskite thin film processing

### Substrate preparation

Within the scope of this work, three types of substrates were used: microscope slide borosilicate glass (1 mm thick), optically polished sapphire (1 mm thick), and crystalline silicon (c-Si) (500  $\mu\text{m}$  thick). Glass substrates were cut in  $1\text{ cm}^2 - 1.5\text{ cm}^2$  pieces with a glass cutter by scratching the glass surface with a cutting wheel and manually separating each piece. Sapphire substrate discs were purchased from Ted Pella, Inc., Redding, CA, and silicon substrates were diced from a 150 mm diameter c-Si wafer. Before use, all substrates underwent a cleaning process in an ultrasonic bath (D-7700 Singen/Htw., Elma Schmidbauer GmbH), where they were immersed first in acetone and then in isopropanol for 10 min each. This process removes contamination from the substrate surfaces. A few minutes before depositing the perovskite solution onto the substrates, their surfaces were cleaned and activated in an oxygen plasma at 100 W for 3 to 5 min (PlasmaFlecto 30, plasma technology GmbH). The oxygen plasma removes remnant organic residuals on the substrate surface and, most importantly, increases the wettability and adhesion properties of the substrate for polar solution systems, like the perovskite precursor, by introducing polar functional groups on the surface.<sup>[62]</sup>

### Perovskite precursor solution preparation

The perovskite solution preparation consisted of mixing the precursor salts in the appropriate ratio in a small vial, adding the solvents to it, and shaking until the mixture was fully dissolved. The **standard triple-cation perovskites** used throughout this thesis possess

the composition  $\text{Cs}_{0.1}(\text{MA}_{0.17}\text{FA}_{0.83})_{0.9}\text{Pb}_{0.84}(\text{I}_{0.83}\text{Br}_{0.17})_{2.68}$  and were fabricated using the following precursors: caesium iodide (CsI, 7789-17-5, Alfa Aesar), methylammonium bromide (MABr, 6876-37-5, GreatCell Solar), formamidinium iodide (FAI, 879643-71-7, GreatCell Sola), lead iodide ( $\text{PbI}_2$ , 10101-63-0, TCI), and lead bromide ( $\text{PbBr}_2$ , 10031-22-8, TCI). All precursors were mixed in a single vial, and the solvents *N,N*-dimethylformamide (DMF) (68-12-2, Sigma Aldrich) and dimethyl sulfoxide (DMSO) (67-68-5, Sigma Aldrich) were added in a 3:1 (DMF:DMSO) volume ratio. The total volume was 1 ml to achieve a final perovskite concentration (of the A cation) of 1.3 M. The solution was diluted before spin-coating to achieve the desired film thickness. A concentration of 0.8 M typically resulted in a film thickness of  $d \approx 230$  nm (Section 5.5.3).

For the **quasi-2D CsPbBr<sub>3</sub> perovskites** (Section 4.1), the precursor solution was prepared by mixing three individual stock solutions:  $\text{CsPbBr}_3$ , polyethylene glycol (PEG), and butylammonium bromide (BABr).  $\text{CsPbBr}_3$  was either supplied as a one powder mixture (Cesium Lead Tribromide  $\text{CsPbBr}_3$ , 15243-48-8, TCI) or a two powder mixture ( $\text{CsBr}$ , 7787-69-1, Alfa Aesar, and  $\text{PbBr}_2$ , 10031-22-8, TCI), and it was dissolved in DMSO with a concentration of 0.4 M. The solution was then heated at 60 °C for 10 - 30 min until completely dissolved. The BABr/DMSO stock solution was prepared by mixing BABr (98 %, 15567-09-6, Sigma-Aldrich) in DMSO with a 2.8 M concentration. Polyethylene glycol (PEG, 25322-68-3, Sigma-Aldrich) with an average molecular weight of  $M_w \sim 4,000$  was dissolved in DMSO with a concentration of 100 mg/ml. The final solution was a mix of 1 ml perovskite stock solution with the addition of 100  $\mu\text{l}$  BABr/DMSO (2.8 M) and 24  $\mu\text{l}$  PEG/DMSO (100 mg/ml), resulting in a molar ratio of BABr/ $\text{CsPbBr}_3$  = 0.7/1, and a weight ratio of PEG/ $\text{CsPbBr}_3$  = 0.01/1.

### Spin-coating

Spin-coating is a simple, fast, and inexpensive technique to deposit uniform thin films via solution processing onto flat substrates. The coating process consists of four main steps: solution deposition onto the substrate, uniform spreading of the solution and fluid outflow (due to the spinning of the substrate), thinning of the film through drying, and finally, evaporation of the solvent. The latter is usually assisted with an annealing step on a hotplate. The spin speed and the solution's viscosity determine the final film thickness. In this work, the spin-coating process can be divided into two categories: static and dynamic spin-coating, depending on whether the fluid is deposited on a static or already spinning substrate. Typical thicknesses for spin-coated films are in the range of tens of nm up to a few  $\mu\text{m}$ . The drawbacks of this method are the poor material efficiency and the unsuitability for large-scale deposition.<sup>[63]</sup>

One central method employed for the perovskite spin-coating is the anti-solvent method. It consists of inducing a fast and sudden crystallisation of the perovskite film by a solvent, which is miscible with the perovskite solvents but not with its precursors.<sup>[64]</sup> When an anti-solvent is added in a dynamic step after perovskite deposition, it removes most of the solvent and thereby initialises a uniform crystallisation across the entire film. This fast crystallisation process leads to a flat and morphologically homogeneous perovskite layer.

The anti-solvents used during this work were anhydrous chlorobenzene (CB) (108-90-7, Sigma Aldrich) and isopropanol (IPA) (67-63-0, Sigma Aldrich), depending on compatibility requirements with the underlying material.

All triple-cation perovskite thin films in this work were fabricated inside a nitrogen-filled glovebox via a two-step spin-coating process: In the first step, the perovskite precursor solution is dynamically spin-coated onto a rotating substrate at 1000 rpm, with a step duration of 10 s. The second step increases the speed to 6000 rpm with a 2000 rpm<sup>2</sup> ramp and a step duration of 20 s. After approximately 12 s of the second step, an anti-solvent is dripped with a continuous flow on the film. Upon spin-coating, the substrate is placed on a hotplate at 100 °C for 1 h to finalise the crystallisation process and remove remnant solvents.

The quasi-2D CsPbBr<sub>3</sub> films (Section 7.2) were fabricated in the same glovebox via a two-step spin-coating process: the first step is at 1000 rpm for 20 s, and the second at 4000 rpm for 40 s, both with a ramp of 1000 rpm<sup>2</sup>. In this case, the perovskite solution is dripped onto the static substrate immediately before the first step starts. These coating parameters yield a film with a thickness of approximately 90 nm. Including a polymer additive in the precursor solution ensures a homogeneous film formation, so no anti-solvent is necessary. Films were annealed for 15 min (at different temperatures between 90-170 °C, Section 7.2) to finalise the crystallisation process.

## 5.2 Surface treatment methods

Various surface treatment methods were employed throughout this thesis: In Section 7.1, two surface passivation strategies for triple cation perovskites are explored based on the following: i) a surface treatment with trioctylphosphine oxide (TOPO), and ii) the addition of a poly(methyl methacrylate) (PMMA) cladding layer. Moreover, samples used as stamps in the NIL process underwent an anti-adhesion surface treatment to render them hydrophobic. The fabrication details of these three processes are explained in detail in the following.

### **Trioctylphosphine oxide (TOPO)**

TOPO is an organophosphorus compound (Figure 5.1a) commonly employed as a passivation agent for hybrid perovskites (Section 7.1). The surface treatment used in this work is based on the proposed approach by deQuilettes *et al.*<sup>[65]</sup> TOPO (Trioctylphosphine oxide, Acros Organics, 78-50-2) was mixed in CB with a concentration of 0.04 M. 70 µl (for 15 x 15 mm<sup>2</sup> samples) were deposited on the film surface, followed by a waiting step of ca. 10 s and a spinning step at 2000 rpm for 60 s. Subsequently, a washing process was performed by dripping 150 µl of CB continuously on the sample while spinning at 6000 rpm for 60 s. According to deQuilettes *et al.*, this enables surface passivation without surface residuals. However, in these experiments, the surfaces had a slightly purple tinted surface, suggesting a thin TOPO residual remains on the surface.<sup>[65]</sup>

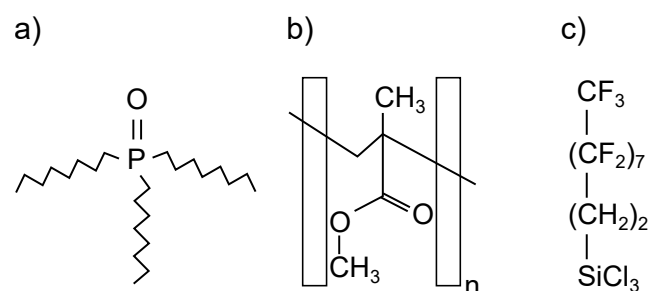


**Figure 5.1:** Molecular structure of chemicals used for surface treatments. a) TOPO, a defect passivation treatment, b) PMMA, a typical cladding and encapsulation layer, and c) FDTS, a silane employed for rendering surfaces hydrophobic.

### Poly(methyl methacrylate) (PMMA)

For the PMMA cladding layer, PMMA (average molecular weight  $M_w \sim 15,000$ , 9011-14-7, Sigma Aldrich) was dissolved in anisole (anhydrous,  $\geq 99\%$ , 100-66-3, Sigma Aldrich) with a concentration of 150 mg/ml. The PMMA molecular structure is schematically represented in Figure 5.1b. The spin-coating consists of a two-step process: The first step is at 500 rpm for 10 s, and the second is at 4000 rpm for 30 s. Finally, the films were annealed at  $100^\circ\text{C}$  for 1.5 min to remove any solvent remnant. This process resulted in PMMA films with a thickness of approximately 480 nm.

### Perfluorodecyltrichlorosilane (FDTS)

A silanisation treatment with perfluorodecyltrichlorosilane (FDTS) (78560-45-9, VWR International GmbH) was performed to render surfaces hydrophobic, in particular, for the NIL process (Section 5.3), to prevent the adhesion of stamp and sample. The molecular structure of this silane is illustrated in Figure 5.1c, and the corresponding surface treatment was conducted via a multi-step process: First, sample surfaces were activated with an oxygen plasma for 5 min at 100 W (similar to the plasma step before spin-coating described previously). Next, inside a nitrogen-filled glovebox, these samples were placed inside a closed Petri dish with approximately 10-20  $\mu\text{l}$  FDTS in the form of droplets spread on the Petri dish next to the samples. The closed Petri dish was heated up to  $150^\circ\text{C}$  for 60 min. Finally, the samples were washed with toluene (99%, Alfa Aesar, 108-88-3) to remove residuals from the surface.

## 5.3 Thermal nanoimprint lithography

Thermal nanoimprint lithography (NIL) involves transferring a nano-pattern into a thin film through direct mechanical deformation while applying high pressures and temperatures, resulting in plastic deformation of the thin film. The setup used for this work consists of a self-built hot embossing machine in cooperation with Jenoptik Mikrotechnik that can reach high temperatures ( $T \leq 190^\circ\text{C}$ ) and forces ( $F \leq 290\text{ kN}$ ).<sup>[66]</sup> A photograph of the NIL machine is presented in Figure 5.2. In the scope of this thesis, NIL was utilised

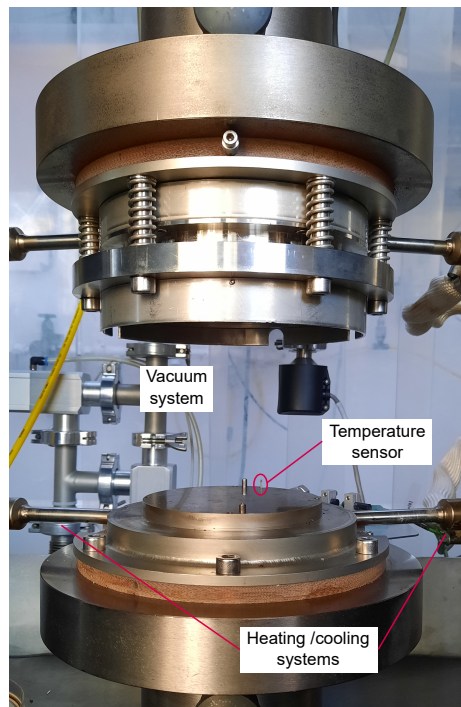


**Figure 5.2:** Photograph of the hot embossing machine employed for thermal nanoimprint lithography. The two large plates are connected on the sides with an oil heating system and a water cooling unit. The chamber enclosing the two small tool plates is connected to a vacuum system (on the left) and can either be pumped down to  $10^{-3}$  mbar or flushed with nitrogen. This allows for imprinting under a vacuum or with an inert nitrogen atmosphere. The temperature sensor can be recognised as a needle on the bottom tool plate in direct contact with the bottom tool plate.

for three main processes: i) to transfer nano-structures from a mould stamp to a perovskite thin film as mentioned above, ii) to smoothen the perovskite surface by performing a hot pressing step with a flat silicon stamp (roughness of  $< 1$  nm)<sup>[67]</sup>, and iii) to laminate two single samples into one. The latter is used to build a fully micro-cavity with two separate mirrors (Section 8.2.2).

For an imprinting procedure, the stamp is manually placed on top of the perovskite sample, and both are placed on the bottom tool plate of the machine (Figure 5.2). The stamp is pre-treated with an anti-adhesion layer as discussed in Section 5.2 and has the smallest area of the stack *A*, which is used to calculate the imprint pressure based on the measured force. An example of a complete NIL process diagram is illustrated in Figure 5.3, and the individual steps are detailed in the following:

1. At the start of the process, the upper part of the machine goes down until the top tool plate touches the stamp;
2. The chamber enclosing the samples is evacuated and filled with nitrogen three times to ensure a clean, inert atmosphere, preventing perovskite degradation;
3. Bottom and top plates are heated to reach the standard temperature of  $95^\circ$  (unless stated otherwise), which takes approximately 7 min;

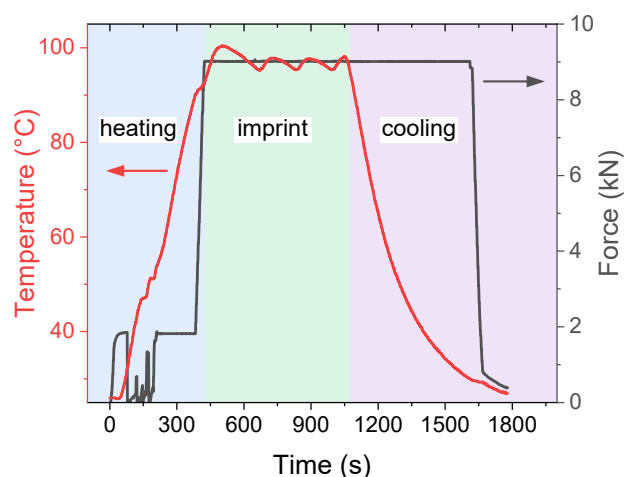


**Figure 5.3:** Diagram of a standard NIL process. The evolution of temperature (red line, left y-axis) and force (black line, right y-axis) during the entire procedure are depicted as a function of time, and the three main parts are marked with different colours: heating (blue), imprint (green), and cooling (pink). The imprint force of 9 kN corresponds to a pressure of 900 bar given the stamp area of 10 mm<sup>2</sup>.

4. Meanwhile, an initial contact pressure of 200 bar is set between the top plate and sample while the plates heat up;
5. Once the set temperature is reached, the target pressure of 600 bar (unless stated otherwise) is applied. A force sensor constantly monitors the applied force, and the pressure  $P$  is calculated by  $P = F/A$ .
6. Next, a timer, typically set between 5 - 15 min, controls the duration for which the pressure is applied;
7. After the set time, the system cools down to 30 °C;
8. Once that temperature is reached, the plates slowly open, releasing the pressure and ending the imprint process.

All NIL procedures performed in this work follow these steps, and only the parameters pressure, temperature or time are adjusted for specific applications. For the transfer of nanostructures, these parameters were optimised in the master thesis of Christian Rainer.<sup>[68]</sup> The terms (thermal) NIL, (nano-)imprint, and hot pressing are used interchangeably throughout this thesis to refer to this process.

## 5.4 Optical characterization techniques

Three main optical characterisation methods were used for studying the perovskite films: i) photoluminescence spectroscopy, encompassing steady-state and transient measurements, which are described in Sections 5.4.1 and 5.4.4, respectively; ii) transient reflection, detailed in Section 5.4.5; and iii) ultraviolet–visible (UV-VIS) spectroscopy, presented in Section 5.4.3. Steady-state PL is employed to analyse perovskite emission spectra, including PL, ASE, and lasing. Transient methods are utilised to gain insights into the material carrier dynamics, and UV-VIS spectroscopy mainly provides information about the absorption spectrum of the perovskite films.

### 5.4.1 Steady-state photoluminescence spectroscopy

The measurements of steady-state PL were performed with the intensified charge-coupled device (ICCD) setup (Figure 5.4), which is used for the studies in Chapters 7 and 8. In this setup, samples are placed in a vacuum chamber mounted on a 3-axis stage. The chamber possesses a transparent window for optical characterisation, and its atmosphere can be either vacuum, gaseous nitrogen, or air. After mounting the sample, the chamber can be pumped down to a vacuum pressure of  $\approx 10^{-5}$  mbar, filled with gaseous nitrogen, or left open (in air) to enable different measurement conditions. Due to the perovskites' sensitivity to oxygen and moisture, a vacuum or an inert atmosphere is better for long-term measurements to avoid performance changes due to degradation. Measurements were typically performed in a nitrogen atmosphere unless specified otherwise. Therefore, the vacuum chamber was first evacuated to a high vacuum (around  $10^{-5}$  mbar) and consequently flooded with gaseous nitrogen. The 3-axis stage, where the vacuum chamber is attached, allows the change of the sample position in the x-y-plane (to change the coordinate on the sample where the laser hits) and in the z-direction (along the excitation laser axis) to change the spot size of the laser on the sample. The laser spot size as a function of the z-position was calibrated before the measurements using the knife-edge method, which consists of scanning a razor blade across the laser spot and measuring the transmitted power.<sup>[69]</sup>

In the ICCD setup (Figure 5.4), perovskite samples are optically excited perpendicularly to their surface, with a frequency-doubled Nd:YLF laser (InnoLas Laser GmbH) with a pulse width of  $\Delta t_{pulse} \approx 0.8$  ns, repetition rate of 1 kHz and wavelength of 532 nm. The laser energy at the sample position is constantly monitored with a calibrated photodiode (PD) installed in the setup. A glass slide placed in the laser path at approximately  $20^\circ$  reflects around 4 % of the light into the PD, and the laser energy can be adjusted by moving a variable neutral density (ND) filter placed before the glass slide. The sample's emission is collected perpendicularly through a dichroic mirror that reflects the excitation wavelength (green lines) and transmits the emitted wavelength range (red lines). Due to the coaxial excitation and collection, one single lens ( $f = 10$  mm) is used to focus and collimate the incoming and outgoing beams. The perovskite emission is coupled to a spectrograph (Acton SpectraPro SP-2300, Princeton Instruments), which includes three diffraction gratings with different spectral resolutions (150, 600, and 1800 lines/mm). A linear polariser fixed on a

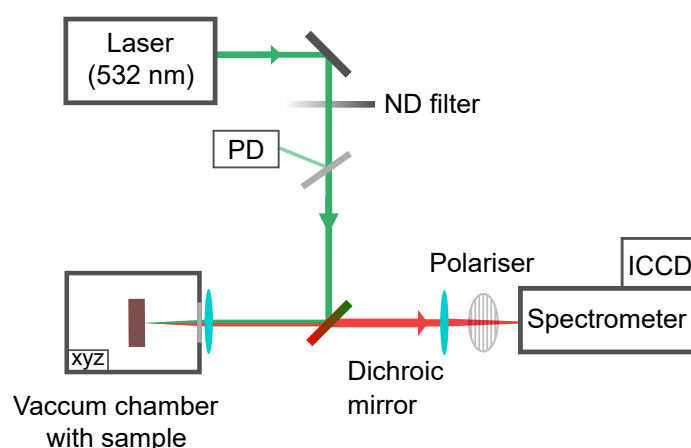


**Figure 5.4:** Schematic of the ICCD setup for spectroscopic measurements with an excitation laser (532 nm, 0.8 ps, 1kHz); a neutral density (ND) filter to regulate the pump energy; a glass plate directing a reference beam to a calibrated photodiode (PD) to constantly monitor the laser energy at the sample position; a dichroic mirror to divide excitation and emission and allow for surface excitation and detection; a vacuum chamber on a XYZ stage; lenses to focus and collimate the excitation and emission; a polariser (only mounted in the setup for performing polarisation measurements); and a spectrometer with an ICCD camera.

motorised rotation mount (K10CR1, Thorlabs) was placed at the spectrograph entrance slit for polarisation measurements. The slit width of the spectrometer entrance can be adjusted with a micrometre screw, up to a maximum width of 3 mm (maximum intensity, minimum spectral resolution). Example spectra acquired with different spectrometer gratings and polarisation measurements are presented in Chapter 8, Figures 8.8 - 8.11. The spectrograph is coupled to a gated ICCD (PI-MAX4:1024f-HR, Teledyne Princeton Instruments), triggered by the excitation laser. The ICCD possesses a photocathode followed by a multichannel plate and a phosphor screen. The incoming photons are converted to electrons at the photocathode via the photoelectric effect; these electrons are multiplied at the multichannel plate to amplify the received signal, and the phosphor screen converts these electrons into photons, which are finally collected by a charge-coupled device (CCD). The detection gate width was typically set to 3 ns for steady-state measurements, so the detected emission consisted of a cumulative signal from two consecutive excitation pulses, as a rule. The gating of the ICCD is controlled by the voltage between the photocathode and multichannel plate so that only photons arriving within the time interval of interest are amplified and detected.

#### 5.4.2 Photoluminescence quantum yield

A material's photoluminescence quantum yield (PLQY) is defined by the ratio of the number of emitted photons to the number of absorbed photons. It is a relevant parameter for characterising optical materials employed in light-emitting applications since it quantifies the ability of a material to convert absorbed light into emitted light. PLQY measurements are performed inside an integrating sphere (or Ulbricht sphere) – a hollow cavity covered

with a uniformly scattering material – with entrance and exit ports for excitation and detection.

The setup used for the PLQY measurements, conducted in Section 7.1, was a LuQY Pro (LP20-32, QYB Quantum Yield Berlin GmbH), with a pump laser with a wavelength of 532 nm, a laser spot size of 0.1 cm<sup>2</sup>, and an intensity of 1 Sun. In this system, the samples are placed inside an integrating sphere and excited from the top surface by the pump laser. A spectrometer is connected to an opening in the sphere to measure the emitted PL. The software integrates the acquired spectrum to calculate the emitted photons (luminescence flux density) and divides it by the absorbed photons (absorbed excitation flux density) to calculate the PLQY. The absorbed photons are calculated from the difference between incident photons (excitation photon flux density) and reflected photons (at the excitation wavelength 532 nm) inside the sphere.

### 5.4.3 Ultraviolet-visible spectroscopy

UV-VIS spectroscopy is a measurement technique to characterise sample transmittance and reflectance in the spectral regions corresponding to ultraviolet (UV) and visible wavelengths. The measurement principle consists of having two light beams: one impinging on the sample and a second beam serving as a reference arm. Hence, their ratio gives the total transmittance or reflectance, depending on which light is measured (transmitted or reflected). The setup employed in this thesis was a PerkinElmer LAMBDA 1050 UV-VIS/near-infrared (NIR) spectrophotometer equipped with a 150 mm integrating sphere. The excitation source is a tungsten lamp followed by a monochromator enabling wavelength selection, typically set between  $\approx 500 - 900$  nm for the standard triple-cation perovskite. At each wavelength, the intensity of the reference and sample beam are acquired, and the total transmittance (reflectance) is calculated. For transmission measurements, the sample is placed at the entrance of the integrating sphere. For reflection measurements, the sample is positioned on an area of a black wall inside the sphere so that only the reflected light is detected. In the context of this work, this setup was employed to measure the absorptance of perovskite thin films to determine either the shape of the spectrum (e.g., exciton peaks, bandgap) or the fraction of pump light absorbed in the film upon optical excitation. Absorptance ( $A$ ) measurements are performed only indirectly, as  $A$  is calculated from the transmittance ( $T$ ) and reflectance ( $R$ ) spectra, according to  $A = 1 - R - T$ . It is important to note that perovskite reflectance is considerable and must be considered in the previous calculation.

### 5.4.4 Time-resolved photoluminescence spectroscopy

TRPL measurements during this work were acquired with two different setups: the ICCD setup, and a time-correlated single photon counting (TCSPC) device. The **ICCD setup** is detailed in the Section 5.4.1 for steady-state measurements, and it can be adapted to enable time-resolved analysis by changing the gating settings of the ICCD: The smallest gate width achievable with this system is around 3 ns, enough to resolve processes with

lifetimes of tenths to hundreds of ns. Thus, for TRPL measurements, the gate width is set to 3 ns (unless specified otherwise), and the camera trigger is synchronised with the laser pulse so the initial time  $t = 0$  corresponds to the arrival of the laser pulse. Each acquisition records an emission spectrum at a specific gate delay in 3 ns steps. The LabVIEW software then integrates each spectrum and plots this value against the corresponding gate delay, resulting in a TRPL curve (Section 4.3.2).

The measurements performed with the **TCSPC setup** make use of an FLS920 fluorescence spectrometer (Edinburgh Instruments Ltd 2006). An light-emitting diode (LED) (LDH-P-635, PicoQuant) excites the sample at an angle of  $45^\circ$  with a wavelength of 634-637 nm, a minimum pulse width of  $\Delta t < 83$  ps and a maximum pulse energy of 79 pJ. The exit spectrometer collects the emission under the same angle and measures its intensity at the maximum wavelength of the PL spectrum.<sup>1</sup> A TCC900 card contains the timing electronics for TCSPC experiments, which is connected to the excitation LED and the detector: The LED excitation pulse *starts* the ‘timer’ of the experiment and the detected signal at the PMT R928P detector *stops* the clock. The time difference between start and stop is added to a histogram depicting counts versus photon arrival time, which is the final TRPL curve. Typical dead times of the detection electronics are around 100 ns, so only one photon per pulse can be detected for short delays. Due to the power limitation of the available sources with the TCSPC device, this measurement setup was only employed to measure TRPL at extremely low intensity, i.e., at carrier densities below typical trap densities in perovskites (Section 7.1).

### 5.4.5 Transient reflection spectroscopy

The technique of transient reflection (TR) spectroscopy is commonly employed to investigate excited-state dynamics in a material. This is achieved by monitoring the material’s photophysical changes following the absorption of an intense light pulse. In this context, a probe pulse is utilised to assess variations in the reflection signal at various time intervals following the initial pump pulse, enabling the acquisition of a time-dependent signal. Time windows for TR measurements range from tens of femtoseconds to a few nanoseconds.<sup>[70]</sup> The setup is depicted in Figure 5.5 and explained in the following, along with the underlying working principle of this method.

An initial pulse signal (red line) is generated by a femtosecond source (Pharos, from LightConversion) with a wavelength of 1026 nm, a pulse width of approximately 260 fs, and a repetition rate of 2 kHz (Figure 5.5). A 3/1 beam splitter (BS) divides this beam into two where the smaller portion is focused onto a sapphire crystal to generate a white light continuum probe beam (yellow line), and the larger part is directed into an optical parametric amplifier (OPA) to create excitation pulses at 532 nm. Inside the OPA (Orpheus, from LightConversion), first, a part of the incoming beam is directed through a second harmonic generation (SHG) crystal to generate a pump signal  $\lambda_p = 513$  nm. The rest goes through a sapphire crystal that can provide a signal beam with the desired

---

<sup>1</sup> This wavelength is determined before the time-resolved experiment by scanning the emission intensity over the wavelength with the exit spectrometer.

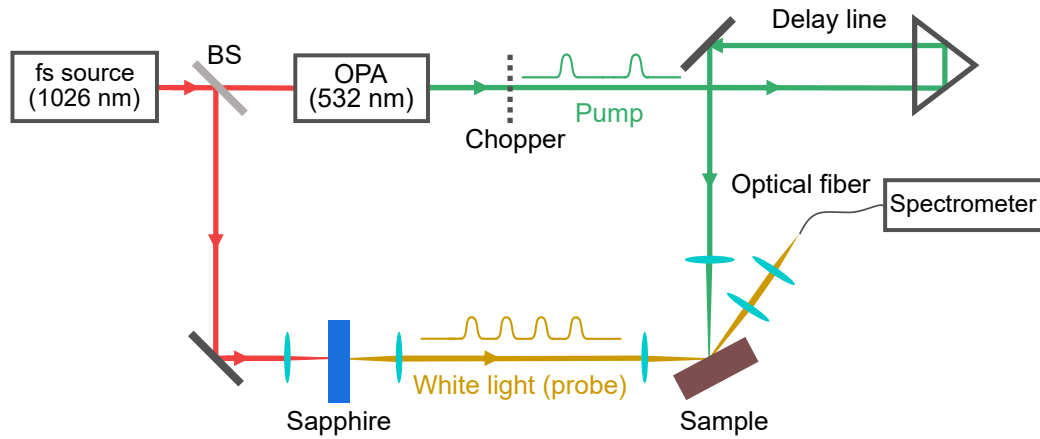


**Figure 5.5:** Schematic of the TR setup with a beam splitter (BS) and an optical parametric amplifier (OPA). A sapphire crystal generates the white light of the probe pulse and has twice the frequency as the pump pulse to allow for consecutive measurements with pump on and pump off. The optical delay line introduces a time delay between pump and probe pulses in the order of picoseconds. The sample emission is coupled to an optical fibre connected to a spectrometer.

wavelength  $\lambda_s = 532$  nm. The pump and signal are then directed to the optical parametric amplifier (OPA) crystal to generate an amplified signal pulse at 532 nm at the output (green line). This pulse passes through a chopper, which reduces its repetition rate to 1 kHz, and subsequently through a delay line determining the time delay  $\tau$  between pulse and probe for the TR measurement. Both pump and probe pulses are spatially aligned to overlap on the sample, and the probe beam spot size is slightly smaller than the pump to ensure an accurate measurement. In the framework of this thesis, TR was used for the study in Chapter 6 where only the change in reflection signal was measured due to the opaque silicon substrates. The change in reflection is calculated by

$$\Delta R/R(\lambda, t) = \frac{R_{\text{on}}(\lambda, t) - R_{\text{off}}(\lambda)}{R_{\text{off}}(\lambda)} \quad (5.1)$$

where  $R_{\text{on}}$  and  $R_{\text{off}}$  represent the reflection signal of the excited (pump *on*) and unexcited (pump *off*) sample. The software employed for data analysis is detailed elsewhere.<sup>[71]</sup>

In a TR measurement, the pump pulse generates free electron-hole pairs in the material with concentration  $N$ . This changes the medium's dielectric constant – a measure of its polarisability – and therefore its (complex) refractive index  $\tilde{n} = n + i\alpha$ , so that  $\Delta N \propto \Delta \tilde{n}$ . The main processes changing a material absorption (typically considered in the more commonly employed TA spectroscopy technique) are i) ground state bleach, ii) stimulated emission, and iii) excited state absorption. The ground-state bleach usually appears as a negative change in absorption. The negative signal ( $\Delta A/A < 0$ ) is a result of the ground state photo-bleaching by the initial pump pulse, so the probe pulse experiences a lower absorption than when the pump is off (Chapter 6, Figure 6.3). The TA signal can be calculated analogously to the TR signal by changing  $R$  by  $A$  in Equation 5.1. Next, stimulated emission also gives rise to a negative change in absorbance, equivalent to a higher transmission. The probe beam can trigger stimulated emission at wavelengths

around the PL range (slightly red-shifted with respect to the ground state bleach) after the pump beam generates enough excited-state density. Finally, the last process – excited state absorption – describes the absorption of the probe beam by the excited states in the material by the initial pump beam. It leads to a positive change in absorption due to the increased absorption of the probe beam. For wavelengths below the bandgap, far from electronic resonances, changes in absorption are negligible ( $\Delta\alpha \approx 0$ ), and changes in the complex refractive index are given primarily by changes in the real part of the refractive index. Thus, changes in reflection due to changes in  $n$  are proportional to changes in carrier density  $N$ , i.e.,  $\Delta\tilde{n} \approx \Delta n \propto \Delta N$ .<sup>[40, 72, 73]</sup> Hence, for the standard triple-cation perovskite, the NIR transient TR signal can be used to study the carrier dynamics since  $\Delta R/R \propto \Delta n$ . This effect is exploited for the measurements in Chapter 6 and exemplary TR spectra with a strong NIR signal are illustrated in Chapter 6, Figure 6.3.

## 5.5 Morphological characterization techniques

The following methods were employed to characterise the morphology of perovskites, both pristine and imprinted samples: atomic force microscope (AFM), detailed in Section 5.5.1, scanning electron microscope (SEM), explained in Section 5.5.2, and profilometry, presented in Section 5.5.3.

### 5.5.1 Atomic force microscopy

AFM is a scanning probe microscopy method employed in the context of this work to investigate samples' topography. The measurement principle is based on the interaction forces between a sharp tip on a cantilever and the sample surface. Scanning the tip over the sample in the x-y-plane and recording the height at each point enables acquiring a 3D topography image of the scanned area. The AFM system used in this thesis consists of the NanoWizard<sup>®</sup> 3 AFM (JPK Instruments AG, Berlin). Figure 5.6 illustrates the AFM setup with its main components: a cantilever (with a tip), a laser and a 4-quadrant photo-detector. The cantilever is attached to a silicon chip and is scanned over the sample with piezoelectric elements. All measurements in this work employ the intermittent contact mode: The cantilever oscillates at a constant frequency near its resonance, barely in contact with the sample, touching it briefly at the valley of each oscillation. During scanning, the different surface characteristics interact with the tip and cause an attenuation of the oscillation amplitude. The AFM system continuously monitors the oscillation amplitude by the laser reflection off the cantilever on the photo-detector. This amplitude change is directly related to the sample topography, enabling the acquisition of a topographic image. AFM characterisation is employed in Chapters 7 and 8 for studying surface roughness, topology and morphology of either flat or structured perovskite films.

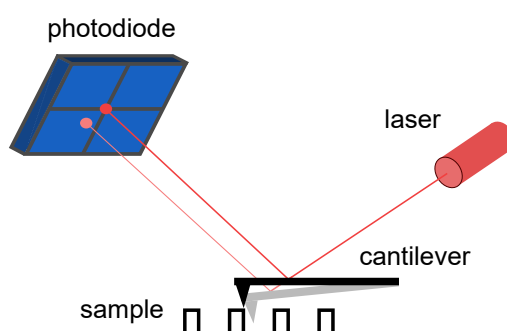


**Figure 5.6:** Illustration of the AFM working principle with the main components: 4-quadrant photodiode, laser, and cantilever with tip, at two different sample positions (or cantilever deflections).

### 5.5.2 Scanning electron microscopy

SEM is another scanning imaging method employed in this thesis to study perovskite surfaces. It involves scanning a sample's surface with a beam of electrons, enabling high-resolution imaging in the nanometer range. Different signals are generated through the interaction of primary electrons (from the scanning beam) and the sample, such as secondary electrons. These signals are detected and analysed to provide information about the sample surface morphology and composition.<sup>[60]</sup> Herein, the sample must be electrically conductive or coated with an appropriate conductive layer. This technique is especially relevant for nano-structures utilised, e.g., in laser resonators (Chapter 8). SEM acquisitions in the scope of this thesis were performed in collaboration with Emil R. Mamleyev with a Zeiss Supra60 VP microscope with selected accelerated voltage of 3 kV unless stated otherwise. Examples of SEM images are presented in Chapter 8.

### 5.5.3 Profilometry

This work uses profilometry to measure the thickness of perovskite thin films. The samples are prepared by making a few scratches with a needle tip on the film to remove the complete layer without scratching the substrate below (typically glass). The profilometer employed here was a DektakXT<sup>®</sup> profilometer (Bruker), which performs a one-line scan with a diamond stylus in contact with the sample and records the stylus position. By measuring the height distance between the top surface and the bottom of the scratch line from the sample profile, it is possible to calculate the total film thickness. Figure 5.7 presents the thickness of different perovskite films as a function of precursor solution concentration measured by this technique. The inset illustrates an exemplary curve acquired with the profilometer. These thickness measurements of perovskite films enable the precise calculation of charge carrier density in the film, relevant for carrier dynamics and laser analysis (Chapters 7 and 8). The thickness of different surface layers can also be calculated with this method, such as the PMMA cladding investigated in Section 7.1, by combining multiple measurements.

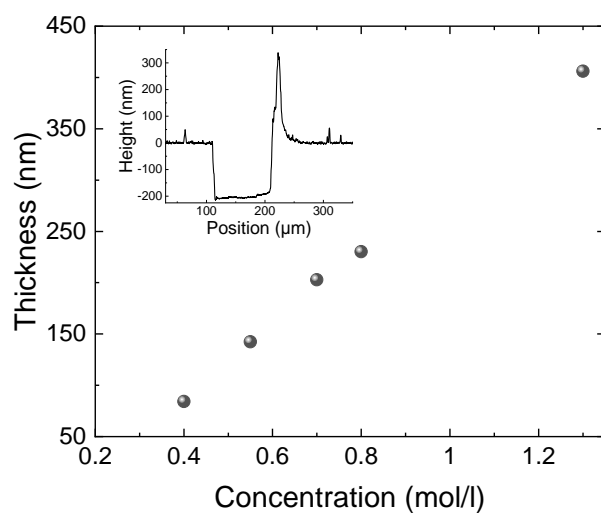


**Figure 5.7:** Profilometer measurements of perovskite film thickness as a function of precursor solution concentration, between 0.4 M and 1.3 M. Inset shows an exemplary profile measurement of a sample with a concentration of 0.7 M and a thickness of  $\approx 200$  nm. The peak at the edge of the scratch profile likely originates from material accumulation on the edge of the scratch line after scratching.

# **Part III**

## **Results and Discussion**



# 6 Temperature-dependent Carrier Dynamics and Amplified Spontaneous Emission

This chapter is dedicated to the spectroscopic investigation of carrier dynamics in triple-cation perovskites. The objective is to understand their photophysics and gain valuable insights for optimising the material for light amplification applications. In particular, this chapter presents a study about the radiative and non-radiative recombination channels and emission characteristics of triple-cation perovskites. This study is conducted from cryogenic to room temperature to unravel the underlying causes of perovskite's temperature-dependent ASE threshold. Section 6.1 delves into the temperature-dependent carrier dynamics measured on high-index substrates. This approach mitigates the fast carrier depletion caused by ASE and enables the investigation of radiative and non-radiative processes under intense excitation conditions. Following this analysis, Section 6.2 explores the factors contributing to the temperature-dependent ASE threshold. This investigation is based on the temperature-dependent recombination rates and spectral broadening.

## Acknowledgements and Contributions

This chapter elaborates on the results discussed in the publication

- Allegro, I.; Li, Y.; Richards, B. S.; Paetzold, U. W.; Lemmer, U.; Howard, I. A. Bimolecular and Auger Recombination in Phase-Stable Perovskite Thin Films from Cryogenic to Room Temperature and Their Effect on the Amplified Spontaneous Emission Threshold. *J. Phys. Chem. Lett.* **2021**, *12* (9), 2293–2298 [74]

The author and I. A. Howard conceptualised the temperature-dependent study by transient reflection; Y. Li arranged the experimental setup and performed the data acquisition. U. Lemmer supervised the project. All authors contributed to the discussion of the results.

## 6.1 Temperature-dependent bimolecular and Auger recombination rates

This study investigates the temperature-dependent recombination rates in triple-cation films to understand the limits of CW lasing and ASE in this material. Section 6.1.1 introduces the state of the art on perovskite CW lasing and the relevance of this study. Section 6.1.2 then discusses the impact of high-index substrates on suppressing ASE. Finally, Section 6.1.3 presents the carrier dynamics study by transient reflection, which yields the recombination rate coefficients.

### 6.1.1 Introduction

Realising CW lasing in solution-processed semiconductors is a significant milestone towards the advancement of electrically-driven perovskite lasers.<sup>[12, 74]</sup> Several reports have demonstrated CW lasing in perovskite materials, including polariton lasing in perovskite nanowires<sup>[75]</sup> and nanoplatelets<sup>[76]</sup>, as well as exciton lasing in quasi-2D perovskites with a DFB structure.<sup>[5]</sup> However, achieving CW lasing based on bimolecular recombination of free carriers in 3D perovskite thin films is currently limited to cryogenic temperatures.<sup>[19, 77]</sup> The first demonstration of this phenomenon was based on a mixed-phase structure of a MAPI perovskite thin film. The sample was cooled to 100 K to induce its orthorhombic phase, and the CW pump locally heated the film, forming small tetragonal inclusions due to the increase in temperature (Section 4.1). These regions acted as energy wells, enhancing carrier recombination.<sup>[19]</sup> In another report, Brenner *et al.* demonstrated CW ASE from 80 K to 120 K in phase-stable triple-cation perovskite films with the standard triple-cation composition used in this work.<sup>[28]</sup> Here, the CW ASE threshold increased with temperature, and above 120 K, no ASE was observed. Under pulsed excitation, these samples also exhibited a temperature-dependent ASE threshold, similar to the behaviour reported for MAPI by Jia *et al.*<sup>[78]</sup> More recently, Moon *et al.* achieved quasi-CW lasing at 260 K from a MAPbBr<sub>3</sub> film patterned with a 2D DFB resonator structure.<sup>[77]</sup> However, sustaining CW ASE in 3D perovskite films at room temperature remains challenging.

In 3D perovskites, the rates  $k_{\text{bi}}$  and  $k_{\text{Auger}}$  are of particular interest since they describe the dominant recombination mechanisms at high carrier densities, a condition necessary for lasing. The carrier density necessary to reach the lasing threshold in 3D films at room temperature is typically in the order of  $n \approx 10^{18} \text{ cm}^{-3}$ , in line with the estimations by the Bernard-Duraffourg condition (Section 3.1).<sup>[54, 78–80]</sup> To accurately determine these rates experimentally, measuring them within the fluence regime where they dominate is essential. This corresponds to initial carrier densities ranging between  $10^{17}$  and  $10^{19} \text{ cm}^{-3}$ .<sup>[51, 54]</sup> However, the fast ASE dynamics at carrier densities above threshold density ( $n_{\text{th}} \approx 10^{18}$ ) dominates the recombination processes, posing a challenge in resolving the second and third-order carrier processes under high excitation. Hence, suppressing ASE is necessary for accurately determining  $k_{\text{bi}}$  and  $k_{\text{Auger}}$ . In this chapter, a new layer stack is proposed with a high refractive index silicon (Si) substrate to suppress ASE and allow for a carrier dynamics analysis at appropriate fluences. A similar approach of using high-index

substrates to suppress ASE dynamics was previously reported for studying high-order population dynamics in polymer films.<sup>[81]</sup> The study presented here constitutes the first analysis of perovskite carrier dynamics at high fluences while effectively suppressing ASE effects. The analysis is primarily based on TR spectroscopy and yields the recombination rate coefficients as a function of temperature.

### 6.1.2 Amplified spontaneous emission suppression

The ASE dynamics, occurring on the ps timescale, quickly depletes the excited state population through stimulated emission, hindering the measurement of the actual bimolecular and Auger processes. Therefore, to suppress ASE and study the intrinsic material dynamics, a high refractive index Si substrate was utilised to eliminate the waveguiding effect that leads to ASE in the perovskite film ( $n_{\text{Si}} \approx 3.7$  at  $\lambda_{\text{ASE}} = 770$  nm). ASE in perovskite films originates from the waveguiding provided by the high-index perovskite ( $n_{\text{pero}} \approx 2.5$ ) compared to common bottom substrates, such as glass or sapphire ( $n < 2$ ). By employing a high-index substrate ( $n \gg 2.5$ ), light is no longer confined to the perovskite film due to total internal reflection, as the substrate possesses the highest  $n$  (Figure 6.1a). For these experiments, the high-index substrates consist of Si substrates cut from a polished Si wafer with a conductivity of 0.33 S/m. A thin insulating layer of silicon dioxide ( $\text{SiO}_2$ ) of approximately 10 nm was deposited on these substrates using electron-beam evaporation to prevent charge extraction (Figure 6.1b). Reference samples on sapphire substrates ( $n_{\text{sapphire}} \approx 1.76$  at  $\lambda_{\text{ASE}} = 770$  nm) were also fabricated for comparison, and to study the ASE dynamics. All perovskite films in this chapter were flattened by an imprinting step (95 °C, 600 bar, 7 min) with a flat Si substrate to reduce surface roughness and achieve an identical morphology to the films, which exhibited CW ASE.<sup>[28]</sup> A schematic of the two substrates utilised for this study is illustrated in Figure 6.1. The presence of ASE becomes evident in the emission spectra through the emergence of a narrower peak at the long-wavelength side of the spectrum after a specific threshold fluence (Figure 6.1a) and in the input-output characteristics by an increase in slope beyond this threshold (Figure 6.2). Effective suppression of ASE for films deposited on Si substrates is also apparent in both measurements: The emission spectra maintain their shape even at high fluences (Figure 6.1b), and no increase in slope is observed in the light-in-light-out curves (Figure 6.2). For the sapphire substrates, ASE is observed at all temperatures, and an increase in threshold with temperature between 80 - 290 K is also confirmed (Figure 6.2). In contrast, when Si substrates are used, ASE is effectively suppressed for the entire temperature and fluence range (Figure 6.2).

A noticeable difference between the PL spectra originated from the different substrates is a narrower and blue-shifted emission for Si substrates compared to reference films on sapphire. For instance, for the PL spectra measured at 200 K, spectra measured on Si have a central wavelength of  $\lambda_c = 764$  nm and a full width at half maximum (FWHM) of  $\Delta\lambda \approx 28$  nm. In contrast, PL spectra on sapphire (below ASE threshold) exhibit  $\lambda_c = 770$  nm and  $\Delta\lambda \approx 32$  nm (Figure 6.1). The broader and red-shifted spectra of reference films result from re-absorption and photon recycling effects caused by light confinement in the perovskite layer. The slight Stokes shift of perovskites leads to an overlap of the absorption

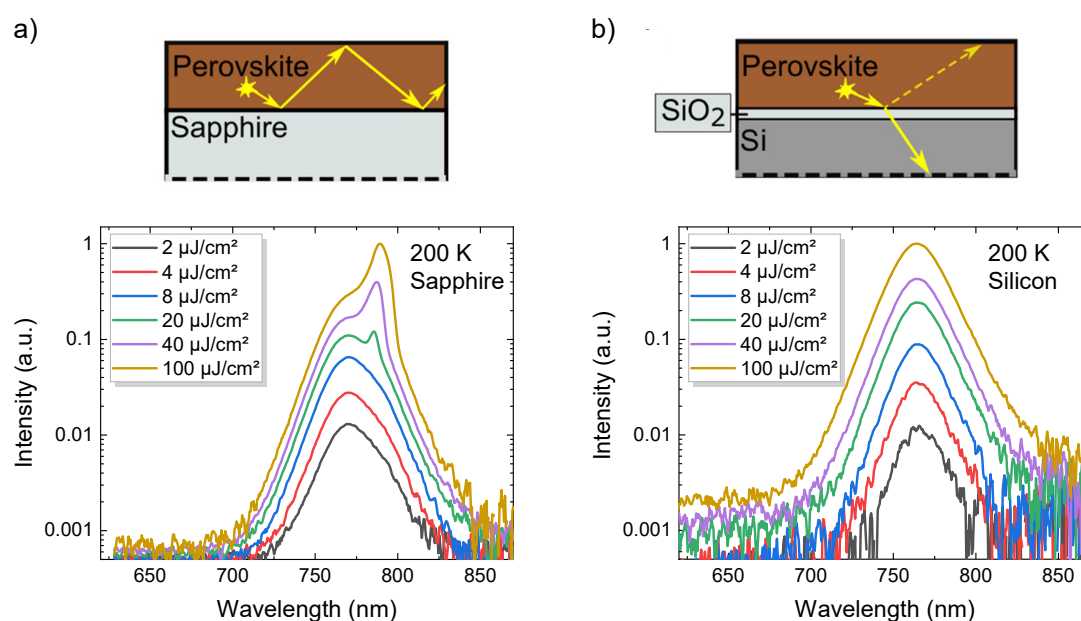


**Figure 6.1:** Substrate configuration with and without waveguiding and respective emission spectra. a) Top: Schematic of perovskite thin film acting as a waveguide on a lower index sapphire substrate. Bottom: Exemplary fluence-dependent emission spectra at 200 K exhibiting an increase in PL signal with excitation density and an emission narrowing for high excitation fluences, characteristic of ASE. The emission spectra are centred around 770 nm. b) Top: Schematic of perovskite thin film on a high-index Si substrate, suppressing waveguiding in the perovskite film. A thin oxide layer prevents charge extraction from the perovskite to the Si substrate. Bottom: Exemplary fluence-dependent emission spectra at 200 K exhibiting an increase in PL with excitation density, similar to a); however, without waveguiding, there is no ASE build-up and no change in spectral shape is observed. In this case, the emission spectra are centred around 764 nm. Adapted with permission from [74]. Copyright 2021 American Chemical Society.

and emission spectra (Chapter 4), resulting in the re-absorption of high-energy photons by the perovskite itself. In the case of a reference film, its strong optical confinement leads to a longer interaction length of the emitted PL with the perovskite layer, resulting in stronger re-absorption the more extended the light propagates within the film.<sup>[42]</sup> Thus, the apparent blueshift observed for Si substrates (Figure 6.1b) is, in fact, closer to the intrinsic perovskite emission spectrum, and the redshift for low-index substrates constitutes a spectral distortion originated from re-absorption effects. Alongside re-absorption, there is photon recycling, which involves the re-emission of re-absorbed photons, leading to delayed emission. This effect contributes to an apparent slower  $k_{bi}$ , masking the intrinsic bimolecular recombination process. Changes in sample geometries, such as film thickness or substrate index, lead to differences in re-absorption and photon recycling and are likely the cause of the wide range of reported values in the literature for  $k_{bi}$ .<sup>[42, 55]</sup> Both effects (re-absorption and photon recycling) are significantly suppressed for measurements on Si substrates due to the lack of optical confinement, making the measured spectra and dynamics on these substrates much closer to the actual intrinsic perovskite properties than typical measurements on low-index substrates.

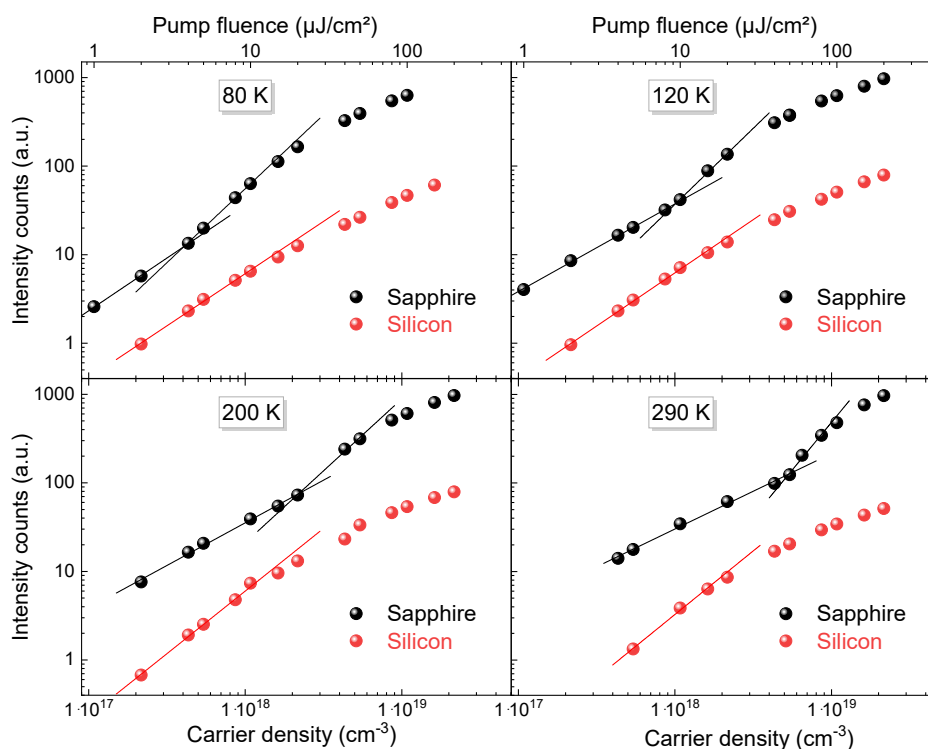


**Figure 6.2:** Temperature-dependent input-output characteristics of perovskite emission on sapphire (black) and Si (red) substrates for 80 K, 120 K, 200 K, and 290 K. The vertical offset is for better visualisation. Spheres correspond to measured data and solid lines to linear fits to the emission. Black data represents measurements on sapphire substrates and exhibits an increase in slope after a certain threshold fluence for all temperatures, indicating the onset of ASE. Red data describes measurements on Si substrates and shows a slope decrease at high excitation fluences due to non-radiative Auger losses dominating at these densities. Adapted with permission from [74]. Copyright 2021 American Chemical Society.

### 6.1.3 Transient reflection and carrier dynamics modelling

The rate coefficients  $k_{bi}$  and  $k_{Auger}$  dominate at high carrier densities and lead to decays with lifetimes in the order of  $\approx 1 - 10$  ns. Hence, the temperature-dependent carrier dynamics study must have a high temporal resolution and fs-TR spectroscopy with a total delay of 4 ns is employed for the analysis. Since the Si samples are not transparent, the measurement is performed in the reflection geometry. Section 5.4.5 elucidates the fundamental working principle of TR spectroscopy and presents the setup configuration utilised for this measurement. Exemplary TR spectra at different time delays are displayed in Figure 6.3: The ground state bleach is visible as a negative peak around the bandgap region at  $\lambda \approx 765$  nm, and there is a strong NIR signal between 800 - 900 nm (blue-shaded region), dominated by refractive index changes in the film and proportional to the carrier density.<sup>[40, 82]</sup> This NIR signal was integrated and plotted as a function of delay time to extract the carrier dynamics curves  $n(t)$  at different fluences and temperatures. Figure 6.4 depicts the respective data as open circles for 80 K, 120 K, 200 K, and 290 K, and fits as solid lines.

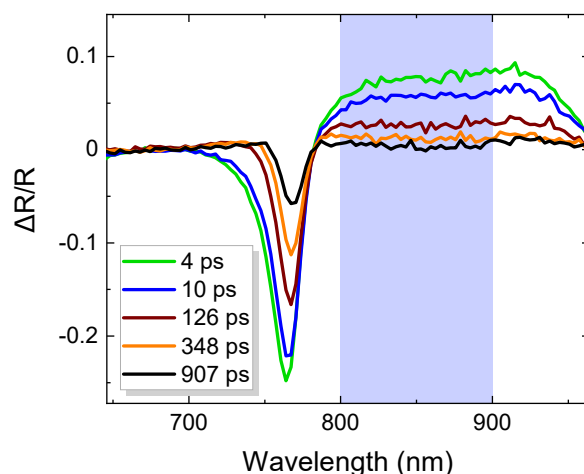


**Figure 6.3:** Transient reflection spectra measured at 80 K for a perovskite film on a Si substrate at different time delays (different colours). Blue shaded area highlights the NIR region used to extract the carrier dynamics. Adapted with permission from [74]. Copyright 2021 American Chemical Society.

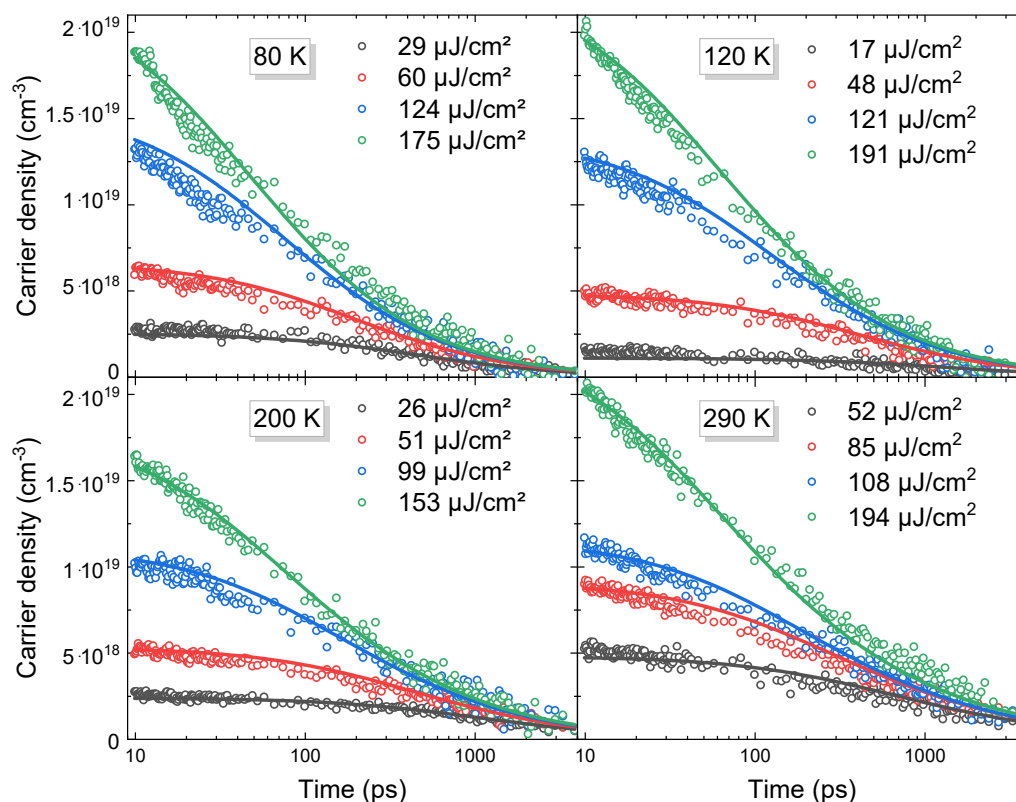


**Figure 6.4:** Fluence-dependent carrier density as a function of time for 80 K, 120 K, 200 K, and 290 K. The depicted time delay ranges from 10 ps to 4 ns. Open circles represent measured data, solid lines correspond to the global fit with the (A)BC model, and the respective colours correspond to the different excitation fluences. Adapted with permission from [74]. Copyright 2021 American Chemical Society.

The fits illustrated in Figure 6.4 correspond to a global fit across all four decay curves at different fluences. This fitting procedure is performed individually for each temperature to extract temperature-specific recombination rate coefficients. The initial carrier density of each curve  $n_0$  was calculated based on the sample's absorption and excitation conditions. The first 10 ps of the dynamics were excluded, and the initial condition was taken at  $t = 10$  ps since dynamics at  $t < 10$  ps are expected to be dominated by charge carrier thermalisation effects.<sup>[35, 83]</sup> The initial TR signal amplitude at  $t = 10$  ps is plotted as a function of excitation fluence to ensure this approximation of the initial condition is valid. Figure 6.5 displays the linear dependence of the TR initial signal as a function of excitation fluence for all temperatures. This result verifies the validity of this approach and that any carrier recombination occurring at shorter times ( $t < 10$  ps) can be neglected. Thus, the measured TR signal can be directly converted to  $n(t)$  by scaling it with the corresponding  $n_0$ . Given the fluence range and timescale of these measurements, the ABC model (Section 4.3.2) was modified by omitting the trapping term  $A \cdot n$  and replacing the nomenclature of the bimolecular ( $B$ ) and Auger ( $C$ ) coefficients by  $k_{\text{bi}}$  and  $k_{\text{Auger}}$ , resulting in the following equation:

$$\frac{dn(t)}{dt} = -k_{\text{bi}} \cdot n(t)^2 - k_{\text{Auger}} \cdot n(t)^3. \quad (6.1)$$

The justification for this simplification lies in the fact that  $k_{\text{bi}}$  and  $k_{\text{Auger}}$  govern the recombination dynamics in the fluence and temporal range considered here, i.e.,  $n > 10^{17} \text{ cm}^{-3}$  and  $t < 4$  ns. It is possible to calculate the carrier density at which each process dominates (monomolecular, bimolecular, or Auger) by equating the respective rates of the ABC model (Equation 4.2). For instance, the carrier density at which monomolecular and bimolecular recombination processes contribute equally to the dynamics can be calculated by  $A \cdot n = k_{\text{bi}} \cdot n^2$ , resulting in  $n_{\text{bi}} = A/k_{\text{bi}}$ . This carrier density marks the transition from trap-dominated to bimolecular-dominated dynamics. Hence, at higher densities ( $n > n_{\text{bi}}$ ), bimolecular recombination governs the dynamics, and the majority of carriers recombine radiatively. In contrast, for  $n < n_{\text{bi}}$ , trap-assisted recombination controls the dynamics and non-radiative losses are substantial. This transition carrier density  $n_{\text{bi}}$  can be approximated by using typical recombination rate values reported in the literature for 3D perovskites.<sup>[23, 54]</sup> The minimum  $n_{\text{bi}}$  can be calculated by taking the fastest  $A$  and the slowest  $k_{\text{bi}}$  reported, which are around  $A \approx 10^7 \text{ s}^{-1}$ , and  $k_{\text{bi}} \approx 10^{-11} \text{ cm}^3 \text{ s}^{-1}$ . These coefficients lead to  $n_{\text{bi}} \approx 10^{18} \text{ cm}^{-3}$ . This calculation is based on values at room temperature; however, since  $k_{\text{bi}}$  decreases with temperature and  $A$  remains approximately constant,  $n_{\text{bi}} \approx 10^{18} \text{ cm}^{-3}$  serves as an upper limit.<sup>[23]</sup> A temperature-dependent  $n_{\text{bi}}$  can be estimated by taking the  $k_{\text{bi}}$  values determined in the next section as a function of temperature. The result is displayed in Figure 6.6 and shows that  $n_{\text{bi}}$  is even lower than the estimate, for all temperatures, with a maximum of  $n_{\text{bi}} \approx 10^{17}$ . The lowest fluence employed in this study to measure the dynamics is higher than the previously calculated  $n_{\text{bi}}$ . Hence, bimolecular or higher-order recombination processes dominate over monomolecular recombination, so the term  $A \cdot n$  can be excluded from the ABC model, and Equation 6.1 can accurately describe the acquired data.

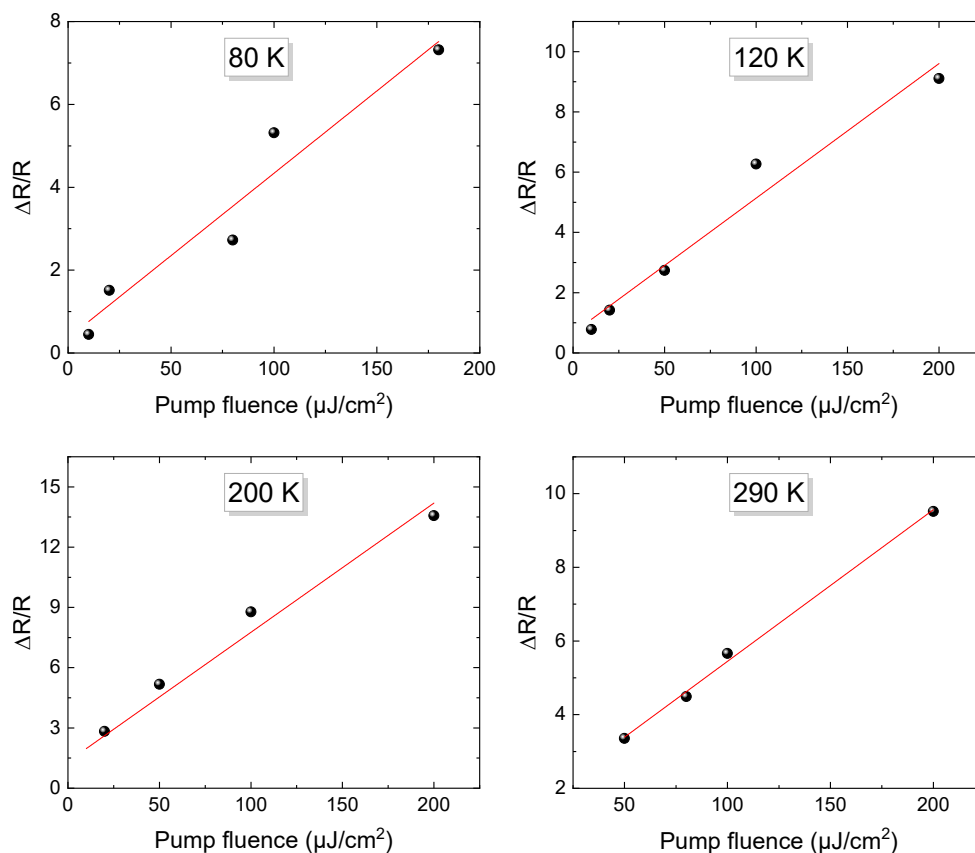


**Figure 6.5:** Initial transient reflection signal (at  $t = 10$  ps) as a function of excitation fluence revealing a linear relation at all temperatures (80 K, 120 K, 200 K, and 290 K). Black spheres represent measured data, and red lines indicate linear fits. Adapted with permission from [74]. Copyright 2021 American Chemical Society.

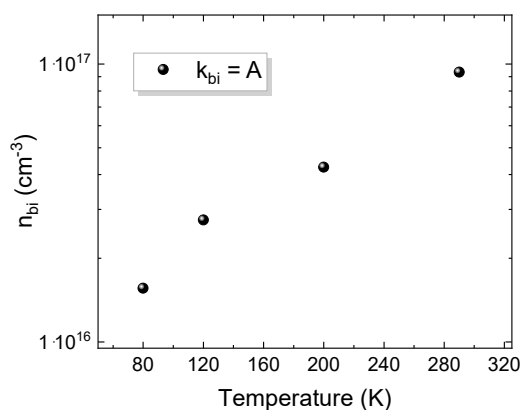


**Figure 6.6:** Carrier density  $n_{\text{bi}}$  at which the bimolecular process starts to dominate the recombination dynamics, as a function of temperature, given by  $n_{\text{bi}} = A/k_{\text{bi}}$ . Adapted with permission from [74]. Copyright 2021 American Chemical Society.

Finally, the light-in-light-out curves were also investigated to exclude a significant contribution from the monomolecular term  $A \cdot n$  (neglected in Equation 6.1) to the perovskite emission. Therefore, the measured data was compared with simulated data using the modified BC model (ABC without the  $A$  term). The simulation consists of solving Equation 6.1 for an initial condition  $n_0$  corresponding to the specific excitation fluence, and integrating the complete PL decay emission ( $k_{bi} \cdot n(t)^2$ ). A contribution from a non-radiative trapping term in the dynamics would result in changes in PL emission as a function of excitation fluence. Similarly to the decrease in PL emission at high excitation densities caused by the non-radiative Auger process, trap-assisted recombination would reduce PL intensity at low fluences. The comparison between simulation and measured data displayed in Figure 6.7 reveals that the modelled and experimental data match and validates the proposed model (Equation 6.1). Further, the simulation was performed for the standard ABC model (Section 4.3.2) and the adapted BC model (Equation 6.1) and yielded analogous results. Thus, the BC model should provide accurate results for determining the  $k_{bi}$  and  $k_{Auger}$  rates. The temperature-dependent rate coefficients determined based on the TR measurements using the BC model are presented and discussed in the following.

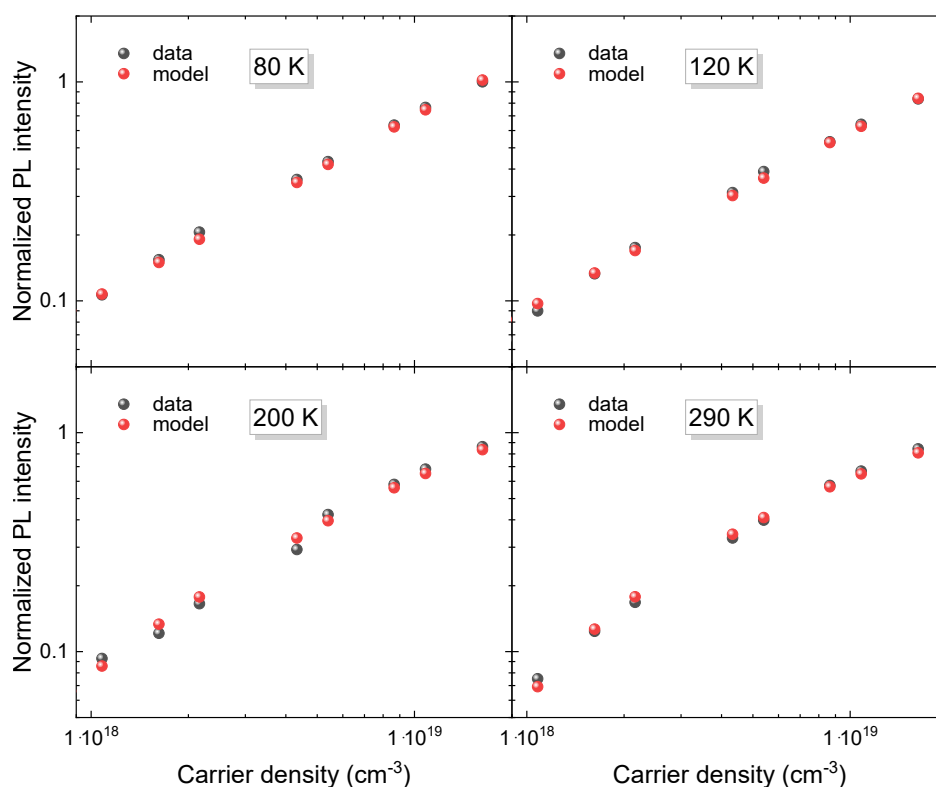


**Figure 6.7:** Comparison of measured (black spheres) and modelled (red spheres) light-in-light-out curves at 80 K, 120 K, 200 K, and 290 K. Modelled data is simulated with the BC model that neglects trap-assisted recombination processes ( $A \cdot n$ ). The overlap of experimental and simulated data confirms the suitability of the BC model to analyse the data acquired under the considered fluence range. Adapted with permission from [74]. Copyright 2021 American Chemical Society.

**Recombination rates  $k_{bi}$  and  $k_{Auger}$** 

The coefficients  $k_{bi}$  and  $k_{Auger}$  extracted from the global fit of the TR dynamics are depicted in Figure 6.8, as a function of temperature. The  $k_{bi}$  rate decreases exponentially with increasing temperature, from  $6.4 \cdot 10^{-10} \text{ cm}^3 \text{ s}^{-1}$  at 80 K down to  $1.1 \cdot 10^{-10} \text{ cm}^3 \text{ s}^{-1}$  at 290 K (black spheres). The Auger rate remains approximately constant throughout the entire temperature range at approximately  $(3 \pm 0.7) \cdot 10^{-29} \text{ cm}^6 \text{ s}^{-1}$  (blue stars). The red error bars on the black spheres in Figure 6.8 correspond to the possible error in  $k_{bi}$ , associated with pump-induced heating. Given the high excitation densities employed in this study, a relevant aspect to examine is the effect of pump-induced heating, especially considering the thermal dependence of these rates. An upper limit of the increase in temperature due to the laser excitation pulse can be calculated by assuming the complete pulse energy is converted into heat. The respective increase in temperature  $\Delta T$  was calculated by taking the film thickness  $d$ , excitation fluence  $F$ , perovskite mass density  $\rho$  and heat capacity  $C$  as follows:

$$\Delta T = \frac{F}{d \cdot \rho \cdot C}. \quad (6.2)$$

Typical ranges of reported values in literature for  $\rho$  and  $C$  are around  $\rho \approx 4 - 4.2 \text{ g/cm}^3$  and  $C \approx 200 - 500 \text{ J/(kg}\cdot\text{K)}$ .<sup>[84–89]</sup> Hence,  $\Delta T_{\text{max}}$  can be calculated with Equation 6.2 by taking the lower limits of  $\rho$  and  $C$ , and the maximum employed fluence in the TR measurements, i.e.,  $F = 200 \text{ }\mu\text{J/cm}^2$ . This yields a maximum temperature increase of  $\Delta T_{\text{max}} = 14 \text{ K}$ . Accumulated heating resulting from consecutive excitation pulses is ruled out based on the similarity of the TR signals in sequential acquisitions. Consequently, it is reasonable to assume that the material reaches the cryostat's equilibrium temperature between pulses within the 1 ms duration.

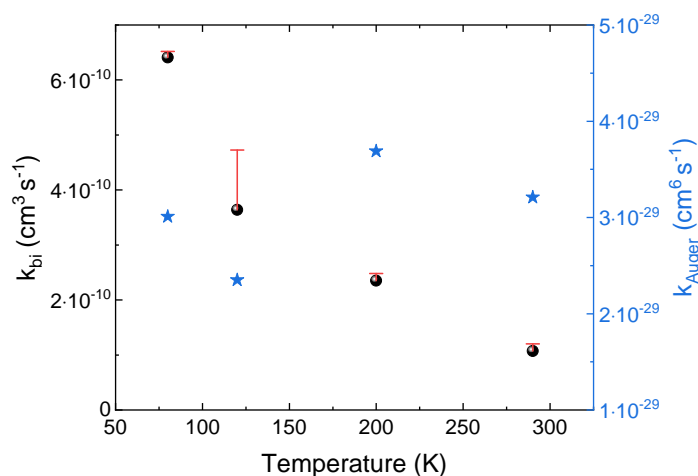


**Figure 6.8:** Recombination coefficients  $k_{bi}$  (black spheres) and  $k_{Auger}$  (blue stars) as a function of temperature. Values extracted from the global fit of the TR dynamics. The red error bars represent the possible error associated with pump-induced heating of the material. Adapted with permission from [74]. Copyright 2021 American Chemical Society.

The process for calculating the error bars associated with potential pump-induced heating in the perovskite is explained below. Initially, the values of  $k_{bi}$  were determined under the assumption of no heating caused by the excitation pulse. These values will be higher than the ones considering a pump-induced temperature increase, given the exponential decrease of  $k_{bi}$  with temperature. Thus, the error bars in Figure 6.8 accounting for heating effects only go upwards. A graphical approach is employed to quantify the magnitude of these error bars at each temperature: The extracted  $k_{bi}$  values from the TR dynamics are depicted in Figure 6.9 as a function of temperature, represented by black spheres. Given the exponential nature of  $k_{bi}(T)$ , the results are presented in a semi-logarithmic plot by taking  $\log(k_{bi})$  as a function of temperature. This enables a simpler and more accurate data fit with a linear function, indicated by the red line. To evaluate the maximum error in  $k_{bi}$  due to potential heating effects, the previously calculated upper limit of  $\Delta T_{\max} = 14$  K is considered. This upper limit results in a shift of +14 K for the original temperatures, namely 80 K, 120 K, 200 K, and 290 K (corresponding to 94 K, 134 K, 214 K, and 304 K). This shift is visually represented by the blue dashed line in Figure 6.9, corresponding to the linear fit (red line) with a +14 K shift. Consequently, the  $k_{bi}$  coefficients under the assumption of a +14 K temperature shift are extracted from this shifted curve. These values correspond to the upper limits of  $k_{bi}$  and determine the magnitude of the error bars for  $k_{bi}$ .

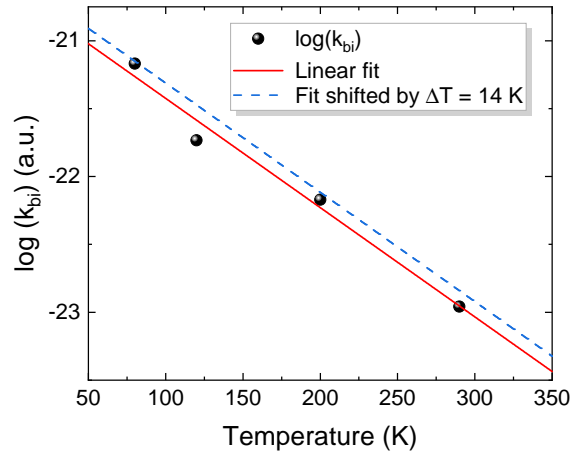


**Figure 6.9:** Graphical estimation of the error in  $k_{bi}$  considering pump-induced heating effects. The maximum temperature increase based on the excitation conditions and material characteristics is  $\Delta T_{\max} \approx 14$  K. Black spheres represent the determined  $k_{bi}$  values from the carrier dynamics analysis as  $\log(k_{bi})$ . The red solid line corresponds to the linear fit of  $\log(k_{bi})$ , and the dashed blue line corresponds to the linear fit (red solid line) with a horizontal offset of  $\Delta T_{\max} = 14$  K representing the maximum shift in temperature due to heating effects.

Overall, the determined values for  $k_{\text{bi}}$  and  $k_{\text{Auger}}$  are consistent with previously reported coefficients for similar 3D perovskites with different compositions (Appendix, Table A.1). Moreover, the exponential decrease of  $k_{\text{bi}}$  with temperature agrees with previous results for MAPI. This decrease can be attributed to the broadening of the Fermi-Dirac distribution, resulting in a thermal spreading of carriers across the bands.<sup>[8, 23]</sup>

Regarding Auger rates, they strongly depend on the material's band structure and phonon statistics given the energy and momentum conservation condition for this process.<sup>[90-94]</sup> In inorganic semiconductors,  $k_{\text{Auger}}$  typically increases with temperature, and the nature of this process determines its temperature dependence: The band-to-band (phonon-less) Auger recombination is characterised by a strong temperature dependence due to momentum conservation, whereas the phonon-assisted process does not exhibit such a strong temperature dependence.<sup>[94-100]</sup> The temperature dependence of  $k_{\text{Auger}}$  can include contributions from both processes, where the phonon-assisted process was reported to dominate at low temperatures and compete with the phonon-less process at room temperature.<sup>[96, 101]</sup> For instance,  $k_{\text{Auger}}$  in InGaAs exhibits a twofold increase, rising from  $1.5 \cdot 10^{-28} \text{ cm}^6\text{s}^{-1}$  at 200 K to  $3 \cdot 10^{-28} \text{ cm}^6\text{s}^{-1}$  at 300 K.<sup>[96]</sup> Similarly, for GaInAsP,  $k_{\text{Auger}}$  experiences an increase from  $(4.01 \text{ to } 5.9) \cdot 10^{-29} \text{ cm}^6\text{s}^{-1}$  within the same temperature interval.<sup>[102]</sup> For perovskites,  $k_{\text{Auger}}$  is highly affected by the crystal phase and depends on perovskite composition and lattice disorder.<sup>[23, 24, 93]</sup> For MAPI, in the orthorhombic phase,  $k_{\text{Auger}}$  undergoes a decrease of over three orders of magnitude between 4 - 150 K; in the tetragonal phase, it stays almost constant between 150 - 300 K, and in the cubic phase, it experiences a decrease of about one order of magnitude from 300 K to 400 K.<sup>[24]</sup> The origin of the results observed here of a roughly constant Auger coefficient from 80 K to 290 K of  $k_{\text{Auger}}(T) \approx 3 \cdot 10^{-29} \text{ cm}^6\text{s}^{-1}$  is not evident. The constant phase of the triple-cation perovskites is a possible explanation for the approximately constant  $k_{\text{Auger}}(T)$ . These results represent the first temperature-dependent measurements of Auger rates in a phase-stable perovskite, so no comparative literature is available. In summary, the temperature-dependent  $k_{\text{bi}}$  and  $k_{\text{Auger}}$  were determined using TR spectroscopy at high carrier densities with a high-index substrate to suppress ASE. The following section investigates the origin of a temperature-dependent ASE based on the influence of these rates and emission spectral broadening.

## 6.2 Factors determining the amplified spontaneous emission threshold

This section investigates the underlying causes responsible for the increase in ASE threshold with temperature in triple-cation perovskites. Section 6.2.1 introduces the topic of temperature-dependent lasing and ASE thresholds in perovskites and the currently supported theories to explain this behaviour. Next, Section 6.2.2 discusses the results of the temperature-dependent ASE thresholds in triple-cation perovskites, and Section 6.2.3 investigates the contribution of non-radiative Auger losses to the ASE process as a function of temperature. Finally, Section 6.2.4 elucidates how the results from the study in Section 6.1 and the emission spectral broadening can explain the increase in threshold with temperature.

### 6.2.1 Introduction

Perovskite semiconductors exhibit an increase in lasing and ASE thresholds under both pulsed and CW excitation.<sup>[28, 78, 103–105]</sup> This behaviour presents a fundamental limitation in achieving CW lasing at room temperature due to the significant heating effects caused by the CW pump.<sup>[78]</sup> Different hypotheses have been proposed to explain this increase in threshold for perovskite materials, drawing on considerations from inorganic semiconductors. Currently, the accepted theories that offer explanations for this phenomenon include i) an exponential dependency based on the theory for laser diodes and ii) a band-tail model proposed for semiconductors with shallow defect states. These are detailed in the following.

In the context of inorganic semiconductor laser diodes, an exponential relation is observed between temperature and the threshold current  $I_{\text{th}}$ . This relation can be expressed as  $I_{\text{th}} \propto e^{T/T_0}$ , where  $T_0$  represents a characteristic temperature associated with this behaviour, typically exceeding 120 K.<sup>[102, 106]</sup> This exponential dependency on temperature can be attributed to several factors. Firstly, the gain parameter decreases with increasing temperature.<sup>[104]</sup> Additionally, the transparency carrier density and cavity loss increase with rising temperature. These temperature-dependent factors collectively influence the threshold current, with the  $T_0$  value quantifying the extent of the temperature dependency. A smaller  $T_0$  corresponds to a more pronounced temperature dependency. Both Brenner *et al.* and Jia *et al.* applied this exponential relationship to different perovskite materials and demonstrated that it suitably fits their temperature-dependent thresholds.<sup>[28, 78]</sup> The resulting characteristic temperature fell within the range of  $T_0 \approx 46 - 75$  K. Notably, these values are lower than what is commonly observed in inorganic laser diodes ( $T_0 > 120$  K), indicating a stronger temperature dependency of perovskite lasing thresholds.<sup>[28, 78]</sup>

An additional model proposed to explain the increase in perovskites' lasing threshold with temperature is the band-tail model, developed by M.J. Adams.<sup>[107]</sup> This model was developed to describe carrier concentrations and emission rates in semiconductors with exponential band tails, leading to the following simplified expression for describing the temperature-dependent threshold:  $n_{\text{th}} \propto T^3 [\cot^2(k_b T \pi / E_0) + 1]$ .<sup>[78]</sup> Here,  $k_b$  is the Boltzmann constant,

and  $E_0$  represents the characteristic decay energy of the band state distribution into the bandgap. Jia *et al.* also employed this model to elucidate the temperature-dependent lasing threshold in a MAPI perovskite within the temperature range of 150 to 300 K. In addition to the exponential fit, the band-tail model successfully explained the data and yielded a decay energy of approximately  $E_0 \approx 39$  meV, larger than the Urbach energy typically measured for MAPI.<sup>[78]</sup> It is important to note that this model is generally applicable to lower temperatures, i.e.,  $T \lesssim 120$  K.<sup>[107]</sup> In conclusion, both models are used to describe the behaviour of perovskites. However, they produce characteristic values ( $T_0, E_0$ ) that differ from those typically observed in inorganic semiconductors. Additionally, there has yet to be a consensus regarding the underlying physical mechanisms responsible for the behaviour of perovskites. In the following, both proposed models are employed to fit the acquired data for triple-cation perovskites.

### 6.2.2 Temperature-dependent amplified spontaneous emission threshold

Next to the TR analysis on Si substrates, the temperature-dependent ASE threshold in analogous triple-cation films was measured on sapphire substrates. Figure 6.10 summarises the threshold carrier density as a function of temperature, between 80 and 290 K, and both the exponential and band-tail models explained in the previous section are employed to describe this data. The curves are indicated in Figure 6.10 as a red line for the exponential fit and a blue dashed line for the band-tail fit. Both exponential and band-tail models can reasonably fit the data, and their fit values align with those reported for perovskite semiconductors. The exponential fit yields a characteristic temperature of  $T_0 = 73$  K, while the band-tail model results in a characteristic energy of approximately  $E_0 \approx 44$  meV. The latter value is roughly consistent with the Urbach energy extracted from fitting the absorption edge of the triple-cation perovskites, i.e.,  $E_U \approx 48$  meV. However, considering the temperature limitation of the band-tail model, the fit similarity may be accidental. Despite the reasonable fit of both models, a unified model that thoroughly explains the observed increase in threshold with temperature in perovskite materials has yet to be established. In the following sections, the temperature-dependent ASE threshold is explored through a detailed analysis of the contributions from i) the recombination rates  $k_{\text{bi}}(T)$  and  $k_{\text{Auger}}(T)$ , and ii) the spectral broadening with increasing temperature.

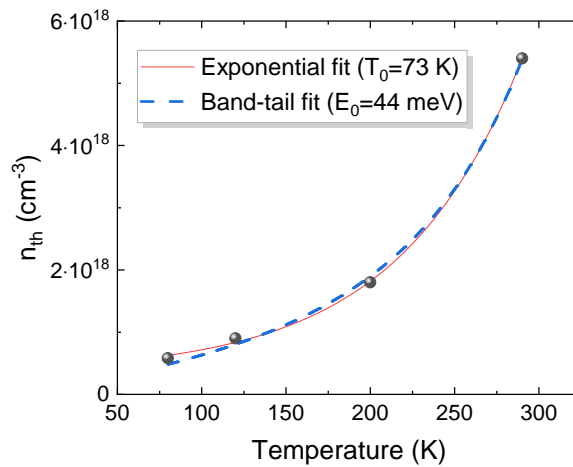


**Figure 6.10:** Temperature-dependent ASE threshold carrier density  $n_{th}$  of triple-cation perovskites represented with black spheres. The red solid line corresponds to the exponential fit, and the dashed blue line indicates the band-tail fit, with respective fit values  $T_0$  and  $E_0$ .

### 6.2.3 Impact of non-radiative Auger losses

This section explores the two primary recombination channels relevant while generating ASE: i) the radiative bimolecular process, contributing solely to ASE, and ii) Auger recombination, the dominant non-radiative pathway at high carrier densities. For pumping conditions above the threshold ( $n \geq n_{th}$ ), non-radiative trap-assisted recombination can be accurately neglected (Section 6.1.3). This study examines the interplay between these two recombination channels, bimolecular (proportional to  $n^2$ ) and Auger (proportional to  $n^3$ ), to elucidate how non-radiative Auger losses impact the temperature-dependent ASE threshold in the triple-cation perovskite. Given their dependency on carrier density  $n$ , a transition point  $n_A$  exists, above which Auger recombination dominates over bimolecular recombination. This density is estimated by equating the bimolecular and Auger terms in Equation 6.1, leading to  $n_A = k_{bi}/k_{Auger}$ . Figure 6.11a visually presents  $n_A$  as a function of temperature (black spheres), calculated using the previously determined  $k_{bi}$  and  $k_{Auger}$ . For lower carrier densities ( $n < n_A$ ), bimolecular recombination is the dominating recombination channel (green shaded area). In contrast, at higher densities ( $n > n_A$ ), Auger recombination governs the dynamics. The semi-logarithmic plot in Figure 6.11a illustrates that  $n_A(T)$  decreases approximately linearly with temperature (indicating an exponential decrease). This behaviour arises from the exponentially decreasing  $k_{bi}(T)$  and constant  $k_{Auger}(T)$  (Section 6.1.3). A comparison between  $n_A$  and  $n_{th}$  in Figure 6.11a (black and red spheres, respectively) reveals essential insights. Firstly, it is important to understand that for densities  $n > n_A$ , there is a higher ratio of excited carriers undergoing non-radiative recombination than carriers recombining radiatively and generating ASE. Consequently, these higher non-radiative losses result in an increased ASE threshold, as more excited carriers are needed to achieve the same radiative output. In contrast, for  $n \ll n_A$ , Auger losses are negligible and bimolecular or lower-order processes dominate the dynamics. Figure 6.11a demonstrates that at low temperatures (below 200 K),  $n_{th}$  remains significantly

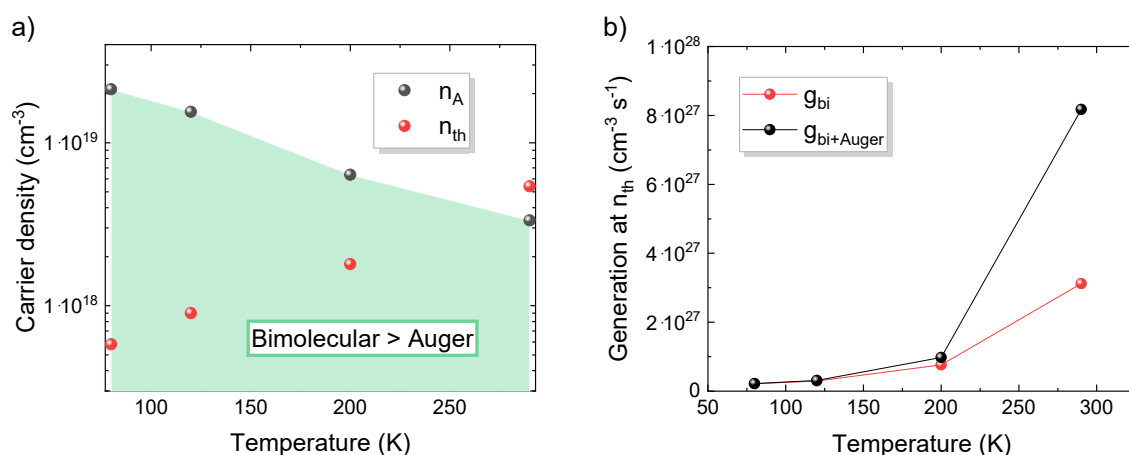


**Figure 6.11:** Effect of non-radiative Auger losses on the ASE threshold as a function of temperature. a) Density  $n_A$ , at which the radiative bimolecular process equals the non-radiative Auger process (black spheres). The green shaded area ( $n < n_A$ ) indicates the densities at which radiative recombination dominates over Auger recombination. For  $n > n_A$ , Auger governs the dynamics. Red spheres represent  $n_{th}(T)$ . A comparison of these two data sets ( $n_A$  and  $n_{th}$ ) reveals that at  $n_{th}$ , radiative recombination dominates the dynamics until 200 K (red spheres lie within the shaded area). In contrast, at 290 K,  $n_{th}$  lies above the green area and non-radiative losses govern the dynamics. b) Generation rate  $g$  needed to reach the ASE threshold at steady-state ( $dn/dt = 0$ ). Black data ( $g_{bi+Auger}$ ) is calculated with Equation 6.1, which includes bimolecular and Auger recombination, whereas red data ( $g_{bi}$ ) is calculated assuming all recombination occurs radiatively. Adapted with permission from [74]. Copyright 2021 American Chemical Society.

below the point where Auger influences the dynamics. The two data sets ( $n_A$  and  $n_{th}$ ) diverge by more than an order of magnitude, indicating that the Auger process does not substantially impact the dynamics or the ASE threshold. However, as the temperature increases, the two curves converge. At around 200 K, they come within the same order of magnitude, crossing at around  $T \approx 250$  K. At room temperature,  $n_{th}$  surpasses  $n_A$ , evidencing that non-radiative Auger recombination becomes the dominant process in the dynamics. This finding implies that at room temperature, a higher generation rate  $g$  is required to achieve  $n_{th}$  and generate ASE due to the additional Auger losses.

In order to assess how Auger losses influence the generation rate needed to reach the threshold, an estimation of the generation rate is performed by assuming the steady-state condition  $dn/dt = 0$ . Calculations were conducted for two cases: i) for the case where the dynamics is described by Equation 6.1 where the bimolecular and Auger recombination channels describe the total carrier dynamics ( $g_{bi+Auger}$ ), and ii) for the hypothetical case where there are no non-radiative Auger losses, and all carriers recombine radiatively upon excitation ( $g_{bi}$ ). The generation rates were calculated for the steady-state condition with Equation 6.1, including a generation rate term, given by  $g_{bi+Auger} = k_{bi} \cdot n^2 + k_{Auger} \cdot n^3$  for the first case, and  $g_{bi} = k_{bi} \cdot n^2$  for the second (hypothetical) case. The results are depicted in Figure 6.11b and match the previous conclusions: At temperatures below 200 K,  $g_{bi} \approx g_{bi+Auger}$ , indicating that Auger losses have minimal influence on the recombination dynamics. However, as the temperature increases beyond 200 K, the two curves diverge

due to the increasing impact of Auger losses. Consequently, a higher generation rate is needed to achieve the threshold when accounting for Auger losses.

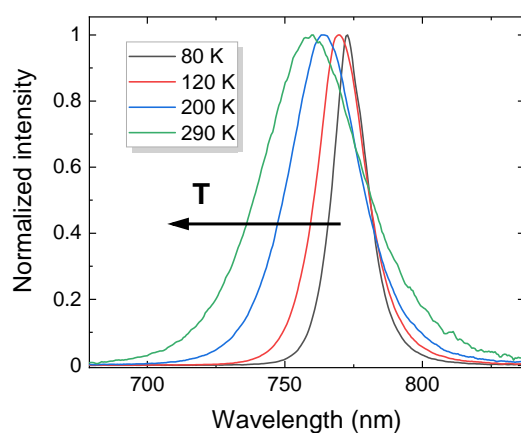
In conclusion, these results demonstrate that non-radiative Auger losses contribute to an increase in the threshold at room temperature (290 K); however, they cannot account for the observed increase in ASE threshold between 80 - 200 K, as supported by the temperature dependence of  $g_{bi}$ : Even if Auger losses are disregarded, and all excited charge carriers recombine radiatively,  $g_{bi}$  still increases with rising temperature (Figure 6.11b). The following section explores how the temperature dependency of  $k_{bi}(T)$  and emission broadening can explain the increase in ASE threshold at lower temperatures.

#### 6.2.4 Contribution of bimolecular rate and spectral broadening

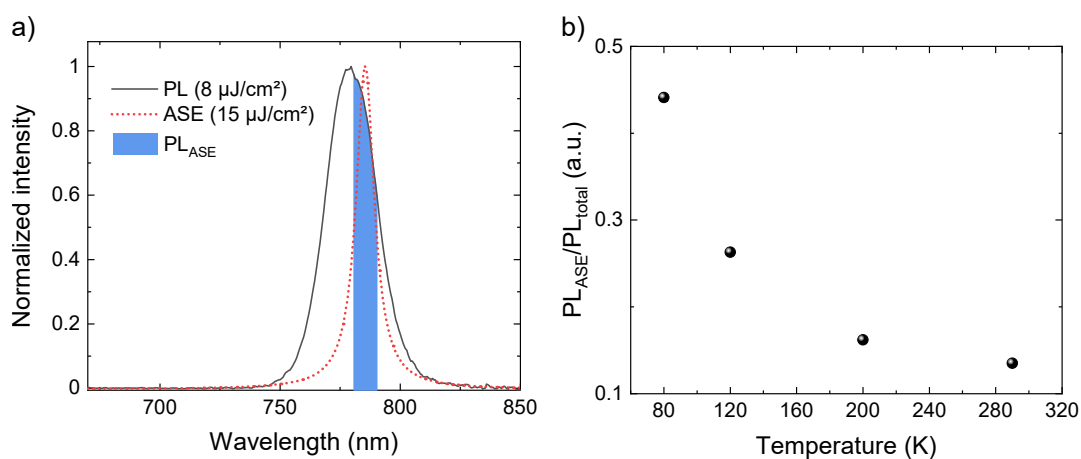
The previous section clarified the impact of non-radiative Auger losses on the ASE threshold. This section examines the temperature-dependent light emission at threshold in these triple-cation films, mainly the radiative emission fraction of the PL contributing to ASE. Up to this point, the discussion on the ASE threshold condition centred on the carrier density  $n_{th}$ . However, achieving ASE requires not only  $n_{th}$  but also a threshold photon density  $n_{ph}$ , as detailed in Section 3.4, Equation 3.6. The onset of ASE depends on the product  $n \cdot n_{ph}$  exceeding the necessary threshold value. This explains why ASE does not occur in Si substrates: the absence of light confinement by waveguiding prevents the photon density from reaching the essential threshold value. The total PL emission rate at threshold is determined by the radiative bimolecular term  $k_{bi}(T) \cdot n_{th}^2(T)$ . Above threshold, only the emission within the ASE energy band contributes to the ASE process. In the following, the total emission and fraction of PL emission contributing to the ASE process are examined as a function of temperature.

Figure 6.12 illustrates the PL spectra below threshold, revealing a significant broadening with rising temperature. Notably, a blueshift in the central wavelength  $\lambda_c$  of the PL is evident, shifting from  $\lambda_c \approx 773$  nm at 80 K to  $\lambda_c \approx 760$  nm at 290 K.<sup>1</sup> The relevant photon emission rate per unit volume contributing to the ASE process solely encompasses PL emission within the ASE energies, denoted as  $PL_{ASE}$  – the integral of the PL spectrum within the ASE band. The graphical representation of  $PL_{ASE}$  is visible in Figure 6.13a as a blue shaded region. Here, the ASE band was determined by taking the ASE spectrum above threshold (dashed red line) and identifying the FWHM wavelengths.  $PL_{ASE}$  was then calculated by integrating the PL spectrum below threshold (solid black line) within that region (blue shaded area).  $PL_{ASE}$  was determined for each temperature, along with the fraction of total PL emission within the ASE band, calculated as  $PL_{ASE}/PL_{total}$ . Consequently, the total ASE emission rate at threshold is given by  $PL_{ASE}/PL_{total} \cdot k_{bi} \cdot n_{th}^2$ . The ratio factor  $PL_{ASE}/PL_{total}$  is depicted in Figure 6.13b as a function of temperature, which reveals a rapid decrease in emission contributing to ASE with increasing temperature.

<sup>1</sup> These broadening and blueshift phenomena are consistent with previous observations in different perovskites.<sup>[78, 108]</sup>



**Figure 6.12:** Normalised PL spectra for perovskite films on sapphire substrates measured at 80 K (black), 120 K (red), 200 K (blue), and 290 K (green). These PL spectra were acquired at the highest excitation fluence before the ASE threshold (of each temperature). The displayed spectra exhibit a significant spectral broadening and blueshift with increasing temperature (black arrow).



**Figure 6.13:** PL emission contributing to the ASE band. a) Graphical determination of the ASE band. The black solid line corresponds to the PL emission (on Si substrates), red dashed line represents the ASE emission (consists of the Lorentzian fit to the ASE peak measured on sapphire substrates), and blue shaded region corresponds to the PL emission within the ASE band  $PL_{ASE}$ , determined by the FWHM of the ASE peak. Adapted with permission from [74]. Copyright 2021 American Chemical Society. b) Fraction of the total PL contributing to the ASE emission  $PL_{ASE}/PL_{total}$  as a function of temperature, revealing a fast decrease with increasing temperature due to spectral broadening.

To finalise this analysis, Figure 6.14 illustrates the temperature-dependent radiative emission rate at threshold, both for the overall PL depicted as black spheres and for the PL within the ASE band represented by red spheres. These values are computed based on the previously discussed measurements of  $k_{bi}$  and  $n_{th}$ . The total emission rate at threshold demonstrates an increase with rising temperature, as shown by the black spheres when solely accounting for the decrease in  $k_{bi}(T)$ . This outcome implies that the exponential reduction in  $k_{bi}(T)$  alone does not account for the temperature-dependent ASE threshold. However, when also considering the decrease in  $PL_{ASE}/PL_{total}$ , the emission rate remains approximately constant at around  $10^{26} \text{ cm}^{-3} \text{ s}^{-1}$  below room temperature. At room temperature, there is a slight increase, by a factor of  $\approx 3.5$ , possibly due to increased photon loss. In conclusion, these findings reveal that the increase in  $n_{th}(T)$  for temperatures below 290 K can be entirely attributed to carrier dilution, resulting in the decrease in  $k_{bi}(T)$ , and spectral broadening, leading to a decrease in  $PL_{ASE}/PL_{total}$ . However, it is important to note that the contribution of trap-assisted recombination processes was not considered, which could potentially influence the dynamics and thresholds for CW excitation.<sup>[78]</sup> Efforts to mitigate these factors responsible for the increase in  $n_{th}(T)$  and limiting CW operation in perovskite thin films should be explored. These strategies may encompass material or optical approaches to enhance the radiative rate coefficient  $k_{bi}$  and the  $PL_{ASE}/PL_{total}$  ratio. This enhancement can be through carrier or photon confinement or by narrowing the PL spectrum. The subsequent chapter presents findings from various optical and material engineering approaches aimed at addressing these challenges.

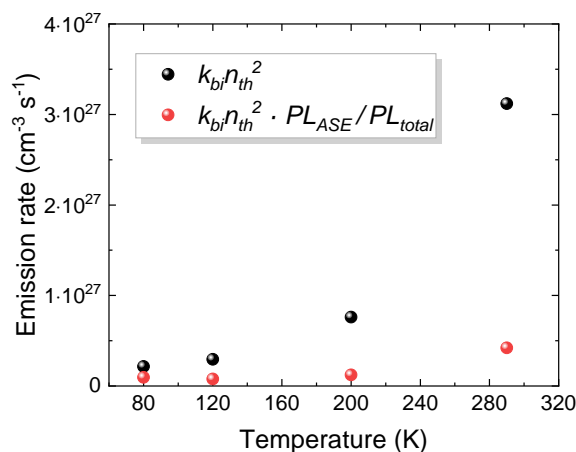


**Figure 6.14:** Comparison of the photon emission at threshold into the total PL (black spheres) and the ASE band (red spheres), as a function of temperature. Adapted with permission from [74]. Copyright 2021 American Chemical Society.

### 6.3 Summary

This chapter explores the photophysics of perovskite materials and its impact on light amplification, focusing on the temperature-dependent ASE threshold. The chapter examines the temperature-dependent behaviour of the bimolecular and Auger recombination processes, spectral broadening with temperature, and the contribution of PL to the ASE band. Transient reflection measurements were performed on Si substrates to study carrier dynamics at high carrier densities. These substrates effectively suppress ASE in the film and enable accurate measurements of intrinsic recombination rates without carrier depletion through stimulated emission. The results demonstrate that at temperatures below room temperature, the rapid increase in ASE threshold with temperature is influenced by two primary factors. Firstly,  $k_{bi}(T)$  decreases exponentially as the temperature rises, so higher carrier densities are needed to maintain the same radiative rate. Secondly, as the PL spectrum broadens with temperature, the fraction of PL within the ASE band strongly decreases. At temperatures exceeding  $\approx 250$  K, non-radiative Auger losses also contribute to an increase in the pump threshold. Under the excitation conditions employed in this study, trap-assisted recombination can be neglected; nevertheless, under (quasi-)CW excitation, trap-related processes might no longer be negligible. This could influence the CW lasing thresholds in addition to the aspects considered here. The new insights provided in this work pave the way for investigating material and optical strategies that sustain a higher  $k_{bi}$  and a narrower PL to increase the temperature at which CW ASE can be maintained.

## 7 Strategies for Enhanced ASE by Tuning of Optical and Compositional Properties

This chapter focuses on implementing optical and material strategies for improving light amplification in perovskite films. First, Section 7.1 investigates the effect of surface passivation layers on the ASE performance in perovskite films. In particular, two contributions of a cover layer are studied: its influence on perovskite's defect density and optical waveguide propagation scattering losses. Next, Sections 7.2 and 7.3 focus on material engineering strategies. In particular, Section 7.2 investigates quasi-2D perovskites based on CsPbBr<sub>3</sub> as their confinement effect has the potential to promote stronger radiative recombination and enhance ASE performance. The optimisation of process parameters reveals that a high-temperature annealing (HTA) of quasi-2D films consists of a novel and efficient approach to fabricating high-quality 3D films. Therefore, quasi-2D perovskites and their 3D counterparts are analysed and compared regarding their potential as laser gain media. Finally, in Section 7.3, potassium is incorporated in the standard triple-cation perovskite as a bulk passivation agent. The ASE performance is optimised by tuning the potassium content, and the doping effect is studied by optical and morphological characterisation.

### Acknowledgements and Contributions

This chapter primarily elaborates on the concepts presented in the publication

- Allegro, I.; I. A. Howard; Lemmer, U. Improving Light Amplification in Perovskites by Light Confinement and Defect Passivation. *in preparation*

The author conceptualised the study and conducted the experimental work and analysis. I. A. Howard and U. Lemmer supervised the project.

The author conceptualised and performed the study in Section 7.2. Y. Li assisted with fabricating the CsPbBr<sub>3</sub> films. The results presented here form the foundation for the publication

- Li, Y.; Allegro, I.; Kaiser, M.; Malla, A. J.; Richards, B. S.; Lemmer, U.; Paetzold, U. W.; Howard, I. A. "Exciton versus free carrier emission: Implications for photoluminescence efficiency and amplified spontaneous emission thresholds in quasi-2D and 3D perovskites" 2021. *Materials Today*, 49, 35–47 [36]

The study in Section 7.3.2 was conceptualised and performed by the author and supervised by U. Lemmer.

## 7.1 Light confinement and defect mitigation via surface passivation

This study investigates optical and defect passivation strategies to enhance light amplification in perovskite thin films. Section 7.1.1 discusses the state of the art and motivation behind the employed strategies. Section 7.1.2 presents the effects of various passivation approaches on the ASE performance. This is followed by an analysis of the defect density in the films using TRPL (Section 7.1.3) and a discussion of how different cladding layers influence propagation scattering losses in perovskite films (Section 7.1.4).

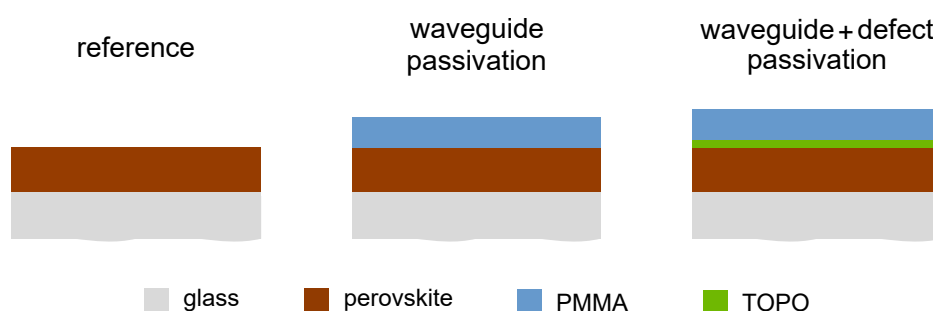
### 7.1.1 Introduction

Defect passivation is a focal point in the ongoing research of perovskite optoelectronic devices, including solar cells, LEDs, and lasers. Poly-crystalline perovskite films possess a variety of defects within their bulk, grain boundaries, and surface, which give rise to primarily shallow trap states within the bandgap and are detrimental to device performance.<sup>[44]</sup> Defect passivation consists in adding a passivation agent either in the bulk or on the surface of the perovskite film to mitigate defect states that promote non-radiative recombination. These defect-assisted recombination processes present a significant loss channel in light-absorbing and light-emitting devices. They are especially relevant for devices operating at low carrier densities, such as solar cells or LEDs, since they govern the carrier dynamics in the low fluence regime.<sup>[23]</sup> Nonetheless, surface passivation strategies successfully enhanced light amplification (lasing, ASE) in perovskite thin films.<sup>[109–113]</sup> These approaches mainly consisted in adding a surface passivation layer to the perovskite waveguide, which led to a significant decrease in ASE thresholds, ranging from approximately  $\approx 10 - 60\%$ . The observed improvement through surface passivation was ascribed to either a reduction in trap density or a combined influence involving symmetric waveguide (SWG) effects. These SWG effects are related to the overlap of the waveguide mode with the perovskite gain material. One relevant and unexplored effect of employing a surface passivation layer with a refractive index larger than  $n_{air} = 1$  is the change in index contrast of the top perovskite surface. This alteration has implications for scattering losses and light detention within the film: A top cover inherently acts as a waveguide passivation (WP), reducing waveguide propagation losses by lowering the index contrast at the interface perovskite/cladding. Thereby, it decreases scattered light losses, leading to an increased photon density inside the film, which is beneficial for light amplification. Thus, a reduction in the ASE threshold for films featuring a surface passivation layer may partly originate from the influence of waveguide passivation; however, this effect was not considered in previous reports. The current study investigates the contribution of a cover layer aimed at surface defect passivation to waveguide passivation effects. Therefore, the following section compares perovskite films subjected to WP and those benefiting from both WP and defect passivation (DP). The layer geometry is designed to suppress any SWG effects, ensuring that only contributions from WP and DP are considered. The results provide insights into the unexplored influence of top cover layers on optical scattering losses and their impact on the ASE performance.

### 7.1.2 ASE performance for different surface layers

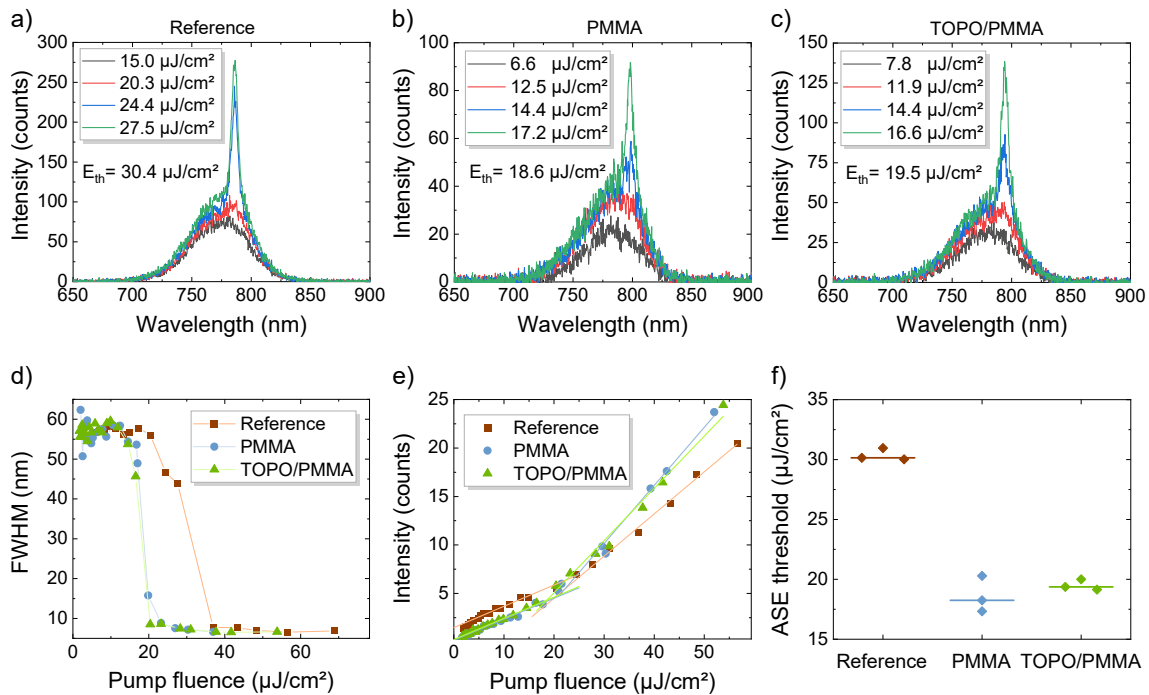
The three layer stacks studied are displayed in Figure 7.1 and consist of a perovskite film on a glass substrate i) without passivation (reference), ii) with WP, and iii) with DP and WP. The perovskite layer consists of a triple-cation perovskite film with a thickness of approximately 180 nm. The WP is achieved by adding a thick PMMA layer on top, with a thickness of approximately 460 nm. This thick layer acts as a waveguide cladding and reduces propagation scattering losses, thereby *passivating* the waveguide. For DP, TOPO is added as a top cover since it was reported to mitigate defect states efficiently (fabrication details provided in Chapter 5).<sup>[65, 114]</sup> Films with double passivation consist of a perovskite film with a TOPO layer followed by a PMMA cladding (Figure 7.1). Although the PMMA layer mainly serves as a waveguide passivation, such a layer was also demonstrated to have a DP effect when deposited on a perovskite film.<sup>[110, 115, 116]</sup> However, according to previous reports, this effect is expected to be minimal compared to the defect passivation provided by TOPO.<sup>[65, 112]</sup> In addition, TOPO molecules may penetrate deeper into the film, thereby passivating defects at greater depths than the surface. The light amplification in the three different configurations is investigated in the following.

Figure 7.2 displays the ASE results of all films and demonstrates an enhanced ASE performance for passivated films. These measurements were performed via surface excitation and collection with the ICCD setup, detailed in Chapter 5. Figures 7.2a-c exhibit exemplary ASE spectra, and Figures 7.2d-e FWHM values, and input-output characteristics, respectively. The onset of stimulated emission is discernible by a narrowing of the PL spectrum (Figures 7.2a-d) and an increase in output intensity (Figure 7.2e) after a specific threshold fluence. The values displayed for threshold fluences  $E_{th}$  in Figures 7.2a-c are an average of several measurements of different spots on each sample. Figure 7.2e illustrates exemplary input-output curves for the three architectures, with linear fits for the emission below and above threshold, respectively. Notably, the ASE slope efficiency of all passivated samples is higher than the reference, indicating lower optical losses in the stimulated emission process. Details on the influence of optical losses on slope efficiency



**Figure 7.1:** Schematic of reference and passivated samples with PMMA and TOPO/PMMA. (layers not to scale). The reference is a triple-cation perovskite film with a thickness of  $\approx 180$  nm (brown layer) spin-coated on a glass substrate (grey layer). Waveguide passivation refers to adding a PMMA cover layer, approximately 460 nm thick (blue layer). Defect passivation involves the treatment of a perovskite film with a surface TOPO layer to mitigate defects (green layer). Waveguide + defect passivation combines both TOPO and PMMA layers to provide defect and waveguide passivation.

are elucidated in Section 3.4. Figure 7.2f summarises the ASE thresholds of all samples and demonstrates a threshold reduction by a factor of  $> 1.6$  for passivated films corresponding to a 39 % threshold enhancement. In effect,  $E_{th}$  decreases from  $30.4 \mu\text{J}/\text{cm}^2$  (reference) to  $19.5 \mu\text{J}/\text{cm}^2$  for films with both passivations (TOPO/PMMA), to a minimum of  $18.6 \mu\text{J}/\text{cm}^2$  for films with WP (PMMA). The threshold values of the two passivated films lie within the measurement deviation, so these two samples can be assumed to possess approximately the same threshold. The similar ASE results for both passivated samples (Figure 7.2) suggest that the DP layer does not significantly impact the ASE threshold or slope efficiency. To test the individual contribution of DP, a film with only DP (TOPO layer) was tested, which exhibited an  $E_{th} \approx 23.9 \mu\text{J}/\text{cm}^2$ , corresponding to a 21 % threshold reduction compared to the reference film. This configuration (perovskite/TOPO) was not stable enough for further characterisation due to a fast degradation possibly promoted by TOPO. However, once a WP passivation is added on top, the role of DP appears to have no noticeable impact on the ASE performance (Figure 7.2). Consequently, these results indicate that WP is more important than DP for optimising perovskite films for low-threshold lasing applications. To further test this hypothesis and investigate the influence of each passivation on the defect density in the film, the carrier dynamics of each sample is analysed in the following section.



**Figure 7.2:** ASE performance of reference and passivated films with PMMA and TOPO/PMMA. Emission spectra as a function of fluence with average threshold density  $E_{th}$  for a) reference, b) PMMA (WP) and c) TOPO/PMMA (WP+DP). d) FWHM linewidth as a function of pump fluence for all films demonstrating an emission narrowing at threshold from around 60 nm for PL to below 10 nm for ASE. e) Light-in-light-out curves of all films. Symbols represent measured data and solid lines a linear fit to the emission below and above threshold. f) Boxplot of ASE thresholds for all films with individual measurement (scatter) and median (line) values.

### 7.1.3 Defect mitigation by surface passivation

The carrier dynamics analysis of all samples demonstrates a decrease in defect density with additional passivation. As expected from the previous discussion and reported literature, PMMA passivates some defects (compared to the reference film), and TOPO is the most effective passivation agent to reduce trap states. However, these results cannot explain the observed behaviour in ASE performance, which is approximately identical for both PMMA and TOPO passivations. The trap density is examined by measuring TRPL decays for each layer configuration. Figure 7.3 depicts the TRPL curves, measured with initial densities  $n_0$  spanning over three orders of magnitude: From  $n_0 < n_t$ , where most trap states are unoccupied, up to densities where the dynamics is dominated by bimolecular recombination and any Auger contribution is negligible  $n_t < n_A$ . As expected, the higher  $n_0$ , the faster the decay due to a more substantial contribution of high-order recombination processes (Figure 7.3a-c). The decay at  $n_0 \approx 10^{14} \text{ cm}^{-3}$  is nearly mono-exponential (linear on the semi-logarithmic scale), whereas the decays for  $n_0 > 10^{16} \text{ cm}^{-3}$  exhibit a faster multi-exponential decay. Figure 7.3d presents a summary of TRPL decays of the three architectures at low and high fluence for a better direct comparison. These curves reveal an increase in lifetime  $\tau$  with additional passivation, i.e.,  $\tau_{\text{ref}} < \tau_{\text{WP}} < \tau_{\text{WP+DP}}$ . This finding suggests a corresponding decrease in defect density, i.e.,  $n_{t,\text{ref}} > n_{t,\text{WP}} > n_{t,\text{WP+DP}}$ . This qualitative analysis agrees with the premise that TOPO promotes more effective defect passivation than PMMA.

For a quantitative analysis of the TRPL data, the SRH model (introduced in Section 4.3.2) is employed to determine the defect density of each film. The TRPL data of each sample is globally fit, and the respective recombination coefficients and trap densities are determined (Figure 7.3). This model is chosen because it encompasses the trap density  $n_t$  term, unlike the simplified ABC model (Section 4.3.2). Furthermore, the curves for the lowest  $n_0$  exhibit a faster initial decay (until about 100 ns) characteristic of a de-trapping process, which is also only considered in the SRH rate equations (Equation 4.1). The fit results are plotted as solid lines in Figures 7.3a-c on top of the measured data represented by open symbols. For the fitting, all rate coefficients except  $n_t$  are kept constant since the passivation layers should primarily modify  $n_t$  and not significantly affect the remaining recombination parameters of the underlying perovskite film. The results for  $n_t$  are summarised in Table 7.1.

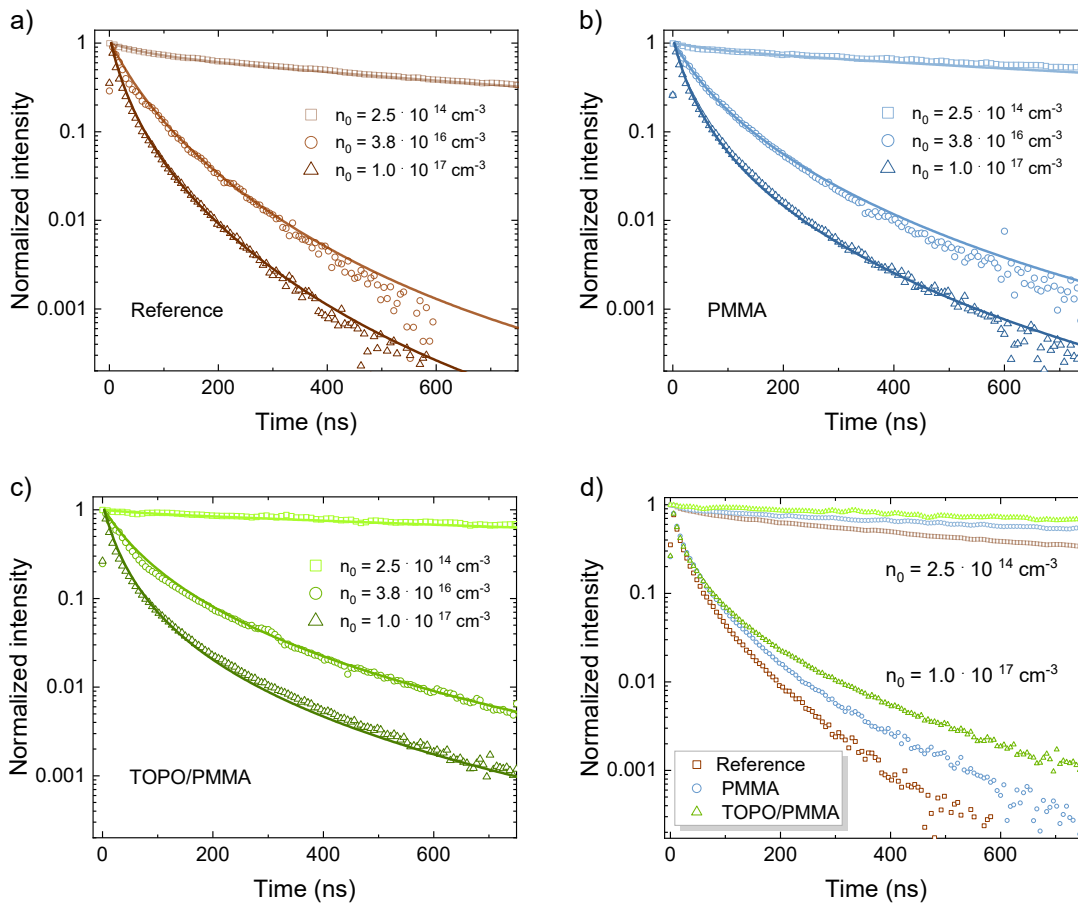


**Figure 7.3:** Fluence-dependent transient PL. Measured (open symbols) and fitted (solid lines) decays for a) reference, b) PMMA (WP) and c) TOPO/PMMA (WP+DP). The fits are calculated with the SRH model with shared parameters except for the trap density. d) Summary of all high and low-fluence decays, at  $n_0 = 2.5 \cdot 10^{14} \text{ cm}^{-3}$  and  $n_0 = 1.0 \cdot 10^{17} \text{ cm}^{-3}$ , for a better visual comparison, demonstrating an increasing lifetime with additional passivation.

Sample	Reference	Reference/PMMA	Reference/TOPO/PMMA
$n_t$	$1.00 \cdot 10^{16} \text{ cm}^{-3}$	$0.58 \cdot 10^{16} \text{ cm}^{-3}$	$0.25 \cdot 10^{16} \text{ cm}^{-3}$

**Table 7.1:** Trap density  $n_t$  determined by the global fit of the SRH model to the fluence-dependent TRPL data of each sample architecture.

An additional characterisation technique that can provide insights about the trap density in a perovskite film is PLQY, explained in Section 5.4.2. The PLQY is proportional to the ratio of radiative emission (bimolecular recombination given by  $k_{\text{bi}} \cdot n^2$ ) to the total recombination processes, i.e., radiative and non-radiative combined. At the low fluence regime, trap-assisted recombination mechanisms are the only relevant non-radiative processes influencing the dynamics. Thus, the low-fluence PLQY can shed light on the defect density in a material since an increase in PLQY implies a decrease in trap density and associated non-radiative recombination. Figure 7.4 presents the PLQY results for the three layer stacks, where  $\text{PLQY}_{\text{reference}} < \text{PLQY}_{\text{WP}} < \text{PLQY}_{\text{WP+DP}}$  (Figure 7.4a). These results imply

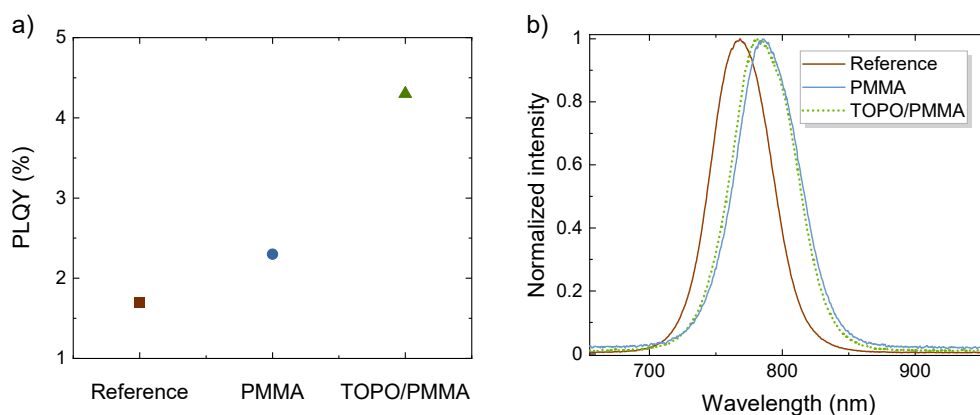


**Figure 7.4:** PLQY of reference, PMMA and TOPO/PMMA films. a) PLQY values for each film depicting an increase in radiative efficiency with additional passivation strategy, and b) respective emission spectra measured in an integrating sphere displaying a red shift for passivated films.

the following relation between the defect density of each film:  $n_{t,reference} > n_{t,WP} > n_{WP+DP}$ , which agrees with the previous TRPL analysis. Notably, these results do not follow the trend observed in ASE threshold nor slope efficiency and, thus, cannot explain this ASE behaviour. However, the PL spectra collected in the integrating sphere of the PLQY setup provide additional insights: A significant spectral shift is observed in Figure 7.4b, which roughly follows the ASE behaviour (Figure 7.2f), where the redshift corresponds to a threshold reduction. The reference PL is centred at around 760 nm, and both passivated samples exhibit a red shift of 20 nm for WP and 18 nm for WP+DP. The slightly higher shift for PMMA matches the marginally lower ASE threshold and likely originates from a smoother interface of perovskite/PMMA than perovskite/TOPO/PMMA. Such a redshift is a typical indication of re-absorption in the perovskite film (discussed in Section 4.2). The higher re-absorption is a result of higher light confinement inside the film. The spectra measured in the integrating sphere comprise the total PL emission from surface scattered and guided light. The longer light resides (propagates) inside the perovskite waveguide, the higher the re-absorption probability and the resulting red-shift.<sup>[42]</sup> Thus, these results point to stronger optical confinement for the passivated samples, which leads to a higher photon density in the perovskite, likely due to lower scattering losses. Therefore, the optical mode confinement and scattering losses of each sample architecture is compared in the following section.

#### 7.1.4 Scattering losses and photon density in cladded films

Previous reports on a perovskite film with a PMMA cladding layer improving light amplification only considered defect mitigation and SWG effects.<sup>[110, 111, 115]</sup> The latter consists of the influence of the layer refractive index ( $n_{PMMA} > n_{air}$ ) on the optical mode overlap with the active waveguide. These reports typically employed a perovskite layer around  $\approx 100$  nm thick in contact with air, exhibiting an asymmetric mode profile with a significant overlap with the substrate layer. In these cases, a PMMA cladding leads to an approximately symmetric waveguide with  $n_{substrate(glass)} \approx n_{cladding(PMMA)}$ . This SWG shifts the

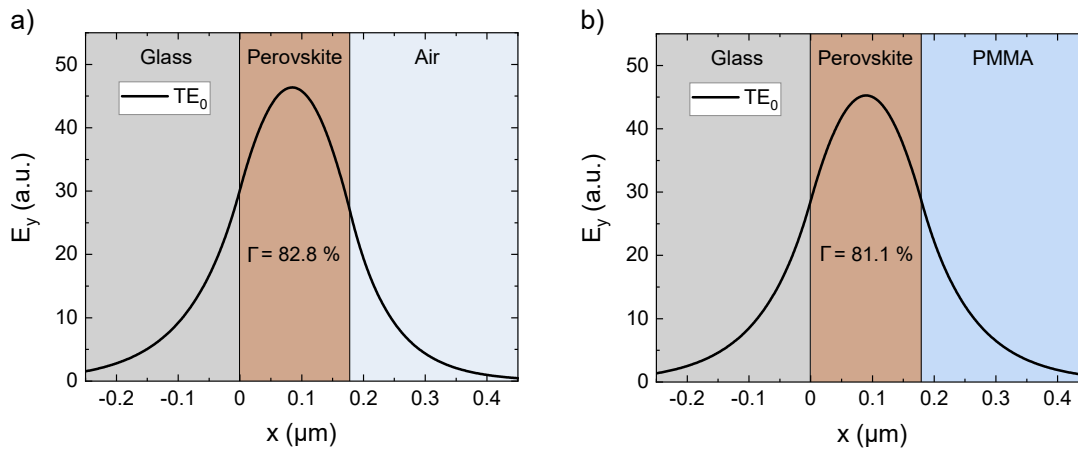


**Figure 7.5:** Electric field profile of the  $TE_0$  waveguide mode, simulated with a 1-D mode solver for dielectric multilayer slab waveguides.<sup>[117]</sup> Layer stack corresponds to a) a reference film and b) a PMMA passivated film. The overlap factor  $\Gamma = \int_{\text{perovskite}} S_z / \int_{\text{total}} S_z$  is slightly higher for a). Here,  $\int_{\text{perovskite}}$  indicates the overlap integral of the mode with the perovskite waveguide (perovskite), and  $S_z$  is the longitudinal component of the Poynting vector.

waveguide mode toward the centre of the active layer and increases the mode overlap factor with the perovskite, thereby enhancing the optical gain. Consequently, the ASE or lasing performance improves. Details on how the optical gain depends on the mode overlap are elucidated in Section 3.3.

For the current layer geometry, however, SWG effects are suppressed by using a thick perovskite layer (180 nm) so that the waveguide mode is roughly centred to the active layer (with or without a PMMA cladding). Figure 7.5 shows the mode profile for this thick perovskite layer with each cladding layer: air in Figure 7.5a and PMMA in Figure 7.5b. The addition of a PMMA layer slightly lowers the overlap factor of the optical mode in the perovskite by 1.7 %, decreasing from  $\Gamma = 82.8 \%$  (for glass/perovskite/air) to  $\Gamma = 81.1 \%$  (for glass/perovskite/PMMA). Hence, considering only the overlap factor, a PMMA cladding results in a lower gain that would lead to higher ASE thresholds and does not explain the observed improvements. Consequently, there must be an additional factor with a more decisive positive influence on the light amplification in the film for the case of a PMMA cladding. This aspect is likely the waveguide passivation effect. Therefore, waveguide propagation scattering losses are explored in the following.

As previously discussed, a high-index cladding layer leading to a lower index contrast at the interface perovskite/cladding reduces waveguide scattering losses. Additionally, the lower ASE threshold and higher slope efficiency point to lower optical losses. The gain remains the same for both WP and WP+DP geometries since the perovskite layer and  $\Gamma$  define it, and they are nearly identical for both cases. Thus, the better ASE performance of the layer stack with a PMMA cladding must arise from lower optical losses. Given the geometry of the measurement setup, relying on surface detection, the collected emission encompasses scattered light orthogonal to the waveguide and propagation direction. As a result, the measured signal is proportional to the scattering losses of the film. Figure 7.6

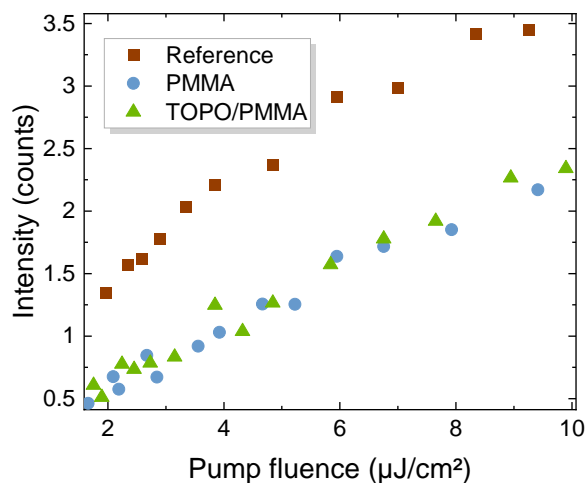


**Figure 7.6:** Surface emission below threshold corresponding to scattered PL for reference and passivated films. The intensity of the reference emission at the highest fluences (around  $8\text{-}10\ \mu\text{J}/\text{cm}^2$ ) is higher than the one of the passivated films by a factor of  $\approx 1.6$ .

displays the light-in-light-out curve for the three sample architectures: reference, PMMA (WP), and TOPO/PMMA (DP+WP). The emission of the reference film is higher than the emission of the two passivated films by a factor  $\approx 1.6$ . The stronger PL intensity detected in the orthogonal direction indicates that the reference film possesses significantly higher scattering losses. Similarly to the ASE and integrating sphere data, the two passivated samples exhibit analogous results. These observations confirm that passivated films possess lower scattering losses, leading to a higher photon density inside the film and, consequently, a better ASE performance. Notably, the factor of 1.6 matches the previously observed ASE enhancement  $n_{\text{th,ref}} \approx 1.6 \cdot n_{\text{th,PMMA}}$ .

To conclude, PMMA and TOPO/PMMA surface layers can improve ASE performance in perovskite films reducing their thresholds by  $\approx 40\%$ . WP with PMMA reduces scattering losses and increases the photon density in the films, which is the main effect leading to an enhanced ASE. Thus, surface passivation of perovskite films to improve light amplification should be investigated and optimised with a focus on the optical passivation effect rather than solely on the trap passivation and defect density. The following section presents strategies to improve ASE in perovskite films based on adding different materials to the bulk of the layer.

## 7.2 Amplified spontaneous emission in quasi-2D and 3D CsPbBr<sub>3</sub> perovskites

This section investigates quasi-2D perovskites based on CsPbBr<sub>3</sub> and compares them to their 3D counterparts. Section 7.2.1 introduces the state of the art and motivates the choice of material in the work presented here. Section 7.2.2 presents the optimisation of processing parameters for quasi-2D films based on the ASE performance. Section 7.2.3 discusses the developed HTA process to produce high-quality 3D films from quasi-2D precursors. Finally, Section 7.2.4 discusses the differences between excitonic and free-carrier recombination in quasi-2D and 3D perovskites, respectively, and how these affect the ASE thresholds.

### 7.2.1 Introduction

This section investigates the optical performance of quasi-2D perovskites using the perovskite material CsPbBr<sub>3</sub>. This material has demonstrated superior performance in perovskite LEDs,<sup>[118, 119]</sup> and as an active medium for light amplification (ASE, lasing),<sup>[115, 120]</sup> culminating in the first demonstration of room-temperature CW lasing in quasi-2D perovskite films.<sup>[5]</sup> There are two additional reasons for using a single cation (Cs) rather than the triple-cation (CsMAFA) perovskite investigated in previous chapters. Firstly, quasi-2D structures fabricated with a single-cation perovskite should produce a more homogeneous composition across the MQW film than quasi-2D structures with multiple-cation perovskites. The morphological and energetic structure of (quasi-)2D perovskites is detailed in Section 4.1. Secondly, aside from the triple-cation perovskite, CsPbBr<sub>3</sub> is the most attractive perovskite composition for laser applications due to i) its emission in the green spectral range, ii) its fully inorganic composition, and iii) its narrow PL spectrum.<sup>[121]</sup> Aside from CsPbBr<sub>3</sub>, quasi-2D perovskites based on other perovskite compositions, such as MA or FA-based single-cation perovskites with different spacers, were investigated and demonstrated decent performance in terms of ASE, as well as in devices such as LEDs and lasers.<sup>[122–127]</sup> Their narrower emission linewidth and quantum confinement suggest that quasi-2D perovskites can promote a higher radiative recombination rate and, consequently, a lower ASE threshold. In the following, the optical performance of quasi-2D films with different compositions and annealing temperatures is examined, aiming at optimising their ASE performance. This process leads to the development of a novel approach enabling the fabrication of high-quality 3D films from quasi-2D films through a HTA step. With these films, it is possible to directly compare the ASE performance between quasi-2D films and their corresponding 3D counterparts.

### 7.2.2 Optimisation of quasi-2D films

As introduced in the previous section, quasi-2D CsPbBr<sub>3</sub> films are investigated to achieve efficient ASE. The spacer BAbR forms the layered quasi-2D structure, and the polymer PEG is added to produce homogeneous pinhole-free films. This material combination was

reported to produce high-quality films resulting in high-performing perovskite LEDs.<sup>[128]</sup> Further, two fabrication routes are tested: CsPbBr<sub>3</sub> taken from a single precursor powder and the same composition achieved by mixing the two salts CsBr and PbBr<sub>2</sub>. Details on the fabrication process are included in Section 5.1. Table 7.2 presents a summary of the investigated films fabricated with different annealing temperatures and additives to optimise the material in terms of ASE performance. The optical characterisation in this section was performed with the ICCD setup, presented in Section 5.4.1.

The ASE performance of the different samples is depicted in Figure 7.7 as a function of annealing temperature  $T_{\text{anneal}}$ , from 70 °C to 170 °C. Figure 7.7a displays the threshold as boxplots for each  $T_{\text{anneal}}$ . The statistics include data from two identical samples of each powder mixture and three measurements of different spots on each sample. For samples annealed at 70 °C, measuring an ASE threshold curve was only possible on one spot since the excitation fluence was limited to approximately 800  $\mu\text{J}/\text{cm}^2$ . Overall, the ASE thresholds decrease from around 730  $\mu\text{J}/\text{cm}^2$  at 70 °C down to approximately 77  $\mu\text{J}/\text{cm}^2$  at 150 °C and 94  $\mu\text{J}/\text{cm}^2$  at 170 °C. These values correspond to the median of the combined results from samples fabricated with one and two powders. The difference in threshold between the two highest  $T_{\text{anneal}}$  is not significant as it lies within the standard variation, so the thresholds are considered to be approximately the same for  $T \geq 150$  °C. The results in Figure 7.7a exhibit no significant difference between the samples fabricated with the one-powder (light colours) or two-powder (intense colours) mixtures, so the more uncomplicated one-powder mixture is employed for further analysis. The corresponding median values and standard deviations are presented in Table 7.3.

Figure 7.7b displays example threshold curves for each  $T_{\text{anneal}}$ . The data reveals that with increasing  $T_{\text{anneal}}$ , the threshold decreases and the slope efficiency increases, indicating an overall improvement in ASE performance. The observed enhancement of threshold and slope efficiency is likely due to lower total losses, possibly originating from non-radiative recombination channels or optical losses. In conclusion, the results illustrated in Figure 7.7 indicate that the lowest ASE threshold of the BAbR:CsPbBr<sub>3</sub> samples is achieved with

Precursor	Additive	$T_{\text{anneal}}$ (°C)	ASE threshold ( $\mu\text{J}/\text{cm}^2$ )
CsPbBr <sub>3</sub> / CsBr+PbBr <sub>2</sub>	none	70	–
CsPbBr <sub>3</sub> / CsBr+PbBr <sub>2</sub>	PEG	70	$\geq 730$
CsPbBr <sub>3</sub> / CsBr+PbBr <sub>2</sub>	PEG	RT	–
CsPbBr <sub>3</sub> / CsBr+PbBr <sub>2</sub>	PEG	120	231.5
CsPbBr <sub>3</sub> / CsBr+PbBr <sub>2</sub>	PEG	150	76.7
CsPbBr <sub>3</sub> / CsBr+PbBr <sub>2</sub>	PEG	170	93.6

**Table 7.2:** Summary of tested material systems with respective fabrication details and ASE thresholds. All films have a BAbR/CsPbBr<sub>3</sub> molar ratio of 0.7/1 and a PEG/CsPbBr<sub>3</sub> weight ratio of 0.01/1. Three samples of each composition were measured on two spots, and the presented threshold is the mean of all results (CsPbBr<sub>3</sub> and CsBr+PbBr<sub>2</sub>). For samples with PEG additive and  $T_{\text{anneal}} = 70$  °C, only one sample provided a decent threshold curve to extract a threshold value.

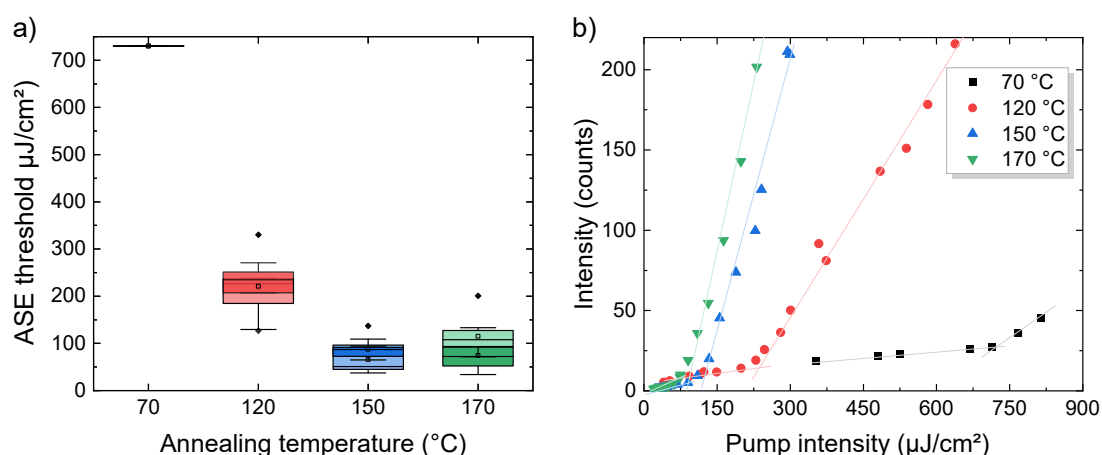


**Figure 7.7:** ASE performance of quasi-2D films as a function of annealing temperature. a) Boxplot of ASE thresholds measured on different samples and sample locations for  $\text{CsPbBr}_3$  fabricated by the one (light colours) and two (vivid colours) powder mixtures. b) Light-in-light-out curves with measured data (symbols) and linear fit above and below threshold (solid lines) exhibiting the characteristic kink at the threshold intensity.

$T_{\text{anneal}} \geq 150$   $^\circ\text{C}$ . Samples annealed at room temperature did not exhibit any ASE (up to the maximum available excitation density of approximately  $800$   $\mu\text{J}/\text{cm}^2$ ). Similarly, ASE was not observed in samples without the PEG additive. The optimal ASE thresholds reached with these samples of around  $80$   $\mu\text{J}/\text{cm}^2$  are comparable to the thresholds observed for the standard triple-cation perovskite.

$T_{\text{anneal}}$ ( $^\circ\text{C}$ )	Precursor	ASE threshold ( $\mu\text{J}/\text{cm}^2$ )
150	$\text{CsPbBr}_3$	$65.6 \pm 28.1$
150	$\text{CsBr}+\text{PbBr}_2$	$87.5 \pm 21.2$
170	$\text{CsPbBr}_3$	$115.1 \pm 37.7$
170	$\text{CsBr}+\text{PbBr}_2$	$74.3 \pm 31.0$

**Table 7.3:** Mean threshold values and standard deviation of samples fabricated with one and two-powder precursors of  $\text{CsPbBr}_3$ , corresponding to the data illustrated in Figure 7.7 and demonstrating the range overlap between ASE values.

### 7.2.3 Formation of 3D films by high-temperature annealing

Further spectroscopic investigations are performed to understand the origin of the ASE threshold behaviour as a function of  $T_{\text{anneal}}$ . In effect, the emission and absorption spectra are examined for the samples analysed in Figure 7.7. Figure 7.8 displays these results, demonstrating the forming of 3D films by HTA of quasi-2D films. Figure 7.8a depicts the emission spectra as a function of  $T_{\text{anneal}}$ , acquired under high excitation densities, above the ASE threshold of each film. ASE peaks and PL spectra exhibit a clear red shift with increasing  $T_{\text{anneal}}$ . Moreover, the relative ASE magnitude relative to the background PL increases with rising  $T_{\text{anneal}}$ . In particular, the ASE peak wavelength  $\lambda$  shifts from

$\lambda = 522$  nm at  $T_{\text{anneal}} = 70$  °C to  $\lambda = 528$  nm at  $T_{\text{anneal}} = 120$  °C, and it reaches a maximum of  $\lambda = 539$  nm for  $T_{\text{anneal}} \geq 150$  °C. Notably, the redshift follows the threshold trend, and an increase in  $\lambda$  corresponds to a lowering of the ASE threshold. For the two highest annealing temperatures  $T_{\text{anneal}} = 150$ °C and  $T_{\text{anneal}} = 170$ °C, no significant threshold change or redshift is observed. In quasi-2D films, a red shift of the emission spectrum typically indicates an increase in quantum well thickness (Section 4.1).

To further investigate the quasi-2D structure and bandgap of the films, absorption curves of each sample were measured, and the results are presented in Figure 7.8b. The film annealed at 70 °C has three peaks, at 402 nm, 434 nm, and 462 nm, corresponding to the exciton absorption of the mixed-phase film corresponding to the phases  $n = 1$ ,  $n = 2$ , and  $n = 3$ , respectively.<sup>[36, 128]</sup> These multiple peaks confirm the heterogeneous nature of the quasi-2D films with various phases and a predominant  $n = 2$  phase, whose peak exhibits the highest absorptance. The intensity of the excitonic peaks decreases with increasing  $T_{\text{anneal}}$  until they are no longer discernible for  $T_{\text{anneal}} \geq 150$ °C. Concurrently with the extinction of these absorption peaks, the absorption edge experiences a redshift, which coincides with the shift in PL emission. In these quasi-2D films, the emission primarily originates from the highest phase quantum well due to the fast energy cascade from high to low-energy wells.<sup>[128]</sup> The progressive vanishing of excitonic peaks and bandgap shift indicates an increase in quantum well thickness. A similar behaviour was observed for the same material system for samples with decreasing spacer content.<sup>[128]</sup> In fact, the PL and absorption spectra of samples annealed at  $T \geq 150$ °C correspond to the spectra of pure 3D CsPbBr<sub>3</sub> films.<sup>[36, 128]</sup> Hence, the high-temperature annealing (HTA) process of quasi-2D BABr:CsPbBr<sub>3</sub> films at  $T_{\text{anneal}} \geq 150$  °C results in pure 3D perovskites with the lowest ASE threshold. Based on these experiments, it could not be excluded that 3D films contain rest amounts of BABr. Nevertheless, any potential residual BABr does not affect the optical characteristics of the 3D films by HTA.<sup>[36]</sup> This finding represents a significant achievement in the fabrication of high-quality 3D CsPbBr<sub>3</sub> films, known for their inherent processing difficulties.<sup>[120, 129, 130]</sup> Moreover, these 3D films display better performance than directly fabricated 3D films, which did not exhibit ASE.<sup>[36]</sup>

#### 7.2.4 Excitonic versus free-carrier recombination

The previous results reveal that 3D films possess lower ASE thresholds than their quasi-2D counterparts. This section explains this initially counter-intuitive behaviour based on further optical characterisation. The main difference between quasi-2D and 3D films is the nature of their excited-state species. In quasi-2D perovskites, excitons are the predominant carrier type, whereas, for 3D films, free carriers dominate the recombination process. Radiative emission from excitonic recombination stems from a mono-molecular process exhibiting a high efficiency at low carrier densities. For this case, the emission is given by  $PL(t) \propto k_x \cdot n_x(t)$ , where  $k_x$  is the exciton recombination rate, and  $n_x$  is the exciton density. As the carrier density increases, second-order non-radiative exciton-exciton annihilation (EEA) dominates the dynamics, and the radiative efficiency decreases. In contrast, the PL originating from free charge carriers is a second-order process following the relation  $PL(t) \propto k_{bi} \cdot n^2(t)$ . This process is inefficient at low excitation densities but

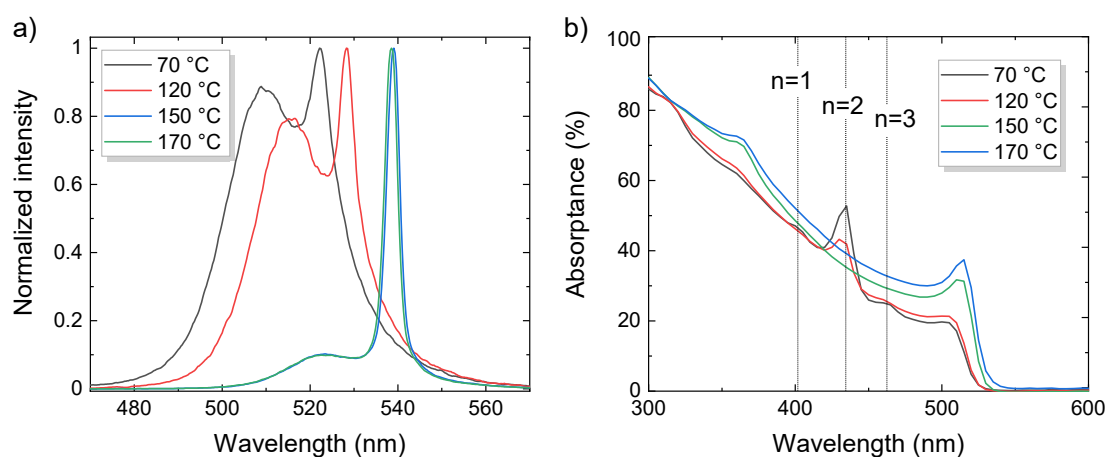


**Figure 7.8:** Band-gap red shift indicating the transition from quasi-2D to 3D CsPbBr<sub>3</sub> with increasing annealing temperature. a) ASE emission spectra as a function of temperature at an excitation of 205  $\mu\text{J}/\text{cm}^2$  for  $T_{\text{anneal}} \geq 120^\circ\text{C}$  and 710  $\mu\text{J}/\text{cm}^2$  for  $T_{\text{anneal}} = 70^\circ\text{C}$ . b) Absorbance spectra of all films with vertical dashed lines marking the exciton absorbance peaks at 402 nm, 434 nm, and 462 nm, corresponding to the phases  $n = 1$ ,  $n = 2$ , and  $n = 3$ , respectively.

governs the dynamics at higher carrier densities. Figure 7.9 illustrates these differences based on the emission analysis of the previously discussed quasi-2D and 3D films fabricated at different  $T_{\text{anneal}}$ . Figure 7.9a displays the PL emission at low excitation densities (below threshold) for quasi-2D films and their 3D counterparts. Quasi-2D films demonstrate an intensity approximately twice as high as their HTA counterparts. The stronger PL signal directly correlates with a higher radiative efficiency since all films possess similar extraction efficiency.<sup>[36, 48]</sup> Hence, quasi-2D films perform better in terms of radiative efficiency at low excitation densities than their 3D counterparts.

Figure 7.9b depicts the relative PLQY (rPLQY) of each sample at excitation densities below the respective ASE threshold. These observations support the previous findings regarding PL emission intensity and support the conclusions that the dynamics is governed by excitons in quasi-2D films and free carriers in their HTA 3D counterparts. The rPLQY presented in Figure 7.9b is calculated by taking the ratio of the emitted PL ( $\propto$  number of photons emitted) to the excitation power ( $\propto$  number of photons absorbed). At the lowest pump density of  $\approx 20 \mu\text{J}/\text{cm}^2$ , quasi-2D samples, dominated by excitonic recombination, exhibit an rPLQY more than three times higher than 3D films. As the excitation fluence increases, the rPLQY curves for quasi-2D and 3D films demonstrate opposite behaviours: rPLQY decreases with increasing excitation density for quasi-2D films, while for 3D samples, rPLQY increases with excitation density. The decrease in rPLQY for quasi-2D perovskites reflects the increase in EEA losses for excitonic recombination. In contrast, the increase in rPLQY for 3D films indicates the increasing contribution of the radiative bimolecular process over mono-molecular non-radiative losses. In conclusion, films with radiative emission governed by exciton dynamics that exhibit high rPLQY at low intensity do not necessarily correspond to suitable gain materials for lasing applications. Similar results where higher  $n$ -phase quasi-2D (and ultimately 3D) perovskites display lower ASE thresholds were reported.<sup>[125, 131]</sup> Yet, lower dimensional perovskites have also been

demonstrated to possess higher gain and lower ASE thresholds and ultimately sustain CW lasing.<sup>[5, 124]</sup> Consequently, material optimisation strategies of perovskites for lasing applications should consider the contribution of excitons and free carriers to the stimulated emission process and the optimal quantum-well thickness and phase ratios in a quasi-2D perovskite film.<sup>[36]</sup>

In summary, the potential of quasi-2D BAbBr:CsPbBr<sub>3</sub> perovskites as laser gain media was explored in this chapter. HTA of quasi-2D films leads to the formation of high-quality 3D films exhibiting better ASE performance than their 2D counterparts and than directly fabricated 3D films. These CsPbBr<sub>3</sub> 3D samples displayed comparable ASE thresholds to those of the 3D triple-cation perovskites. Thus, the subsequent section investigates the standard triple-cation perovskite with a potassium additive to enhance its radiative efficiency and ASE performance.

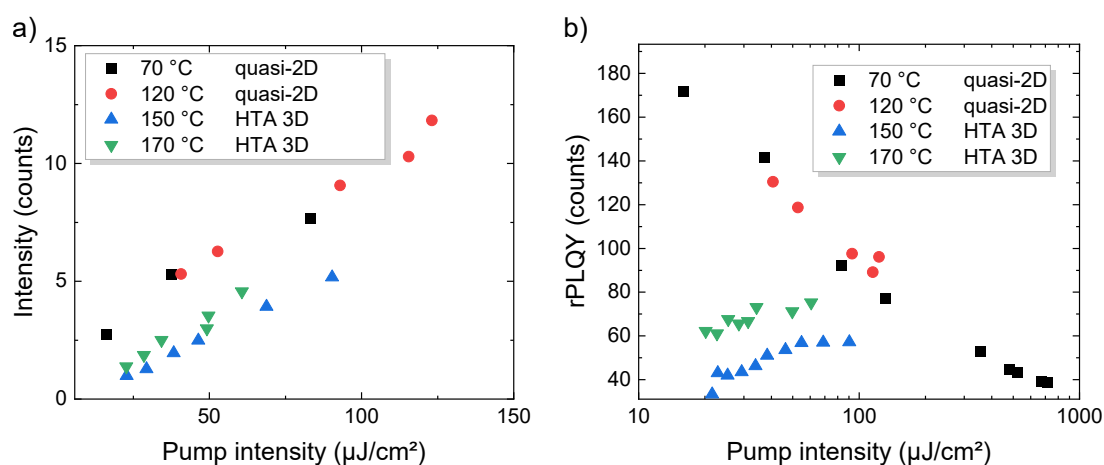


**Figure 7.9:** Emission characteristics of quasi-2D and 3D perovskites, indicating typical excitonic and free-carrier recombination behaviour, respectively. a) Light-in-light-out curves for the PL emission of quasi-2D and 3D perovskites at excitation densities below ASE threshold. The emission intensity of quasi-2D films is approximately twice as high as HTA 3D films. b) Relative PLQY (rPLQY) as a function of pump intensity. Quasi-2D films exhibit a decreasing rPLQY with excitation fluence due to increased non-radiative EEA losses. In contrast, rPLQY increases with fluence for HTA 3D films caused by increased radiative bimolecular recombination.

## 7.3 Triple-cation perovskites with potassium additive

This section reports a study on incorporating a potassium additive in triple-cation perovskite films as a bulk passivation agent. First, Section 7.3.1 presents the state-of-the-art potassium doping for perovskite materials and its relevance for lasing applications. Finally, Section 7.3.2 presents the influence of potassium doping on the light amplification, i.e., ASE, in triple-cation films.

### 7.3.1 Introduction

Potassium was used as a passivation agent for different perovskite compositions, leading to improved device efficiency in solar cells<sup>[132–137]</sup> and LEDs,<sup>[138–140]</sup> and overall enhanced optoelectronic properties in thin-films.<sup>[141, 142]</sup> The main outcomes of incorporating potassium in perovskites are the suppression of ion migration and increased radiative efficiency. Additionally, potassium doping was demonstrated to increase carrier mobility, reduce trap density and increase photo-stability of perovskite films. The exact physical mechanism of the effect of potassium doping on perovskites has been under debate.<sup>[132, 140]</sup> The addition of potassium in single and multi-cation perovskites was demonstrated to form mainly KBr-complexes at the grain boundaries and interfaces that act as passivation agents.<sup>[132, 136, 142]</sup> The reason for the forming of KBr-complexes is the stronger ionic bond between K and Br than between K and I. Hence, potassium binds preferably to bromide even when added as a KI-complex. This binding of K with Br was reported to result in an emission red-shift for potassium-passivated films due to the increase in I/Br ratio in the perovskite lattice.<sup>[26, 132, 135–137]</sup> Besides the formation of KBr-complexes, another study demonstrated that potassium doping resulted in a potassium-rich phase based on KI compounds ( $K_2PbI_4$ ) at grain boundaries, which can enhance the dielectric confinement within grains.<sup>[135]</sup> Other reports suggest that K is incorporated into the lattice as an interstitial,<sup>[140]</sup> or can enter A-site defects and prevent the rotation of large organic cations.<sup>[134]</sup> However, these interpretations have been intensely debated.<sup>[135, 142]</sup>

So far, neat potassium-doped 3D perovskite films have not been investigated in terms of ASE or lasing performance. Zhao *et al.* investigated K-doped MAPI films in a perovskite light-emitting diode (PeLED) configuration with a DFB grating, which exhibited optically-pumped lasing with a threshold reduction of  $\approx 20\%$  compared to undoped films.<sup>[143]</sup> For quasi-2D perovskites, potassium thiocyanate (KSCN) was used as an additive, resulting in almost 80% lower ASE thresholds. However, the enhancement was most likely due to the addition of  $SCN^-$  ions, which were demonstrated as an effective passivation for perovskites.<sup>[144, 145]</sup> This section investigates the potential of potassium-doped triple-cation perovskite films as an active medium for light amplification. The focus here lies on the overall ASE performance and not on the fundamental chemical effects of the potassium in the perovskite since this was previously reported in the literature.<sup>[136, 142]</sup> Here, thin films processed with different potassium concentrations are studied in terms of their ASE thresholds, PL characteristics and morphology to assess the relevance of potassium as an additive for lasing applications. Films with K concentration between 0% and 9% were fabricated following typical reported values for optimal concentrations.

### 7.3.2 Optical and morphological properties of K-doped films

The potassium-doped films investigated here are fabricated as follows: Like other reported procedures, the films are spin-coated from a precursor solution consisting of a mix of the standard triple-cation perovskite precursor and a potassium iodide (KI) solution.<sup>[133, 137, 142]</sup> The KI stock solution was prepared by mixing KI (potassium iodide, Sigma-Aldrich) in DMF/DMSO (3/1, volume ratio) to get a concentration of 0.8 M. The KI/perovskite precursors were prepared by mixing the KI and perovskite precursor solutions with the desired molar ratios of K/A-cation. Finally, each solution with different K concentrations was diluted with the same solvent (DMF/DMSO) to achieve a perovskite concentration of 0.8 M, corresponding to a thickness of approximately 230 nm (Chapter 5). The optical characterisation was performed with the ICCD setup, presented in Section 5.4.1.

Figure 7.10 illustrates the ASE characteristics of the six investigated film compositions, with a potassium concentration between 0 - 9 %. The ASE thresholds are depicted as boxplots in Figure 7.10a, including statistics of 4 measurements at different spots on each sample. The median of each sample is used to compare results. The ASE threshold decreases with increasing K concentration from 47.1  $\mu\text{J}/\text{cm}^2$  for 0 % K down to a minimum of 33.9  $\mu\text{J}/\text{cm}^2$  for 6 % K (Figure 7.10a). A further increase in potassium concentration increases the ASE threshold, reaching a maximum of 70  $\mu\text{J}/\text{cm}^2$  for 9 % K. Thus, doping triple-cation perovskite with potassium can effectively lower the ASE threshold for concentrations  $\leq 7.5$  % K, with an optimum threshold for 6 % K, leading to an approximately 30 % reduction in ASE threshold. The corresponding ASE spectra are illustrated in Figure 7.10b, and the peak positions are detailed in Table 7.4. The peaks exhibit a progressive red shift with increasing potassium content consistent with previous reports, explained by the selective reaction of K with Br, increasing the I/Br ratio.<sup>[132, 135–137, 142]</sup> An increase in I/Br ratio in perovskites gives rise to a red shift in the ASE peak as demonstrated by Brenner *et al.*<sup>[26]</sup> Table 7.4 shows the calculated I/Br ratio in the perovskite lattice as a function of potassium

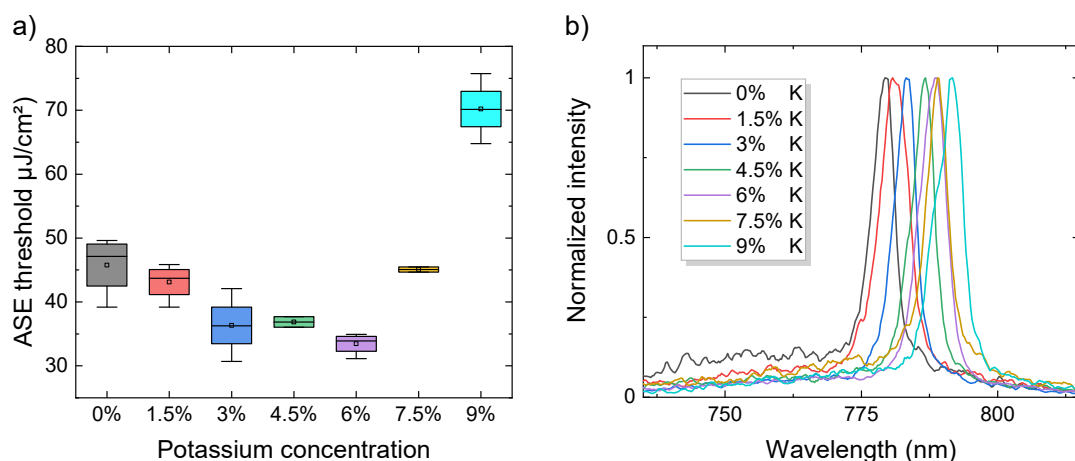


**Figure 7.10:** ASE performance of potassium-doped triple-cation films with a potassium concentration ranging from 0 - 9 %. a) Boxplots with ASE thresholds, including the statistics of 4 measurements per sample. b) Example ASE spectra from each perovskite composition at an excitation density of 94  $\mu\text{J}/\text{cm}^2$ .

K %	Br %	I %	$\lambda_{\text{ASE}}$
0	16	84	779.4
1.5	15	85	781.0
3	14	86	783.5
4.5	12	88	786.5
6	11	89	788.7
7.5	10	90	789
9	9	91	791.5

**Table 7.4:** Bromine (Br %) and iodine (I %) content as a function of potassium (K %) concentration and respective ASE resonance wavelength  $\lambda_{\text{ASE}}$ . Br and I concentrations are calculated based on the assumption that the added K from the KI precursor binds exclusively with Br from the perovskite crystal structure and that the remaining I (from the KI additive) is integrated into the lattice, replacing the Br ions.

concentration. This ratio is computed based on the assumption that the added potassium content binds entirely with bromine from the triple-cation crystal. The added iodine from the potassium additive then replaces the missing bromide in the perovskite lattice. The measured ASE peak wavelength  $\lambda_{\text{ASE}}$  from the data illustrated in Figure 7.10b is displayed in Table 7.4 along with the halide ratio. A red shift of around around 10 nm is observed for a 5 % increase in iodine content, i.e., from  $\lambda_{\text{ASE}} = 779.4$  nm at 84 % I, to  $\lambda_{\text{ASE}} = 788.7$  nm at 89 % I. This shift corresponds approximately to the shift observed by Brenner *et al.* by changing the I/Br ratio in triple-cation perovskites.<sup>[26]</sup> An increase of iodine content by 10 % caused a shift of around 20 nm (between 80 % - 100 % iodine, around the wavelength of  $\lambda_{\text{ASE}} = 790$  nm). These results imply that the added potassium binds with bromine, likely forming the previously reported KBr-complexes at grain boundaries, serving as passivation agents.<sup>[132, 136, 142]</sup>

The proposed grain boundary passivation effect is further investigated by analysing the TRPL of the fabricated films. Figure 7.11 presents transient PL results as a function of potassium concentration, in particular, the normalised TRPL decay curves (Figure 7.11a) and the initial PL emission (Figure 7.11b). The TRPL curves in Figure 7.11a were measured with an excitation density of  $n_0 \approx 3.7 \cdot 10^{17} \text{ cm}^{-3}$ . The initial decay up to around 200 ns is similar for all samples, whereas the tail decay, commonly associated with trap-assisted recombination processes, is noticeably slower for doped samples. This result matches previous observations and confirms the trap-passivation effect of potassium in these films. Figure 7.11b compares the initial PL emission ( $PL_0$ ) of each sample, which is proportional to the radiative recombination in the material  $PL_0 \propto k_{\text{bi}} \cdot n_0^2$ . Given the limited gate width of 3 ns for TRPL measurements with the ICCD setup (Section 5.4, this  $PL_0$  consideration is a rough approximation. The boxplots include statistics of three measurements per composition to account for spatial inhomogeneities and fluctuations of the pump laser. All samples possess approximately the same absorption and extraction efficiency (same thickness and roughness), so the emitted  $PL_0$  signal should depend only on intrinsic recombination factors. This approximate analysis demonstrates a higher radiative efficiency for potassium-doped samples, with an increase in  $PL_0$  with increasing potassium

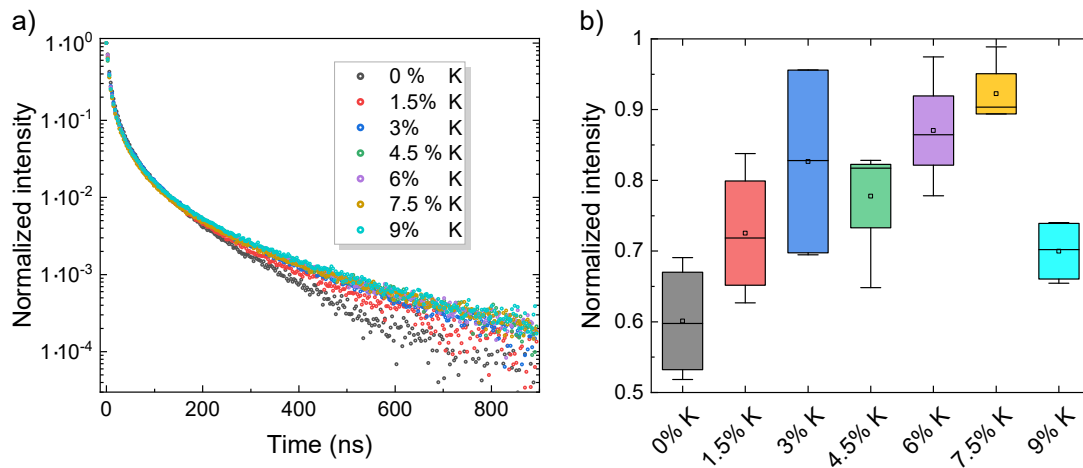


**Figure 7.11:** Potassium doping effect on TRPL lifetime and radiative emission. a) TRPL and b) initial PL ( $PL_0$ ) as a function of potassium content, at an excitation density of  $n_0 \approx 3.7 \cdot 10^{17} \text{ cm}^{-3}$ .

concentration up to 7.5 % K, followed by a decrease of  $PL_0$  for a concentration of 9 % K (Figure 7.11b). Notably, the  $PL_0$  behaviour is analogous to the ASE threshold trend as a function of potassium content, except for the outlier sample with 7.5 % K. The increase in radiative efficiency ( $PL_0$ ) implies an increase in either  $k_{\text{bi}}$  or  $n_0$ . A higher  $n_0$  may result from a reduced initial carrier loss due to trapping, caused by the defect passivation effect of KBr-complexes.<sup>[136, 142]</sup>

Finally, Figure 7.12 includes example AFM measurements for selected potassium contents, illustrating the films' morphology. The different samples have no apparent grain size or roughness trends. However, there is a clear qualitative difference between doped and undoped films: Films with potassium additive display rounder and more uniform grains, with fewer grain boundaries than the reference films. Thus, potassium appears to assist the crystallisation and the formation of uniform crystallites, consistent with the grain boundary passivation hypothesis. In conclusion, potassium doping can reduce the ASE threshold by 30 % at an optimum concentration of 6 % K. This enhancement is attributed to the grain-boundary passivation effect of the potassium additive, which likely reduces non-radiative recombination losses associated with trap states.

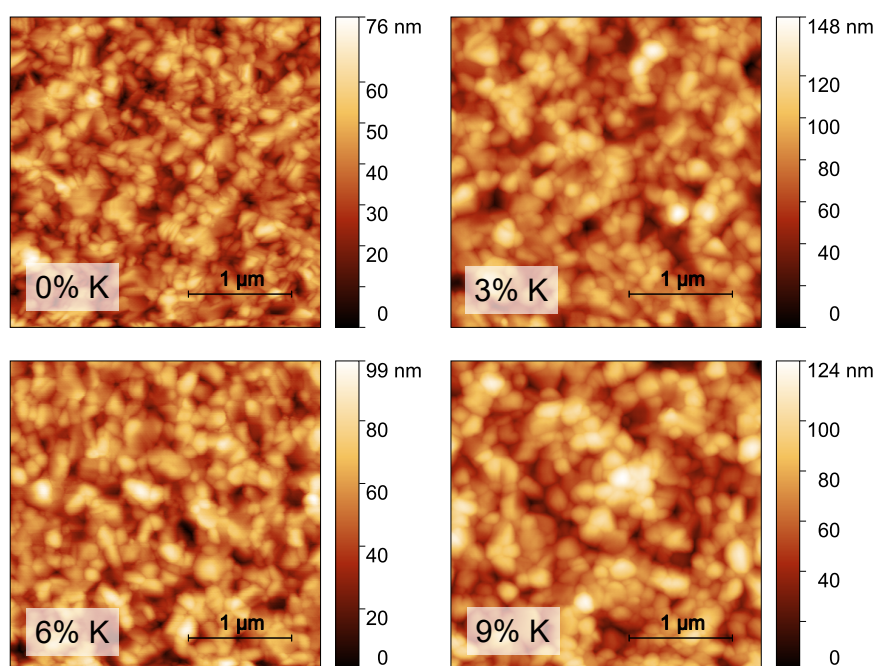


**Figure 7.12:** AFM images of films with different potassium concentrations – 0 %, 3 %, 6 %, 9 %, – as indicated. The sample’s topography reveals a distinct contrast between doped and pristine films in their grain structures: Doped films exhibit noticeably rounder grains with fewer boundaries, which can help reduce non-radiative losses.

## 7.4 Summary

This chapter proposes different optical and material approaches to improve perovskite performance for lasing applications. Thin films are analysed based on their ASE performance to assess their suitability as a laser-active medium. Additionally, their optical performance is investigated to gain insights into the underlying effects of each approach. The first method investigates the optical effect of surface defect passivation layers, specifically their role as waveguide passivation. Two coatings are tested: a thick PMMA cladding acting as a WP, and a TOPO treatment serving as defect passivation, followed by the previously referred PMMA layer (WP+DP). Although the defect density diminishes with increased passivation, the ASE performance does not follow the same trend. Instead, both strategies yield identical optical results, significantly reducing the ASE threshold by approximately 40 %, compared to pristine reference films. The primary mechanism responsible for these outcomes is the waveguide passivation effect of the cover layer. A decrease in refractive index contrast of the top perovskite layer by adding a cladding with  $n > 1$  leads to fewer scattering losses. Therefore, there is an enhanced photon density within the film, ultimately lowering the ASE onset threshold. Hence, this previously unexplored optical effect should be the primary focus of passivation strategies utilising surface cover layers. One promising approach for future investigations is to combine defect passivation and optical passivation, such as using a bulk additive to mitigate defects and a top cladding to minimise scattering losses.

Additionally, material strategies with bulk additives are investigated. Mixed-phase quasi-2D films are inspected regarding ASE performance, given their potential for enhanced radiative emission due to quantum confinement. A novel method involving a HTA step of quasi-2D films is developed to fabricate 3D films, representing a significant milestone in producing high-quality 3D CsPbBr<sub>3</sub> thin films, given the typical challenges associated with their fabrication.<sup>[120, 130]</sup> HTA 3D films exhibit ASE thresholds of 77  $\mu\text{J}/\text{cm}^2$ , approximately ten times lower than those of the initial quasi-2D films annealed at 70 °C with thresholds of around 730  $\mu\text{J}/\text{cm}^2$ . Quasi-2D perovskites exhibit a stronger PL emission at low fluences; nonetheless, at high excitation densities close to the ASE threshold, the radiative efficiency of quasi-2D perovskites is strongly reduced due to non-radiative EEA. In contrast, 3D films demonstrated a lower ASE threshold and higher ASE efficiency at high fluences (> 100  $\mu\text{J}/\text{cm}^2$ ), given their dominant bimolecular radiative recombination. These findings emphasise the importance of material optimisation for perovskite lasers, focusing on their performance at high excitation densities and on their ASE thresholds rather than the low-fluence PLQE typically prioritised for LED applications.<sup>[128]</sup>

Finally, bulk passivation with a potassium additive in triple-cation films is examined. Potassium doping benefits light amplification in perovskites as it improves their radiative emission and ASE performance. Adding 6 % K to triple-cation perovskite films reduces ASE thresholds by 30 %, reaching an optimum at 34  $\mu\text{J}/\text{cm}^2$ . Optical and morphological characterisations demonstrate that potassium-doped films possess a higher radiative emission, longer PL lifetime, and improved morphology. The latter is likely responsible for the lower non-radiative losses. This approach can be combined with optical surface passivation as discussed in Section 7.1 to improve ASE performance further. The following chapter implements and tests pristine triple-cation perovskite layers in different resonator geometries. The stimulated emission performance of these lasers can be further enhanced by combining them with the passivation strategies proposed in this chapter.



## 8 Triple-cation Perovskite Lasers

This chapter explores the application of triple-cation perovskites as laser active media in thin-film lasers with a main focus on DFB resonators. The primary goal is to develop novel techniques enabling the fabrication of low-cost perovskite lasers. Section 8.1 investigates a cost-efficient and versatile technique based on NIL using gelatin nano-grating stamps to produce high-quality perovskite DFB lasers. This study includes a discussion on the DFB grating parameters, the quality of the fabricated nano-structures, the lasing performance of the resulting devices, and finally, the repeatability of this approach. Section 8.2 presents initial demonstrations of two different perovskite lasers with fully-printed resonators: Section 8.2.1 introduces the first perovskite DFB laser with nano-printed SU-8 gratings. Finally, Section 8.2.2 discusses a perovskite micro-cavity with state-of-the-art, fully printed distributed Bragg reflector (DBR) mirrors.

### Acknowledgements and contributions

The present chapter mainly builds on the publication

- Allegro, I.; Bonal, V.; Mamleyev, E. R.; Villalvilla, J. M.; Quintana, J. A.; Jin, Q.; Díaz-García, M. A.; Lemmer, U. "Distributed Feedback Lasers by Thermal Nanoimprint of Perovskites Using Gelatin Gratings" 2023. ACS Applied Materials & Interfaces, 15 (6), 8436–8445 [146]

The author conceptualised the study, fabricated the devices, and performed the optical characterisation and analysis of results; V. Bonal contributed to the experiments; J.M. Villalvilla and J.A. Quintana developed the fabrication of the gelatin gratings; E.R. Mamleyev and Q. Jin performed the SEM and contact angle analysis, respectively. M.A. Díaz-García and U. Lemmer supervised the project.

The results presented in Section 8.2.1 were a collaboration with the start-up Hummink and are based on the proceedings

- Pascual, M; Bigan, N.; M'Barki, A.; Mental, R.; Allegro, I. and Lemmer, U. "All-printed SU8-perovskite DFB laser" 2023. Proc. SPIE 12433, Advanced Fabrication Technologies for Micro/Nano Optics and Photonics XVI, 124330E [147]

The author designed the grating parameters, fabricated the perovskite layer, and carried out the optical characterisation and analysis of results; M. Pascual and the Hummink team developed and performed the nano-printing of the SU-8 gratings. U. Lemmer supervised the project.

Section 8.2.2 presents the results of a collaboration with Qiaoshuang Zhang, who developed and processed the DBRs by inkjet printing. The author fabricated the micro-cavities (perovskite layer and imprint process) and performed the optical characterisation and analysis of results. U. Lemmer supervised the project.

## **8.1 Distributed feedback lasers by nanoimprint lithography with polymeric gratings**

This section presents the fabrication of DFB lasers based on triple-cation thin films with a nano-grating imprinted on the surface by NIL. Section 8.1.1 presents the state-of-the-art fabrication approaches for perovskite DFB lasers and the significance of the method developed in this study. The following sections discuss the realisation of these lasers in terms of the DFB design (Section 8.1.2), the gelatin grating fabrication (Section 8.1.3), the implementation and evaluation of the thermal nanoimprint lithography process (Section 8.1.4), and the optical performance (Section 8.1.5).

### **8.1.1 Introduction**

One of the key advantages of perovskites as laser gain media is their low-cost and versatile fabrication options.<sup>[148]</sup> Consequently, it is crucial to develop an equally flexible and cost-effective method to realise high-quality laser resonators. A straightforward choice for a cavity design is a DFB resonator. Reports on CW operation in lead halide perovskites have primarily used second-order DFB resonators.<sup>[5, 19, 28, 77, 149]</sup> These resonators possess the advantages of supporting single-mode lasing, emitted perpendicular to the waveguide plane, and providing low lasing thresholds and narrow linewidths. Furthermore, DFBs rely on a mirror-free cavity based on a diffraction grating, which is suitable for low-cost fabrication techniques and thin-film diode architectures.<sup>[12, 148, 150–152]</sup> Two main approaches are commonly considered to realise perovskite DFB lasers: i) processing a perovskite thin film on a pre-structured substrate, or ii) imprinting a pristine perovskite layer with a structured stamp, transferring the pattern to the film surface. In this study, the latter strategy is pursued to realise DFB lasers due to its multiple advantages: The perovskite crystal quality is improved through the re-crystallisation process during imprinting, resulting in a reduced defect density for surface and bulk defects and better stability against degradation.<sup>[67, 153, 154]</sup> An additional practical benefit of a surface grating is the access to the grating structure for characterisation purposes (e.g. with AFM). In addition, spin-coating a film on a structured substrate leads to more significant variations in thickness profile than a flat substrate, making it more challenging to predetermine the precise perovskite thickness. This poses a problem for the laser design since the film thickness significantly influences the effective refractive index of the propagating waveguide mode and, thus, the lasing wavelength. Moreover, when processing on a structured substrate, each grating yields one laser device. In contrast, employing the grating as a stamp enables fabricating multiple laser devices using only one reusable stamp.

Numerous techniques have been proposed for patterning DFB gratings for perovskite lasers. Typically, these methods involve an expensive electron beam lithography (EBL) step to write the nano-pattern and a final etching step of a (hard) material, which is usually carried out using reactive ion etching (RIE) or ion beam etching (IBE). To pattern stamps, the etching step is performed either directly on the stamp intended for imprint lithography,<sup>[12, 77, 120, 155]</sup> or on a master grating that can be used as a template for low-cost replication.<sup>[126, 151, 156–158]</sup> An alternative approach involves structuring the perovskite film instead of transferring a pattern via imprint lithography. This can involve etching the perovskite layer itself<sup>[159–161]</sup> or using a soft stamp for template-assisted crystallisation.<sup>[160, 162–164]</sup> However, these methods generally lead to lower film quality and pose additional fabrication challenges, such as controlling the crystallisation process and film thickness and maintaining a uniform contact between the template and the film during imprinting. The method proposed in this study combines the advantages of a cost-efficient fabrication process of nano-patterned stamps in gelatin films with the benefits of NIL for perovskite structuring. The outcome is the realisation of cost-efficient, high-quality perovskite DFBs.

### 8.1.2 Design of perovskite distributed feedback lasers

This section presents the necessary design considerations for the fabrication of perovskite second-order DFB lasers by thermal nanoimprinting. In particular, how the design parameters for the grating stamp are chosen (Section 8.1.2.1) and how the perovskite strong refractive index dispersion influences the laser output (Section 8.1.2.2).

#### 8.1.2.1 Design parameters

The main parameters for lasing action in a DFB are the resonance condition defining the emission wavelength and the cavity gain and loss mechanisms determining the lasing threshold (Section 3.4).<sup>[15, 165, 166]</sup> One essential aspect to consider when designing a DFB laser is that most resonator parameters influence more than one property of the laser, making its design complex. In particular, for perovskite semiconductors, it is essential to carefully consider their high refractive index and index dispersion around the PL

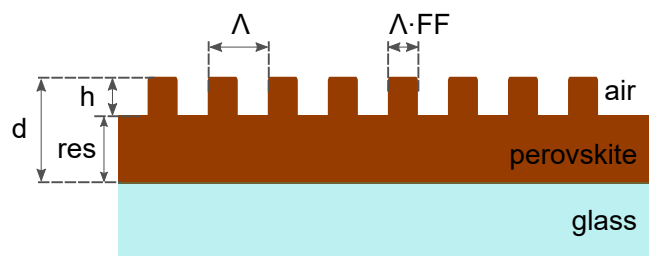


**Figure 8.1:** Schematic cross-sectional view of DFB laser encompassing a perovskite layer (brown) spin-coated on a glass substrate (light blue layer) with a grating structure imprinted onto the perovskite film. Resonator parameters include film thickness  $d$ , grating height  $h$ , residual waveguide  $res$ , grating period  $\Lambda$  and fill factor  $FF$ , calculated as indicated in the illustration.

spectral region, leading to a strong interdependence of wavelength and refractive index  $n$  (Section 8.1.2.2).<sup>[167]</sup> Consequently, a slight shift in emission wavelength can significantly change  $n$  and vice-versa. The tangled connection between these parameters poses a challenge when designing perovskite DFB lasers. Hence, it is vital to investigate the resonator parameters of such lasers and how they affect the cavity and laser performance. The design parameters discussed here are based on the geometry used in the following sections, illustrated in Figure 8.1: A surface engraved perovskite film on a glass substrate and in contact with air on the top. The parameters of interest are the grating height  $h$ , film thickness  $d$ , fill factor  $FF$ , and period  $\Lambda$ . The choice of each for the fabrication of the grating stamp is discussed in the following.

The stamp height determines  $h$ , which should be smaller than  $d$  to achieve a geometry with  $h = d - res$ , where  $res$  is the height of the bottom residual waveguide (Figure 8.1). The parameter  $h$  mainly determines the coupling coefficient of the resonator and also influences the effective refractive index  $n_{eff}$ . The feedback coupling coefficient  $\kappa$  can be calculated using known equations;<sup>[156, 168, 169]</sup> however, an analysis of the complete coupling coefficient  $\kappa_t$ , including radiation coupling, needs more elaborate calculations that lie outside the scope of this work.<sup>[16, 17]</sup> Thus, the most straightforward approach is to use an initial  $h$  based on reported values for similar perovskite DFB geometries exhibiting state-of-the-art performance. These range from 60 nm to 140 nm, so the average of  $h = 100$  nm was chosen for the current study.<sup>[5, 67, 157, 158]</sup>

The parameter  $d$  is defined as the total thickness of the pristine spin-coated film, which is given by  $d = h + res$  and is determined by the molarity of the perovskite solution. The film thickness as a function of precursor concentration is displayed in Figure 5.7 in Section 5.5.3. Various parameters of the DFB laser are affected by  $d$ , such as the gain and  $n_{eff}$ , since  $d$  determines the waveguide mode (Section 3.3). To calculate  $n_{eff}$  and the waveguide modes of a perovskite waveguide, an equivalent three-layer stack was simulated with a 1-D mode solver for dielectric multilayer slab waveguides (Figure 8.3).<sup>[117]</sup> The standard

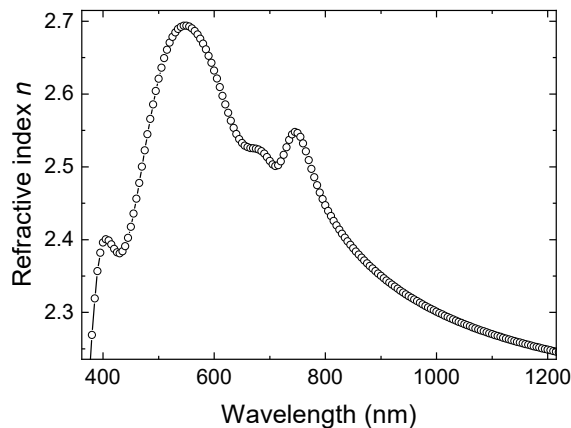


**Figure 8.2:** Refractive index as a function of wavelength for standard triple-cation perovskite thin films measured by ellipsometry. A strong negative dispersion is observed for wavelengths around the PL spectral range.

triple-cation perovskite exhibits a PL emission between 700 - 800 nm, so  $n_{\text{perovskite}} = 2.55$  (at 750 nm) was considered as a first approximation (Figure 8.2). The values for the top and bottom layers are  $n_{\text{air}} = 1$  and  $n_{\text{glass}} = 1.51$ , and both layer thicknesses were set to infinity for the simulation. Figure 8.3a presents  $n_{\text{eff}}$  of the supported modes in such a waveguide as a function of thickness, and Figure 8.3b an exemplary mode profile of the  $TE_0$  mode for a perovskite thickness of  $d = 130$  nm. The maximum  $d$  enabling a single-mode waveguide, supporting only the fundamental TE and TM modes, was chosen, resulting in  $d = 230$  nm, and  $res = 130$  nm.

Taking the selected parameters,  $\kappa$  was calculated as a function of  $FF$ , and the result is depicted in Figure 8.4. The results exhibit a maximum of  $|\kappa|_{\text{max}} \approx 2500 \text{ cm}^{-1}$ , matching previously reported values for a similar perovskite DFB laser with  $|\kappa|_{\text{max}} \approx 3000 \text{ cm}^{-1}$ .<sup>[156]</sup> Like  $h$ , the  $FF$  also influences the resonator coupling, the mode profile, and  $n_{\text{eff}}$ . An  $FF$  of approximately 0.75 (25 % air gap) is chosen for the grating stamp to provide strong feedback (Figure 8.4), corresponding to an imprinted perovskite grating with  $FF = 0.25$  (25 % perovskite). Finally, the grating period  $\Lambda$  is the main parameter determining the laser resonance. Given the high  $n$  and index contrast to air of perovskites ( $\Delta n \approx 1.5$ ), this DFB geometry is approximated as a purely index-coupled grating, and the following resonance condition is used:<sup>[15]</sup>

$$\lambda_{\text{lasing}} \approx \Lambda \cdot n_{\text{eff}}(\lambda). \quad (8.1)$$

Calculating  $n_{\text{eff}}$  is not straightforward and was approximated by the equivalent three-layer stack considered previously. The equivalent perovskite layer thickness  $d_{\text{eq}}$  was estimated by adding the bottom waveguide thickness  $res$  and the perovskite portion of the grating, resulting in  $d_{\text{eq}} = res + FF \cdot h$ . This calculation results in a 155 nm perovskite layer and an  $n_{\text{eff}} \approx 2.15$  for the  $TE_0$  mode (Figure 8.3b). Consequently,  $\Lambda \approx 349$  nm was chosen for the DFB design aiming at a resonance around  $\lambda = 750$  nm (Equation 8.1). It is crucial to recall that this  $n_{\text{eff}}$  calculation is an approximation and is affected by changes in  $FF$ ,  $d$ ,

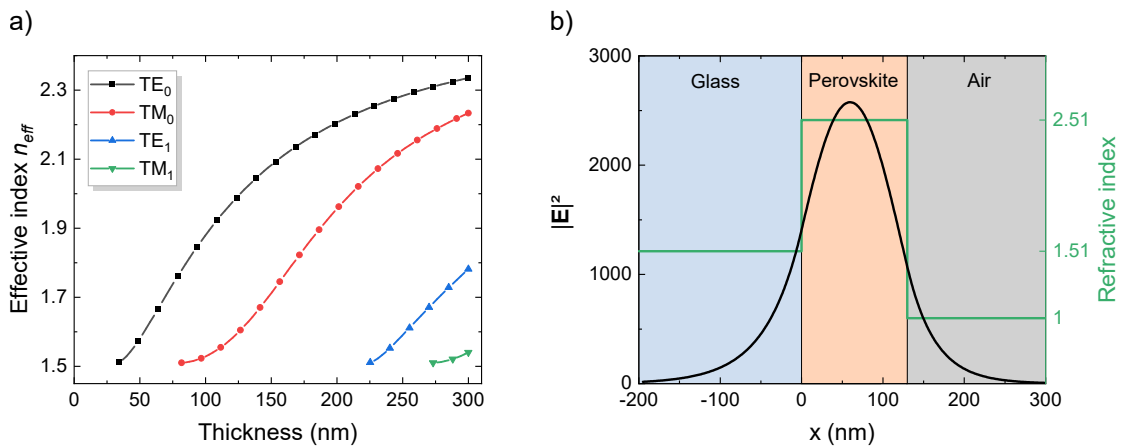


**Figure 8.3:** Waveguide modes of an equivalent three-layer slab waveguide configuration glass/perovskite/air. a)  $n_{\text{eff}}$  as a function of perovskite thickness for different waveguide modes ( $TE_0$ ,  $TE_1$ ,  $TM_0$ ,  $TM_1$ ). b) Profile of the electric field intensity ( $|E|^2$ ) of the fundamental  $TE_0$  mode for a perovskite thickness of 130 nm, at the wavelength of 770 nm.

$d$	$h$	$FF$	$\Lambda$
230 nm	100 nm	0.25	349 nm

**Table 8.1:** Design parameters for perovskite layer and grating stamp used for fabricating second-order DFB lasers by NIL, where  $d$  is the perovskite film thickness,  $h$  the grating height,  $FF$  the grating fill factor and  $\Lambda$  the grating period. A sketch of the geometry with the visual representation of these parameters is illustrated in Figure 8.1.

and  $h$ , which can vary slightly due to experimental deviations. The final parameters are summarised in Table 8.1, and these values are used in the following sections to fabricate imprinted perovskite DFB lasers. The following section discusses the implications of perovskites' high  $n$  and index dispersion on DFB lasers.

### 8.1.2.2 Implications of refractive index dispersion on laser resonance

As discussed in the previous section, the resonance of a DFB laser is determined by  $\Lambda$  and  $n_{\text{eff}}$  following Equation 8.1. Typically, for organic semiconductor lasers,  $n_{\text{eff}}$  is taken as a constant for a specific geometry, and the lasing wavelength can be easily tuned by changing the  $\Lambda$ .<sup>[170, 171]</sup> For the case of perovskites, however, it is vital to consider their substantial dispersion of  $n$ , and thus,  $n_{\text{eff}}$ . The refractive index dispersion of perovskites is particularly strong around the spectral range of the PL and laser emission.<sup>[172–174]</sup> Figure 8.5 illustrates the effect of the strong refractive index dispersion of perovskites on  $n_{\text{eff}}$  and on the grating period calculation. The long wavelength side of the PL spectrum, where ASE is typically observed, corresponds to the region between  $\approx 740 - 800$  nm. As mentioned previously,  $n$ , and thus  $n_{\text{eff}}$ , experiences a negative dispersion within this range, i.e.,  $dn/d\lambda < 0$  so that  $n_{\text{eff}}$  decreases with increasing wavelength. In particular, the standard triple-cation

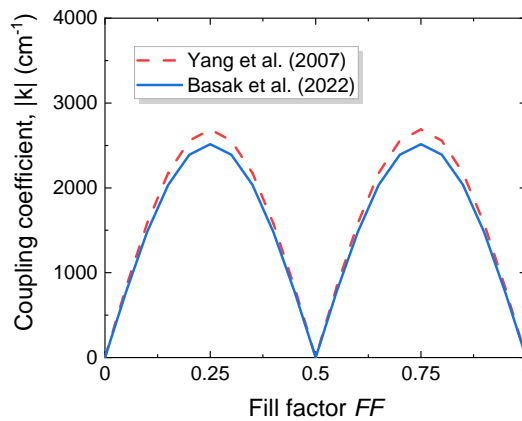


**Figure 8.4:** Absolute value of the feedback coupling coefficient  $\kappa$  as a function of fill factor for a second-order perovskite DFB resonator with  $d = 230$  nm and  $h = 100$  nm, computed for a rectangular grating based on the derivations by Yang *et al.*<sup>[169]</sup> (dashed red line) and Basak *et al.*<sup>[156]</sup> (blue solid line). The feedback reaches a maximum at  $FF = 0.25(0.75)$  and a minimum at  $FF = 0.5$ .

perovskite exhibits a shift in  $n$  of  $\Delta n \approx 0.1$ , corresponding to a significant change in  $n_{\text{eff}}$  of  $\Delta n_{\text{eff}} \approx 0.13$ . This result is illustrated in Figure 8.5a. Besides the refractive index dispersion, fabrication irregularities in, e.g.,  $d$ ,  $FF$  or roughness, can lead to considerable shifts in  $n_{\text{eff}}$ . For instance, a difference of 15 nm in  $d$ , which is within the deviation observed for these samples, results in a change of the  $n_{\text{eff}}$  of  $\Delta n_{\text{eff}} > 0.05$ . These changes directly affect the lasing wavelength (Equation 8.1), making it difficult to precisely calculate the resulting  $\lambda_{\text{lasing}}$ . In the worst-case scenario,  $\lambda_{\text{lasing}}$  moves beyond the gain spectral region, resulting in the absence of lasing. This challenge is graphically represented in Figure 8.5b, displaying  $\Lambda$  as a function of lasing wavelength for three different cases: i) for the case where dispersion is neglected and  $n_{\text{eff}}$  is constant; ii) when dispersion is considered, and  $n_{\text{eff}}$  is a function of the wavelength, i.e.,  $n_{\text{eff}}(\lambda)$ , and iii) in case the final  $d$  is higher than estimated due to fabrication variations, taking into account the dispersive  $n_{\text{eff}}(\lambda)$ . The latter considers a 15 nm thicker film corresponding to the maximum measured deviation. The  $n_{\text{eff}}$  employed to calculate  $\Lambda$  as a function of emission wavelength is determined by the equivalent slab waveguide simulation. In the equivalent waveguide structure used to calculate  $n_{\text{eff}}$ , a change in  $h$  was included as a change in total film thickness. The value for the constant  $n_{\text{eff}}$  (no dispersion) is taken for the resonance at 770 nm. Consequently, the period at this wavelength is identical for the case with and without dispersion. A thickness fluctuation of  $\Delta d = 15$  nm results in a significant period and wavelength shift. A vertical comparison of  $\Lambda$  values of the data for  $n_{\text{eff}}$  (black down-pointing triangles) and  $n_{\text{eff}}$ ,  $\Delta d = 15$  nm (blue up-pointing triangles) reveals a difference of approximately 10 nm in the

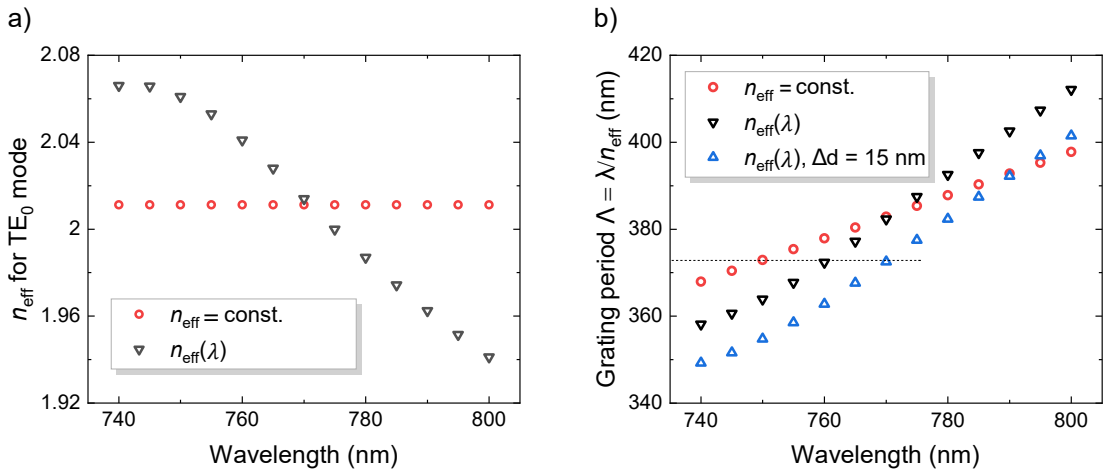


**Figure 8.5:** Effect of refractive index dispersion on the  $\text{TE}_0$  effective index  $n_{\text{eff}}$  and on the grating period  $\Lambda$ . The calculation of  $n_{\text{eff}}$  is performed with the mode solver for dielectric waveguides<sup>[117]</sup> for the architecture glass/perovskite/air, with  $d = 130$  nm. a)  $n_{\text{eff}}$  of the  $\text{TE}_0$  mode as a function of wavelength for the case where  $n$  is approximated as a constant (red circles) and where its dispersion is taken into account (black down-pointing triangles). b) Grating period  $\Lambda$ , given by  $\Lambda = \lambda/n_{\text{eff}}$ , as a function of laser resonance wavelength for three different cases: Taking the values from a) for a constant  $n$  (red circles), taking the values from a) for  $n(\lambda)$  (black triangles), and for a 15 nm thicker film, which corresponds to the maximum difference in thickness measured for reference films (blue up-pointing triangles). The black dashed horizontal line visualises that for a fixed grating period, the resonance wavelength strongly depends on the  $n_{\text{eff}}$  assumptions and  $d$  value.

grating period. This means that in a 15 nm thicker film, a period decrease of  $\approx 10$  nm is necessary to keep the same lasing wavelength. A horizontal comparison demonstrates that for a fixed grating period, the resonance wavelength of a thicker film exhibits a redshift, whose magnitude increases with increasing wavelength, from  $\Delta\lambda \approx 9$  nm at 740 nm, to  $\Delta\lambda \approx 10.6$  nm at 800 nm. Taking the period  $\Lambda = 372$  nm as an example (horizontal dashed line) facilitates a comparison of the three cases considered: If  $n_{\text{eff}}$  is taken as a constant, a DFB with period  $\Lambda = 372$  nm results in a lasing resonance at 750 nm (circles). The resonance shifts to 760 nm when considering dispersion (down-pointing triangles) and to 770 nm if the film thickness increases (up-pointing triangles). The practical implications of these shifts are discussed based on experimental results at the end of Section 8.1.5.

To conclude, the main design parameters of a perovskite DFB laser are  $\Lambda$ ,  $h$ ,  $FF$ , and  $d$ . Most parameters are intertwined and affect multiple laser properties, such as feedback and resonance wavelength. Moreover, it is crucial to consider perovskites refractive index dispersion to predict accurate resonance values. Given the high  $n$  of perovskites, small changes in any design parameter can result in substantial resonance shifts and changes in coupling coefficient due to shifts in  $n_{\text{eff}}$ . Consequently, it can be challenging to achieve lasing in some devices if, for instance, the estimated  $n_{\text{eff}}$  is far from the actual experimental value and the period is no longer appropriate for the intended emission wavelength. Refractive index measurements of perovskites are not straightforward and can yield imprecise results, contributing to inaccurate  $n_{\text{eff}}$  estimations.<sup>[173]</sup> Optimising design parameters without a detailed, quantitative analysis of the DFB coupling coefficient and  $n_{\text{eff}}$  is challenging. Therefore, fine-tuning these parameters based on experimental results is the best approach to improve DFB performance.

### 8.1.3 Dichromated gelatin gratings

Considering the design guidelines discussed in the previous section, the main parameters when fabricating the dichromated gelatin (DCG) gratings to serve as templates for DFB resonators are the grating period  $\Lambda$ , height  $h$ , and fill factor  $FF$ . These values and the perovskite film thickness  $d$  are determined in the previous section and summarised in Table 8.1. Regarding period, various gratings were fabricated with different periods (from 344 nm to 354 nm) to test the laser tunability. Preliminary experiments showed that only lasers fabricated with longer periods exhibited a clear lasing peak on the blue side of the PL spectrum, likely due to an inaccurate initial approximation of  $n_{\text{eff}}$ . Hence, the perovskite composition was fine-tuned to adjust the PL and ASE spectra to the available periods to utilise the already prepared stamps. The final composition was  $\text{Cs}_{0.1}(\text{MA}_{0.17}\text{FA}_{0.83})_{0.9}\text{Pb}_{0.84}(\text{I}_{0.8}\text{Br}_{0.20})_{2.68}$  with a slightly higher Br/I ratio than the standard triple-cation. This resulted in a centre PL wavelength of approximately 760 nm.

The DCG gratings were fabricated by holographic lithography (HL) using the Lloyd configuration with an average exposure of  $45 \text{ mJ/cm}^2$  from a CW argon ion laser with an emission wavelength of 364 nm (Figure 8.6a). The angle  $\delta$  between the substrate (mirror) and laser beam determines the line period on the sample (Figure 8.6a) Three different periods were fabricated by changing  $\delta$ : 344 nm, 349.2 nm, and 353.5 nm. The grating  $h$  is determined by the total film thickness of the DCG layer since the entire thickness of

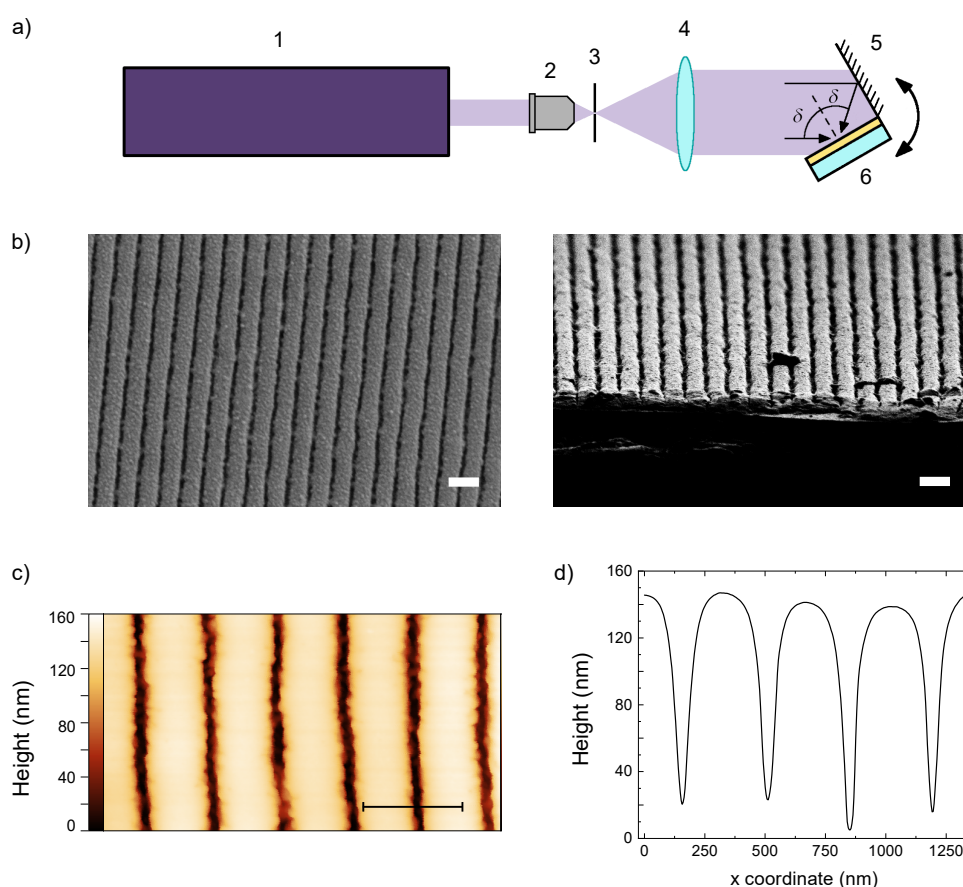


**Figure 8.6:** DCG nano-gratings fabricated by holographic lithography (HL). a) HL setup schematic in Lloyd configuration with 1) laser (Coherent Innova 308C), 2) microscope objective (40x), 3) pinhole (10  $\mu\text{m}$ ), 4) collimation lens, 5) mirror, and 6) DCG thin film on a silica substrate. b) SEM images of DCG grating with a period of 344 nm from the top (left) and at a  $37^\circ$  angle (right). c) AFM image and d) respective line profile. All scale bars represent 500 nm. Reprinted with permission from [146]. Copyright 2023 American Chemical Society.

the gelatin film was exposed and developed during fabrication. To achieve the desired  $h = 100$  nm, a solution of 2.2 wt % of gelatin (Russelot, 200 bloom) and 35 wt % of the sensitizer ammonium dichromate (Merck), with respect to water, was used. The solution was spin-coated at  $40^\circ\text{C}$  on fused silica substrates at 4000 rpm. Since the DCG film acts as a negative photoresist, the unexposed regions of the gelatin are developed and removed. The development consists of desensitisation in a water bath at  $15^\circ\text{C}$  followed by dry development in an oxygen plasma (Diener Zepto).

SEM and AFM measurements are employed to examine the morphology of the fabricated gratings. Figure 8.6b presents two SEM images at different angles, confirming the accuracy and homogeneity of both period and duty cycle over large areas. Figures 8.6c and 8.6d display the AFM results. The DCG stamps exhibit a roughness of 2.2 nm (RMS). Although the roughness is higher than typical flat silicon stamps (ca. 0.6 nm),<sup>[175]</sup> these DCG stamps are smooth enough to produce perovskite gratings with a roughness that is low enough

to enable good lasing performance (discussed in detail in Section 8.1.5). The AFM results also provide information on the DCG stamp height, as shown in Figure 8.6d, which is around 120 nm. This value is slightly higher than the designed value of 100 nm; however, based on previous reports, it is anticipated that the grating grooves are only partially filled during imprinting and the final perovskite grating height is slightly lower and closer to the designed value.<sup>[153]</sup>

#### 8.1.4 Nanoimprint lithography with gelatin gratings

For the thermal NIL process, DCG gratings were coated with FDTS, forming a robust hydrophobic layer on the stamp. The fabrication details for this anti-adhesion layer are elucidated in Section 5.2. This silanisation process is the only additional treatment to the DCG gratings after fabrication to allow for an easy release of the stamp from the perovskite film after imprinting. For the NIL process, an in-house developed hot embossing machine was used.<sup>[154]</sup> Details on the setup and process are included in Section 5.3. At the start of the process, the perovskite and DCG samples were placed on top of each other on the bottom plate of the imprint machine, with the grating facing the perovskite (Figure 8.7a). Two Teflon-coated silicon substrates were placed between the machine plates and the samples for uniform force distribution. The imprint process was performed with the optimised parameters of 900 bar and 95 °C for 10 min.

Following the imprint, it is possible to verify the successful completion of the process by visual inspection of the samples (Figure 8.7b). The perovskite surface grating diffracts ambient light efficiently, and the 1 cm<sup>2</sup> imprinted area exhibits different scattering colours depending on the observation angle. Some imperfections at the edges can originate from the stamp splitting from the perovskite or due to uneven-edged stamps since the DCG gratings were fabricated on larger area substrates of 2 x 2 cm<sup>2</sup> and cut into smaller pieces. The cutting was done by scratching the substrate with a glass cutter and subsequent hand splitting. Improving this process by, e.g., laser cutting or using smaller substrates for the HL process is likely to solve these edge issues. However, the imperfections did not noticeably affect the lasing performance since lasing originates from the 200 µm diameter spot of the pump laser.

AFM and SEM measurements were performed to study the imprinted perovskite grating and the utilised stamp. Thereby, the accuracy of the transferred, inverted pattern in the perovskite film was verified. Moreover, the used stamps were investigated for damage or deformations, which could limit their re-usability. The SEM results are displayed in Figure 8.7c and show that the perovskite pattern corresponds to the negative pattern of the DCG gratings and that the period accurately matches the one determined after the HL process. The *FF* of the perovskite grating extracted from the SEM data is approximately 0.37, higher than the one of the stamp negative (0.25), which is likely a result of an "under-filling" of the stamp grooves during imprinting.<sup>[153]</sup> Nevertheless, the resulting *FF* = 0.37 is still within the range of high feedback coupling coefficient (Section 8.1.2).

AFM results presented in Figures 8.7d and 8.7e reveal  $h \approx 100$  nm, which corresponds to the intended design value, confirming the expectation that the stamp grooves were only

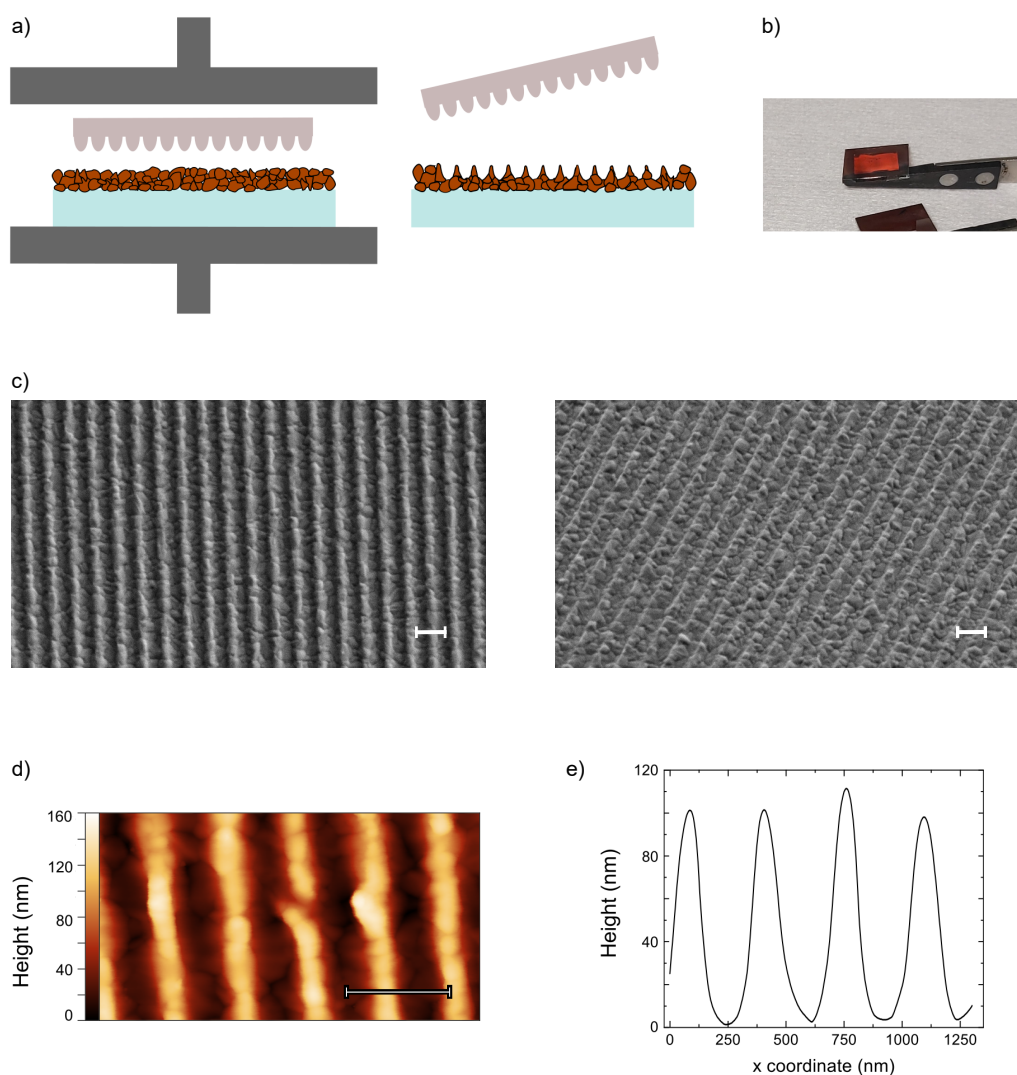


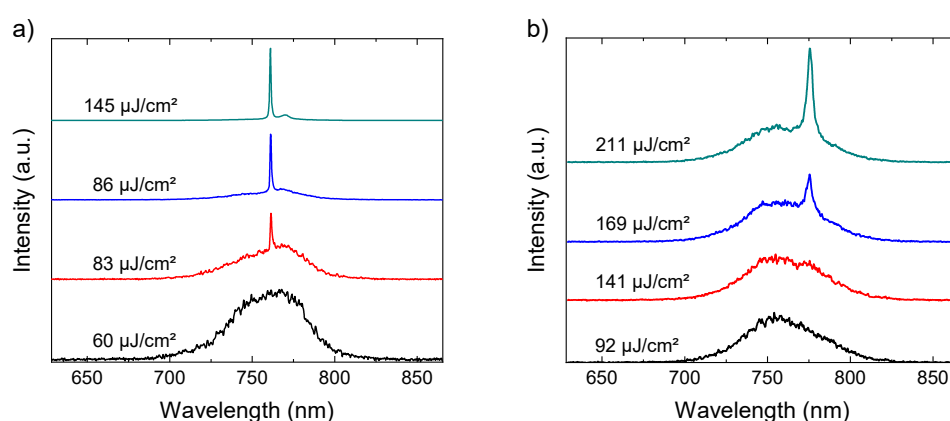
**Figure 8.7:** Thermal NIL of DCG stamps and resulting perovskite nano-structured films. a) Schematic of the NIL process. b) Perovskite film showing transferred grating pattern, indicated by the bright red square caused by ambient light diffraction of the imprinted area of 1 cm<sup>2</sup>. c) SEM images of the perovskite film after four imprint procedures, displaying the transferred pattern. The left image displays a top view, and the right image is taken with a 30° inclination. d) AFM image and e) respective height profile of the perovskite grating. All scale bars represent a length of 500 nm. Adapted with permission from [146]. Copyright 2023 American Chemical Society.

partially filled during the imprint process. The roughness was calculated based on said AFM data. Therefore, separate regions for the peak and valley areas of the grating were selected, and an average of their individual RMS values was extracted. The imprinted films exhibited a roughness of 4.4 nm, corresponding to an approximately 3-fold enhancement compared to pristine films before imprinting, which displayed a roughness of 13 nm (Appendix, Figure C.1). A similar reduction in roughness via imprinting was previously demonstrated, and other reported values for perovskite DFB lasers are in the range of 0.75 - 12 nm, placing this result close to current record values.<sup>[77, 176]</sup> Similar behaviour during an imprint process was also observed by Pourdavoud *et al.* for different perovskite compositions, so it is expected that this process is versatile regarding the employed perovskite materials.<sup>[67]</sup> SEM images of DCG stamps used for multiple imprints show that their structure remains intact and that it is possible to utilise the same stamp repeatedly (Appendix, Figure D.1). Moreover, no reduction in the optical performance of the DFB lasers fabricated by used stamps was observed (Section 8.1.5), confirming the stamp suitability for multi-use.

### 8.1.5 Optical characteristics of distributed feedback lasers

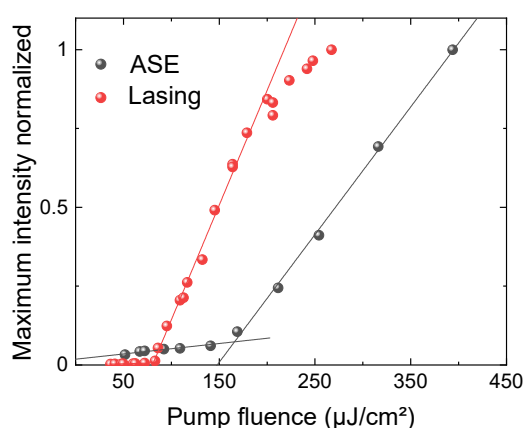
The following analysis examines the lasing performance of imprinted perovskite DFB laser. The lasing characterisation followed in this chapter is based on the guidelines by I.D.W. Samuel *et al.* and includes light-in-light-out characteristics, an investigation of emission linewidth narrowing and laser beam polarisation.<sup>[13]</sup> Finally, to demonstrate that the laser emission is characterised and influenced by the resonator, the tunability of the DFB lasers is demonstrated.

Figure 8.8 displays the emission characteristics of a DFB laser and an unpatterned reference film under different excitation powers. The optical characterisation was performed with the ICCD setup (Section 5.4.1). This geometry with an excitation perpendicular to the film was reported as the most efficient pump geometry to increase the absorption of pump light in



**Figure 8.8:** Fluence-dependent emission of a DFB laser and an unpatterned perovskite film. a) Laser emission spectra at different excitation fluences, ranging from 60  $\mu\text{J}/\text{cm}^2$  (below threshold) up to 145  $\mu\text{J}/\text{cm}^2$ . b) ASE emission spectra as a function of excitation fluence, spanning from 92  $\mu\text{J}/\text{cm}^2$  (below threshold) up to 211  $\mu\text{J}/\text{cm}^2$ . A vertical offset is used for better visualization. Adapted with permission from [146]. Copyright 2023 American Chemical Society.

the DFB.<sup>[156]</sup> The excitation spot size of the laser is measured to be  $3 \cdot 10^{-4} \text{ cm}^2$  by the knife edge method. The pump fluence is varied from  $\approx 30 \text{ }\mu\text{J}/\text{cm}^2$  up to  $250 \text{ }\mu\text{J}/\text{cm}^2$ , to investigate the DFB lasers and un-patterned reference films. Four selected spectra within this range are displayed in Figure 8.8. Both samples exhibit a broad PL spectrum at low fluences, below the lasing or ASE threshold. For the laser, in Figure 8.8a, starting at approximately  $80 \text{ }\mu\text{J}/\text{cm}^2$ , a narrow lasing peak is visible at a wavelength of  $\lambda \approx 760 \text{ nm}$ , on top of the PL spectrum. The lasing peak dominates with increasing fluence, and the background PL becomes indiscernible in the emission spectrum. At  $145 \text{ }\mu\text{J}/\text{cm}^2$ , a small shoulder is observed on the long-wavelength side of the lasing peak, around one order of magnitude lower in intensity, originating from background ASE that is not entirely suppressed by the resonator. A similar effect was reported for different perovskite compositions and was associated with the strong ASE in perovskites.<sup>[77, 157, 176]</sup> One possible strategy to mitigate this effect, compatible with our fabrication process, could be using 2D DFB gratings.<sup>[152]</sup> The ASE characteristics are also investigated to get an approximation of the gain and stimulated emission threshold in the bare perovskite film. This method is commonly employed to study the ability of a material to amplify light. The fluence-dependent spectra exhibit a similar behaviour to the lasing results, with an ASE peak emerging at the low-energy side of the PL spectrum at an excitation fluence of  $\approx 169 \text{ }\mu\text{J}/\text{cm}^2$  (Figure 8.8b). The respective input-output curves for the lasing and ASE emission are presented in Figure 8.9. Here, the emission spectrum maximum at each excitation fluence is plotted against the corresponding pump fluence. Both curves exhibit a substantial and sudden increase in slope, observed at  $\approx 80 \text{ }\mu\text{J}/\text{cm}^2$  for the DFB laser (red spheres) and at  $\approx 160 \text{ }\mu\text{J}/\text{cm}^2$  for the unpatterned sample (black spheres). This kink in each curve indicates the onset of stimulated emission: lasing and ASE, respectively. The black and red lines correspond to linear fits to the two processes below and above the threshold. The threshold is defined as the pump fluence at the intersection of the two linear fits, which corresponds to a fluence of  $81 \text{ }\mu\text{J}/\text{cm}^2$  for the lasing process and  $166 \text{ }\mu\text{J}/\text{cm}^2$  for the ASE. Generally, the ASE performance gives a lower limit of a material performance intended for use as a laser



**Figure 8.9:** Input-output characteristics of a DFB laser (red spheres) and a pristine perovskite film (black spheres). The solid lines correspond to linear fits to the emission below and above threshold. The lasing emission demonstrates a threshold of around  $81 \text{ }\mu\text{J}/\text{cm}^2$  and the ASE a threshold of  $166 \text{ }\mu\text{J}/\text{cm}^2$ . Adapted with permission from [146]. Copyright 2023 American Chemical Society.

active medium. Given that the ASE consists of a "single-pass" lasing in the material, there is no additional feedback mechanism to enhance light amplification. Once this material is included in a resonator, the feedback effect of the cavity enhances the optical gain and improves the stimulated emission process. Thus, the threshold for lasing in a cavity is reduced, and the slope efficiency is increased, compared to the case of ASE. This behaviour is confirmed by the comparison of ASE and lasing results: The laser threshold is around half of the ASE threshold, i.e.,  $F_{th,laser} = 0.49 \cdot F_{th,ASE}$ , and the slope efficiency of the laser is around twice as high as that of the ASE, i.e.,  $\eta_{laser} \approx 1.8 \cdot \eta_{ASE}$  (Figure 8.9).

The laser emission was further analysed by investigating its linewidth and polarisation. The linewidth was measured by acquiring a laser spectrum using the spectrometer grating with the highest resolution (Chapter 5). Figure 8.10a depicts the high-resolution spectrum of the laser peak, exhibiting a linewidth at FWHM of  $\Delta\lambda = 0.32$  nm, over one order of magnitude narrower than that of the ASE peak exhibiting  $\Delta\lambda = 5.04$  nm (Figure 8.10b). The spectrometer resolution limits the observed laser linewidth value, so the measurement represents an upper boundary of the actual linewidth. This result is among the best reported regarding perovskite DFB lasers, with linewidths in the range of 0.1-5 nm.<sup>[12]</sup> Polarisation measurements were performed by adding a linear polariser on a rotating stage before the spectrometer entrance. The results are presented in Figure 8.11, depicting the emission intensity as a function of the polariser angle for the lasing peak in red and for the ASE peak in black. The red curve possesses two maxima, at  $10^\circ$  and  $190^\circ$ , and two minima at  $100^\circ$  and  $280^\circ$ , characteristic of linear polarisation. For the black curve, the emission intensity does not depend on the polariser angle, revealing that the ASE is unpolarised. Regarding angle direction, the vertical direction (between  $0^\circ$  and  $180^\circ$ ) aligns with the DFB grating lines. As a result, a polarisation along this direction corresponds to a TE polarisation of the lasing mode. The slight tilt between this direction and the polarisation orientation observed in Figure 8.11 originates from the manual positioning of the sample, resulting in imperfect alignment of the grating lines along the vertical axis.

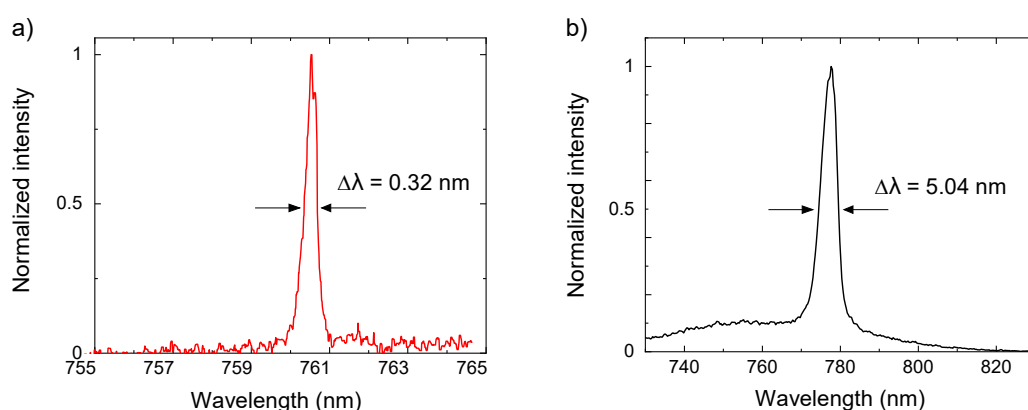


**Figure 8.10:** High-resolution spectra of laser and ASE spectra above threshold. a) Laser peak with a linewidth of  $\Delta\lambda = 0.32$  nm, and b) ASE peak with a linewidth of  $\Delta\lambda = 5.04$  nm. Adapted with permission from [146]. Copyright 2023 American Chemical Society.

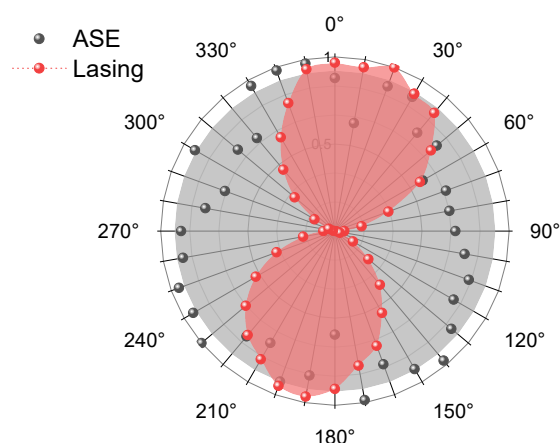


**Figure 8.11:** Polarisation measurement of the lasing (red spheres) and ASE (black spheres) peaks above threshold revealing a pronounced linear polarisation for the laser and an unpolarised emission of the ASE. A red shaded area is used for better visualisation, and the grey shaded area represents the average ASE amplitude over all angles, which fluctuated with time due to instabilities of the excitation laser. Reprinted with permission from [146]. Copyright 2023 American Chemical Society.

In addition, it is relevant to investigate the polarisation of the PL emission on a structured sample to test whether the laser polarisation is merely a grating effect. Figure 8.12 illustrates these results and reveals a preference in emission direction due to the grating; however, this corresponds to 56 % TE and 44 % TM polarisation, rendering this effect negligible. Since the perovskite film with the specified thickness only supports two fundamental modes,  $TE_0$  and  $TM_0$ , these results reveal that the measured lasing mode corresponds to the  $TE_0$  mode. This is in line with the expectations since the TE mode provides stronger mode confinement (and therefore gain) than the TM mode and is therefore anticipated to provide a lower lasing threshold. This fundamental aspect is discussed in more detail in Section 3.3.

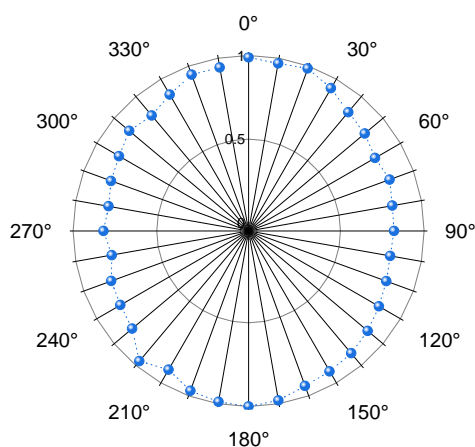


**Figure 8.12:** Polarisation measurement of the PL emitted from the distributed feedback grating region, below threshold, displaying a minor TE polarisation preference (56 % TE and 44 % TM).

Finally, the influence of the resonator on the laser emission is investigated to verify that the resonance originates from the cavity effect. Therefore, the imprinting procedure is performed with DCG stamps with different periods, and the laser emission wavelength is measured as a function of  $\Lambda$ . According to the resonance condition of a second-order DFB laser (Equation 8.1), a shift in  $\Lambda$  directly translates into a change in laser wavelength  $\lambda$ , with  $n_{\text{eff}}$  as the proportionality factor. Notably,  $n_{\text{eff}}$  is not a constant but a function of the wavelength, as previously discussed in Section 8.1.2. Gratings with periods of  $\Lambda = 344.0$ , 349.2, and 353.5 nm were employed to test the tunability of the emission wavelength and larger periods are expected to shift  $\lambda$  to longer wavelengths. Figure 8.13 depicts three laser spectra for each period analysed, and these findings verify the expected emission redshift with increasing  $\Lambda$ . This demonstrates unequivocally that the lasing process originates from the DFB cavity imprinted on the perovskite films. The observed shift in peak wavelength is smaller than predicted, assuming a constant  $n$ , as discussed in Section 8.1.2. The exact estimation of  $n_{\text{eff}}$  is challenging; however, this value can be calculated using the resonance condition and the measured  $\Lambda$  and  $\lambda$ . Figure 8.14 illustrates  $n_{\text{eff}}$  for each lasing mode. As expected,  $n_{\text{eff}}$  decreases with increasing  $\Lambda$ . The total shift between the smallest and largest periods corresponds to  $\Delta n_{\text{eff}} = 0.05$ . By increasing  $\Lambda$  by  $\approx 10$  nm, a shift in  $\lambda$  of approximately 4 nm is observed, confirming the tunability of these DFB lasers. This shift matches the shift reported in the literature for similar perovskite DFB lasers.<sup>[151]</sup> These observations highlight the importance of considering perovskites' pronounced refractive index dispersion to predict and design accurate resonant structures.

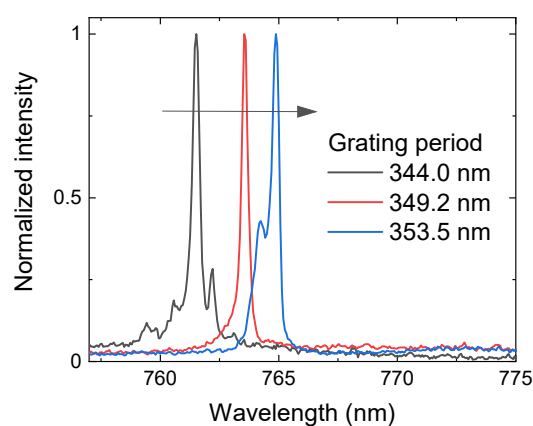


**Figure 8.13:** High-resolution spectra of lasing emission as a function of the grating period. The red shift of the emission wavelength with an increasing grating period validates the laser tunability by changing the cavity parameters. Adapted with permission from [146]. Copyright 2023 American Chemical Society.

Overall, the observed laser thresholds are comparable to other reported values for pulsed DFBs, typically in the order of tenths of  $\mu\text{J}/\text{cm}^2$  (Appendix Table B.1). However, considering the pumping conditions, i.e., the relatively long nanosecond pulses used, this threshold result is among the best (Appendix, Figure B.1), especially considering that these are the only reported DFB lasers fabricated completely with cost-effective methods. Further, it is remarkable that the DFB lasers developed here outperform a similar laser fabricated with more complex techniques.<sup>[156]</sup> Regarding stamp re-usability and process repeatability, the results demonstrate that it is possible to reuse the same DCG grating for the NIL process without a decrease in laser performance (Appendix, Figure D.2). In conclusion, this study successfully demonstrated the implementation of low-cost DCG gratings as efficient NIL stamps, enabling efficient DFB lasers based on surface-patterned perovskite films. This cost-effective fabrication method offers a promising solution for transferring high-quality nano-structures to perovskite films, presenting many opportunities for photonic applications. The following section presents the preliminary results of two state-of-the-art, low-cost printed resonators compatible with perovskite materials.

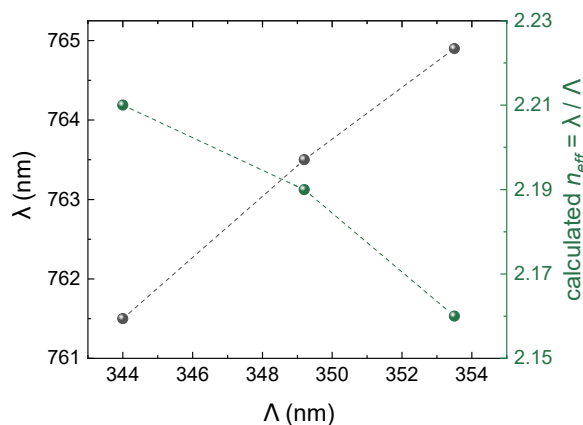


**Figure 8.14:** Wavelength of the lasing peak  $\lambda$  as a function of grating period  $\Lambda$  (black) and the resulting  $n_{\text{eff}}$  of each laser mode (green), calculated with the respective parameters by  $n_{\text{eff}} = \lambda / \Lambda$ . Reprinted with permission from [146]. Copyright 2023 American Chemical Society.

## 8.2 Proof-of-concept studies on printed laser resonators

This section explores the field of printed laser resonators, presenting two proof-of-concept experiments that showcase the feasibility and potential of emerging technologies. Directly printed resonators offer a promising avenue for scalable and cost-effective resonators in addition to the NIL approach introduced in the previous section. Section 8.2.1 presents DFB resonators achieved by a novel nano-printing technology. In Section 8.2.2, a micro-cavity is demonstrated based on state-of-the-art inkjet-printed DBR mirrors. The limitations and potential of these two approaches are discussed based on the optical performance of the fabricated samples.

### 8.2.1 Lasers with nano-printed SU-8 gratings

This section presents an alternative low-cost fabrication process for perovskite DFB lasers with printed SU-8 gratings. This new nano-printing approach enables state-of-the-art resolution down to 100 nm, at least one order of magnitude lower than other printing techniques, such as inkjet printing.<sup>[177, 178]</sup> Thus, it has the potential to enable printed customisable laser geometries on the nano-scale, such as ring or spiral resonators, and connecting waveguides, which is particularly attractive for the low-cost fabrication of integrated photonic circuits.<sup>[77, 179–182]</sup> Here, DFB gratings were fabricated via direct nano-printing of SU-8 lines with periods of 360 - 380 nm on glass substrates. To finalise the DFB laser, a perovskite layer was spin-coated on top and its surface smoothed via a flat imprint step (Figure 8.15a). The standard triple-cation composition was used for these experiments, exhibiting an ASE peak at  $\approx 770$  nm. Further, to ensure compatibility with the underlying SU-8 gratings, the spin-coating procedure was adjusted to include 200  $\mu$ l of IPA acting as an anti-solvent. Considering the shift of  $\lambda$  with  $\Lambda$  observed experimentally in the previous section, periods between 365 nm and 375 nm were fabricated for this experiment with NAZCA V1 (HumminK). This fabrication approach's maximum achievable grating height was around 20 - 30 nm (Figure 8.15b). As a consequence, the design values used in the previous section are no longer appropriate, and the total film thickness was adjusted to keep the equivalent waveguide structure identical to the last section, i.e.  $d_{\text{eq}} = 155$  nm. Considering a grating height of 30 nm, the total film thickness was chosen to be 180 nm, with 150 nm residual waveguide, resulting in an equivalent waveguide thickness of 158 nm (assuming an  $FF$  of  $\approx 25\%$ ). It is worth noting that such resonators possess much weaker coupling strength than those designed in Section 8.1 due to the lower grating height ( $30 \text{ nm} \ll 100 \text{ nm}$ ) and refractive index contrast ( $\Delta n_{\text{SU-8/pero}} = 0.99 \ll \Delta n_{\text{pero/air}} 1.55$ ).

The surface topography of the printed gratings was measured by AFM before spin-coating, and the height profile is illustrated in Figure 8.15b. The printed gratings exhibit a height of

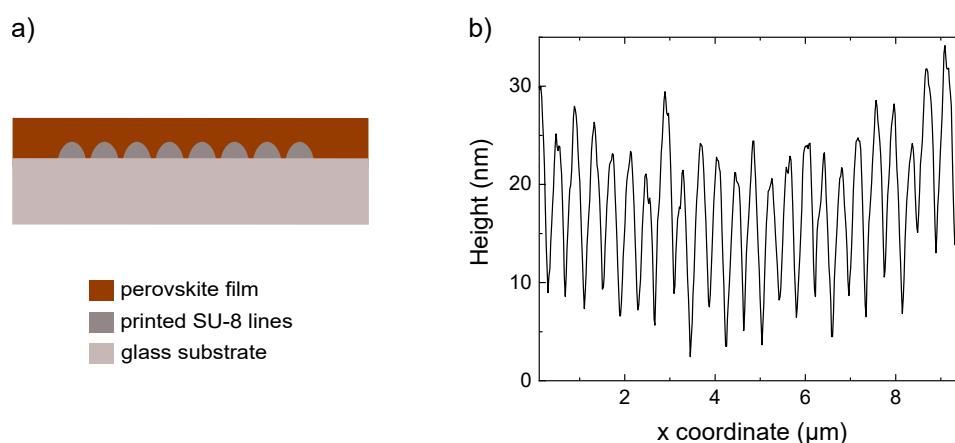


**Figure 8.15:** Nano-printed DFB laser with SU-8 lines. a) Sketch of a DFB laser comprised of printed SU-8 lines on a glass substrate with a flat perovskite film on top. b) AFM height profile of printed SU-8 lines forming the distributed feedback cavity with a height of 20-25 nm, and an average period of 381 nm with a standard deviation of 30 nm.

20 - 30 nm, well below the typical reported range for similar gratings (60 nm to 140 nm) and are thus expected to provide a low feedback.<sup>[5, 67, 157, 158]</sup> The grating period, extracted from the profile data (Figure 8.15b), exhibited an average of 381 nm and a standard deviation of ca. 30 nm. Variations in the DFB period can lead to the emergence of multiple resonant modes, potentially rendering the laser nonfunctional, especially if the deviation is large enough to cause significant resonance shifts, e.g., outside the gain spectrum. A further optimisation of the fabrication approach is expected to provide more homogeneous periods and higher grating height.

Optical characterisation was performed analogously to the one in Section 8.1. The DFB lasers were excited from the top, and the emission was collected along the same direction, separated by a dichroic mirror. The laser spot size is set to  $6 \cdot 10^{-4} \text{cm}^2$  to fit the resonator size (ca.  $300 \mu\text{m} \times 300 \mu\text{m}$ ). The emission spectra exhibited a broad PL emission at low excitation fluences with multiple narrow peaks emerging at higher fluences (Figure 8.16a). These peaks are neither characteristic of a single-moded DFB laser output nor ASE in the film (one single broad peak). Instead, this emission pattern is originating from multi-mode lasing. The input-output characteristics are plotted in Figure 8.16b by considering both the PL maximum for spectra below threshold (broad emission line) and the maximum of the dominant lasing peak (centred at 762.5 nm) illustrated in Figure 8.16a. A threshold behaviour is recognisable in Figure 8.16b between the spontaneous emission (black spheres) and the lasing process (red spheres). The intersection of the two linear fits yields a threshold value of  $292 \mu\text{J}/\text{cm}^2$ . A spectral narrowing is observed down to a linewidth of  $\Delta\lambda \approx 2 \text{ nm}$ , narrower than the ASE peak and lies within the range of reported values for perovskite lasers.<sup>[12]</sup> The multiple side peaks make it challenging to determine the FWHM, so assuming an approximately symmetric peak, half the linewidth was measured from the long wavelength side and multiplied by 2 to estimate the total linewidth. The peak positions and intensities were short-term stable for further analysis.

The origin of multi-mode lasing is likely due to random lasing in the corrugated perovskite film, where scattering is enhanced by the weak DFB cavity. The film regions outside the resonator area showed no lasing and only typical ASE at high excitation fluences. Thus, the cavity effect is evident and ASE is suppressed, a successful first milestone towards a functional DFB laser. However, the resonator is not producing single-mode DFB lasing, most likely due to fabrication irregularities responsible for deviations in the grating period (Figure 8.15b). An optimisation of the fabrication process is envisioned to enhance the line printing control and enable a uniform period and a higher grating to provide stronger feedback.

In summary, these results show a successful proof-of-concept of a new fabrication method for all-printed perovskite DFB lasers. Multi-mode lasing was observed, and optimising the printing process is expected to lead to the fabrication of single-mode DFB lasers. The versatility of the nano-printing approach allows for the exploration of different structures and layer designs for perovskites and potentially other solution-processed laser materials.

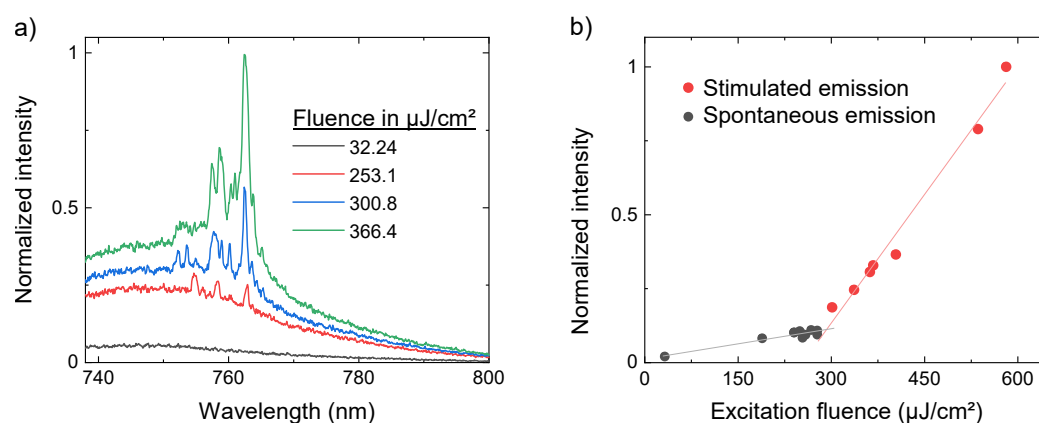
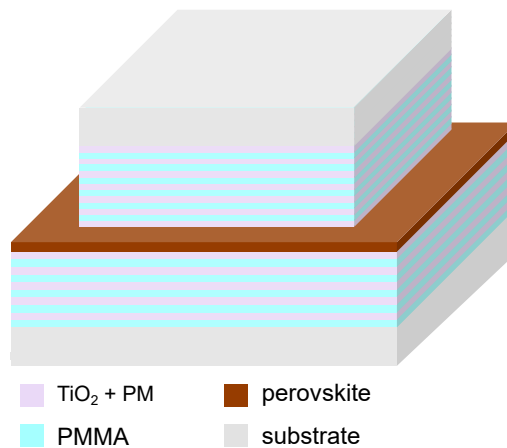


**Figure 8.16:** Laser emission of printed DFB with SU-8 lines. a) Emission as a function of excitation fluence, from 32  $\mu\text{J}/\text{cm}^2$  up to 366  $\mu\text{J}/\text{cm}^2$ . Below threshold, the emission corresponds to the broad PL spectrum of unpatterned films, centred around  $\approx 748$  nm. At higher excitation fluences ( $\geq 253$   $\mu\text{J}/\text{cm}^2$ ), multiple narrow peaks emerge on top of the broad PL with a dominant peak around 762.5 nm. b) Input-output characteristics of the data in a). Black spheres correspond to the spontaneous emission given by the PL peak counts (at  $\approx 748$  nm), and the red spheres correspond to the lasing emission of the dominant laser peak at 762.5 nm. The solid lines correspond to the respective linear fits and their intersection results in a threshold value of 292  $\mu\text{J}/\text{cm}^2$ .

### 8.2.2 Perovskite micro-cavities with inkjet printed mirrors

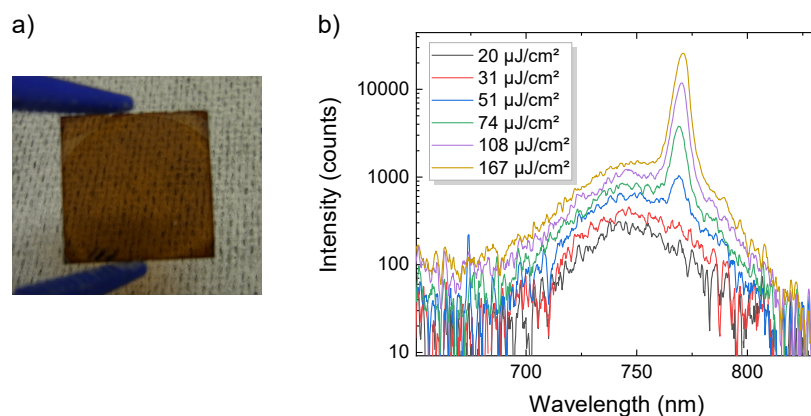
Next to DFB lasers, vertical-cavity surface-emitting lasers (VCSELs) offer an additional resonator geometry that is compact, planar, easy to integrate, and enables surface emission. Consequently, several perovskite VCSELs were reported, demonstrating a variety of emission wavelengths and perovskite materials, including 2D, 3D, and nanoparticle thin-films.<sup>[120, 183–188]</sup> Fabricating multilayered DBRs for VCSELs often involves costly methods such as electron-beam evaporation, sputtering, or metalorganic vapour-phase epitaxy (MOCVD).<sup>[183–186, 188]</sup> Hence, there is a desire to develop cost-efficient fabrication methods for DBRs while maintaining their high quality. Recently, perovskite VCSELs incorporating solution-processed DBRs based on cellulose acetate and polyvinyl carbazole polymers were fabricated, offering a more economical approach.<sup>[187, 189]</sup> Additionally, inkjet-printed DBRs with superior optical quality were demonstrated, providing a promising avenue for fabricating cost-efficient and fully solution-processable perovskite VCSELs.<sup>[190]</sup> This work presents a novel fabrication approach for a vertical micro-cavity using inkjet printed DBR mirrors, envisioning its application for perovskite VCSELs. The lamination process overcomes the technical challenges typically encountered when fabricating the top DBR on perovskite films.<sup>[188]</sup>

Figure 8.17 schematically depicts the complete layer stack of the laminated perovskite cavity. The two DBRs comprise nine bi-layers of alternating titanium dioxide in a polymer matrix and PMMA, inkjet printed on glass substrates.<sup>[190]</sup> The perovskite film was spin-coated on top of the bottom DBR, and the second DBR was laminated on top, finalising the stack. The lamination process was performed using the same machine and procedure as for the NIL in Section 8.1, at 900 bar, 95 °C, for 20 min. A single-mode cavity with a  $\lambda/2$



**Figure 8.17:** Schematic of the vertical micro-cavity architecture with inkjet printed DBRs on glass substrates sandwiching a thin perovskite layer. Each DBR is composed of 9 bi-layers of alternating PMMA and  $\text{TiO}_2$  in a polymer matrix (PM). The bottom DBR is cut in 15 mm x 15 mm pieces while the top DBR is cut into smaller substrates (10 mm x 10 mm) to enable the imprint process.

active layer was designed aiming at a low threshold and narrow emission lasing. Taking the centre of the ASE peak as the reference wavelength, and  $n_{\text{pero}} \approx 2.51$  (at 770 nm) results in a layer thickness of 153 nm. The molarity of the precursor solution was hence adjusted to 0.55 M to achieve the desired thickness. The perovskite spin-coating process was adjusted, and 200  $\mu\text{l}$  of IPA were used as an anti-solvent at a delay time of 10 s of the second step since the typically used CB would dissolve the PMMA in the bottom DBR. The successful spin-coating is confirmed by the uniformity and complete coverage of the perovskite thin film on the bottom DBR (Figure 8.18a). The resulting film exhibited similar ASE characteristics, i.e. centre wavelength and threshold, to a reference film on a glass substrate, evidencing its high quality on the multilayered DBR (Figure 8.18b).



**Figure 8.18:** Perovskite film on bottom DBR exhibiting ASE. a) Image of a homogeneous film spin-coated on the bottom DBR. b) Fluence-dependent emission spectra displaying ASE after a threshold of around 50  $\mu\text{J}/\text{cm}^2$ , similar to the ASE results of films processed on glass substrates.

The lamination process was also successful, and the two substrates were effectively joined into one sample, although the contact was not uniform across the sample (Figure 8.19a). For the lamination of the top DBR, a thin, flexible substrate would be advantageous for achieving better adhesion (glass/DBR/perovskite). The contacted regions are visible in Figure 8.19a as the dark brown parts, and it was possible to focus the pump laser within these areas to perform the optical characterisation of the cavity. The reflection spectra of the entire cavity and individual DBRs were recorded, and the perovskite emission was measured at different excitation fluences. The reflection spectra of the individual DBRs exhibit a maximum reflectance of  $R_{max} \approx 92\%$  and a stopband centred at  $\approx 765$  nm (Appendix X). Figure 8.19b illustrates the cavity reflection and PL. The reflection (dashed line) exhibits a stopband between 720 - 783 nm divided into two parts by a centre dip at 782 nm. Each stopband side possesses a very high reflectance with  $R_{max} \approx 98\%$  (Figure 8.19), and some other fabricated devices reached  $R_{max} \approx 100\%$ . The central dip corresponds to the single cavity mode designed to approximately match the ASE wavelength at 770 nm. The cavity exhibits a narrow PL with a linewidth of 6.5 nm (FWHM) centred at 768 nm, resulting in a cavity with an estimated Q-factor  $\approx 118$ . This value is within the same order of magnitude of reported VCSELs<sup>[187-189, 191, 192]</sup> and in the lower range of reported Q-factors for perovskite lasers.<sup>[12]</sup> Hence, this cavity presents a Q-factor comparable to reported values, which is expected to sustain lasing; however, at very high excitation fluences, only ASE was observed. Shifting the DBR stopband to suppress the ASE wavelength should control the depletion of gain by ASE and is expected to enable lasing in these cavities. Optimising the imprint process to achieve homogeneous films could also improve the cavity. In summary, the lamination of two inkjet-printed DBRs sandwiching a perovskite film was employed as a novel and cost-effective approach for fabricating vertical micro-

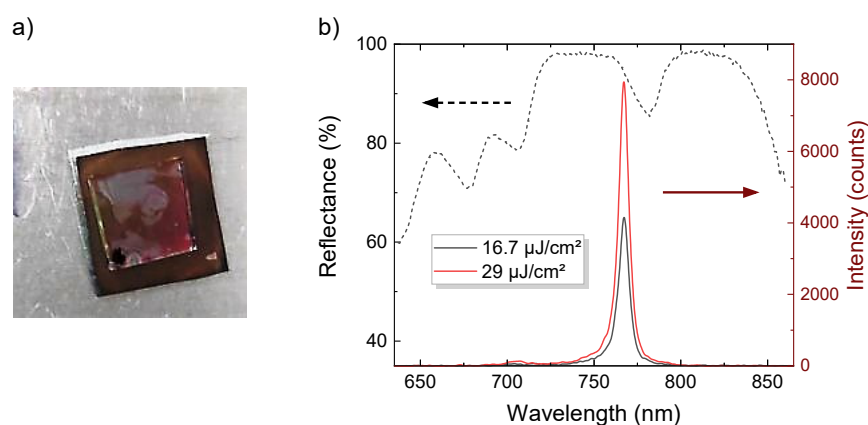


**Figure 8.19:** Laminated DBR with perovskite inter-layer forming a single-moded micro-cavity. a) Image of the laminated sample. Dark brown regions reflect a contact between the top and bottom layers. b) Reflection (dashed line) and PL spectra (solid lines) of micro-cavity measured within the dark region displayed in a). The reflection stopband exhibits a high reflectance between 720 - 783 nm with a centre dip at 782 nm, corresponding to the cavity mode. The PL spectrum centred at 768 nm possesses a linewidth of 6.5 nm, yielding a cavity Q-factor of 118.

cavities. The cavities exhibited high reflectance, a narrow PL emission and a Q-factor comparable to values in the literature.

### 8.3 Summary

This chapter demonstrates the efficient integration of solution-processed perovskite thin films in various resonator geometries. In particular, three different cost-efficient approaches to fabricate perovskite lasers were presented: Perovskite DFB lasers by NIL using DCG gratings were developed as the first fully low-cost perovskite DFB laser to date.<sup>[146]</sup> The gelatin gratings were fabricated by HL and a dry development step, and the NIL process was performed at 900 bar, 95 °C, for 10 min. The DCG stamps possess enough robustness to maintain their quality throughout multiple NIL rounds without visible degradation of the stamps or a decrease in lasing performance of the fabricated devices. The imprinted perovskite gratings exhibited a high quality, and the resulting lasers showed good lasing performance with a threshold of 81  $\mu\text{J}/\text{cm}^2$ , a linewidth of 0.32 nm, and an intense TE polarisation.

Moreover, two proof-of-concept prototypes of perovskite lasers with printed resonators were presented. The first consisted of printing an SU-8 grating with a novel direct nano-printing technology developed by Hummink.<sup>[147]</sup> A preliminary demonstration of an all-printed DFB resonator with a perovskite thin film as an active medium was successfully demonstrated. This laser exhibited multi-mode lasing, likely originating from random lasing in the film. Improving the printing process to increase the grating height to at least 60 nm is a future optimisation step needed so the DFB can provide enough feedback to enable lasing. Overall, the two novel cost-efficient fabrication techniques presented here for DFB lasers are versatile and compatible with different resonator structures, such as 2D photonic crystals, ring and spiral resonators. The final approach was based on a vertical micro-cavity with state-of-the-art inkjet printed DBRs laminated together, sandwiching a perovskite layer. A single-mode, fully solution-processed perovskite micro-cavity was successfully fabricated with high reflectance and a Q-factor of 118, comparable to reported perovskite VCSELs.<sup>[187]</sup> ASE was observed at high excitation fluences, and future efforts should focus on optimising the vertical cavity to enable lasing.



**Part IV**  
**Conclusion**



## 9 Conclusion and Outlook

This chapter provides a comprehensive overview of the scientific advancements achieved in this research on carrier dynamics and light amplification in triple-cation perovskites and their prospective impact on the field of perovskite lasers. Additionally, it explores relevant research directions to improve current state-of-the-art achievements and expand the possibilities of perovskites to be used in lasing applications. Hybrid perovskites have demonstrated rapid progress as laser materials, showing significant potential for realising a cost-effective, solution-processed laser diode. Electrically-driven laser devices are the ultimate practical application of perovskite lasers. A key milestone in reaching this goal is sustaining CW lasing at room temperature. Addressing the obstacles limiting their performance is imperative to bring perovskite lasers closer to commercial relevance. This thesis contributes to the current research on perovskites for lasing applications in three significant ways:

1. Empirical studies provide insights into perovskite photophysics and elucidate the factors influencing the ASE threshold in these materials, particularly concerning temperature variations.
2. Proof-of-concept experiments explore various strategies to reduce ASE thresholds by enhancing the radiative efficiency in perovskites.
3. Further experimental investigations involve the development of new cost-effective fabrication methods for laser resonators that can be integrated with perovskite thin films.

The main findings and prospects of these three topics are presented below.

### **Factors determining ASE thresholds in 3D perovskites**

The first result chapter of this work presents a novel method for investigating carrier dynamics in perovskite thin films without the influence of carrier depletion effects caused by ASE. The inherent waveguiding in the high refractive index triple-cation perovskite is suppressed by employing high refractive index Si substrates, eliminating ASE in the film. Hence, it is possible to investigate the intrinsic photophysics of the material at excitation densities relevant to lasing operation. This versatile method can be applied to various perovskite compositions or other optical materials with a refractive index lower than silicon. It is particularly relevant for studying carrier dynamics in gain media, where behaviour at high carrier densities needs to be explored.

This approach elucidated the effects influencing the ASE threshold: the exponential decrease of  $k_{bi}$  and PL spectral broadening with increasing temperature. Both effects explain the increase in the ASE threshold with temperatures up to approximately 250 K. Consequently, future efforts to reduce laser thresholds should focus on mitigating these aspects to suppress the significant threshold rise with temperature, especially under CW or electrical excitation, where pump-induced or Joule heating significantly increases the perovskite's temperature. Strategies for maintaining a high  $k_{bi}$  or a narrower PL linewidth at high temperatures should be investigated. One approach can involve adjusting electron-phonon interactions through strain or by enhancing the rigidity of the perovskite lattice with the use of matrix materials that are miscible in the perovskite precursor.<sup>[193]</sup> Strategies to enhance  $k_{bi}$  may entail optical confinement methods: for instance, tailoring the ligand and well thickness in quasi-2D perovskites to maximise the fraction of large quantum wells.<sup>[36]</sup> This allows for maintaining a dominant species of free charge carriers and helps avoid non-radiative EEA in small wells dominated by exciton effects. Additionally, it is essential to investigate the existence of a non-radiative bimolecular recombination process of free carriers, which has been debated in the literature. Understanding the origins of such a non-radiative bimolecular recombination can provide valuable insights into mitigating non-radiative losses, ultimately improving the radiative efficiency. Lastly, it is crucial to develop thermal management strategies for efficient heat dissipation from the perovskite layer during laser operation to suppress the pronounced threshold increase. These strategies should be compatible with a diode geometry since Joule heating in perovskite LED structures has been identified as the primary limiting aspect in achieving electrically-pumped perovskite lasers<sup>[4]</sup>. Here, the temperature region accessible by Peltier cooling ( $>220$  K) is of particular interest for future commercial applications.<sup>[28]</sup>

### **Optical and material strategies for enhanced perovskite lasing**

Chapter 7 presents three materials and fabrication strategies to enhance the radiative efficiency in perovskite films. Firstly, Section 7.1 emphasises the significance of optical waveguide passivation on the perovskite layer, which strongly reduces waveguide propagation losses and improves ASE performance by 39 % by reducing the index contrast and, consequently, scattering losses. This effect is particularly pronounced in perovskite films due to their high refractive index and rough surface, distinguishing them from conjugated polymers or other gain media with lower indices and smoother surfaces. Therefore, the roughness and index contrast must be considered in the design of perovskite lasers. An optimisation of the confinement factor, assuming flat layers, may not necessarily yield optimal results, as demonstrated in Section 7.1. For multi-layer LED or laser diode structures, it becomes especially pertinent to account for these roughness and refractive index effects due to the layer stack with varying optical and electrical properties, which impact the optical mode in the perovskite waveguide.

Next, the comparative study of quasi-2D and 3D perovskites in Section 7.2 highlights the significance of evaluating new materials for lasing applications based on characterisations at high excitation density, rather than relying on typical low-density figures of merit like PLQY and SRH lifetime. 3D perovskites exhibited an approximately 90 % reduction in ASE

---

threshold compared to their quasi-2D counterparts, despite the latter displaying more than two times higher radiative emission and PLQY at low excitation. Thus, spectroscopic studies of new gain media should be conducted at carrier densities within the range of ASE thresholds. Additionally, this study underscores the importance of gaining insights into the excited state species in a material, whether they are excitons or free carriers. These insights are crucial for designing efficient laser devices with optimised radiative efficiency under ASE threshold conditions. Finally, the ASE results of potassium passivated samples discussed in Section 7.3.2 provide evidence that an efficient grain boundary passivation, such as potassium doping of triple-cation perovskites, can improve the ASE performance in thin films by around 30 %. This suggests a significant non-radiative loss channel associated with grain boundaries. Potassium doping can additionally suppress halide and ion migration (Section 7.3.2), potentially offering a dual passivation effect in optoelectronic devices, where mobile ions can be particularly detrimental to device performance.

Future research in material engineering strategies to optimise perovskites for laser applications should emphasise tailoring the optical and compositional properties of perovskite thin films, such as by combining the two approaches: waveguide and bulk passivation. Furthermore, until now, CW lasing or ASE demonstrations have been limited to specific wavelengths in the green or NIR spectral range. As a first milestone toward electrical pumping, optimising materials and fabrication processes to achieve CW light amplification across the entire visible spectrum is crucial. This is particularly challenging in the blue region, making it an area deserving of special attention. Achieving this for the blue spectral region is particularly challenging, emphasising the need for more research. Developing and integrating a nanoparticle composite as an alternative to 3D perovskites as a gain medium is a promising avenue to enhance device performance for all material and device fabrication approaches discussed here.<sup>[187]</sup>

### **Cost-effective fabrication approaches for laser resonators**

Chapter 8 reports on various low-cost fabrication strategies for perovskite lasers: i) second-order DFB lasers with high-quality nano-gratings, structured by NIL with gelatin stamps; ii) direct nano-printed SU-8 DFB gratings; and iii) a vertical micro-cavity composed of two inkjet-printed DBR mirrors. All three approaches can be applied to other materials, such as organic semiconductors, polymers hosting functional compounds, or quantum dot dispersion. Ultimately, tuning these resonators to different spectral regions should be easily achievable, enabling the application of materials emitting in a wide spectral range and the development of tunable lasers.

The results of the NIL process employing gelatin gratings discussed in Section 8.1 demonstrate that perovskite films are soft enough to be patterned with relatively soft nano-structured moulds (such as DCG), which can be fabricated using low-cost methods. The resulting lasers display a threshold of approximately  $81 \mu\text{J}/\text{cm}^2$ , consistent with reported values. They also demonstrate pronounced linear polarisation and an exceptionally narrow linewidth of 0.32 nm, one of the lowest observed thus far. This NIL method utilising gelatin stamps contrasts the typically employed hard stamps that require more expensive

fabrication routes and can be exploited for other structured optoelectronic devices, such as displays, LEDs, photodetectors, or solar cells. Regarding DFB lasers, it is relevant to experimentally optimise the resonator parameters discussed in Section 8.1.2 and explore new resonator geometries based on the same fabrication approach, such as 2D DFB resonators, to achieve lower thresholds, i.e., higher gain and lower losses. Possible approaches to reduce output coupling losses in DFBs involve optimising the grating shape, such as using a mixed-order grating or fabricating sub-structured gratings to control feedback and out-coupling independently.<sup>[194]</sup>

The thermal nanoimprint process can also be used to laminate a cavity composed of two parts, such as the vertical micro-cavity presented in Section 8.2.2, or a perovskite heterostructure,<sup>[109]</sup> and is compatible with a multi-layer diode architecture.<sup>[154]</sup> The preliminary study on the micro-cavity with printed DBRs can be further investigated by processing the top distributed Bragg reflector (DBR) on foil to achieve a more homogeneous adhesion with the bottom DBR. The resonator can be improved by increasing the reflectivity of either or both DBRs or fine-tuning the perovskite thickness to achieve a narrower cavity resonance. Building on the significant progress achieved in fully-printed perovskite solar cells,<sup>[195]</sup> and based on the preliminary results in Section 8.2.2, there is good potential for a fully inkjet-printed, and eventually electrically-driven, perovskite VCSEL. Finally, the direct nano-printing technology developed by Hummink (Section 8.2.1) is suitable for creating new resonator geometries, particularly in combination with printed waveguides for applications with integrated laser sources.

## Bibliography

- [1] T. H. Maiman. “Stimulated optical radiation in Ruby”. *Nature* 187.4736 (1960), 493–494.
- [2] “Filling the green gap”. *Nature Photonics* 3.8 (2009), 421–421.
- [3] Brandon R. Sutherland and Edward H. Sargent. “Perovskite photonic sources”. *Nature Photonics* 10.5 (2016), 295–302.
- [4] Kaichuan Wen, Yu Cao, Lianghui Gu, Saixue Wang, Dongmin Qian, Jingmin Wang, Zhiyuan Kuang, Mengyi Luo, Gang Wang, Shuzhen Guan, Mengmeng Li, Heng Yang, Guichuan Xing, Nana Wang, Lin Zhu, Qiming Peng, Wei Huang, and Jianpu Wang. “Continuous-Wave Lasing in Perovskite LEDs with an Integrated Distributed Feedback Resonator”. *Advanced Materials* n/a.n/a (2023), 2303144.
- [5] Chuanjiang Qin, Atula S.D. Sandanayaka, Chenyang Zhao, Toshinori Matsushima, Dezhong Zhang, Takashi Fujihara, and Chihaya Adachi. “Stable room-temperature continuous-wave lasing in quasi-2D perovskite films”. *Nature* 585.7823 (2020), 53–57.
- [6] M. Eichhorn. *Laser Physics*. 2017.
- [7] Lei Lei, Qi Dong, Kenan Gundogdu, Franky So, L Lei, Q Dong, F So, and K Gundogdu. “Metal Halide Perovskites for Laser Applications”. *Advanced Functional Materials* 31.16 (2021), 2010144.
- [8] Christopher L. Davies, Marina R. Filip, Jay B. Patel, Timothy W. Crothers, Carla Verdi, Adam D. Wright, Rebecca L. Milot, Feliciano Giustino, Michael B. Johnston, and Laura M. Herz. “Bimolecular recombination in methylammonium lead triiodide perovskite is an inverse absorption process”. *Nature Communications* 9.1 (2018), 293.
- [9] Thomas Wellinger. “Design and Characterisation of Blue Polymer Lasers”. July (2010).
- [10] Marianne Aellen and David J Norris. “Understanding Optical Gain: Which Confinement Factor is Correct?” (2022).
- [11] F. P. Payne and J. P.R. Lacey. “A theoretical analysis of scattering loss from planar optical waveguides”. *Optical and Quantum Electronics* 26.10 (1994), 977–986.
- [12] Anqi Liu, Gangyun Guan, Xiaomei Chai, Nannan Feng, Min Lu, Xue Bai, and Yu Zhang. “Metal Halide Perovskites toward Electrically Pumped Lasers”. *Laser & Photonics Reviews* (2022), 2200189.
- [13] Ifor D W Samuel, Ebinazar B. Namdas, and Graham A. Turnbull. “How to recognize lasing”. *Nature Photonics* 3.10 (2009), 546–549.

- [14] Stefania Milanese, Maria Luisa De Giorgi, Luis Cerdán, Maria-Grazia La-Placa, Nur Fadilah Jamaludin, Annalisa Bruno, Henk J. Bolink, Maksym V. Kovalenko, and Marco Anni. “Amplified Spontaneous Emission Threshold Dependence on Determination Method in Dye-Doped Polymer and Lead Halide Perovskite Waveguides”. *Molecules* 2022, Vol. 27, Page 4261 27.13 (2022), 4261.
- [15] H. Kogelnik and C. V. Shank. “Coupled-Wave Theory of Distributed Feedback Lasers”. *Journal of Applied Physics* 43.5 (1972), 2327–2335.
- [16] Rudolf F Kazarinov. “Second-Order Distributed Feedback Lasers”. *IEEE Journal of Quantum Electronics* QE-21.2 (1985), 144–150.
- [17] Stefan Riechel. “Organic semiconductor lasers with two-dimensional distributed feedback”. PhD thesis. Ludwig-Maximilians-Universität München, 2002.
- [18] Ali M. Shams-Zadeh-Amiri, Jin Hong, Xun Li, and Wei Ping Huang. “Second- and higher order resonant gratings with gain or loss - Part II: designing complex-coupled DFB lasers with second-order gratings”. *IEEE Journal of Quantum Electronics* 36.12 (2000), 1431–1437.
- [19] Yufei Jia, Ross A. Kerner, Alex J. Grede, Barry P. Rand, and Noel C. Giebink. “Continuous-wave lasing in an organic–inorganic lead halide perovskite semiconductor”. *Nature Photonics* 11.12 (2017), 784–788.
- [20] Maria Luisa De Giorgi, Franziska Krieg, Maksym V. Kovalenko, and Marco Anni. “Amplified Spontaneous Emission Threshold Reduction and Operational Stability Improvement in CsPbBr<sub>3</sub> Nanocrystals Films by Hydrophobic Functionalization of the Substrate”. *Scientific reports* 9.1 (2019), 17964.
- [21] Martin A. Green, Anita Ho-Baillie, and Henry J. Snaith. “The emergence of perovskite solar cells”. *Nature Photonics* 2014 8:7 8.7 (2014), 506–514.
- [22] Bayrammurad Saparov and David B. Mitzi. *Organic-Inorganic Perovskites: Structural Versatility for Functional Materials Design*. 2016.
- [23] Michael J. Trimpl, Adam D. Wright, Kelly Schutt, Leonardo R. V. Buizza, Zhiping Wang, Michael B. Johnston, Henry J. Snaith, Peter Müller-Buschbaum, and Laura M. Herz. “Charge-Carrier Trapping and Radiative Recombination in Metal Halide Perovskite Semiconductors”. *Advanced Functional Materials* 30.42 (2020), 2004312.
- [24] Rebecca L. Milot, Giles E. Eperon, Henry J. Snaith, Michael B. Johnston, and Laura M. Herz. “Temperature-Dependent Charge-Carrier Dynamics in CH<sub>3</sub>NH<sub>3</sub>PbI<sub>3</sub> Perovskite Thin Films”. *Advanced Functional Materials* 25.39 (2015), 6218–6227.
- [25] Michael Saliba, Taisuke Matsui, Ji-Youn Seo, Konrad Domanski, Juan-Pablo Correa-Baena, Mohammad Khaja Nazeeruddin, Shaik M. Zakeeruddin, Wolfgang Tress, Antonio Abate, Anders Hagfeldt, and Michael Grätzel. “Cesium-containing triple cation perovskite solar cells: improved stability, reproducibility and high efficiency”. *Energy & Environmental Science* 9.6 (2016), 1989–1997.

- 
- [26] Philipp Brenner, Tim Glöckler, Diana Rueda-Delgado, Tobias Abzieher, Marius Jakoby, Bryce S. Richards, Ulrich W. Paetzold, Ian A. Howard, and Uli Lemmer. “Triple cation mixed-halide perovskites for tunable lasers”. *Optical Materials Express* 7.11 (2017), 4082.
- [27] Guanwei Sun, Xinyan Liu, Zhe Liu, Denghui Liu, Fanyuan Meng, Zhenchao Li, Linghao Chu, Weidong Qiu, Xiaomei Peng, Wentao Xie, Chenyang Shen, Jiting Chen, Hin-Lap Yip, and Shi-Jian Su. “Emission Wavelength Tuning via Competing Lattice Expansion and Octahedral Tilting for Efficient Red Perovskite Light-Emitting Diodes”. *Advanced Functional Materials* (2021), 2106691.
- [28] Philipp Brenner, Ofer Bar-On, Marius Jakoby, Isabel Allegro, Bryce S. Richards, Ulrich W. Paetzold, Ian A. Howard, Jacob Scheuer, and Uli Lemmer. “Continuous wave amplified spontaneous emission in phase-stable lead halide perovskites”. *Nature Communications* 10.1 (2019), 988.
- [29] Meili Li, Qiuyu Shang, Chun Li, Shuai Li, Yin Liang, Wenjin Yu, Cuncun Wu, Liyun Zhao, Yangguang Zhong, Wenna Du, Xianxin Wu, Zhili Jia, Yan Gao, Hui Chen, Xinfeng Liu, Shaojun Guo, Qing Liao, Guichuan Xing, Lixin Xiao, and Qing Zhang. “High Optical Gain of Solution-Processed Mixed-Cation CsPbBr<sub>3</sub> Thin Films towards Enhanced Amplified Spontaneous Emission”. *Advanced Functional Materials* (2021), 2102210.
- [30] Yuanzhi Jiang, Junli Wei, and Mingjian Yuan. *Energy-Funneling Process in Quasi-2D Perovskite Light-Emitting Diodes*. 2021.
- [31] Lu Cheng, Tao Jiang, Yu Cao, Chang Yi, Nana Wang, Wei Huang, and Jianpu Wang. “Multiple-Quantum-Well Perovskites for High-Performance Light-Emitting Diodes”. *Adv. Mater.* 32.15 (2020), 1–9.
- [32] Fabian Ruf, Meltem F. Aygüler, Nadja Giesbrecht, Bettina Rendenbach, Alice Magin, Pablo Docampo, Heinz Kalt, and Michael Hetterich. “Temperature-dependent studies of exciton binding energy and phase-transition suppression in (Cs,FA,MA)Pb(I,Br)<sub>3</sub> perovskites”. *APL Materials* 7.3 (2019), 031113.
- [33] Martin A. Green, Yajie Jiang, Arman Mahboubi Soufiani, and Anita Ho-Baillie. “Optical Properties of Photovoltaic Organic-Inorganic Lead Halide Perovskites”. *Journal of Physical Chemistry Letters* 6.23 (2015), 4774–4785.
- [34] Michele Saba, Michele Cadelano, Daniela Marongiu, Feipeng Chen, Valerio Sarritzu, Nicola Sestu, Cristiana Figus, Mauro Aresti, Roberto Piras, Alessandra Geddo Lehmann, Carla Cannas, Anna Musinu, Francesco Quochi, Andrea Mura, and Giovanni Bongiovanni. “Correlated electron–hole plasma in organometal perovskites”. *Nature Communications* 2014 5:1 5.1 (2014), 1–10.
- [35] Laura M. Herz. “Charge-Carrier Dynamics in Organic-Inorganic Metal Halide Perovskites”. *Annual Review of Physical Chemistry* 67.1 (2016), 65–89.
- [36] Yang Li, Isabel Allegro, Milian Kaiser, Aditya J. Malla, Bryce S. Richards, Uli Lemmer, Ulrich W. Paetzold, and Ian A. Howard. “Exciton versus free carrier emission: Implications for photoluminescence efficiency and amplified spontaneous emission thresholds in quasi-2D and 3D perovskites”. *Materials Today* 49 (2021), 35–47.

- [37] Valerio Sarritzu, Nicola Sestu, Daniela Marongiu, Xueqing Chang, Qingqian Wang, Maria Antonietta Loi, Francesco Quochi, Michele Saba, Andrea Mura, and Giovanni Bongiovanni. “Perovskite Excitonics: Primary Exciton Creation and Crossover from Free Carriers to a Secondary Exciton Phase”. *Advanced Optical Materials* 6.3 (2018), 1700839.
- [38] Yaxin Zhai, Kang Wang, Fei Zhang, Chuanxiao Xiao, Aaron H. Rose, Kai Zhu, and Matthew C. Beard. “Individual Electron and Hole Mobilities in Lead-Halide Perovskites Revealed by Noncontact Methods”. *ACS Energy Letters* 5.1 (2020), 47–55.
- [39] Samuel D. Stranks, Giles E. Eperon, Giulia Grancini, Christopher Menelaou, Marcelo J. P. Alcocer, Tomas Leijtens, Laura M. Herz, Annamaria Petrozza, and Henry J. Snaith. “Electron-Hole Diffusion Lengths Exceeding 1 Micrometer in an Organometal Trihalide Perovskite Absorber”. *Science* 342.6156 (2013), 341–344.
- [40] Patrik Ščajev, Ramu nas Aleksieju nas, Saulius Miasojedovas, Saulius Nargelas, Munetomo Inoue, Chuanjiang Qin, Toshinori Matsushima, Chihaya Adachi, and Saulius Juršėnas. “Two Regimes of Carrier Diffusion in Vapor-Deposited Lead-Halide Perovskites”. *The Journal of Physical Chemistry C* 121.39 (2017), 21600–21609.
- [41] Thomas Kirchartz, José A. Márquez, Martin Stolterfoht, and Thomas Unold. “Photoluminescence-Based Characterization of Halide Perovskites for Photovoltaics”. *Advanced Energy Materials* 10.26 (2020), 1904134.
- [42] Paul Fassel, Vincent Lami, Felix J. Berger, Lukas M. Falk, Jana Zaumseil, Bryce S. Richards, Ian A. Howard, Yana Vaynzof, and Ulrich W. Paetzold. “Revealing the internal luminescence quantum efficiency of perovskite films via accurate quantification of photon recycling”. *Matter* 4.4 (2021), 1391–1412.
- [43] Johannes M. Richter, Federico Branchi, Franco Valduga de Almeida Camargo, Baodan Zhao, Richard H. Friend, Giulio Cerullo, and Felix Deschler. “Ultrafast carrier thermalization in lead iodide perovskite probed with two-dimensional electronic spectroscopy”. *Nature Communications* 8.1 (2017), 376.
- [44] Mahdi Malekshahi Byranvand and Michael Saliba. “Defect Passivation of Perovskite Films for Highly Efficient and Stable Solar Cells”. *Solar RRL* 5.8 (2021), 2100295.
- [45] Himchan Cho, Young-Hoon Kim, Christoph Wolf, Hyeon-Dong Lee, and Tae-Woo Lee. “Improving the Stability of Metal Halide Perovskite Materials and Light-Emitting Diodes”. *Advanced Materials* (2018).
- [46] Tomas Leijtens, Giles E Eperon, Alex J Barker, Giulia Grancini, Wei Zhang, James M Ball, Ajay Ram, Srimath Kandada, Henry J Snaith, and Annamaria Petrozza. “Carrier trapping and recombination: the role of defect physics in enhancing the open circuit voltage of metal halide perovskite solar cells †”. *This journal is Cite this: Energy Environ. Sci* 9 (2016), 3472.

- 
- [47] Florian Staub, Thomas Kirchartz, Karsten Bittkau, and Uwe Rau. “Manipulating the Net Radiative Recombination Rate in Lead Halide Perovskite Films by Modification of Light Outcoupling”. *The Journal of Physical Chemistry Letters* 8.20 (2017), 5084–5090.
- [48] Johannes M. Richter, Mojtaba Abdi-Jalebi, Aditya Sadhanala, Maxim Tabachnyk, Jasmine P.H. Rivett, Luis M. Pazos-Outón, Karl C. Gödel, Michael Price, Felix Deschler, and Richard H. Friend. “Enhancing photoluminescence yields in lead halide perovskites by photon recycling and light out-coupling”. *Nature Communications* 7.1 (2016), 13941.
- [49] Florian Staub, Uwe Rau, and Thomas Kirchartz. “Statistics of the Auger Recombination of Electrons and Holes via Defect Levels in the Band Gap—Application to Lead-Halide Perovskites”. *ACS Omega* 3.7 (2018), 8009–8016.
- [50] Milian Kaiser, Yang Li, Saba Gharibzadeh, Bryce S. Richards, Ulrich W. Paetzold, and Ian A. Howard. “Charge Carrier and Exciton Dynamics in Perovskites Revealed by Time-Integrated Photoluminescence after Double-Pulse Excitation”. *Advanced Materials Technologies* (2022), 2200152.
- [51] Emmanuel V. Péan, Stoichko Dimitrov, Catherine S. De Castro, and Matthew L. Davies. “Interpreting time-resolved photoluminescence of perovskite materials”. *Physical Chemistry Chemical Physics* 22.48 (2020), 28345–28358.
- [52] Johannes M. Richter, Mojtaba Abdi-Jalebi, Aditya Sadhanala, Maxim Tabachnyk, Jasmine P.H. Rivett, Luis M. Pazos-Outón, Karl C. Gödel, Michael Price, Felix Deschler, and Richard H. Friend. “Enhancing photoluminescence yields in lead halide perovskites by photon recycling and light out-coupling”. *Nature Communications* 7.1 (2016), 13941.
- [53] Alexander Kiligaridis, Pavel A. Frantsuzov, Aymen Yangui, Sudipta Seth, Jun Li, Qingzhi An, Yana Vaynzof, and Ivan G. Scheblykin. “Are Shockley-Read-Hall and ABC models valid for lead halide perovskites?” *Nature Communications* 12.1 (2021), 3329.
- [54] Jiajun Qin, Xiao Ke Liu, Chunyang Yin, and Feng Gao. “Carrier Dynamics and Evaluation of Lasing Actions in Halide Perovskites”. *Trends in Chemistry* 3.1 (2021), 34–46.
- [55] Timothy W. Crothers, Rebecca L. Milot, Jay B. Patel, Elizabeth S. Parrott, Johannes Schlipf, Peter Müller-Buschbaum, Michael B. Johnston, and Laura M. Herz. “Photon Reabsorption Masks Intrinsic Bimolecular Charge-Carrier Recombination in CH<sub>3</sub>NH<sub>3</sub>PbI<sub>3</sub> Perovskite”. *Nano Letters* 17.9 (2017), 5782–5789.
- [56] Timothy W. Crothers, Rebecca L. Milot, Jay B. Patel, Elizabeth S. Parrott, Johannes Schlipf, Peter Müller-Buschbaum, Michael B. Johnston, and Laura M. Herz. “Photon Reabsorption Masks Intrinsic Bimolecular Charge-Carrier Recombination in CH<sub>3</sub>NH<sub>3</sub>PbI<sub>3</sub> Perovskite”. *Nano Letters* 17.9 (2017), 5782–5789.
- [57] Joseph S. Manser and Prashant V. Kamat. “Band filling with free charge carriers in organometal halide perovskites”. *Nature Photonics* 8.9 (2014), 737–743.

- [58] Fabrizio Mariano, Arianna Cretì, Luigi Carbone, Armando Genco, Stefania D'Agostino, Sonia Carallo, Giovanni Montagna, Mauro Lomascolo, and Marco Mazzeo. "The enhancement of excitonic emission crossing Saha equilibrium in trap passivated CH<sub>3</sub>NH<sub>3</sub>PbBr<sub>3</sub> perovskite". *Communications Physics* 3.1 (2020), 1–10.
- [59] Waqaas Rehman, Rebecca L. Milot, Giles E. Eperon, Christian Wehrenfennig, Jessica L. Boland, Henry J. Snaith, Michael B. Johnston, and Laura M. Herz. "Charge-Carrier Dynamics and Mobilities in Formamidinium Lead Mixed-Halide Perovskites". *Advanced Materials* 27.48 (2015), 7938–7944.
- [60] Somayeh Moghadamzadeh. "Multi-Cation Perovskite Semiconductors for All-Perovskite Tandem Solar Cells". PhD thesis. Karlsruhe Institute of Technology, 2021.
- [61] Susana Ramos-Terrón, José Francisco Illanes, Diego Bohoyo-Gil, Luis Camacho, and Gustavo de Miguel. "Insight into the Role of Guanidinium and Cesium in Triple Cation Lead Halide Perovskites". *Solar RRL* 5.12 (2021), 2100586.
- [62] Konrad Terpilowski and Diana Rymuszka. "Surface properties of glass plates activated by air, oxygen, nitrogen and argon plasma". *Glass Physics and Chemistry* 42.6 (2016), 535–541.
- [63] Bekir Sami Yilbas, Abdullah Al-Sharafi, and Haider Ali. "Surfaces for Self-Cleaning". *Self-Cleaning of Surfaces and Water Droplet Mobility*. Elsevier, 2019, 45–98.
- [64] Manda Xiao, Fuzhi Huang, Wenchao Huang, Yasmina Dkhissi, Ye Zhu, Joanne Etheridge, Angus Gray-Weale, Udo Bach, Yi-Bing Cheng, Leone Spiccia, M D Xiao, L Spiccia, F Z Huang, W C Huang, Y Dkhissi, Y Zhu, J Etheridge, U Bach, Y-b Cheng, and A Gray-Weale. "A Fast Deposition-Crystallization Procedure for Highly Efficient Lead Iodide Perovskite Thin-Film Solar Cells". *Angewandte Chemie International Edition* 53.37 (2014), 9898–9903.
- [65] Dane W. Dequilettes, Susanne Koch, Sven Burke, Rajan K. Paranj, Alfred J. Shropshire, Mark E. Ziffer, and David S. Ginger. "Photoluminescence Lifetimes Exceeding 8  $\mu$ s and Quantum Yields Exceeding 30% in Hybrid Perovskite Thin Films by Ligand Passivation". *ACS Energy Letters* 1.2 (2016), 438–444.
- [66] Matthias Worgull. *Hot embossing: theory and technology of microreplication*. Elsevier Inc., 2009.
- [67] Neda Pourdavoud. "Dissertation - Stimulated Emission and Lasing in Metal Halide Perovskites by Direct Thermal Nanoimprint" (2020).
- [68] Christian Rainer. "Triple Cation Perovskite Distributed Feedback Lasers by Thermal Nanoimprint Lithography" (2019).
- [69] Marcos A.C. De Araújo, Rubens Silva, Emerson De Lima, Daniel P. Pereira, and Paulo C. De Oliveira. "Measurement of Gaussian laser beam radius using the knife-edge technique: Improvement on data analysis". *Applied Optics* 48.2 (2009), 393–396.
- [70] Rudi Berera, Rienk van Grondelle, and John T.M. Kennis. *Ultrafast transient absorption spectroscopy: Principles and application to photosynthetic systems*. 2009.

- 
- [71] Michael Adams. "Triplet Exciton Transport in Porphyrin-Based Surface-Anchored Metal-Organic Framework Thin Films". PhD thesis. Karlsruher Institut für Technologie, 2019.
- [72] M. P. Halsall, I. F. Crowe, J. Mullins, R. A. Oliver, M. J. Kappers, and C. J. Humphreys. "Photomodulated Reflectivity Measurement of Free-Carrier Dynamics in InGaN/GaN Quantum Wells". *ACS Photonics* 5.11 (2018), 4437–4446.
- [73] Robert E Wagner and Andreas Mandelis. "A generalized calculation of the temperature and drude photo-modulated optical reflectance coefficients in semiconductors". *Journal of Physics and Chemistry of Solids* 52.9 (1991), 1061–1070.
- [74] Isabel Allegro, Yang Li, Bryce S. Richards, Ulrich W. Paetzold, Uli Lemmer, and Ian A. Howard. "Bimolecular and Auger Recombination in Phase-Stable Perovskite Thin Films from Cryogenic to Room Temperature and Their Effect on the Amplified Spontaneous Emission Threshold". *The Journal of Physical Chemistry Letters* 12.9 (2021), 2293–2298.
- [75] Tyler J. S. Evans, Andrew Schlaus, Yongping Fu, Xinjue Zhong, Timothy L. Atallah, Michael S. Spencer, Louis E. Brus, Song Jin, and X.-Y. Zhu. "Continuous-Wave Lasing in Cesium Lead Bromide Perovskite Nanowires". *Advanced Optical Materials* 6.2 (2018), 1700982.
- [76] Rui Su, Carole Diederichs, Jun Wang, Timothy C. H. Liew, Jiaxin Zhao, Sheng Liu, Weigao Xu, Zhanghai Chen, and Qihua Xiong. "Room-Temperature Polariton Lasing in All-Inorganic Perovskite Nanoplatelets". *Nano Letters* 17.6 (2017), 3982–3988.
- [77] Jiyoung Moon, Masoud Alahbakhshi, Abouzar Gharajeh, Quanwei Li, Zhitong Li, Ross Haroldson, Sunah Kwon, Roberta Hawkins, Moon J. Kim, Walter Hu, Xiang Zhang, Anvar Zakhidov, and Qing Gu. "Quasi-CW Lasing from Directly Patterned and Encapsulated Perovskite Cavity at 260 K". *ACS Photonics* 9.6 (2022).
- [78] Yufei Jia, Ross A. Kerner, Alex J. Grede, Barry P. Rand, and Noel C. Giebink. "Factors that Limit Continuous-Wave Lasing in Hybrid Perovskite Semiconductors". *Advanced Optical Materials* 8.2 (2020), 1901514.
- [79] Guichuan Xing, Nripan Mathews, Swee Sien Lim, Natalia Yantara, Xinfeng Liu, Dharani Sabba, Michael Grätzel, Subodh Mhaisalkar, and Tze Chien Sum. "Low-temperature solution-processed wavelength-tunable perovskites for lasing". *Nature Materials* 13.5 (2014), 476–480.
- [80] P. Brenner, U. W. Paetzold, G. A. Turnbull, N. C. Giebink, I. D.W. Samuel, U. Lemmer, and I. A. Howard. "Comment on "Room-Temperature Continuous-Wave Operation of Organometal Halide Perovskite Lasers"". *ACS Nano* 13.11 (2019), 12257–12258.
- [81] A. Haugeneder, M. Neges, C. Kallinger, W. Spirkl, Uli Lemmer, J. Feldmann, M. C. Amann, and U. Scherf. "Nonlinear emission and recombination in conjugated polymer waveguides". *Journal of Applied Physics* 85.2 (1999), 1124–1130.

- [82] Hannu P. Pasanen, Paola Vivo, Laura Canil, Antonio Abate, and Nikolai Tkachenko. “Refractive index change dominates the transient absorption response of metal halide perovskite thin films in the near infrared”. *Physical Chemistry Chemical Physics* 21.27 (2019), 14663–14670.
- [83] Kai Chen, Alex J. Barker, Francis L. C. Morgan, Jonathan E. Halpert, and Justin M. Hodgkiss. “Effect of Carrier Thermalization Dynamics on Light Emission and Amplification in Organometal Halide Perovskites”. *The Journal of Physical Chemistry Letters* 6.1 (2015), 153–158.
- [84] Henning Mescher, Fabian Schackmar, Helge Eggers, Tobias Abzieher, Marcus Zuber, Elias Hamann, Tilo Baumbach, Bryce S. Richards, Gerardo Hernandez-Sosa, Ulrich W. Paetzold, and Uli Lemmer. “Flexible Inkjet-Printed Triple Cation Perovskite X-ray Detectors”. *ACS Applied Materials and Interfaces* 12.13 (2020), 15774–15784.
- [85] Haotong Wei and Jinsong Huang. “Halide lead perovskites for ionizing radiation detection”. *Nature Communications* 10.1 (2019).
- [86] Tobias Haeger, Maximilian Wilmes, Ralf Heiderhoff, and Thomas Riedl. “Simultaneous Mapping of Thermal Conductivity, Thermal Diffusivity, and Volumetric Heat Capacity of Halide Perovskite Thin Films: A Novel Nanoscopic Thermal Measurement Technique”. *Journal of Physical Chemistry Letters* 10.11 (2019), 3019–3023.
- [87] T. A. Tyson, W. Gao, Y. S. Chen, S. Ghose, and Y. Yan. “Large thermal motion in Halide Perovskites”. *Scientific Reports* 7.1 (2017), 1–10.
- [88] Noriko Onoda-Yamamuro, Takasuke Matsuo, and Hiroshi Suga. “Calorimetric and IR spectroscopic studies of phase transitions in methylammonium trihalogenoplumbates (II)<sup>†</sup>”. *Journal of Physics and Chemistry of Solids* 51.12 (1990), 1383–1395.
- [89] Tobias Haeger, Ralf Heiderhoff, and Thomas Riedl. “Thermal properties of metal-halide perovskites”. *Journal of Materials Chemistry C* 8.41 (2020), 14289–14311.
- [90] Jacky Even, Laurent Pedesseau, Jean Marc Jancu, and Claudine Katan. “Importance of spin-orbit coupling in hybrid organic/inorganic perovskites for photovoltaic applications”. *Journal of Physical Chemistry Letters* 4.17 (2013), 2999–3005.
- [91] Jacky Even, Laurent Pedesseau, Claudine Katan, Mikaël Kepenekian, Jean-Sébastien Lauret, Daniel Saponi, and Emmanuelle Deleporte. “Solid-State Physics Perspective on Hybrid Perovskite Semiconductors”. *The Journal of Physical Chemistry C* 119.19 (2015), 10161–10177.
- [92] Huyen T. Pham, The Duong, Klaus J. Weber, and Jennifer Wong-Leung. “Insights into Twinning Formation in Cubic and Tetragonal Multi-cation Mixed-Halide Perovskite”. *ACS Materials Letters* 2.4 (2020), 415–424.

- 
- [93] Patrik Ščajev, Džiugas Litvinas, Vaiva Sorišū Tė, Gediminas Kreiza, Sandra Stanionytė, and Saulius Juršėnas. “Crystal Structure Ideality Impact on Bimolecular, Auger, and Diffusion Coefficients in Mixed-Cation Cs<sub>x</sub>MA<sub>1-x</sub>PbBr<sub>3</sub> and Cs<sub>x</sub>FA<sub>1-x</sub>PbBr<sub>3</sub> Perovskites”. *Journal of Physical Chemistry C* 123.39 (2019).
- [94] K. G. Svantesson and N. G. Nilsson. “The temperature dependence of the Auger recombination coefficient of undoped silicon”. *J. Phys. C Solid State Phys.* 12.23 (1979), 5111–5120.
- [95] N. K. Dutta and R. J. Nelson. “The case for Auger recombination in In<sub>1-x</sub>Ga<sub>x</sub>As<sub>y</sub>P<sub>1-y</sub>”. *Journal of Applied Physics* 53.1 (1982), 74–92.
- [96] S. Hausser, G. Fuchs, A. Hangleiter, K. Streubel, and W. T. Tsang. “Auger recombination in bulk and quantum well InGaAs”. *Applied Physics Letters* 56.10 (1990), 913–915.
- [97] L. Huldt, N. G. Nilsson, and K. G. Svantesson. “The temperature dependence of band-to-band Auger recombination in silicon”. *Appl. Phys. Lett.* 35.10 (1979), 776–777.
- [98] W. Lochmann. “Phonon-assisted auger recombination in indirect gap semiconductors”. *Phys. status solidi* 45.2 (1978), 423–432.
- [99] K. G. Svantesson and N. G. Nilsson. “The temperature dependence of the Auger recombination coefficient of undoped silicon”. *Journal of Physics C: Solid State Physics* 12.23 (1979), 5111–5120.
- [100] L. Huldt. “Band-to-band auger recombination in indirect gap semiconductors”. *Phys. status solidi* 8.1 (1971), 173–187.
- [101] W. Lochmann. “Phonon-assisted auger recombination in semiconductors”. *Phys. status solidi* 40.1 (1977), 285–292.
- [102] H. C. Casey. “Temperature dependence of the threshold current density in InP-Ga<sub>0.28</sub>In<sub>0.72</sub>As<sub>0.6</sub>P<sub>0.4</sub> ( $\lambda=1.3 \mu\text{m}$ ) double heterostructure lasers”. *Journal of Applied Physics* 56.7 (1984), 1959–1964.
- [103] Liang Qin, Longfeng Lv, Chunhai Li, Lijie Zhu, QiuHong Cui, Yufeng Hu, Zhidong Lou, Feng Teng, and Yanbing Hou. “Temperature dependent amplified spontaneous emission of vacuum annealed perovskite films”. *RSC Adv.* 7 (26 2017), 15911–15916.
- [104] Antonio Balena, Andrea Perulli, Manuel Fernandez, Maria Luisa De Giorgi, Georgian Nedelcu, Maksym V. Kovalenko, and Marco Anni. “Temperature Dependence of the Amplified Spontaneous Emission from CsPbBr<sub>3</sub> Nanocrystal Thin Films”. *The Journal of Physical Chemistry C* 122.10 (2018), 5813–5819.
- [105] Giovanni Morello, Stefania Milanese, Maria Luisa De Giorgi, Nicola Calisi, Stefano Caporali, Francesco Biccari, Naomi Falsini, Anna Vinattieri, and Marco Anni. “Temperature-Dependent Amplified Spontaneous Emission in CsPbBr<sub>3</sub> Thin Films Deposited by Single-Step RF-Magnetron Sputtering”. *Nanomaterials* 13.2 (2023).
- [106] Larry A. Coldren, Scott W. Corzine, and Milan L. Mašanović. “Diode Lasers and Photonic Integrated Circuits”. *Diode Lasers Photonic Integr. Circuits* (2012).

- [107] M.J. Adams. “Theoretical effects of exponential band tails on the properties of the injection laser”. *Solid-State Electronics* 12.8 (1969), 661–669.
- [108] Adam D. Wright, Carla Verdi, Rebecca L. Milot, Giles E. Eperon, Miguel A. Pérez-Osorio, Henry J. Snaith, Feliciano Giustino, Michael B. Johnston, and Laura M. Herz. “Electron–phonon coupling in hybrid lead halide perovskites”. *Nature Communications* 7.1 (2016), 11755.
- [109] Yang Li, Julie Roger, Isabel Allegro, Jan C. Fischer, Qihao Jin, Uli Lemmer, Ian A. Howard, and Ulrich W. Paetzold. “Lasing from Laminated Quasi-2D/3D Perovskite Planar Heterostructures”. *Advanced Functional Materials* 32.27 (2022), 1–8.
- [110] Jing Li, Junjie Si, Lu Gan, Yang Liu, Zhizhen Ye, and Haiping He. “Simple Approach to Improving the Amplified Spontaneous Emission Properties of Perovskite Films”. *ACS Applied Materials and Interfaces* 8.48 (2016), 32978–32983.
- [111] Xin Zeng, Zhengzheng Liu, Huijun Du, Zhujun Wang, Maohan Li, Mingyu Pi, Jianjun Tan, Dingke Zhang, Jie Yang, and Juan Du. “Achieving Low Threshold and High Optical Gain Amplified Spontaneous Emission in MAPbI<sub>3</sub> Perovskite Films via Symmetric Waveguide Effect”. *Advanced Optical Materials* 10.23 (2022), 1–11.
- [112] Li Jiang, Zhishan Fang, Haoran Lou, Chen Lin, Zhanhang Chen, Jing Li, Haiping He, and Zhizhen Ye. “Achieving long carrier lifetime and high optical gain in all-inorganic CsPbBr<sub>3</sub> perovskite films via top and bottom surface modification”. *Physical Chemistry Chemical Physics* 21.39 (2019), 21996–22001.
- [113] Woochul Lee, Huashan Li, Andrew B Wong, Dandan Zhang, Minliang Lai, Yi Yu, Qiao Kong, Elbert Lin, Jeffrey J Urban, Jeffrey C Grossman, and Peidong Yang. “Ultralow thermal conductivity in all-inorganic halide perovskites.” *Proceedings of the National Academy of Sciences of the United States of America* 114.33 (2017), 8693–8697.
- [114] Zema Chu, Qiufeng Ye, Yang Zhao, Fei Ma, Zhigang Yin, Xingwang Zhang, Jingbi You, Z Chu, Q Ye, Y Zhao, F Ma, Z Yin, X Zhang, and J You. “Perovskite Light-Emitting Diodes with External Quantum Efficiency Exceeding 22% via Small-Molecule Passivation”. *Advanced Materials* 33.18 (2021), 2007169.
- [115] Jingzhen Li, Ling Zhang, Zema Chu, Chenhao Dong, Ji Jiang, Zhigang Yin, Jingbi You, Jinliang Wu, Wei Lan, and Xingwang Zhang. “Amplified Spontaneous Emission with a Low Threshold from Quasi-2D Perovskite Films via Phase Engineering and Surface Passivation”. *Advanced Optical Materials* 10.6 (2022), 2102563.
- [116] Yanqin Feng, Yuman Zhang, Chengyi Duan, Minglin Zhao, and Jun Dai. “Optical properties of CsFAMA-based perovskite film and its application in the inverted solar cells with poly(methyl methacrylate) passivation layer”. *Opt. Mater. Express* 12.8 (2022), 3262–3272.
- [117] M. Hammer. *1D mode solver for dielectric multilayer slab waveguides*. Available at <https://www.computational-photonics.eu/oms.html>.

- 
- [118] Shu Yu Liang, Yue Feng Liu, Hai Jing Zhang, Zhi Kun Ji, and Hong Xia. "High-Quality Patterning of CsPbBr<sub>3</sub> Perovskite Films through Lamination-Assisted Femtosecond Laser Ablation toward Light-Emitting Diodes". *ACS Applied Materials and Interfaces* 14.41 (2022), 46958–46963.
- [119] Chi Ta Li, Kuan Lin Lee, Sea Fue Wang, and Lung Chien Chen. "Low turn-on voltage CsPbBr<sub>3</sub> perovskite light-emitting diodes with regrowth crystal MAPbBr<sub>3</sub> hole transport layer". *Journal of Materials Research and Technology* 22 (2023), 375–381.
- [120] Neda Pourdavoud, Tobias Haeger, Andre Mayer, Piotr Jacek Cegielski, Anna Lena Giesecke, Ralf Heiderhoff, Selina Olthof, Stefan Zaefferer, Ivan Shutsko, Andreas Henkel, David Becker-Koch, Markus Stein, Marko Cehovski, Ouacef Charfi, Hans-Hermann Johannes, Detlef Rogalla, Max Christian Lemme, Martin Koch, Yana Vaynzof, Klaus Meerholz, Wolfgang Kowalsky, Hella-Christin Scheer, Patrick Görrn, and Thomas Riedl. "Room-Temperature Stimulated Emission and Lasing in Recrystallized Cesium Lead Bromide Perovskite Thin Films". *Advanced Materials* 31.39 (2019), 1903717.
- [121] Sjoerd A. Veldhuis, Pablo P. Boix, Natalia Yantara, Mingjie Li, Tze Chien Sum, Nripan Mathews, and Subodh G. Mhaisalkar. "Perovskite Materials for Light-Emitting Diodes and Lasers". *Advanced Materials* 28.32 (2016), 6804–6834.
- [122] Yang Tang, Junhan Guo, Bin Liu, Liang Qin, Zhenbo Deng, Yufeng Hu, Feng Teng, Zhidong Lou, and Yanbing Hou. "Amplified Spontaneous Emission from waveguide based on Hybrid Quasi-2D Perovskite of Dion-Jacobson and Ruddlesden-Popper phases". *Journal of Materials Chemistry C* (2023).
- [123] Xue Lou, Lianfei Yao, Jiaqi Zhang, Ning Sui, Min Wu, Wei Zhang, Zhihui Kang, Xiaochun Chi, Qiang Zhou, Hanzhuang Zhang, and Yinghui Wang. "Competition of Carrier Kinetics Contributes to Amplified Spontaneous Emission in Quasi-2D/3D (PBA)<sub>2</sub>MA<sub>n</sub>-1Pb<sub>n</sub>Br<sub>3n+1</sub> Thin Films under Strip Light Mode". *Journal of Physical Chemistry Letters* 14.17 (2023), 4050–4057.
- [124] Meili Li, Qinggang Gao, Peng Liu, Qing Liao, Haihua Zhang, Jiannian Yao, Wenping Hu, Yishi Wu, Hongbing Fu, M Li, P Liu, W Hu, H Fu, Q Gao, Q Liao, H Zhang, J Yao, and Y Wu. "Amplified Spontaneous Emission Based on 2D Ruddlesden–Popper Perovskites". *Advanced Functional Materials* 28.17 (2018), 1707006.
- [125] Haihua Zhang, Qing Liao, Yishi Wu, Zhaoyi Zhang, Qinggang Gao, Peng Liu, Meili Li, Jiannian Yao, and Hongbing Fu. "2D Ruddlesden-Popper Perovskites Microring Laser Array". *Advanced Materials* 30.15 (2018), 1706186.
- [126] Lei Lei, Dovletgeldi Seyitliyev, Samuel Stuard, Juliana Mendes, Qi Dong, Xiangyu Fu, Yi-an Chen, Siliang He, Xueping Yi, Liping Zhu, Chih-hao Chang, Harald Ade, Kenan Gundogdu, and Franky So. "Efficient Energy Funneling in Quasi-2D Perovskites: From Light Emission to Lasing". *Advanced Materials* 32.16 (2020), 1906571.

- [127] Matthew R. Leyden, Shinobu Terakawa, Toshinori Matsushima, Shibin Ruan, Kenichi Goushi, Morgan Auffray, Atula S. D. Sandanayaka, Chuanjiang Qin, Fatima Bencheikh, and Chihaya Adachi. “Distributed Feedback Lasers and Light-Emitting Diodes Using 1-Naphthylmethylammonium Low-Dimensional Perovskite”. *ACS Photonics* 6.2 (2019), 460–466.
- [128] Zhibin Wang, Fuzhi Wang, Wenda Sun, Ruihao Ni, Siqian Hu, Jiyan Liu, Bing Zhang, Ahmed Alsaed, Tasawar Hayat, and Zhan’ao Tan. “Manipulating the Trade-off Between Quantum Yield and Electrical Conductivity for High-Brightness Quasi-2D Perovskite Light-Emitting Diodes”. *Advanced Functional Materials* 28.47 (2018), 1804187.
- [129] Bong Woo Kim, Jin Hyuck Heo, Jin Kyoung Park, David Sunghwan Lee, Hyunik Park, Seong Yeon Kim, Jun Ho Kim, and Sang Hyuk Im. “Morphology controlled nanocrystalline CsPbBr<sub>3</sub> thin-film for metal halide perovskite light emitting diodes”. *Journal of Industrial and Engineering Chemistry* 97 (2021), 417–425.
- [130] Linlin Liu, Shi E. Yang, Ping Liu, and Yongsheng Chen. “High-quality and full-coverage CsPbBr<sub>3</sub> thin films via electron beam evaporation with post-annealing treatment for all-inorganic perovskite solar cells”. *Solar Energy* 232 (2022), 320–327.
- [131] Matthew R. Leyden, Toshinori Matsushima, Chuanjiang Qin, Shibin Ruan, Hao Ye, and Chihaya Adachi. “Amplified spontaneous emission in phenylethylammonium methylammonium lead iodide quasi-2D perovskites”. *Physical Chemistry Chemical Physics* 20.22 (2018), 15030–15036.
- [132] Fei Zheng, Weijian Chen, Tongle Bu, Kenneth P. Ghiggino, Fuzhi Huang, Yibing Cheng, Patrick Tapping, Tak W. Kee, Baohua Jia, and Xiaoming Wen. “Triggering the Passivation Effect of Potassium Doping in Mixed-Cation Mixed-Halide Perovskite by Light Illumination”. *Advanced Energy Materials* 9.24 (2019).
- [133] Wenjian Shen, Zhengli Wu, Gaoyuan Yang, Yingjie Kong, Wangnan Li, Guijie Liang, Fuzhi Huang, Yi Bing Cheng, and Jie Zhong. “Differentiated Functions of Potassium Interface Passivation and Doping on Charge-Carrier Dynamics in Perovskite Solar Cells”. *Journal of Physical Chemistry Letters* 13.14 (2022), 3188–3196.
- [134] Pingli Qin, Jiliang Zhang, Guang Yang, Xueli Yu, and Gang Li. “Potassium-intercalated rubrene as a dual-functional passivation agent for high efficiency perovskite solar cells”. *Journal of Materials Chemistry A* 7.4 (2019), 1824–1834.
- [135] Liang Kuai, Yusheng Wang, Zixiang Zhang, Yingguo Yang, Yuanshuai Qin, Tian Wu, Yajuan Li, Youyong Li, Tao Song, Xingyu Gao, Lu Wang, and Baoquan Sun. “Passivating Crystal Boundaries with Potassium-Rich Phase in Organic Halide Perovskite”. *Solar RRL* 3.5 (2019), 1900053.
- [136] Mojtaba Abdi-Jalebi, Zahra Andaji-Garmaroudi, Stefania Cacovich, Camille Stavrakas, Bertrand Philippe, Johannes M. Richter, Mejd Alsari, Edward P. Booker, Eline M. Hutter, Andrew J. Pearson, Samuele Lilliu, Tom J. Savenije, Håkan Rensmo, Giorgio Divitini, Caterina Ducati, Richard H. Friend, and Samuel D. Stranks. “Maximizing and stabilizing luminescence from halide perovskites with potassium passivation”. *Nature* 555.7697 (2018), 497–501.

- 
- [137] Zeguo Tang, Takeru Bessho, Fumiyasu Awai, Takumi Kinoshita, Masato M. Maitani, Ryota Jono, Takuro N. Murakami, Haibin Wang, Takaya Kubo, Satoshi Uchida, and Hiroshi Segawa. "Hysteresis-free perovskite solar cells made of potassium-doped organometal halide perovskite". *Scientific Reports* 7.1 (2017), 12183.
- [138] Cheng Chen, Tongtong Xuan, Yang Yang, Fan Huang, Tianliang Zhou, Le Wang, and Rong Jun Xie. "Passivation Layer of Potassium Iodide Yielding High Efficiency and Stable Deep Red Perovskite Light-Emitting Diodes". *ACS Applied Materials and Interfaces* 14.14 (2022), 16404–16412.
- [139] Fei Yang, Hongting Chen, Rui Zhang, Xiaoke Liu, Weizhuo Zhang, Ji Bin Zhang, Feng Gao, and Lei Wang. "Efficient and Spectrally Stable Blue Perovskite Light-Emitting Diodes Based on Potassium Passivated Nanocrystals". *Advanced Functional Materials* 30.10 (2020), 1–7.
- [140] Minh Tam Hoang, Amandeep Singh Pannu, Cheng Tang, Yang Yang, Ngoc Duy Pham, Ke Gui, Xiaoxiang Wang, Soniya Yambem, Prashant Sonar, Aijun Du, and Hongxia Wang. "Potassium Doping to Enhance Green Photoemission of Light-Emitting Diodes Based on CsPbBr<sub>3</sub> Perovskite Nanocrystals". *Advanced Optical Materials* 8.18 (2020), 2000742.
- [141] Shouqiang Huang, Bo Wang, Qi Zhang, Zhichun Li, Aidang Shan, and Liang Li. "Postsynthesis Potassium-Modification Method to Improve Stability of CsPbBr<sub>3</sub> Perovskite Nanocrystals". *Advanced Optical Materials* 6.6 (2018), 1–7.
- [142] Mojtaba Abdi-Jalebi, Zahra Andaji-Garmaroudi, Andrew J. Pearson, Giorgio Divitini, Stefania Cacovich, Bertrand Philippe, Håkan Rensmo, Caterina Ducati, Richard H. Friend, and Samuel D. Stranks. "Potassium- and Rubidium-Passivated Alloyed Perovskite Films: Optoelectronic Properties and Moisture Stability". *ACS Energy Letters* 3.11 (2018), 2671–2678.
- [143] Lianfeng Zhao, Kwangdong Roh, Sara Kacmoli, Khaled Al Kurdi, Xiao Liu, Stephen Barlow, Seth R Marder, Claire Gmachl, Barry P Rand, L Zhao, K Roh, S Kacmoli, X Liu, C Gmachl, B P Rand, K Al Kurdi, S Barlow, and S R Marder. "Nanosecond-Pulsed Perovskite Light-Emitting Diodes at High Current Density". *Adv. Mater.* 33.44 (2021), 2104867.
- [144] Guangrong Jin, Tanghao Liu, Yuanzhao Li, Jiadong Zhou, Dengliang Zhang, Peiyuan Pang, Ziqing Ye, Zhaohui Xing, Guichuang Xing, Jiangshan Chen, and Dongge Ma. "Low-dimensional phase suppression and defect passivation of quasi-2D perovskites for efficient electroluminescence and low-Threshold amplified spontaneous emission". *Nanoscale* 14.3 (2022), 919–929.
- [145] Daehan Kim, Hee Joon Jung, Ik Jae Park, Bryon W. Larson, Sean P. Dunfield, Chuanxiao Xiao, Jekyung Kim, Jinhui Tong, Passarut Boonmongkolras, Su Geun Ji, Fei Zhang, Seong Ryul Pae, Minkyu Kim, Seok Beom Kang, Vinayak Dravid, Joseph J. Berry, Jin Young Kim, Kai Zhu, Dong Hoe Kim, and Byungha Shin. "Efficient, stable silicon tandem cells enabled by anion-engineered wide-bandgap perovskites". *Science* 368.6487 (2020), 155–160.

- [146] Isabel Allegro, Víctor Bonal, Emil R. Mamleyev, José M. Villalvilla, José A. Quintana, Qihao Jin, María A. Díaz-García, and Uli Lemmer. “Distributed Feedback Lasers by Thermal Nanoimprint of Perovskites Using Gelatin Gratings”. *ACS Applied Materials & Interfaces* 15.6 (2023), 8436–8445.
- [147] Marc Pascual, Nathan Bigan, Amin M’Barki, Rick Mental, Isabel Allegro, and Ulrich Lemmer. “All-printed SU8-perovskite DFB laser”. *Advanced Fabrication Technologies for Micro/Nano Optics and Photonics XVI*. Vol. 12433. International Society for Optics and Photonics. SPIE, 2023, 124330E.
- [148] Qing Zhang, Qiuyu Shang, Rui Su, T. Thu Ha Do, and Qihua Xiong. “Halide Perovskite Semiconductor Lasers: Materials, Cavity Design, and Low Threshold”. *Nano Letters* 21.5 (2021), 1903–1914.
- [149] Yang Mi, Yangguang Zhong, Qing Zhang, and Xinfeng Liu. “Continuous-Wave Pumped Perovskite Lasers”. *Advanced Optical Materials* 7.17 (2019), 1900544.
- [150] I D W Samuel and G A Turnbull. “Organic Semiconductor Lasers”. *Chemical Reviews* (2007).
- [151] Michael Saliba, Simon M. Wood, Jay B. Patel, Pabitra K. Nayak, Jian Huang, Jack A. Alexander-Webber, Bernard Wenger, Samuel D. Stranks, Maximilian T. Hörantner, Jacob Tse-Wei Wang, Robin J. Nicholas, Laura M. Herz, Michael B. Johnston, Stephen M. Morris, Henry J. Snaith, and Moritz K. Riede. “Structured Organic-Inorganic Perovskite toward a Distributed Feedback Laser”. *Advanced Materials* 28.5 (2016), 923–929.
- [152] Alexander Palatnik, Changsoon Cho, Chonghe Zhang, Markas Sudzius, Martin Kroll, Stefan Meister, and Karl Leo. “Control of Emission Characteristics of Perovskite Lasers through Optical Feedback”. *Advanced Photonics Research* 2.12 (2021), 2100177.
- [153] Andre Mayer, Maximilian Buchmüller, Si Wang, Christian Steinberg, Marc Papenheim, Hella-Christin Scheer, Neda Pourdavoud, Tobias Haeger, and Thomas Riedl. “Thermal nanoimprint to improve the morphology of MAPbX<sub>3</sub> (MA = methylammonium, X = I or Br)”. *Journal of Vacuum Science & Technology B, Nanotechnology and Microelectronics: Materials, Processing, Measurement, and Phenomena* 35.6 (2017), 06G803.
- [154] Julie Roger, Luisa K. Schorn, Minasadat Heydarian, Ahmed Farag, Thomas Feeney, Daniel Baumann, Hang Hu, Felix Laufer, Weiyuan Duan, Kaining Ding, Andreas Lambertz, Paul Fassel, Matthias Worgull, and Ulrich W. Paetzold. “Laminated Monolithic Perovskite/Silicon Tandem Photovoltaics”. *Advanced Energy Materials* 12.27 (2022), 2200961.
- [155] Sergey V Makarov, Valentin Milichko, Elena V Ushakova, Mikhail Omelyanovich, Andrea Cerdan Pasaran, Ross Haroldson, Balasubramaniam Balachandran, Honglei Wang, Walter Hu, Yuri S Kivshar, and Anvar A Zakhidov. “Multifold Emission Enhancement in Nanoimprinted Hybrid Perovskite Metasurfaces”. *ACS Photonics* 4 (2017), 735.

- 
- [156] Supratim Basak, Ofer Bar-On, and Jacob Scheuer. “Metal-halide perovskite-based edge emitting lasers”. *Optical Materials Express* 12.2 (2022), 375.
- [157] Guy L. Whitworth, Jonathan R. Harwell, David N. Miller, Gordon J. Hedley, Wei Zhang, Henry J. Snaith, Graham A. Turnbull, and Ifor D. W. Samuel. “Nanoimprinted distributed feedback lasers of solution processed hybrid perovskites”. *Optics Express* 24.21 (2016), 23677.
- [158] Philipp Brenner, Mareike Stulz, Dorothee Kapp, Tobias Abzieher, Ulrich W. Paetzold, Aina Quintilla, Ian A. Howard, Heinz Kalt, and Uli Lemmer. “Highly stable solution processed metal-halide perovskite lasers on nanoimprinted distributed feedback structures”. *Applied Physics Letters* 109.14 (2016), 141106.
- [159] Ofer Bar-On, Philipp Brenner, Uli Lemmer, and Jacob Scheuer. “Micro Lasers by Scalable Lithography of Metal-Halide Perovskites”. *Advanced Materials Technologies* 1800212 (2018), 1800212.
- [160] Xiaoyu Yang, Jiang Wu, Tanghao Liu, and Rui Zhu. “Patterned Perovskites for Optoelectronic Applications”. *Small Methods* 2.10 (2018), 1800110.
- [161] Piotr J. Cegielski, Anna Lena Giesecke, Stefanie Neutzner, Caroline Porschatis, Marina Gandini, Daniel Schall, Carlo A. R. Perini, Jens Bolten, Stephan Suckow, Satender Kataria, Bartos Chmielak, Thorsten Wahlbrink, Annamaria Petrozza, and Max C. Lemme. “Monolithically Integrated Perovskite Semiconductor Lasers on Silicon Photonic Chips by Scalable Top-Down Fabrication”. *Nano Letters* 18.11 (2018), 6915–6923.
- [162] Lumeng Liang, Teng Ma, Ziyi Chen, Jiabin Wang, Jinning Hu, Yucong Ji, Weili Shen, and Jun Chen. “Patterning Technologies for Metal Halide Perovskites: A Review”. *Advanced Materials Technologies* (2022), 2200419.
- [163] Beomjin Jeong, Hyowon Han, Hong Hee Kim, Won Kook Choi, Youn Jung Park, and Cheolmin Park. “Polymer-Assisted Nanoimprinting for Environment- And Phase-Stable Perovskite Nanopatterns”. *ACS Nano* 14.2 (2020), 1645–1655.
- [164] Qi Dong, Xiangyu Fu, Dovletgeldi Seyitliyev, Kasra Darabi, Juliana Mendes, Lei Lei, Yi-An Chen, Chih-Hao Chang, Aram Amassian, Kenan Gundogdu, and Franky So. “Cavity Engineering of Perovskite Distributed Feedback Lasers”. *ACS Photonics* 9.9 (2022), 3124–3133.
- [165] Shyh Wang. “Principles of Distributed Feedback and Distributed Bragg-Reflector Lasers”. *IEEE Journal of Quantum Electronics* (1974).
- [166] William Streifer, Donald R. Scifres, and Robert D. Burnham. “Coupled Wave Analysis of DFB and DBR Lasers”. *IEEE Journal of Quantum Electronics* 13.4 (1977), 134–141.
- [167] Chongjun He, Guoan Zha, Chenguang Deng, Yang An, Rong Mao, Youwen Liu, Yuangang Lu, and Ziyun Chen. “Refractive Index Dispersion of Organic–Inorganic Hybrid Halide Perovskite  $\text{CH}_3\text{NH}_3\text{PbX}_3$  ( $\text{X}=\text{Cl}, \text{Br}, \text{I}$ ) Single Crystals”. *Crystal Research and Technology* 54.5 (2019).

- [168] William Streifer, D. Scifres, and R. Burnham. “Coupling coefficients for distributed feedback single- and double-heterostructure diode lasers”. *IEEE Journal of Quantum Electronics* 11.11 (1975), 867–873.
- [169] Sidney S. Yang, Yun-Ching Chang, Pei-Chun Yen, and Ya-Chang Chou. “Effects of duty cycle on the characteristics of a composite surface-emitting organic distributed feedback laser”. *Journal of the Optical Society of America B* 24.8 (2007), 1857.
- [170] Xin Liu. “Organic Semiconductor Lasers and Tailored Nanostructures for Raman Spectroscopy”. PhD thesis. Karlsruhe Institute of Technology, 2015.
- [171] Víctor Bonal, José A. Quintana, José M. Villalvilla, Pedro G. Boj, Rafael Muñoz-Mármol, Jose C. Mira-Martínez, and María A. Díaz-García. “N,N’-Bis(3-methylphenyl)-N,N’-dyphenylbenzidine Based Distributed Feedback Lasers with Holographically Fabricated Polymeric Resonators”. *Polymers* 13.21 (2021), 3843.
- [172] Jérémie Werner, Gizem Nogay, Florent Sahli, Terry Chien Jen Yang, Matthias Bräuning, Gabriel Christmann, Arnaud Walter, Brett A. Kamino, Peter Fiala, Philipp Löper, Sylvain Nicolay, Quentin Jeangros, Bjoern Niesen, and Christophe Ballif. “Complex Refractive Indices of Cesium-Formamidinium-Based Mixed-Halide Perovskites with Optical Band Gaps from 1.5 to 1.8 eV”. *ACS Energy Letters* 3.3 (2018), 742–747.
- [173] Philipp Löper, Michael Stuckelberger, Bjoern Niesen, Jérémie Werner, Miha Filipič, Soo Jin Moon, Jun Ho Yum, Marko Topič, Stefaan De Wolf, and Christophe Ballif. “Complex refractive index spectra of CH<sub>3</sub>NH<sub>3</sub>PbI<sub>3</sub> perovskite thin films determined by spectroscopic ellipsometry and spectrophotometry”. *Journal of Physical Chemistry Letters* 6.1 (2015), 66–71.
- [174] S. Collin, J. Rousset, D. Coutancier, A. Yaiche, S. Rives, S. Jutteau, R. Bodeux, and E. Raoult. “Optical Characterizations and Modelling of Semitransparent Perovskite Solar Cells for Tandem Applications”. *36th European Photovoltaic Solar Energy Conference and Exhibition* (2019), 757–763.
- [175] Neda Pourdavoud, André Mayer, Maximilian Buchmüller, Kai Brinkmann, Tobias Häger, Ting Hu, Ralf Heiderhoff, Ivan Shutsko, Patrick Görn, Yiwang Chen, Hella-Christin Scheer, and Thomas Riedl. “Distributed Feedback Lasers Based on MAPbBr<sub>3</sub>”. *Advanced Materials Technologies* 3.4 (2018), 1700253.
- [176] Florian Mathies, Philipp Brenner, Gerardo Hernandez-Sosa, Ian A. Howard, Ulrich W. Paetzold, and Uli Lemmer. “Inkjet-printed perovskite distributed feedback lasers”. *Optics Express* 26.2 (2018), A144.
- [177] H. Sirringhaus, T. Kawase, R. H. Friend, T. Shimoda, M. Inbasekaran, W. Wu, and E. P. Woo. “High-resolution inkjet printing of all-polymer transistor circuits”. *Science* 290.5499 (2000), 2123–2126.
- [178] Xiantao Jiang, Wenjia Li, Ting Hai, Rui Yue, Zhangwei Chen, Changshi Lao, Yanqi Ge, Guoqiang Xie, Qiao Wen, and Han Zhang. “Inkjet-printed MXene micro-scale devices for integrated broadband ultrafast photonics”. *npj 2D Materials and Applications* 2019 3:1 3.1 (2019), 1–9.

- 
- [179] Jing Zhang, Grigorij Muliuk, Joan Juvert, Sulakshna Kumari, Jeroen Goyvaerts, Bahawal Haq, Camiel Op De Beeck, Bart Kuyken, Geert Morthier, Dries Van Thourhout, Roel Baets, Guy Lepage, Peter Verheyen, Joris Van Campenhout, Agnieszka Gocalinska, James O'Callaghan, Emanuele Pelucchi, Kevin Thomas, Brian Corbett, António José Trindade, and Gunther Roelkens. "III-V-on-Si photonic integrated circuits realized using micro-transfer-printing". *APL Photonics* 4.11 (2019), 110803.
- [180] Daria Kohler, Isabel Allegro, Sentayehu Fetene Wondimu, Lothar Hahn, Wolfgang Freude, and Christian Koos. "Lasing in Si<sub>3</sub>N<sub>4</sub>-organic hybrid (SiNOH) waveguides". *Optics Express* 28.4 (2020), 5085.
- [181] Wenzhao Sun, Yilin Liu, Geyang Qu, Yubin Fan, Wei Dai, Yuhan Wang, Qinghai Song, Jiecai Han, and Shumin Xiao. "Lead halide perovskite vortex microlasers". *Nature Communications* 2020 11:1 11.1 (2020), 1–7.
- [182] Shuai Wang, Yilin Liu, Gang Li, Jing Zhang, Nan Zhang, Shumin Xiao, Qinghai Song, S Wang, Y Liu, G Li, J Zhang, N Zhang, S Xiao, and Q Song. "Lead Halide Perovskite Based Microdisk Lasers for On-Chip Integrated Photonic Circuits". *Advanced Optical Materials* 6.6 (2018), 1701266.
- [183] Songtao Chen and Arto Nurmikko. "Stable Green Perovskite Vertical-Cavity Surface-Emitting Lasers on Rigid and Flexible Substrates". *ACS Photonics* 4.10 (2017), 2486–2494.
- [184] Hongbo Zhang, Yuzhong Hu, Wen Wen, Bowen Du, Lishu Wu, Yu Chen, Shun Feng, Chenji Zou, Jingzhi Shang, Hong Jin Fan, and Ting Yu. "Room-temperature continuous-wave vertical-cavity surface-emitting lasers based on 2D layered organic-inorganic hybrid perovskites". *APL Materials* 9.7 (2021).
- [185] Songtao Chen, Cheng Zhang, Joonhee Lee, Jung Han, and Arto Nurmikko. "Hybrid Perovskite Vertical-Cavity Surface-Emitting Laser Deploying Nanoporous GaN Dielectric Reflector Technology". *2016 Conference on Lasers and Electro-Optics (CLEO)* (2016), 3–4.
- [186] Songtao Chen, Joonhee Lee, and Arto Nurmikko. "Green Vertical-Cavity Surface-Emitting Laser from Perovskite (CH(NH<sub>2</sub>)<sub>2</sub>PbBr<sub>3</sub>) Thin Films". *2017 Conference on Lasers and Electro-Optics (CLEO), San Jose, CA, USA 2* (2017), 5–6.
- [187] Modestos Athanasiou, Paris Papagiorgis, Andreas Manoli, Caterina Bernasconi, Maryna I. Bodnarchuk, Maksym V. Kovalenko, and Grigorios Itkos. "Efficient Amplified Spontaneous Emission from Solution-Processed CsPbBr<sub>3</sub> Nanocrystal Microcavities under Continuous Wave Excitation". *ACS Photonics* 8.7 (2021), 2120–2129.
- [188] Xiang Gao, Jie Lin, Xiaoyang Guo, Geng He, Deyue Zou, Tomohiro Ishii, Dezhong Zhang, Chenyang Zhao, Hongmei Zhan, Jing Song Huang, Xingyuan Liu, Chihaya Adachi, Chuanjiang Qin, and Lixiang Wang. "Room-Temperature Continuous-Wave Microcavity Lasers from Solution-Processed Smooth Quasi-2D Perovskite Films with Low Thresholds". *Journal of Physical Chemistry Letters* (2023), 2493–2500.

- [189] G. Canazza, F. Scotognella, G. Lanzani, S. De Silvestri, M. Zavelani-Rossi, and D. Comoretto. “Lasing from all-polymer microcavities”. *Laser Physics Letters* 11.3 (2014).
- [190] Qiaoshuang Zhang, Qihao Jin, Adrian Mertens, Christian Rainer, Robert Huber, Jan Fessler, Gerardo Hernandez-Sosa, Uli Lemmer, Q Zhang, Q Jin, A Mertens, C Rainer, R Huber, J Fessler, G Hernandez-Sosa, and U Lemmer. “Fabrication of Bragg Mirrors by Multilayer Inkjet Printing”. *Advanced Materials* 34.33 (2022), 2201348.
- [191] Mohd Sharizal Alias, Zhixiong Liu, Abdullah Al-atawi, Tien Khee Ng, Tom Wu, and Boon S. Ooi. “Continuous-wave optically pumped green perovskite vertical-cavity surface-emitter”. *Optics Letters* 42.18 (2017), 3618.
- [192] Paola Lova, Paolo Giusto, Francesco Di Stasio, Giovanni Manfredi, Giuseppe M. Paternò, Daniele Cortecchia, Cesare Soci, and Davide Comoretto. “All-polymer methylammonium lead iodide perovskite microcavities”. *Nanoscale* 11.18 (2019), 8978–8983.
- [193] Azhar Fakharuddin, Michael Seybold, Antonio Agresti, Sara Pescetelli, Fabio Matteocci, Muhammad Irfan Haider, Susanne T. Birkhold, Hao Hu, Rajiv Giridharagopal, Muhammad Sultan, Iván Mora-Seró, Aldo Di Carlo, and Lukas Schmidt-Mende. “Perovskite-Polymer Blends Influencing Microstructures, Nonradiative Recombination Pathways, and Photovoltaic Performance of Perovskite Solar Cells”. *ACS Applied Materials and Interfaces* 10.49 (2018), 42542–42551.
- [194] Emiliano R. Martins, Yue Wang, Alexander L. Kanibolotsky, Peter J. Skabara, Graham A. Turnbull, and Ifor D. W. Samuel. “Low-Threshold Nanoimprinted Lasers Using Substructured Gratings for Control of Distributed Feedback”. *Advanced Optical Materials* 1.8 (2013), 563–566.
- [195] Fabian Schackmar, Helge Eggers, Markus Frericks, Bryce S. Richards, Uli Lemmer, Gerardo Hernandez-Sosa, and Ulrich W. Paetzold. “Perovskite Solar Cells with All-Inkjet-Printed Absorber and Charge Transport Layers”. *Advanced Materials Technologies* 6.2 (2021), 2000271.
- [196] Rebecca L. Milot, Giles E. Eperon, Thomas Green, Henry J. Snaith, Michael B. Johnston, and Laura M. Herz. “Radiative Monomolecular Recombination Boosts Amplified Spontaneous Emission in  $\text{HC}(\text{NH}_2)_2\text{SnI}_3$  Perovskite Films”. *Journal of Physical Chemistry Letters* 7.20 (2016), 4178–4184.
- [197] Hitoshi Mizuno, Takumi Nishimura, Yuya Mekata, Naho Kurahashi, Momonosuke Odani, Van-Cao Nguyen, Yuhi Inada, Takeshi Yamao, Fumio Sasaki, and Hisao Yanagi. “Distributed feedback laser with methylammonium lead bromide embedded in channel-type waveguides”. *Japanese Journal of Applied Physics* 60.SB (2021), SBBH11.
- [198] Kwangdong Roh, Lianfeng Zhao, and Barry P. Rand. “Tuning Laser Threshold within the Large Optical Gain Bandwidth of Halide Perovskite Thin Films”. *ACS Photonics* 8.8 (2021), 2548–2554.

- 
- [199] Kwangdong Roh, Lianfeng Zhao, William B. Gunnarsson, Zhengguo Xiao, Yufei Jia, Noel C. Giebink, and Barry P. Rand. “Widely Tunable, Room Temperature, Single-Mode Lasing Operation from Mixed-Halide Perovskite Thin Films”. *ACS Photonics* 6.12 (2019), 3331–3337.
- [200] Matthew R. Leyden, Toshinori Matsushima, Fatima Bencheikh, and Chihaya Adachi. “Film transfer of structured organo-lead-halide perovskite for low-cost lasing applications”. *Applied Physics Letters* 115.14 (2019), 141106.
- [201] Junyi Gong, Yue Wang, Sheng Liu, Pan Zeng, Xilu Yang, Rongqing Liang, Qiongrong Ou, Xiang Wu, and Shuyu Zhang. “All-inorganic perovskite-based distributed feedback resonator”. *Optics Express* 25.24 (2017), A1154.
- [202] J. R. Harwell, G. L. Whitworth, G. A. Turnbull, and I. D. W. Samuel. “Green Perovskite Distributed Feedback Lasers”. *Scientific Reports* 7.1 (2017), 11727.



# List of Figures

1.1	Comparison of semiconductors for laser diode applications in terms of resistive heating. . . . .	4
3.1	Fundamental interaction processes of a photon and a two-level material system. . . . .	12
3.2	Schematic of the energy levels and respective transition processes to generate a population inversion and stimulated emission. . . . .	13
3.3	Schematic of a slab waveguide. . . . .	15
3.4	Schematic solution of the laser rate equations. . . . .	17
3.5	Schematic of a DFB laser. . . . .	19
3.6	Schematic illustration of random lasing. . . . .	19
4.1	Perovskite crystal unit cell and organic cation molecules. . . . .	21
4.2	Schematic of (quasi-)2D perovskites. . . . .	23
4.3	Perovskite absorption and PL spectra. . . . .	25
4.4	Recombination mechanisms. . . . .	26
4.5	PLQE as a function of excitation density. . . . .	27
4.6	TRPL decays with ABC and SRH models. . . . .	29
5.1	Molecular structure of chemicals used for surface treatments. . . . .	34
5.2	Hot embossing machine employed for thermal nanoimprint lithography. . . . .	35
5.3	Diagram of a standard nanoimprint process. . . . .	36
5.4	Schematic of the ICCD setup for spectroscopic measurements. . . . .	38
5.5	Schematic of the transient reflection setup. . . . .	41
5.6	Illustration of the AFM working principle. . . . .	43
5.7	Profilometer measurements of perovskite film thickness. . . . .	44
6.1	Substrate configuration with and without waveguiding and respective emission spectra. . . . .	50
6.2	Temperature-dependent input-output characteristics of perovskite emission on sapphire and Si substrates. . . . .	51
6.3	Transient reflection spectra at 80 K. . . . .	52
6.4	Temperature-dependent carrier dynamics. . . . .	52
6.5	Linear relation between initial transient reflection signal and pump fluence. . . . .	54
6.6	Carrier density for bimolecular dominated dynamics as a function of temperature. . . . .	54
6.7	Comparison of measured and modelled light-in-light-out curves for BC model. . . . .	55

6.8	Recombination coefficients as a function of temperature. . . . .	56
6.9	Error estimation for the bimolecular rate considering pump-induced heating.	57
6.10	Temperature-dependent ASE threshold with exponential and band-tail fit.	61
6.11	Influence of non-radiative Auger losses on the ASE threshold as a function of temperature. . . . .	62
6.12	Temperature-dependent broadening of PL emission . . . . .	64
6.13	PL emission within the ASE band. . . . .	64
6.14	Comparison of the temperature-dependent rate of photon emission at threshold into the total PL and the ASE band . . . . .	65
7.1	Schematic of reference and passivated samples with PMMA and TOPO/PMMA.	69
7.2	ASE performance of reference and passivated films with PMMA and TOPO/PMMA. . . . .	70
7.3	Fluence-dependent transient PL. . . . .	72
7.4	PLQY of reference, PMMA and TOPO/PMMA films. . . . .	73
7.5	Waveguide mode profile for air and PMMA cladding and respective overlap factor. . . . .	74
7.6	Emission collected from the surface corresponding to scattered PL. . . .	75
7.7	ASE performance of quasi-2D films as a function of annealing temperature.	78
7.8	Band-gap red shift indicating the transition from quasi-2D to 3D CsPbBr <sub>3</sub> with increasing annealing temperature. . . . .	80
7.9	Emission and relative PLQY characteristics of excitonic and free-carrier recombination. . . . .	81
7.10	ASE performance of potassium-doped triple-cation films. . . . .	83
7.11	Potassium doping effect on lifetime and radiative recombination. . . . .	85
7.12	AFM images of films with different potassium concentrations. . . . .	86
8.1	Schematic cross-sectional view of DFB laser. . . . .	91
8.2	Refractive index as a function of wavelength. . . . .	92
8.3	Waveguide modes of slab waveguide glass/perovskite/air. . . . .	93
8.4	Absolute value of the feedback coupling coefficient as a function of fill factor for the second-order perovskite DFB resonator. . . . .	94
8.5	Effect of refractive index dispersion on the effective index of the waveguide mode and on the grating period. . . . .	95
8.6	DCG nano-gratings fabricated by holographic lithography. . . . .	97
8.7	Thermal nanoimprint lithography of dichromated gelatin (DCG) stamps and resulting perovskite nano-structured films. . . . .	99
8.8	Spectra of imprinted perovskite DFB laser and ASE of an unpatterned film.	100
8.9	Input-output characteristics of a DFB laser and a pristine perovskite film.	101
8.10	High-resolution spectra of laser and ASE peaks. . . . .	102
8.11	Polarisation of the lasing and ASE emission. . . . .	103
8.12	Polarisation of the PL emitted from the DFB grating region. . . . .	103
8.13	High-resolution spectra of lasing emission as a function of the grating period. . . . .	104

---

8.14	Wavelength of the lasing peak as a function of grating period and the resulting $n_{\text{eff}}$ of each mode. . . . .	105
8.15	Printed DFB laser. . . . .	106
8.16	Laser emission of a printed DFB with SU-8 lines. . . . .	108
8.17	Schematic of the vertical micro-cavity architecture with inkjet printed DBRs on glass substrates sandwiching a thin perovskite layer. . . . .	109
8.18	Perovskite film on bottom DBR exhibiting ASE. . . . .	109
8.19	Laminated DBRs with a perovskite inter-layer forming a vertical single-mode micro-cavity. . . . .	110
B.1	Summary of reported laser thresholds for second-order perovskite DFBs since 2016. . . . .	153
C.1	AFM image of a pristine perovskite film. . . . .	154
D.1	SEM images of a DCG stamp after four imprint rounds. . . . .	155
D.2	Emission of a DFB laser imprinted with a used stamp. . . . .	155



# List of Tables

4.1	Parameters used for model simulation, based on reported values of similar perovskite materials in the literature. <sup>[8, 23, 24, 57–61]</sup> . . . . .	30
7.1	Trap density $n_t$ determined by the global fit of the SRH model to the fluence-dependent TRPL data of each sample architecture. . . . .	72
7.2	Summary of tested material systems with respective fabrication details and ASE thresholds. All films have a BABr/CsPbBr <sub>3</sub> molar ratio of 0.7/1 and a PEG/CsPbBr <sub>3</sub> weight ratio of 0.01/1. Three samples of each composition were measured on two spots, and the presented threshold is the mean of all results (CsPbBr <sub>3</sub> and CsBr+PbBr <sub>2</sub> ). For samples with PEG additive and $T_{\text{anneal}} = 70$ °C, only one sample provided a decent threshold curve to extract a threshold value. . . . .	77
7.3	Mean threshold values and standard deviation of samples fabricated with one and two-powder precursors of CsPbBr <sub>3</sub> , corresponding to the data illustrated in Figure 7.7 and demonstrating the range overlap between ASE values. . . . .	78
7.4	Bromine (Br %) and iodine (I %) content as a function of potassium (K %) concentration and respective ASE resonance wavelength $\lambda_{\text{ASE}}$ . Br and I concentrations are calculated based on the assumption that the added K from the KI precursor binds exclusively with Br from the perovskite crystal structure and that the remaining I (from the KI additive) is integrated into the lattice, replacing the Br ions. . . . .	84
8.1	Design parameters for perovskite layer and grating stamp used for fabricating second-order DFB lasers by NIL, where $d$ is the perovskite film thickness, $h$ the grating height, $FF$ the grating fill factor and $\Lambda$ the grating period. A sketch of the geometry with the visual representation of these parameters is illustrated in Figure 8.1. . . . .	94
A.1	Comparison of recombination coefficients $k_{\text{bi}}$ and $k_{\text{Auger}}$ at room temperature for different perovskite composition and measurement techniques. .	151
B.1	Summary of literature reports on lasing thresholds of solution-processed perovskite second-order DFB lasers. The notation of the composition employed in this section ((Cs <sub>0.1</sub> (MA <sub>0.17</sub> FA <sub>0.83</sub> )Pb <sub>0.84</sub> (I <sub>0.8</sub> Br <sub>0.2</sub> ) <sub>2.68</sub> ) is simplified to CsMAFAPb(I <sub>0.8</sub> Br <sub>0.2</sub> ) <sub>2.68</sub> . Threshold values measured at low temperatures are marked with <sup>x</sup> for T = 260 K, and <sup>+</sup> for T = 160 K. . . . .	152



# Acronyms and Abbreviations

<b>HTA</b>	high-temperature annealing
<b>EEA</b>	exciton-exciton annihilation
<b>MOCVD</b>	metalorganic vapour-phase epitaxy
<b>MAPI</b>	methylammonium lead iodide
<b>PMMA</b>	poly(methyl methacrylate)
<b>PEG</b>	polyethylene glycol
<b>CB</b>	chlorobenzene
<b>IPA</b>	isopropanol
<b>BABr</b>	butylammonium bromide
<b>TOPO</b>	trioctylphosphine oxide
<b>FA</b>	formamidinium
<b>MA</b>	methylammonium
<b>DMF</b>	N,N-dimethylformamide
<b>DMSO</b>	dimethyl sulfoxide
<b>EBL</b>	electron beam lithography
<b>RIE</b>	reactive ion etching
<b>IBE</b>	ion beam etching
<b>CW</b>	continuous-wave
<b>NIL</b>	nanoimprint lithography
<b>VCSEL</b>	vertical-cavity surface-emitting laser
<b>MQW</b>	multiple quantum well
<b>LED</b>	light-emitting diode
<b>PeLED</b>	perovskite light-emitting diode
<b>DFB</b>	distributed feedback
<b>TE</b>	transverse electric
<b>TM</b>	transverse magnetic
<b>SWG</b>	symmetric waveguide
<b>FWHM</b>	full width at half maximum
<b>ASE</b>	amplified spontaneous emission
<b>WP</b>	waveguide passivation
<b>DP</b>	defect passivation
<b>SRH</b>	Shockley-Read-Hall
<b>PD</b>	photodiode
<b>ICCD</b>	intensified charge-coupled device
<b>TA</b>	transient absorption
<b>TR</b>	transient reflection
<b>NIR</b>	near-infrared

<b>SHG</b>	second harmonic generation
<b>OPA</b>	optical parametric amplifier
<b>TCSPC</b>	time-correlated single photon counting
<b>UV-VIS</b>	ultraviolet–visible
<b>UV</b>	ultraviolet
<b>FDTS</b>	perfluorodecyltrichlorosilane
<b>PLQY</b>	photoluminescence quantum yield
<b>PLQE</b>	photoluminescence quantum efficiency
<b>TRPL</b>	time-resolved photoluminescence
<b>PL</b>	photoluminescence
<b>AFM</b>	atomic force microscope
<b>SEM</b>	scanning electron microscope
<b>CBM</b>	conduction band minimum
<b>VBM</b>	valence band maximum
<b>DBR</b>	distributed Bragg reflector
<b>HL</b>	holographic lithography
<b>DCG</b>	dichromated gelatin

# Acknowledgements

I am deeply grateful to the following individuals and institutions for their unwavering support and encouragement throughout my doctoral journey:

**Prof. Dr. Uli Lemmer** – My *Doktorvater* – I appreciate the invaluable opportunity to pursue my Ph.D. at LTI and the trust and autonomy granted me. Further, Uli demonstrated exceptional encouragement beyond the realm of research, as he wholeheartedly supported my participation in educational and academic activities, both domestically and abroad. Uli's honest interest in the development of students, both personally and academically, sets an exemplary standard that has inspired me on this academic journey.

**Dr. Ian Howard** – I sincerely appreciate Ian's dedicated supervision while we worked together. His unwavering support, insightful guidance, and curious mindset greatly enriched my research experience.

**Prof. Dr. María Díaz-García, Víctor Bonal, and Dr. Marina Gerhard, Prof. Dr. Martin Koch** – I am thankful for the opportunity to work and learn alongside you in the field of thin film lasers and fundamental carrier interaction processes. Our collaborations have been a great motivation source and significantly enriched my research.

The graduate schools **KSOP and 3DMM2O** offered many valuable development opportunities that have contributed to my academic and professional growth. In the scope of the KSOP program, I am deeply grateful for **my KSOP mentor, Danays Kunka**, for her guidance, mentorship, and invaluable insights throughout my journey. Her support has been vital in shaping my development during these years.

**Astrid, Claudia, and Nicole** – Ich danke den engagierten Mitgliedern des Sekretariats für ihre unermüdlichen Bemühungen um einen reibungslosen Ablauf der administrativen Aspekte und für ihre Geduld, mit der sie mir gezeigt haben, wie man sich in den Feinheiten der deutschen Bürokratie zurechtfindet.

**Mario Süttsch, Hans Vögele und Klaus Ochs** – Ich bin den Mitgliedern des Werkstatt-Teams sehr dankbar. Ihr Fachwissen und ihre Unterstützung ermöglichten die erfolgreiche Umsetzung der technischen Aspekte meiner Forschung.

**Dr. Lothar Hahn, Felix Geislhöringer, Dr. Aina Quintilla, Marc Schneider, Alban Muslija, Uwe Köhler, Andreas Bacher, Christian Kayser, and Judith Hohmann** – Mein herzlicher Dank gilt eurem qualifizierten und engagierten technischen Wissen und Erfahrung, die dafür gesorgt haben, dass meine Forschung Zugang zu den notwendigen Ressourcen hatte. Eure Unterstützung hat mich auf dieser Strecke sehr inspiriert.

I am fortunate to have been surrounded by brilliant and supportive colleagues and friends from the **MNOS, Taskforce, LTI, MZE and IMT** teams. Your generosity and camaraderie made this journey more enjoyable, as well as your cakes, ice creams, and paper beers. I give special thanks to Andres, Pirmin, Ahmed, Saba, Kristina, Adrian, Anne, Robert, Malte M., Donie, Sara, Prof. Dr. Bryce, Dr. Dmitry, Marius, Jan Fischer, Paul, Qihao, Qiaoshuang, Andreas Frölich, Orlando, Nils, Ngei, and Milian, who all shared their knowledge and support with me. To my **office mates**, who shared the ups and downs of the research life from up close, your support provided a welcoming and productive environment, especially Henning, Dominik, Junchi, Mohamed, and Raphael. To those who offered valuable insights and guidance beyond the confines of my university – **Josh Burrow, João Lourenço, Cornelius Nawrath, and my mentors Daria Kohler, and Anda Robotin**, I am grateful for your willingness to contribute to my personal and intellectual growth.

Next to the research activities, I would like to express my sincere appreciation to my dedicated colleagues within the **student chapter OSKar**, especially Ankita, Lilyn, Max, Luna, Onur, and Jesus, for their enthusiasm and unwavering hard work in organising various events. Additionally, I extend my gratitude to the international optical societies **OPTICA** and **SPIE** for their financial and otherwise support, which has played a pivotal role in the success of our initiatives and my personal growth.

Students I had the privilege of supervising and working with – **Gamal, Yvonne, Christian Rainer, Avishek, Saeed, Shamim, Lesly, Jona, Patrick, Max, and Kenta** – our shared research projects have been a constant source of inspiration. I am proud of the contributions you have made to our academic community.

I appreciate those who meticulously reviewed and provided feedback on my thesis, ensuring its clarity and accuracy – Yang, Simon, Max, Robert, Ihteaz, Pirmin, Julie, Christian R, Emil, Kristina, Idoia, Thomas, and Orlando.

I am incredibly grateful for my **friends Cláudia<sup>1</sup>, Gerrit, Matilde, Francisca, Katerina, Filip, Mona, Chris, Alexandra**, and especially the friends I built via the university: **Julie, Simon, Ihteaz, Thomas<sup>2</sup>, Emil M., Lilyn, Luna, Max, and Diana**, who stood by my side through the highs and lows of this journey, your unwavering friendship and encouragement provided the emotional fortitude I needed to persevere. Your belief in me was a constant source of motivation.

Last but certainly not least, my most profound appreciation goes to my **family**, particularly Titi, São, Mãe, Pai, Alex, and to **Diego**, your unconditional love, support, and understanding have been my rock throughout this endeavour. You believed in me when I had doubts, and your unwavering faith has carried me through. You have been a driving force behind my personal and professional achievements. Gracias!

No matter how fleeting, each interaction has contributed to the tapestry of my academic journey, and I am deeply thankful for the collective support that propelled me forward.

---

<sup>1</sup> who blackmailed me into putting her name first

<sup>2</sup> and all his fancy barista cappuccinos.

**Part V**  
**Appendix**



# A Literature Summary of Recombination Rate Coefficients

**Table A.1:** Comparison of recombination coefficients  $k_{bi}$  and  $k_{Auger}$  at room temperature for different perovskite composition and measurement techniques.

Perovskite	$k_{bi}$ ( $\cdot 10^{-10} \text{ cm}^3 \text{ s}^{-1}$ )	$k_{Auger}$ ( $\cdot 10^{-29} \text{ cm}^6 \text{ s}^{-1}$ )	Measurement
Triple cation	1.1	3.2	TR (ASE suppressed)
Double cation <sup>[23]</sup>	0.2	200	THz spectroscopy
MAPbI <sub>3</sub> <sup>[8]</sup>	2.5	-	Absorption
MAPbI <sub>3</sub> <sup>[24]</sup>	0.6	15.5	THz spectroscopy
MAPbI <sub>3</sub> <sup>[57]</sup>	23	-	TA (ASE not suppressed)
MAPbBr <sub>3</sub> <sup>[58]</sup>	1.7	-	TRPL
FAPbI <sub>3</sub> <sup>[59]</sup>	1	2	THz spectroscopy
FAPbBr <sub>3</sub> <sup>[59]</sup>	10	15	THz spectroscopy
MAPbI <sub>3</sub> <sup>[53]</sup>	0.17	2.8	PLQY
MAPbI <sub>3</sub>	0.81	11	TA
MAPb(ICl) <sub>3</sub>	0.79	18	
MAPbBr <sub>3</sub> <sup>[52]</sup>	0.7	6	
FASnI <sub>3</sub> <sup>[196]</sup>	2.3	0.93	TA

## B Literature Summary of Solution-processed Second-order DFB Lasers

Material	Threshold	Pump laser		Year	Ref
CsMAFAPb(I <sub>0.8</sub> Br <sub>0.2</sub> ) <sub>2.68</sub>	81 μJ/cm <sup>2</sup>	532 nm	1 ns	2023	[146]
MAPbI <sub>3</sub>	240 μJ/cm <sup>2</sup>	532 nm	5 ns	2022	[156]
MAPbBr <sub>3</sub>	4.5 mJ/cm <sup>2</sup> <sup>x</sup>	355 nm	17 ns	2022	[77]
MAPbBr <sub>3</sub>	20 μJ/cm <sup>2</sup>	400 nm	150 fs	2022	[164]
MAPbBr <sub>3</sub>	47 μJ/cm <sup>2</sup>			2021	[197]
MAPbI <sub>3</sub> ,MAPbBr <sub>3</sub> , MAPb(I <sub>x</sub> Br <sub>1-x</sub> ) <sub>3</sub>	3 - 9.5 μJ/cm <sup>2</sup>	532nm, 355 nm	40 ps	2021	[198]
(NMA/PEA) <sub>2</sub> - FA <sub>n-1</sub> Pb <sub>n</sub> Br <sub>3n+1</sub>	45 - 59 W/cm <sup>2</sup> / 5 - 33 μJ/cm <sup>2</sup>	488 nm / 337 nm	CW / 3 ns	2020	[54]
PEA <sub>2</sub> FA <sub>3</sub> Pb <sub>4</sub> Br <sub>13</sub>	10 μJ/cm <sup>2</sup>	400 nm	150 fs	2020	[126]
CsPbBr <sub>3</sub>	7.2 μJ/cm <sup>2</sup>	355 nm	0.3 ns	2019	[120]
CsMAPb(I <sub>x</sub> Br <sub>1-x</sub> ) <sub>3</sub>	4 μJ/cm <sup>2</sup>	355 nm	40 ps	2019	[199]
MAPbI <sub>3</sub>	7 μJ/cm <sup>2</sup>	337 nm	0.8 ns	2019	[127]
MAPbI <sub>3</sub>	14 μJ/cm <sup>2</sup>	337 nm	0.8 ns	2019	[200]
MAPbI <sub>3</sub>	75 μJ/cm <sup>2</sup>	532 nm	5 ns	2018	[159]
MAPbI <sub>3</sub>	270 μJ/cm <sup>2</sup>	532 nm	1 ns	2018	[176]
CsPbBrI <sub>2</sub>	33 μJ/cm <sup>2</sup>	355 nm	90 ps	2017	[201]
MAPbI <sub>3</sub>	17 kW/cm <sup>2</sup> <sup>+</sup>	445 nm	CW	2017	[19]
MAPbBr <sub>3</sub>	6 μJ/cm <sup>2</sup>	355 nm	1 ns	2017	[202]
MAPbI <sub>3</sub>	110 μJ/cm <sup>2</sup>	450 nm	4 ns	2016	[157]
MAPbI <sub>3</sub>	120 μJ/cm <sup>2</sup>	532 nm	1 ns	2016	[158]

**Table B.1:** Summary of literature reports on lasing thresholds of solution-processed perovskite second-order DFB lasers. The notation of the composition employed in this section ((Cs<sub>0.1</sub>(MA<sub>0.17</sub>FA<sub>0.83</sub>)Pb<sub>0.84</sub>(I<sub>0.8</sub>Br<sub>0.2</sub>)<sub>2.68</sub>) is simplified to CsMAFAPb(I<sub>0.8</sub>Br<sub>0.2</sub>)<sub>2.68</sub>. Threshold values measured at low temperatures are marked with <sup>x</sup> for T = 260 K, and <sup>+</sup> for T = 160 K.

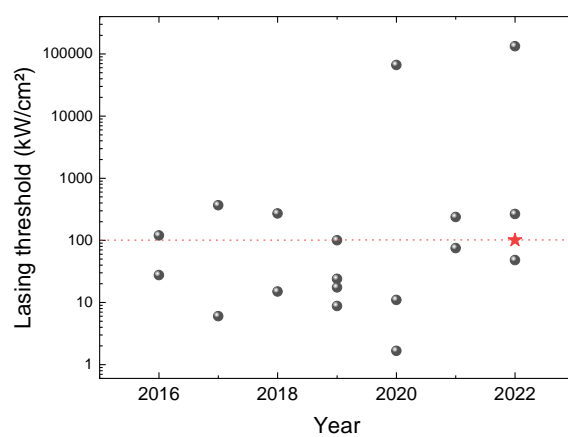


**Figure B.1:** Summary of reported laser thresholds of solution-processed second-order DFB lasers since 2016. Threshold values were converted to kW/cm<sup>2</sup> by considering the excitation pulse duration for better comparison. The red star corresponds to the lasers presented in this chapter, and the red dashed line serves as a visual guideline. Table B.1 in the Appendix details values, pump conditions and references. Reprinted with permission from [146]. Copyright 2023 American Chemical Society.

## C Topography of Triple-cation Perovskite Thin Film

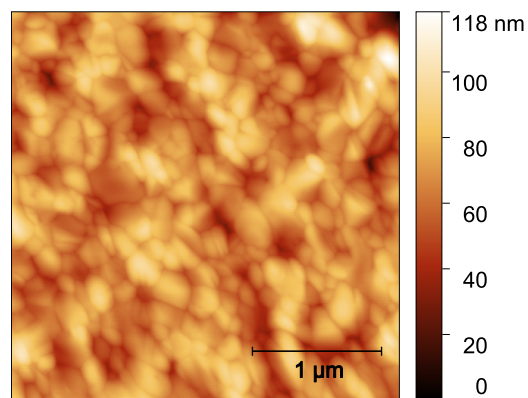


**Figure C.1:** AFM image of a pristine triple-cation perovskite film with an RMS roughness of 13 nm.

## D Characterisation of Nanoimprinted Lasers With Used Stamps

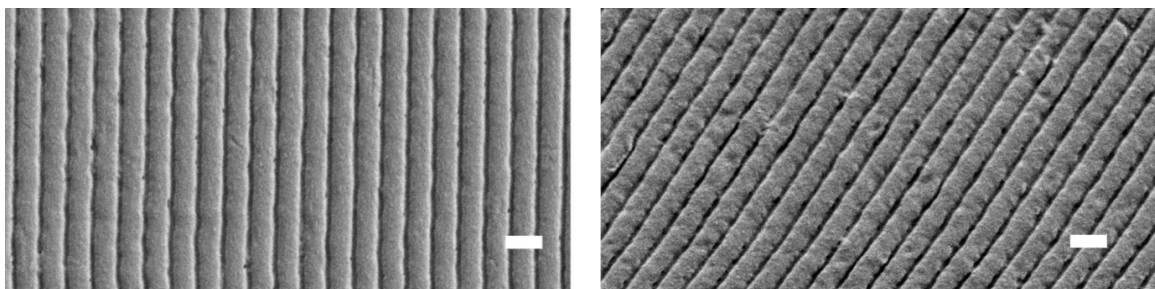


**Figure D.1:** SEM images of a DCG stamp after four imprint rounds. The left image shows a top view, and the right image is taken with a 30 ° inclination. The scale bars represent a length of 500 nm. Reprinted with permission from [146]. Copyright 2023 American Chemical Society.

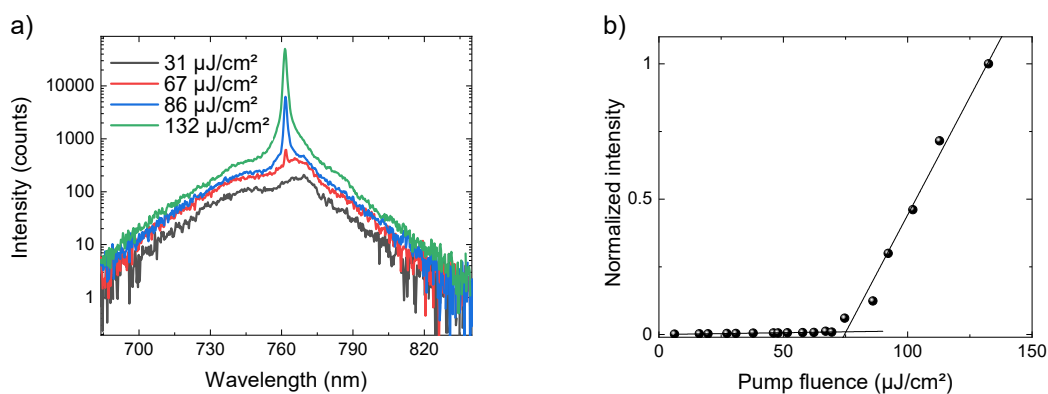


**Figure D.2:** Emission of a DFB laser imprinted with a used DCG stamp. a) Emission spectra as a function of excitation fluence. b) Input-output characteristics displaying a lasing threshold of 75 μJ/cm<sup>2</sup>. Adapted with permission from [146]. Copyright 2023 American Chemical Society.